

RUPERTO-CAROLA-UNIVERSITY  
HEIDELBERG



Florian Huber

---

Elastic and Proton Dissociative  $J/\psi$   
Photoproduction at low  $W_{\gamma p}$  with the H1  
Detector at HERA

2012

DESY-THESIS-2013-004

PHYSICAL INSTITUTE

---



# **Dissertation**

submitted to the  
Combined Faculties of the Natural Sciences and Mathematics  
of the Ruperto-Carola-University of Heidelberg, Germany  
for the degree of

## **Doctor of Natural Sciences**

Put forward by

**Dipl. Phys. ETH Florian Huber**

born in Frauenfeld, Switzerland  
citizen of Pfyn (TG), Switzerland

Oral examination: 20<sup>th</sup> of December 2012



**Elastic and Proton Dissociative  $J/\psi$   
Photoproduction at low  $W_{\gamma p}$  with the H1  
Detector at HERA**

Referees: Prof. Dr. André Schöning

Prof. Dr. Hans-Christian Schultz-Coulon



## Abstract

Elastic and proton dissociative photoproduction of  $J/\psi$  mesons is measured with the H1 detector at the HERA electron proton collider in the photon virtuality phase space of  $Q^2 \lesssim 2.5 \text{ GeV}^2$ . Two data sets are analysed, one measured with a nominal proton beam energy of 920 GeV, corresponding to an  $ep$  centre of mass energy of 318 GeV and one recorded with a reduced beam energy of 460 GeV, corresponding to an  $ep$  centre of mass energy of 225 GeV. The combination of the two data sets allow to perform the  $J/\psi$  measurement with central tracks in an extended kinematic phase space in a photon proton centre of mass energy range of  $20 \text{ GeV} < W_{\gamma p} < 110 \text{ GeV}$ . The integrated luminosity for both data sets are  $130 \text{ pb}^{-1}$  and  $10.8 \text{ pb}^{-1}$ , respectively, corresponding to more than two times the statistics used in previous H1 analyses. Due to an online selection purely based on tracks both leptonic decay channels  $J/\psi \rightarrow ee$  and  $J/\psi \rightarrow \mu\mu$  are available for the analysis. Elastic ( $\gamma p \rightarrow J/\psi p$ ) and proton dissociative ( $\gamma p \rightarrow J/\psi Y$ ) differential  $\gamma p$  cross sections are determined in a simultaneous measurement as function of the squared momentum transfer at the proton vertex  $t$  and as function of  $W_{\gamma p}$  by means of an unfolding procedure, taking not only all bin correlations into account, but also the correlation between the elastic and proton dissociative process. The obtained elastic and proton dissociative differential cross sections are analysed in a simultaneous fit, taking the full statistical covariance matrices and systematic uncertainty sources into account.

## Zusammenfassung

Elastische und protondissoziative Photoproduktion von  $J/\psi$ -Mesonen wurde mit dem H1 Detektor am HERA Elektron-Proton-Kollider im Photon-Virtualitätsphasenraum von  $Q^2 \lesssim 2.5 \text{ GeV}^2$  gemessen. Zwei Datensätze wurden analysiert, der eine, gemessen bei einer nominellen Protonstrahlenergie von 920 GeV, was einer  $ep$ -Schwerpunktsenergie von 318 GeV entspricht, der andere wurde gemessen bei einer reduzierten Strahlenergie von 460 GeV, was zu einer tieferen  $ep$ -Schwerpunktsenergie von 225 GeV führt. Dies erlaubt die  $J/\psi$  Messung mit zentralen Spuren in einem erweiterten kinematischen Phasenraum hin zu einem tieferen Photon-Proton-Schwerpunktsenergiebereich von  $20 \text{ GeV} < W_{\gamma p} < 110 \text{ GeV}$ . Die integrierte Luminosität für beide Datensätze sind  $130 \text{ pb}^{-1}$  und  $10.8 \text{ pb}^{-1}$ , was mehr als dem doppelten an Statistik gegenüber vorherigen H1 Analysen entspricht. Wegen der Onlineselektion basierend auf Spuren, sind beide leptonischen Zerfallskanäle  $J/\psi \rightarrow ee$  und  $J/\psi \rightarrow \mu\mu$  verfügbar. In einer simultanen Messung von  $J/\psi$  Photoproduktion werden elastische ( $\gamma p \rightarrow J/\psi p$ ) und protondissoziative ( $\gamma p \rightarrow J/\psi Y$ ) differentielle  $\gamma p$ -Wirkungsquerschnitte bestimmt als Funktion des quadrierten Impulsübertrages am Protonvertex  $t$  und als Funktion von  $W_{\gamma p}$ , mittels einer Entfaltungs-Prozedure, welche nicht nur die Bin-Korrelationen, sondern auch die Korrelation zwischen elastischem und protondissoziativem Prozess berücksichtigt. Die gemessenen elastischen und protondissoziativen differentiellen Wirkungsquerschnitte wurden untersucht mittels simultan durchgeführten Fits, unter Einbezug der vollen statistischen Kovarianzmatrizen und unter Berücksichtigung der systematischen Fehlerquellen.



# Contents

<b>1</b>	<b>Introduction</b>	<b>1</b>
<b>2</b>	<b>Theory</b>	<b>5</b>
2.1	Diffraction	5
2.1.1	Historical milestones in diffraction	5
2.1.2	Regimes in diffraction	6
2.1.3	The scattering amplitude and cross section	8
2.1.4	Kinematic of two body to two body interactions	10
2.1.4.1	Crossing symmetry	11
2.1.5	$S$ -matrix	12
2.1.6	Regge theory	14
2.1.6.1	Regge's idea	14
2.1.6.2	Regge trajectories	15
2.1.6.3	Cross section behaviour in the context of Regge trajectories	15
2.1.7	The Pomeron	17
2.1.7.1	The Pomeron in the QCD picture	18
2.1.8	Total cross section	18
2.1.9	Diffraction dissociation	20
2.1.9.1	The eikonal ansatz	22
2.1.9.2	The triple Regge model	22
2.1.10	Screening effect	24
2.2	HERA Kinematics	24
2.2.1	Kinematics of electron proton scattering	24
2.2.2	From $ep$ to $\gamma p$ cross sections	26
2.3	Diffraction vector meson production in $ep$ interaction	26
2.3.1	Diffraction kinematics for vector meson production	26
2.3.2	Diffraction vector meson production mechanisms	27
2.3.2.1	The vector dominance model	27
2.3.2.2	Dipole model	28
<b>3</b>	<b>HERA and the H1 detector</b>	<b>29</b>
3.1	The HERA accelerator	29
3.2	The H1 experiment	30
3.2.1	Tracking detectors	31
3.2.1.1	Central track reconstruction	31

3.2.2	The H1 calorimeter detectors . . . . .	34
3.2.3	The H1 central muon detector . . . . .	34
3.2.4	The H1 forward detectors . . . . .	34
3.2.4.1	PLUG calorimeter . . . . .	34
3.2.4.2	Forward tagger system . . . . .	36
3.2.4.3	The forward muon detector . . . . .	36
<b>4</b>	<b>Monte Carlo Simulations</b>	<b>39</b>
4.1	The DiffVM Monte Carlo generator . . . . .	40
4.1.1	$J/\psi$ production . . . . .	40
4.1.1.1	Simulation of photon exchange in DiffVM . . . . .	40
4.1.1.2	Elastic $J/\psi$ production . . . . .	42
4.1.1.3	Proton dissociation $J/\psi$ production . . . . .	42
4.1.1.4	Parameters of generated MC samples . . . . .	43
4.1.2	QED corrections with PHOTOS . . . . .	43
4.1.3	$\psi(2S)$ background production . . . . .	44
4.2	GRAPE – Dilepton Generator . . . . .	44
4.3	The CASCADE generator . . . . .	45
<b>5</b>	<b>Trigger and data periods</b>	<b>47</b>
5.1	What is a trigger and why is it needed? . . . . .	47
5.2	The H1 trigger system . . . . .	48
5.2.1	The level 1 trigger . . . . .	48
5.2.2	The level 2 trigger . . . . .	49
5.2.3	The level 3 trigger . . . . .	50
5.2.4	The level 4 trigger . . . . .	50
5.2.5	HERA II trigger upgrade . . . . .	50
5.2.5.1	The Fast Track Trigger (FTT) . . . . .	51
5.3	Trigger conditions . . . . .	52
5.4	Data periods . . . . .	54
<b>6</b>	<b>Data Analysis</b>	<b>57</b>
6.1	Reconstruction of kinematic variables . . . . .	57
6.1.1	Photoproduction region . . . . .	57
6.1.2	Reconstruction of the $J/\psi$ four-momentum . . . . .	58
6.1.3	Reconstruction of the di-lepton mass . . . . .	58
6.1.4	Reconstruction of $W_{\gamma p}$ . . . . .	58
6.1.5	Reconstruction of $t$ . . . . .	59
6.2	Kinematic phase space definition . . . . .	59
6.3	Track selection . . . . .	60
6.3.1	Standard H1 Lee West track . . . . .	60
6.3.2	$J/\psi$ daughter particles track selection . . . . .	60
6.4	Basic event selection . . . . .	61
6.5	Low $M_{\gamma}^{\text{gen}}$ restriction . . . . .	62
6.5.1	Performance of the empty calorimeter cut . . . . .	62
6.5.2	Contamination of inelastic $J/\psi$ process . . . . .	64
6.6	Lepton identification . . . . .	64
6.6.1	Electron identification . . . . .	64

6.6.2	Muon identification	65
6.6.2.1	Cosmic muon rejection	66
6.6.2.1.1	Cut compositions for cosmic muon rejection	66
6.6.2.1.2	Effect of cosmic muon rejection cut	67
6.6.2.2	Muon identification in the CMD	67
6.6.2.3	Muon identification in the calorimeter	69
6.6.2.3.1	Creation of performance plots for muon identification	69
6.6.2.3.2	KALEP estimator input quantities	70
6.6.2.4	Muon identification correction	70
6.6.2.4.1	Remaining systematic uncertainty after correction	72
6.7	Mass window cut	72
<b>7</b>	<b>Efficiencies</b>	<b>75</b>
7.1	Trigger efficiencies	75
7.1.1	Trigger efficiency distributions	76
7.2	Acceptance and selection efficiencies	81
7.2.1	Discussion of the selection efficiency	81
7.3	Resolutions	85
<b>8</b>	<b>Experimental tagging of proton dissociative events and modeling of forward energy flow</b>	<b>91</b>
8.1	Proton dissociative tagging quantity	92
8.1.1	Why are elastic and proton dissociative events overlapping on reconstruction level?	92
8.1.2	Forward detector quantities	92
8.1.3	Converting information from forward detectors into Boolean statements	94
8.1.4	Combination of single tagging information	96
8.2	Parameter estimation for forward energy flow	96
8.2.1	Procedure description for parameter determination	96
8.2.2	Reconstructed distributions after determination of the optimal parameter set	98
8.2.3	Discussion of fit result	98
<b>9</b>	<b>Cross section determination with <math>t</math> and <math>W_{\gamma p}</math> unfolding</b>	<b>103</b>
9.1	Introduction to unfolding	104
9.2	Collection of unfolding constituents	106
9.2.1	Binning	106
9.2.1.1	Binning on generator level	106
9.2.1.2	Binning on reconstruction level	106
9.2.2	Response matrix	107
9.2.2.1	Response matrix definition for unfolding the differential cross sections in $ t $	107
9.2.2.2	Response matrix definition for unfolding the cross sections in $W_{\gamma p}$	108
9.2.3	Determination of the reconstructed input vectors $y$	109
9.2.3.1	The muon channel	111
9.2.3.1.1	Fit model	111
9.2.3.1.2	Data fits	112
9.2.3.1.3	Bias study	112
9.2.3.2	The electron channel	114

9.2.3.3	$\psi(2S)$ background . . . . .	117
9.2.4	Regularisation . . . . .	120
9.2.4.1	An example for the regularisation matrix $L^2$ . . . . .	120
9.2.4.2	Example for estimation of $\tau$ parameter . . . . .	120
9.3	Cross section construction with unfolding . . . . .	121
9.4	Systematic uncertainties . . . . .	122
9.4.1	Normalisation uncertainty . . . . .	122
9.4.2	Response matrix variations . . . . .	123
9.4.2.1	Averaging mechanism for response matrix variations . . . . .	123
9.4.2.2	Calculating the effect of alternative response matrices on the $x$ vector . . . . .	123
9.4.2.3	Systematic sources . . . . .	124
9.4.2.3.1	Forward tagging . . . . .	124
9.4.2.3.2	Forward energy flow . . . . .	124
9.4.2.3.3	Elastic slope . . . . .	125
9.4.2.3.4	Muon identification . . . . .	125
9.4.2.3.5	Electron identification . . . . .	125
9.4.2.3.6	Empty calorimeter cut (EC) . . . . .	126
9.4.2.3.7	$Q^2$ and $R_{LT}$ dependence . . . . .	126
9.4.2.4	Propagated errors on true vector $x$ . . . . .	126
9.4.3	Input vector variations . . . . .	126
9.5	Control plot distributions . . . . .	131
9.5.1	Control plot construction . . . . .	132
9.5.1.1	Signal contribution . . . . .	132
9.5.1.2	Background contribution . . . . .	132
9.5.2	Control plot discussion . . . . .	133
<b>10</b>	<b>Results</b> . . . . .	<b>143</b>
10.1	Differential cross sections as function of $-t$ for the high energy data period . . . . .	143
10.1.1	Comparison with published results . . . . .	145
10.2	Differential cross sections as function of $-t$ for the low energy data period . . . . .	146
10.3	Cross sections as function of $W_{\gamma p}$ for high and low energy data periods . . . . .	149
10.3.1	Comparison with published results . . . . .	150
10.3.2	Rapidity gap survival probability corrections . . . . .	153
<b>11</b>	<b>Summary, conclusion and outlook</b> . . . . .	<b>155</b>
<b>A</b>	<b>Derivations</b> . . . . .	<b>157</b>
A.1	Derivation of inelasticity $y_{mh}$ using the modified Jacquet Blondel method . . . . .	157
A.2	Derivation of reconstruction of $t$ . . . . .	158
A.3	Derivation of “or” efficiency correction as applied for muon identification . . . . .	159
A.4	Derivation of shift $\Delta x$ on true, unfolded output vector, due to alternative response matrix . . . . .	159
<b>B</b>	<b>Number of <math>J/\psi</math> events</b> . . . . .	<b>161</b>
B.1	Di-muon mass distribution fits . . . . .	162
B.1.1	Di-muon mass distribution fits for the high energy data period . . . . .	162
B.1.2	Di-muon mass distribution fits for the low energy data period . . . . .	167
B.2	Number of $J/\psi$ events from di-muon mass fits . . . . .	171

B.3	Di-electron mass distribution after background subtraction . . . . .	173
B.3.1	Di-electron muon mass distribution after background subtraction for the high energy data period . . . . .	173
B.3.2	Di-electron muon mass distribution after background subtraction for the low energy data period . . . . .	178
B.4	Number of $J/\psi$ signal events from di-electron mass distributions . . . . .	181
<b>C</b>	<b>Least square parameter estimation with normalisation uncertainty</b>	<b>183</b>
C.1	A different representation . . . . .	184
<b>D</b>	<b>Cross section tables</b>	<b>185</b>
	<b>Bibliography</b>	<b>193</b>
	<b>Acknowledgement</b>	<b>209</b>



## Introduction

The driving force behind mankind since the dawn of time appears to be curiosity. Ancient Greek asked fundamental questions like “Where are we coming from?” and “What is the universe made of?”. Though the techniques of experimental observations became more sophisticated over the last couple of thousand years, these *basic* questions are nowadays as current as they have been. They are still hunting dreams of scientists all over the world.

When in the end of the 19<sup>th</sup> century Marie Curie discovered that radiation of uranium is connected with a process inside of the atoms and not due to any molecular composition, it marked the beginning of a new age for physics. The door was opened to ask if atoms, and later after the discovery of the atomic nucleus by Rutherford, Geiger and Marsden, are composed of even smaller objects.

A key tool for further investigation of nature was and is building large machines, so called particle accelerators, which created the possibility to look inside of particles much like a usual light microscope. With each new generation of machines essentially new barriers toward higher energy could be overcome. Since energy is inverse proportional to distance, reaching higher energies means resolving shorter distances. This led to an enormous discovery of a large set of particles. In order to sort this amount of particles with different behaviors and properties, theorists started to classify and group particles, affected by different forces, into types, families and generations. Over the years this ended up in a theory which particle physicists call the *Standard Model* (SM). Until today it is the best theoretical model to describe all aspects of particle properties and especially their interaction with each other.

The Standard Model is composed of twelve fermions (with half integer spins) divided into two families of quarks and leptons. The first group contains six quarks *up*, *down*, *strange*, *charm*, *bottom* and *top*, grouped into three generations each containing two quarks. The mass scale of each quark generation is rather different and starts for the first generation, composed of the up and down quark, at about a thousandth of the proton mass and ends with the third generation in the order of a few up to a hundred proton masses for the top quark. The other

family of particles, the leptons, are also grouped into three generations, of which the first contains the electron and the electron neutrino, while the second and third are composed of a particle similar to an electron and a different kind of neutrino. In addition each fermion has a counterpart an anti-particle with opposite properties (called quantum numbers) but equal mass. It is widely believed that at very high energies only one force is responsible for all interactions of the twelve elementary particles in the SM. At the energy level available in the laboratories this one force appears as three separate ones: the electromagnetic, weak and strong force. Each interaction is described by the exchange of gauge bosons (particles with integral spin values): the photon exchange characterises the electromagnetic force, the weak interaction is explained by the  $W$  and  $Z$  bosons exchange and the strong interaction by gluon exchange. The fourth known force, gravity, is escaping the description in the Standard Model, its effect however is negligible small for particles involved in a typical experiment within the field of high energy physics. The one particle predicted in the SM but not yet found is the *Higgs* boson, required for the mechanism which gives mass to the particles. Very recently a new particle at the Large Hadron Collider (LHC) was found [1, 2] which seems to be a good candidate for the SM Higgs boson.

The strong interaction, described by the *Quantum Chromo Dynamics* (QCD), is experimentally tested in a large variety of experiments up to very high precision, among those the HERA experiments play a rather important role due to their unique collider setup. In theoretical predictions a usual approach is to calculate processes in a so called perturbative manner. This means that an actual process is calculated in a series of elements, each new element adding more precision to the calculation. This kind of calculation however require a scale, usually the coupling strength of the interaction, in which the series is calculated. QCD has an interesting behaviour: The coupling strength is increasing with larger distances or seen vice versa decreasing with increasing momenta. This phenomena is explained theoretically with the self interaction of the gluons.

With the advent of HERA operation a new class of deep inelastic scattering process was observed. While the bulk part of the events could be described by “standard” deep inelastic scattering models, an excess of about 10 % was observed, containing events with no energy flow near the proton direction [3, 4], which “came as a surprise” [5]. It was found that a description using the ideas of diffraction could explain this type of events. However this kind of processes are difficult to describe in the framework of perturbative QCD, since a hard scale is missing. A phenomenological description in the framework of *Regge Theory* is often used instead.

Since the discovery of the  $J/\psi$  particle in 1974 [6, 7] it draw a lot of attention to it. Its existence was explained as a new quarkonia state, a particle composed from a quark-anti-quark pair, also called *vector meson* (VM), of a new quark kind: the charm. In case of the HERA experiments, it is the most heaviest VM produced with a suitable amount of statistics to study it in detail. In general, diffractive VM production as a subclass of diffractive process allows to test for example the transition between the soft and hard regime. It also is a good test ground for studying the difference between elastic events, where the outgoing proton stays intact, and proton dissociative events, where the outgoing proton breaks up into several low mass particles. The two collider experiments of HERA, H1 and ZEUS, have a long tradition of VM measurements ( $\rho^0$  [8–22]  $\phi$  [8, 9, 20, 21, 23–26]  $\omega$  [27, 28]  $J/\psi$  [13, 20–22, 29–39]  $\psi(2S)$  [40, 41]  $\Upsilon$  [33, 42–44]), dating back to the beginning of HERA operation.

This measurement extends previous H1 measurements in several directions. First, by using a data set corresponding to higher integrated luminosity, meaning that a higher statistics is available for the measurement. Second, by using in addition to the data set with a centre

of mass energy of 318 GeV, recorded at a proton energy of 920 GeV, also a data set with a reduced nominal proton energy of 460 GeV, which will push the boundary of the accessible phase space towards a lower photon proton centre of mass energy range for  $J/\psi$  events reconstructed with central tracks. Third, by reconstructing  $J/\psi$  events via both leptonic decay channels  $J/\psi \rightarrow \mu\mu$  and  $J/\psi \rightarrow ee$ . Fourth, by measuring not only elastic but also proton dissociative  $J/\psi$  differential cross sections. Fifth, by using an unfolding technique to properly account for the bin correlations and the correlations for the elastic and the proton dissociative data sets. And sixth, by including the correlations of the unfolded differential cross sections data points in a combined fit of elastic and proton dissociative processes to determine the normalisation and shape parameters of the fit function, also accounting for the correlation of the systematic uncertainties of the different data sets by use of an adequate  $\chi^2$  definition.

In Chapter 2 a brief overview of the theoretical aspects of diffraction, vector meson production and the HERA kinematics are provided. The next chapter gives an overview of the HERA accelerator and explains some details of the H1 detector. It follows an explanation in Chapter 4 about the Monte Carlo simulations used in this analysis. Afterwards the online selection is discussed including the data sets used for this measurement. Chapter 6 explains the events selection and in Chapter 7 trigger, acceptance and selection efficiencies are discussed. The subsequent chapter deals with the forward energy flow and corrections needed to be applied in order for the simulation to describe the data sufficiently well. In Chapter 9 the unfolding techniques are explained, used to determine the differential cross sections, and in the end of the chapter the results are presented and discussed. The main text is finishing with Chapter 11 giving the final remarks and stating the conclusions of this thesis. In the appendix section various additional material can be found, such as: some derivations, di-lepton mass distributions, the number of determined  $J/\psi$  signal events in the reconstructed bins, a discussion of the used  $\chi^2$  fitting definition and the cross section tables.



## Theory

Theories made of elegant conceptions and brilliant ideas may seem reason enough for their existence. A theory must however be compared with measured data to be falsified or to increase confidence in it. Before describing the measurement performed within this thesis, a more general theoretical introduction to diffraction is given. The subject itself is large, hence no claim is made that the following discussion is complete.

The first subsection will discuss in some details diffraction and the concept most often used to describe its appearances and features as they appear in nature. The next section deals with HERA kinematics, while the last section describes diffractive vector meson production in the environment of an electron proton collider.

### 2.1 Diffraction

#### 2.1.1 Historical milestones in diffraction

Before taking the matter to diffraction within HERA physics, maybe a small detour down the history lane can shed a better light on the origin of diffraction. The phenomena itself has a long history and was first observed by Leonardo Da Vinci (1492 – 1519) [45], who reported the occurrence of light maxima under special conditions [46], but did in fact made a wrong interpretation<sup>(1)</sup>. The first written proof of using the word “diffraction” can be found in Jesuit father Francesco Grimaldi (1618 – 1663) posthumous published book [49]. Figure 2.1 shows the quote at the beginning of the first page, it means “Light propagates and diffuses not only directly, refractively and reflectively but also, somehow, in a fourth manner, i.e. diffractively”<sup>(2)</sup>.

---

<sup>(1)</sup>According to a quote in [47], taken from [48].

<sup>(2)</sup>Translation taken from [46].

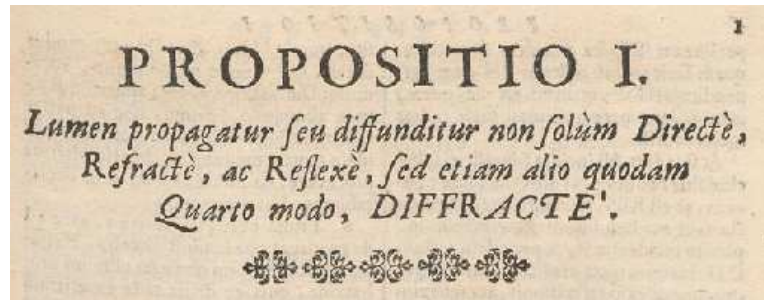


**Figure 2.1:** Preamble given at the beginning of Francesco Grimaldi’s book about light [49]. Translation: “Light propagates and diffuses not only directly, refractively and reflectively but also, somehow, in a fourth manner, i.e. diffractively” [46].

The foundation for the systematical description of diffraction using the idea of propagating waves and Huygen’s construction together with the interference principle was established in the 1818 published memoirs [50] of Augustin Fresnel (1788 – 1827). The full mathematical solution of the Maxwell equations for the situation of waves striking an obstacle was later established by Gustav R. Kirchhoff (1824 – 1887), the eponym for the Kirchhoff institute of the university of Heidelberg.

In the year 1925 Clinton J. Davisson and Lester H. Germer conducted a series of experiments investigating scattering of electrons on a target of ordinary (polycrystalline) nickel [51, 52]. In an accident the used target tube was destroyed by an explosion, causing the nickel crystal to oxidise. In Fig. 2.2 a picture is shown of Germer (left) and Davisson (right) holding such a target tube. Reduction of the oxide layer was achieved by heating. The heating process was fortunately producing, as was determined later, large crystal structures, which created the first observation of diffractive patterns induced by particles. It confirmed the prediction of W. Elasser [53] based on de Broglie’s propositions on wave mechanics [54] that a particles can have wavelike behaviour and hence produce also interference patterns. This stunning observation earned Davisson together with George Thomson the Nobel Prize in physics in 1937.

In the 1950’s the term diffraction in the field of nuclear high energy was introduced by Landau and his school, among others Feinberg and Pomerančuk [55]. A review of hadron diffraction can be found in [56] and references therein. It was discovered soon that the direct translation of optical waves to quantum mechanical diffraction only works in case of *elastic diffraction*, in which initial and final states are equal. The so called, *inelastic diffraction* or *diffractive dissociation*, in which the interacting particles probe each others internal structure, was a new phenomena and first introduced by Good and Walker [57].

At this point the pure historical reflection of diffraction is stopped. For interested readers [45] reveals more historic details on diffraction.

### 2.1.2 Regimes in diffraction

In classical wave optics, three regimes are usually distinguished in diffraction. Lets assume the following setup. A plane wave with wavelength  $\lambda$  is hitting a circular obstacle with



**Figure 2.2:** Clinton J. Davisson (right) and Lester H. Germer (left) showed in 1927 for the first time that electron beams can behave like light waves and produce diffractive patterns.  
Image credit: Bell Laboratories / Alcatel-Lucent USA Inc., courtesy AIP Emilio Segre Visual Archives, Physics Today Collection

transverse dimension  $R$ .

In case the *short wavelength condition*  $kR \gg 1$  with wave number  $k = 2\pi/\lambda$  is fulfilled, the Huygen's principle is applicable. This principle describes the idea that at each point an incoming wave hits the obstacle, the point becomes the source of a spherical wave. The envelope of these waves form then a interference pattern on a screen at distance  $D$ .

If the *large distance condition*  $R/D \ll 1$  is given then the waves arriving at the screen can be seen as parallel and the mathematical solution can be further simplified. The three regions distinguished are the *geometrical optics*  $kR^2/D \gg 1$ , *Fresnel diffraction*  $kR^2/D \sim 1$  and the *Fraunhofer diffraction*  $kR^2/D \ll 1$ , in which the distance of the screen is seen at infinitely large distance.

In case of particle physics always the Fraunhofer regime is safely assumed, because the typical distances of the detectors  $D$  are in the order of 1 cm, the transverse size of the probed object are in the region<sup>(3)</sup>  $\sim 1$  fm and for  $k = p^{(4)}$  with momenta  $p \sim 10$  GeV, the short wavelength condition  $kR \simeq 50 \gg 1$ <sup>(5)</sup>, the large distance condition  $R/D \simeq 10^{-13} \ll 1$  and the Fraunhofer condition  $kR^2/D \simeq 10^{-11}$  are all fulfilled<sup>(6)</sup>.

### 2.1.3 The scattering amplitude and cross section

The description of diffraction in optical theory and classical quantum mechanics is well document, here only a very brief overview is given<sup>(7)</sup>. In particle physics one quantity in particular serves as the eager beaver in comparisons between theory and experimental measurement: the *cross section*  $\sigma$ . In the following a short definition is given of the concept of scattering amplitude and cross section. Although different formal approaches exists for providing a definition, here a more traditional one is chosen, closely to a geometric interpretation, which is more driven by simplicity, intending a clear understanding of the concept.

The setup is the following: An incoming particle, described by a plane wave  $e^{i(\mathbf{k}\cdot\mathbf{r})}$ , is scattering at a potential, illustrated in Fig. 2.3. The wave function of the outgoing, scattered particle must then fulfill

$$\psi_{\mathbf{k}}(\mathbf{r}) \sim e^{i(\mathbf{k}\cdot\mathbf{r})} + \mathcal{A}_k(\Omega) \frac{e^{ikr}}{r} \quad (2.1)$$

in the asymptotic limit of large distance  $r$ . The wave number is denoted by  $k$ , the solid angle by  $\Omega$  and the *scattering amplitude* by  $\mathcal{A}_k$ <sup>(8)</sup>.

For any kind of scattering process the cross section expresses the likelihood of producing a certain final state for a given initial state with well defined momenta. In mathematical terms

<sup>(3)</sup>The charge proton radius is  $0.877 \pm 0.007$  fm [58].

<sup>(4)</sup>Throughout this text natural units are used, i.e.  $c = \hbar = 1$ .

<sup>(5)</sup>With conversion factor in natural units  $200 \text{ MeVfm} = 1$ , a precise value can be found in [58].

<sup>(6)</sup>Even at high momenta, as achieved at the *Large Hadron Collider* (LHC), in the multi-TeV range, the Fraunhofer condition is still fulfilled.

<sup>(7)</sup>A comprehensive discussion of scattering in quantum mechanics can be found in [59]. In the review [60] also optical diffraction is examined, but focuses more on high energy physics.

<sup>(8)</sup>Assumed here is elastic scattering, otherwise the wave number of the outgoing wave function need not to be equal to  $k$ .

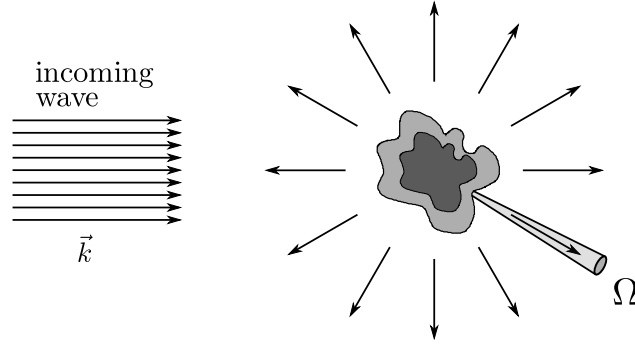


**Figure 2.3:** Schematic illustration of a scattering process. (Figure idea taken from [61].)

the *differential cross section*,  $d\sigma/d\Omega$ , is defined as [61]

$$\frac{d\sigma}{d\Omega} = \frac{\text{number of scattered particles into the solid angle } d\Omega \text{ per second}}{\text{number of incoming particles per second} \cdot d\Omega}. \quad (2.2)$$

The correlation to the scattering amplitude is given by<sup>(9)</sup>

$$\frac{d\sigma}{d\Omega} = |\mathcal{A}(\Omega)|^2. \quad (2.4)$$

In the picture of optical diffraction, if the Fraunhofer condition is fulfilled, or in case of scattering explained in quantum mechanics at large energies the scattering amplitude can be written as [56, 59, 60]

$$\mathcal{A}(q) = \frac{k}{2\pi i} \int d^2b \Gamma(b) e^{-i(\mathbf{q}\cdot\mathbf{b})} \quad (2.5)$$

with  $\mathbf{q}$  the momentum transfer and  $\Gamma(b)$  the *profile function*<sup>(10)</sup>. The variable  $\mathbf{b}$  is usually called *impact parameter*. The scattering amplitude as given in Eq. (2.5) is also referred to as the *eikonal-form* [60]. The profile function itself is also referred to as *eikonal* or *opacity*.

The profile function  $\Gamma(b)$  describes the size of absorption of an incoming wave due to an obstacle or a scattering potential. In the picture of light scattering at a disc with radius  $R$ , the profile function would be 1 if  $b \leq R$  and otherwise 0, as illustrated in Fig. 2.4(a). The corresponding scattering amplitude, shown in Fig. 2.4(b), is  $\mathcal{A}(q^2) \propto J_1(qR)/(qR)$  with  $q = |\mathbf{q}|$  and  $J_1$  the Bessel function first kind. The first mathematical description of the diffractive phenomenon produced by a disc was derived by Airy [62]. In the lower row of Fig. 2.4 the exponential amplitude is shown for a Gaussian profile function. The exponential behaviour of the scattering amplitude and hence also of the differential cross section w.r.t.

<sup>(9)</sup>However as simple as this picture is it causes problems when the task arises to actual calculate cross sections, because the plane wave assumed above is not normalised. Using properly normalised initial and final states Eq. (2.4) transforms into

$$\frac{d\sigma}{d\Omega} = \frac{|\mathcal{M}|^2}{16\pi^2 s} \quad (2.3)$$

written in the centre of mass system for two body to two body scattering with all four particles having equal masses.  $\sqrt{s}$  denotes the centre mass energy and  $\mathcal{M}$  is the matrix element, which is equivalent to the amplitude but used more often in terms of calculations.

<sup>(10)</sup>It is assumed here that the profile function does not depend on the energy of the incoming particle, which is not necessarily true.

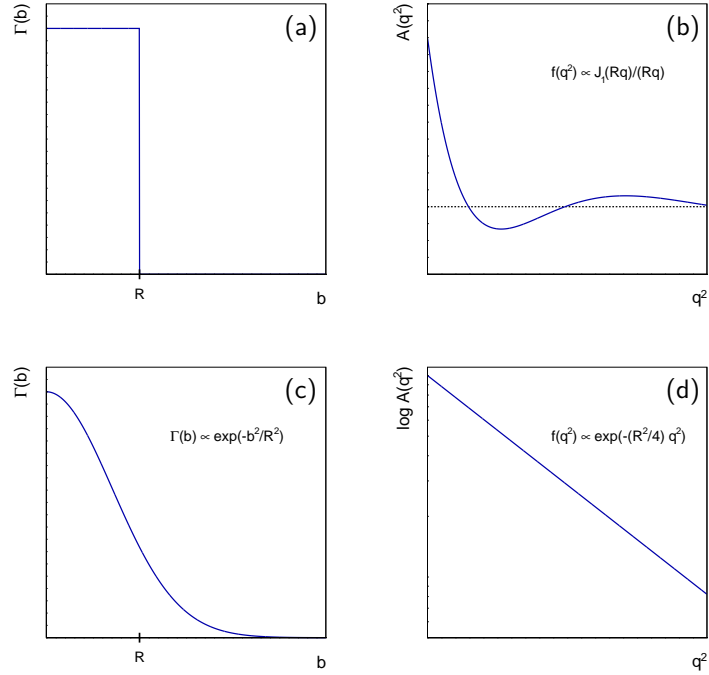


**Figure 2.4:** Two profile functions for a circular slit with radius  $R$  (a) and a Gaussian function with sigma  $R$  (c) are shown. Plot (c) and (d) show the corresponding scattering amplitudes  $A$ . (Idea adapted from [60].)

to the momentum transfer is of great importance, as will be seen later.

Because of the relation between the momentum transfer dependence of the differential cross section and the transverse space distribution (the profile function), one can learn a lot about a scattering potential, once one has measured the differential cross section.

### 2.1.4 Kinematic of two body to two body interactions

Scattering experiments build one of the key tools to investigate the nature of elementary and composite particles. The most general picture of interaction related to processes discussed in this thesis can be seen as two body to two body reactions

$$A + B \rightarrow C + D. \quad (2.6)$$

Figure 2.5 shows a generic Feynman diagram of this type of interaction. The incoming particles  $A$  and  $B$  with the four-momenta  $p_A$  and  $p_B$  do a certain kind of interaction, represented by the blob, resulting in a final state with two particles  $C$  and  $D$  with four-momenta  $p_C$  and  $p_D$ <sup>(11)</sup>. Out of the 4 four-vectors, only 3 are independent due to energy

<sup>(11)</sup>The time line of the Feynman diagram shown in Fig. 2.5 is organised from left to right as indicated by the additional arrow at the left bottom corner. In following diagrams this indication will be dropped but the convention remains the same.

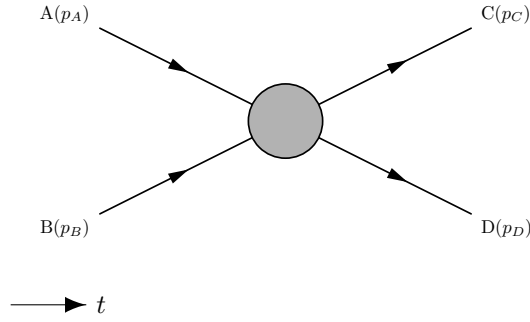


**Figure 2.5:** Generic diagram for two body scattering  $A + B \rightarrow C + D$ .

momentum conservation. The on-shell mass restrictions  $M_i^2 = p_i^2$  for  $i = A, B, C, D$  directly translates into the further restriction that only 2 independent scalars can be constructed from the remaining 3 four-vectors<sup>(12)</sup>.

Though different possibilities exist it is preferable to describe the process with Lorentz invariant variables. Mandelstam [64] introduced first a set of Lorentz invariant variables, the centre of mass energy, the four-momentum transfer squared and the cross momentum transfer squared [65], defined as

$$s = (p_A + p_B)^2 \quad (2.7)$$

$$t = (p_A - p_C)^2 \quad (2.8)$$

$$u = (p_A - p_D)^2. \quad (2.9)$$

Nowadays this set is called Mandelstam variables, which are usually used to characterise two body interactions. Due to energy momentum conservation the condition

$$s + t + u = \sum_{i=\{A,B,C,D\}} M_i^2 \quad (2.10)$$

is fulfilled, with  $M_i$  representing the rest mass of the incoming or outgoing particle  $i$ . Since only two out of the three Mandelstam variables are independent, it is sufficient to write the scattering amplitude as function of  $s$  and  $t$ , i.e.  $\mathcal{A} = \mathcal{A}(s, t)$ .

#### 2.1.4.1 Crossing symmetry

The crossing symmetry principle describes that the amplitude of a process is invariant to the transformation that a particle  $A$  is removed from the initial state and replaced by an antiparticle  $\bar{A}$  in the final state with inverted four-momentum. More details are provided in [66].

Applying the principle of crossing symmetry to the reaction shown above in (2.6) it can be rewritten as

$$A + \bar{C} \rightarrow \bar{B} + D \quad (2.11)$$

<sup>(12)</sup>In the general case of two particle to  $n$  particle scattering process,  $3n - 4$  independent Lorentz invariant variables exist [63].

and

$$A + \bar{D} \rightarrow C + \bar{B}. \quad (2.12)$$

This is illustrated in Fig. 2.6. Since the centre of mass energy is still defined by the incoming particles, i.e. A and B, the actual Mandelstam variable defining the centre of mass energy changes with respect to the corresponding Feynman graph. The process is then named after the Mandelstam variable defining the centre of mass energy, in case of (a), (b) and (c) it is called  $s$ ,  $t$  and  $u$  channel, respectively. This is a useful tool for actual calculation of matrix

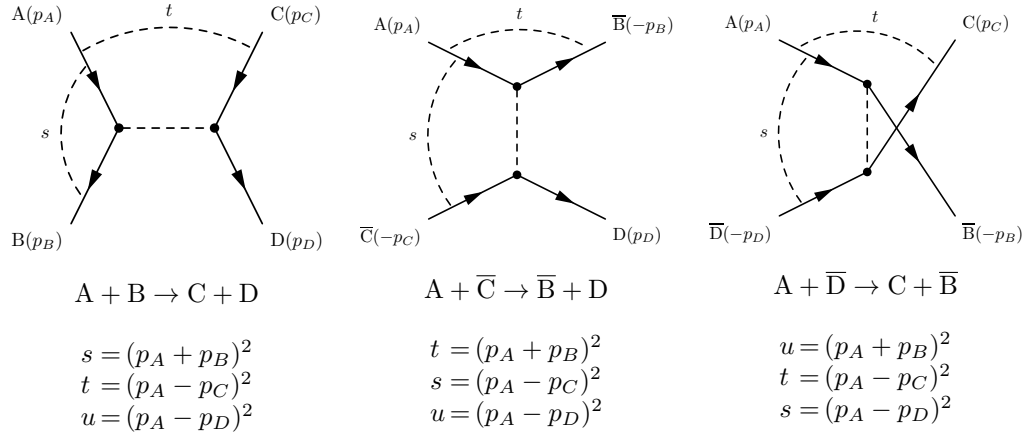


**Figure 2.6:** Two body to two body scattering represented in the  $s$  channel (a),  $t$  channel (b) and  $u$  channel (c).

elements, since for a process more than one channel can contribute (e.g. in Bhabha scattering,  $e^+e^- \rightarrow e^+e^-$ ,  $s$  and  $t$  channel are contributing).

From an experimentalist point of view the channel can simply be read of from the graph and the connection with the centre of mass energy is not of great importance.

### 2.1.5 $S$ -matrix

The theory of *quantum chromo dynamics* (QCD) is nowadays the favoured theory to describe the strong force, responsible for the interaction of coloured quarks and gluons. (A brief review for instance is given in [58].) Before introducing the concept of field theory to describe the strong interaction, other ideas were studied. One approach was to investigate the consequences of the  $S$ -matrix theory by applying a set of postulates to it. Due to its generality  $S$ -matrix theory is still a useful tool to study diffractive processes, especially in regions where perturbative QCD is not applicable<sup>(13)</sup>. Some of its concepts are briefly summarised and discussed in the following. For a text book description of the  $S$ -matrix theory see e.g. [63, 66]. For some early articles about  $S$ -matrix theory to describe the strong interaction see [68, 69].

The  $S$ -matrix was first introduced by Wheeler [70]. It relates in a general manner an *in*-state  $|a\rangle_{\text{in}}$  with an *out*-state  $|b\rangle_{\text{in}}$ . A state here is a set of free particles in the asymptotic time

<sup>(13)</sup>It should be noted that research in the field of  $S$ -matrix theory is still conducted, for a recent article see [67].

limit, i.e.  $t \rightarrow -\infty$  and  $t \rightarrow +\infty$  for the *in*- and *out*-state, respectively. The  $S$ -matrix is then defined as

$$S_{ab} \equiv {}_{\text{out}}\langle b | a \rangle_{\text{in}}. \quad (2.13)$$

The idea is to define a set of postulates and analysing its consequences on the  $S$ -matrix. However the set of postulate is not unique. The most common ones are listed in the following, but e.g. in [71] some additional postulates are listed.

1. Lorentz invariance of the  $S$ -matrix

The  $S$ -matrix should be invariant under Lorentz transformation. The consequence is that the  $S$ -matrix can be written as function of Lorentz invariant variables. For a two to two body interaction usually the Mandelstam variables are used, see 2.1.4.

2. Unitarity of the  $S$ -matrix

Expressed in a formula it takes the form

$$SS^\dagger = S^\dagger S = \mathbb{1} \quad (2.14)$$

The  $S$ -matrix is usually expressed via  $S \equiv \mathbb{1} + iT$ . The operator  $T$  is often called  $T$ -matrix and represents an actual interaction while the unity stands for no interaction.

Evaluating the unitarity in Eq. (2.14) for  $T$  and defining the amplitude by the equation  $(2\pi)^4 \delta^{(4)}(\sum_a p_a - \sum_b p_b) \mathcal{A}_{ab} = \langle a | T | b \rangle$  gives<sup>(14)</sup>

$$2\mathfrak{I}\mathfrak{m}\mathcal{A}_{ab} = (2\pi)^4 \delta^{(4)}\left(\sum_a p_a - \sum_b p_b\right) \sum'_n \mathcal{A}_{an} \mathcal{A}_{nb}^\dagger \quad (2.15)$$

also known as the *Cutkosky rule* [72], which connects the imaginary part of an amplitude with a sum over all possible intermediate states. A special case of the Cutkosky rule is the *Optical theorem*, in which initial and final state are taken to be identical. I.e. forward ( $t = 0$ ) elastic scattering, since the momenta of the initial and final state are equal. The Eq. (2.15) simplifies then to

$$2\mathfrak{I}\mathfrak{m}\mathcal{A}_{aa}(s, t = 0) = (2\pi)^4 \delta^{(4)}\left(\sum_a p_a - \sum_b p_b\right) \sum'_n |\mathcal{A}_{a \rightarrow n}|^2 = \Phi \sigma_{\text{tot}}, \quad (2.16)$$

which is proportional to the total cross section  $\sigma_{\text{tot}}$ . The flux factor  $\Phi$ <sup>(15)</sup> [see also Eq. (2.2)] is in the high energy limit equal to  $2s$ , with  $\sqrt{s}$  being the centre of mass energy.

3. Maximal analyticity

This postulate requires that  $S$ -matrices are analytic functions with only the minimal

<sup>(14)</sup>An intermediate state can contain  $m$  on-shell particles with momenta  $k_m$ . The given primed sum over the  $n$  states therefore means a sum over all particles and an integration over all momenta of the intermediate particles, i.e.

$$\sum'_n = \sum_n \left( \prod_{i=1}^n \int \frac{d^3 k_i}{(2\pi)^3} \frac{1}{2E_i} \right).$$

<sup>(15)</sup>In case of two body scattering the flux factor is  $\Phi = 4E_1 E_2 |v_1 - v_2|$  [66] with  $E_i$  the energy and  $v_i$  the velocity of the particles.

amount of singularities required by unitarity<sup>(16)</sup>. The above two postulates may be regarded as reasonable, but the requirement for analyticity, is often seen as a weak point. In the words of Mandelstam:

*... the possibility of analytically continuing a function into a certain region is a very mathematical notion, and to adopt it as a fundamental postulate rather than a derived theorem appears to us to be rather artificial. [71]*

Nevertheless the consequences are rather interesting. The crossing symmetry (see Sec. 2.1.4), as well as the dispersion relation<sup>(17)</sup> can be derived directly from this postulate.

## 2.1.6 Regge theory

The consequences of general postulates applied to  $S$ -matrix theory, as seen in the last section, produces relations of amplitudes. However at this point no actual amplitudes, nor cross sections are derived. This is changed with Regge theory, which essentially derives the asymptotic behaviour of amplitudes.  $S$ -matrix consequences can then be used for example to connect the imaginary part of the amplitude with the total cross section (optical theorem).

### 2.1.6.1 Regge's idea

Tullio Regge introduced in his studies [73, 74], the concept of a non-discrete complex orbital momenta,  $l$ , for fixed real energies. In this theory the simple poles appearing in the scattering amplitude in the complex  $l$ -plane are called *Regge poles* and are located at

$$l = \alpha(t) \tag{2.17}$$

with  $\alpha(t)$  called *Regge trajectory*. They define the location of the poles in the  $l$ -plane with changing  $t$ .

Given the above postulates for  $S$ -matrix theory and further assuming that the amplitudes have an asymptotic behaviour, then, in combination with analyticity, the amplitudes can be written in the leading Regge pole approximation as [63]

$$\mathcal{A}(s, t) \xrightarrow{s \rightarrow \infty} \frac{\eta + e^{-i\pi\alpha(t)}}{2 \sin \pi\alpha(t)} \frac{\beta_{ac}(t)\beta_{bd}(t)}{\Gamma(\alpha(t))} s^{\alpha(t)}. \tag{2.18}$$

A Feynman diagram describing the process is given in Fig. 2.7 with the exchange of a so called *Reggeon*  $\mathbb{R}$ . The formula is derived using a partial wave expansion, also called Legendre expansion. In the expansion two partial wave amplitudes are used, driven by the additional requirement for uniqueness of the series. The two amplitudes have a different so called *signatures*, represented by  $\eta$ , taking values of  $\pm 1$ .

The coupling of the Reggeon to the particles  $a$  and  $c$  is denoted by  $\beta_{ac}(t)$  and similar is the coupling to  $b$  and  $d$  defined as  $\beta_{bd}(t)$ .

<sup>(16)</sup>The idea is that because the  $n$  intermediate states as used in Eq. (2.15) are only produce above the  $n$  particle thresholds due to their masses. Below a certain threshold in  $s$  therefore no contribution to the imaginary part of the amplitude is present. Using more mathematical theorems this leads to cuts along the  $s$  axis. A detailed description is given in [63].

<sup>(17)</sup>The dispersion relation connects the imaginary with the real part of a scattering amplitude.

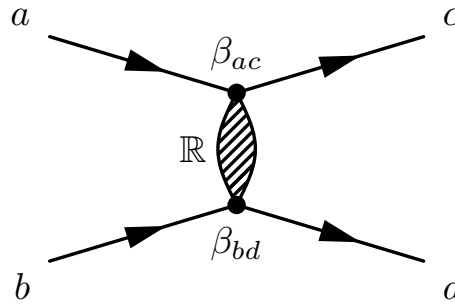


Figure 2.7: Diagram for Reggeon exchange.

### 2.1.6.2 Regge trajectories

Chew and Frautschi [68, 75], and Gribov [76] first plotted the mass  $m_i^2$  of physical particles against their spin  $j_i$ . The expectation was that the actual exchanged particles obey the condition  $\alpha(m_i^2) = j_i$ , i.e. each particle should lay on a Regge trajectory. These kind of plots are called nowadays *Chew-Frautschi plot*. An example is given in Fig. 2.8 showing the trajectories of  $\rho$  and  $\omega$  mesons with positive signature and  $a_2$  and  $f_2$  mesons with negative signatures.

Usually a linear trajectory

$$\alpha(t) = \alpha(0) + \alpha_1 t \quad (2.19)$$

is assumed with  $\alpha(0)$  and  $\alpha_1$  called the intercept and slope of the trajectory. The assumption is motivated by experimental data, such as shown in Fig. 2.8. In the original publication of Chew and Frautschi [75] is stated “... a strict linear behaviour of the trajectories is not to be inferred.” The possibility of a non-linear term contributing therefore is left open. Some analyses show doubt about the linearity of the trajectories [78]<sup>(18)</sup>. However in this thesis a strict linear trajectory behaviour is always assumed.

### 2.1.6.3 Cross section behaviour in the context of Regge trajectories

The differential cross section as function of  $t$  can be derived [66], by using the expression for the amplitude as given in Eq. (2.18) one obtains

$$\frac{d\sigma}{dt} \propto \frac{1}{s^2} |\mathcal{A}|^2 = (\sqrt{s})^{4(\alpha(t)-1)}. \quad (2.20)$$

The behaviour of the differential cross section as given in above equation will be seen through out this text. In the context of HERA kinematics however the variable  $\sqrt{s}$  represents the electron proton centre of mass energy. The relevant centre of mass energy for cross sections discussed in this thesis is in the photon proton rest frame, called  $W_{\gamma p}$ . The relation between  $\sqrt{s}$  and  $W_{\gamma p}$  will be discussed further in Sec. 2.2.

<sup>(18)</sup>In [79] a pion loop correction in the Pomeron trajectory is suggested, leading to a non-linear behaviour. See also [80].

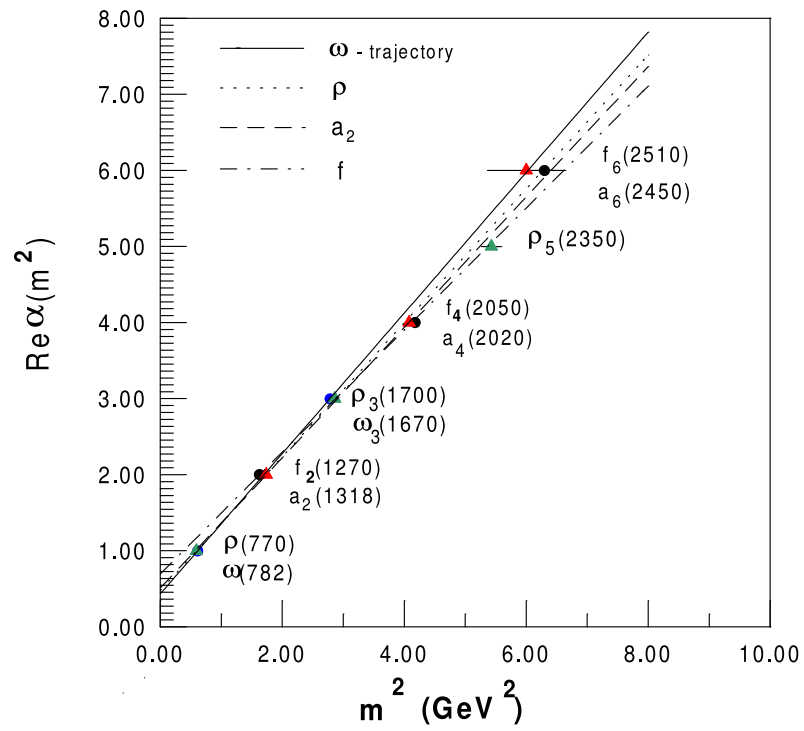


Figure 2.8: Example of a Chew-Frautschi plot for  $\omega$ ,  $\rho$ ,  $a_2$  and  $f$  mesons with linear trajectories. Plot taken from [77].

Using the optical theorem (see. Sec. 2.1.5), which connects the forward ( $t = 0$ ) elastic amplitude with the total cross section gives

$$\sigma_{\text{tot}} \propto s^{\alpha(0)-1} \quad (2.21)$$

in the asymptotic limit. As simple as the formula is, as interesting is it. The consequences will be discussed in the next section.

### 2.1.7 The Pomeron

If  $\alpha(0) < 1$  the total cross section is vanishing with  $s \rightarrow \infty$ , as follows from Eq. (2.21). Since all known actual particles have an intercept below 1 (see e.g. Fig. 2.8) one would expect a decrease of the total cross section with increasing energy. Data however follow a different behaviour. Figure 2.9 shows the total cross section for the reactions  $pp$ ,  $\bar{p}p$ ,  $\pi^\pm p$  and  $K^\pm p$

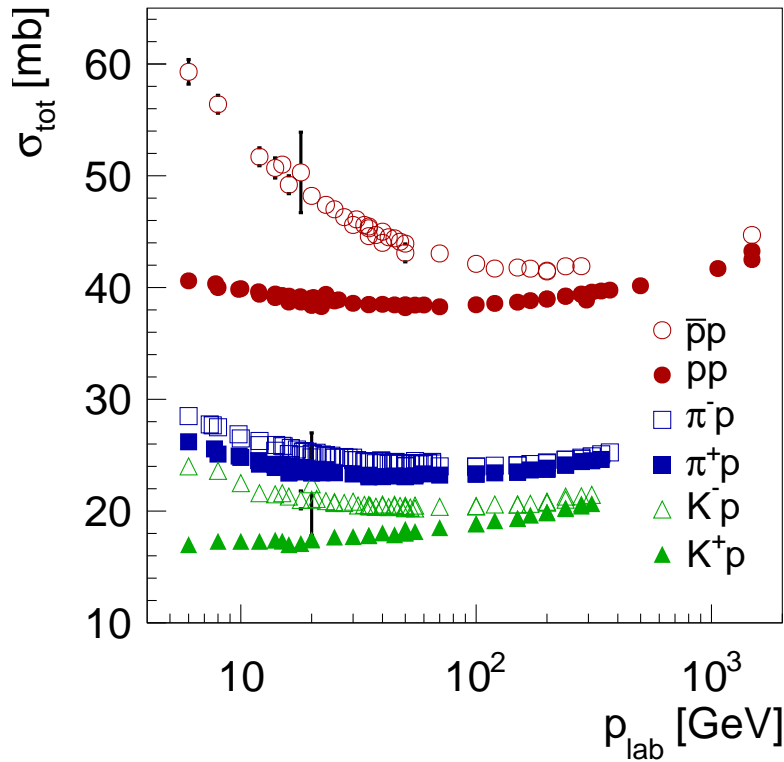


**Figure 2.9:** Total cross sections as function of the incoming beam momentum  $p_{\text{lab}}$  for  $\bar{p}p$ ,  $pp$ ,  $\pi^-p$ ,  $\pi^+p$ ,  $K^-p$  and  $K^+p$  interactions, shown as open red circle, solid red circle, open blue square, solid blue square, open green triangle and open solid triangle, respectively. [81–92]

as function of the beam momentum  $p_{\text{lab}}$ . A clear rise at large energies is visible. Hence to preserve the Regge picture, the intercept of the responsible trajectory must be larger

than 1<sup>(19)</sup>.

Gell-Mann named this new trajectory after Pomernanchuk [5, 93], though originally Gribov was suggesting the idea first [5]. The trajectory name was later abbreviated to *Pomeron*.

Pomernanchuk's name was chosen in honour of the *Pomernanchuk theorem*. However the term is actually used for two different theorems, both will be given here for completeness.

- In case of a scattering experiment in which charge is exchanged, the cross section must asymptotically vanish. [94, 95] (Sometimes this theorem is also called *Okun-Pomernanchuk rule*.)
- The difference between particle and antiparticle total cross sections must be vanishing at sufficient high energies. [96]

Soon later, it was proved that the asymptotically dominant contribution of a scattering process must be due to the exchange of an object with vacuum quantum numbers<sup>(20)</sup> [97, 98]<sup>(21)</sup>. Hence, in the Regge picture it means: the Pomeron has quantum numbers like the vacuum.

A sister trajectory of the Pomeron is the proposed *Odderon* [99, 100] with quantum numbers similar as the Pomeron, but odd charge conjugation. Experimentally however no such trajectory was found.

### 2.1.7.1 The Pomeron in the QCD picture

The success of the quantum chromo dynamics (QCD) to describe strong interactions soon lead to the question what the Pomeron may look like in the QCD formulation. Due to the colour quantum number carried by strong interacting particle, the lowest order Feynman diagrams in perturbation theory describing a Pomeron is the exchange of two gluons, first introduced by Low [101]. The idea was extended by Nussinov [102, 103] to higher orders and non-crossed gluon ladders. This description however had some problems, the potential would be long range and produces singularities in derivatives of  $d\sigma/dt$  at  $t = 0$ , which are inconsistent with experimental data [104]. Some short comings are cured by the BFKL (Balitsky, Fadin, Kuraev, Lipatov) [105–108] approach for describing the Pomeron. It includes also crossed gluon ladders, i.e. takes into account gluon self interaction. A detailed textbook description of the BFKL Pomeron is given in [63].

The BFKL Pomeron description itself is burdened with discussion, especially since the next-to-leading order corrections are large compared to the leading terms [109].

### 2.1.8 Total cross section

The total cross section of various hadronic interactions have been fitted with different phenomenological functions in the early 80's of the 20<sup>th</sup> century. Donnachie and Landshoff (DL) [110] used a two term function

$$\sigma_{\text{tot}} = X s^\epsilon + Y s^\eta, \quad (2.22)$$

<sup>(19)</sup>At the time these discoveries were made the rise with the total cross section has not been experimentally observed. It was assumed that the total cross section would stay constant with increasing energy, i.e.  $\alpha(0) \simeq 1$ . [5]

<sup>(20)</sup>Zero isospin, even parity, even  $G$  parity and even signature.

<sup>(21)</sup>The assumptions required are astonishing weak, only the optical theorem and analyticity is required [98].

where the first term describes the exchange of a Pomeron, while the second represents the combination of exchanged Reggeons at low  $s$  (see also Eq. 2.21). An example for a fit to  $\bar{p}p$  interaction data is provided in Fig. 2.10<sup>(22)</sup>. The fit returns  $\varepsilon = 0.0808$  and  $\eta = -0.4525$ .

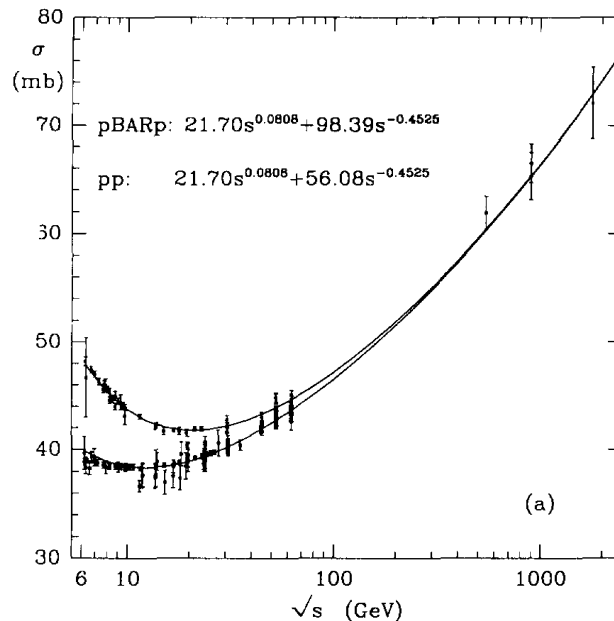


**Figure 2.10:** Fit of total cross section  $\sigma$  as function of the centre of mass energy  $\sqrt{s}$  for  $pp$  and  $\bar{p}p$  interaction performed by Donnachie and Landshoff [110].

Hence the effective Pomeron intercept therefore yields a value  $\alpha_P(0) = 1.0808$  and the effective Reggeon intercept  $\alpha_R(0) = 0.5475$ .

It is however stressed in [110] that the fitted power  $\varepsilon$  is an *effective* power value, in contrast to a *bare* power value, since it incorporates also multiple Pomeron exchange which are expected at higher energies.

Froissart [112] and Martin [113] proved for two-body interactions that the total cross section must obey

$$\sigma_{\text{tot}} < C \ln^2 s, \quad (2.23)$$

in order not to violate unitarity. The constant  $C$  is expected to be in the order of 60 mb [63], derived from the pion mass. Clearly a power law as given in Eq. (2.21) does at some point exceed the given bound. However this does only happen beyond the Planck scale<sup>(23)</sup>. In addition it is expected that multi Pomeron exchange occurs at large energies which reduces the increase of the total cross sections [63].

Before HERA was starting its operation different models were predicting the total photoproduction (see Sec. 2.2.1) cross section  $\sigma_{\text{tot}}(\gamma p)$ . One such prediction came from DL based on the fits to hadronic interaction as described above. Though other models failed to describe  $\sigma_{\text{tot}}(\gamma p)$ , the prediction of DL was in agreement with the measurement, which was

<sup>(22)</sup>A recent measurement of the total  $pp$  cross section performed by the TOTEM collaboration yields  $98.3 \pm 0.2(\text{stat.}) \pm 2.8(\text{syst.}) \text{ mb}$  at  $\sqrt{s} = 7 \text{ TeV}$  [111].

<sup>(23)</sup>Planck mass  $M_p \simeq 1.22 \times 10^{19} \text{ GeV}$  [58].

a remarkable success of the Regge motivated model. Figure 2.11 shows the DL prediction as solid line, together with the later measured HERA data points<sup>(24)</sup>,<sup>(25)</sup>

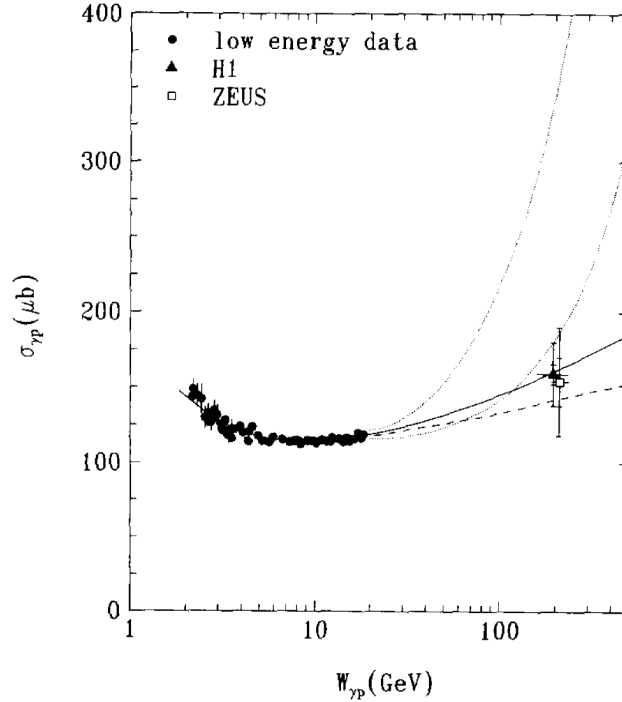


**Figure 2.11:** First total photoproduction cross section of H1 (triangle) and ZEUS (open square) including low energy measurements. The solid line represents the Donnachie and Landshoff fit to the low energy data. (The dashed line represents the ALLM prediction.) Plot taken from [115].

### 2.1.9 Diffractive dissociation

In addition to elastic scattering another class of diffractive interaction is of great interest, the so called *diffractive dissociation*. While in elastic scattering the outgoing state is equal to the incoming one, in diffractive dissociation an incoming hadron may break up into a system of low invariant mass.

The characteristic quantity of proton dissociation is the invariant mass of the dissociated hadron. It will be referred to in this work as  $M_Y$ , though different conventions exist. In Fig. 2.12 an example of the double differential cross section  $d^2\sigma/dt dM_Y^2$  as function of  $M_Y^2$  for the interaction  $p + d \rightarrow X + d$  with proton momentum  $p_{\text{lab}} = 275 \text{ GeV}$  at different  $t$  values is given. Two regions are distinguishable. In the low  $M_Y$  mass ( $M_Y^2 < 4 \text{ GeV}^2$ ) region a resonance structure is visible, while for higher  $M_Y$  values the differential cross section behaves approximately like  $1/M_Y^2$ .

<sup>(24)</sup>The shown HERA measurements are from the first measurement of the total  $\gamma p$  cross section.

<sup>(25)</sup>The Donnachie and Landshoff prediction was not the only Regge based model, also the ALLM (Abramowicz, Levin, Levy and Maor) parametrisation [114] was in good agreement with the measured data, as can be seen in Fig. 2.11 represented by the dashed curve.

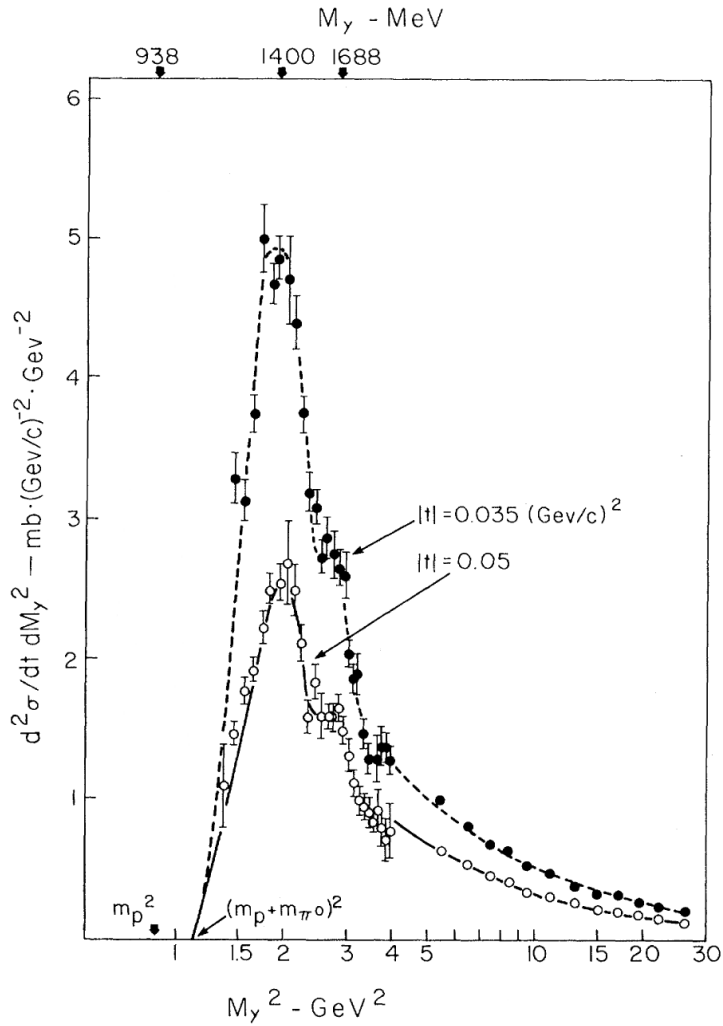


**Figure 2.12:** Example of differential proton dissociative cross sections  $d^2\sigma/dt dM_\gamma^2$  as function of  $M_\gamma^2$  for the interaction  $p + d \rightarrow X + d$  with proton momentum  $p_{\text{lab}} = 275 \text{ GeV}$  at different  $t$  values. Adapted from [116].

### 2.1.9.1 The eikonal ansatz

An approach to describe the resonance region of the  $M_Y$  spectrum is performed within the eikonal framework, see for instance [117]. In this context the profile function, discussed Sec. 2.1.3, is usually called eikonal and can be used to write the total, elastic and inelastic cross section in a rather short form. The cross section satisfy in this approach the  $s$ -channel unitarity automatically [80].

To increase the precision of description using the eikonal ansatz, it was extended to the two-channel eikonal using the Good-Walker formalism [55, 57, 118], which allows an effective<sup>(26)</sup> proton excited intermediate state. (Appendix A in [119] provides a good description of the two-channel eikonal approach.)

Also other ideas have been developed [120] for describing the low  $M_Y$  mass region of proton dissociation.

### 2.1.9.2 The triple Regge model

The most common model to describe proton dissociation above the resonance region is the triple Regge model. Figure 2.13 shows Feynman diagrams illustrating the idea for the calculation of the squared amplitude in this model. The figures are in analogy to illustration in [120]. In the right diagram the interaction of three trajectories is shown, with the  $j$

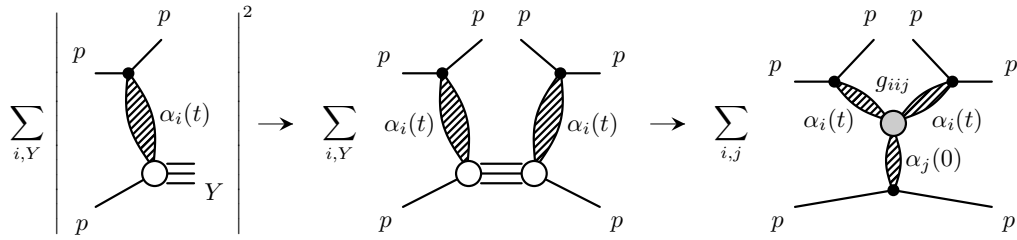


**Figure 2.13:** Illustration of triple Regge model to describe the high mass diffractive dissociation at the example of  $pp \rightarrow pX$  interaction. Given figures are in analogy to illustration in [120].

trajectory being at  $t = 0$ . The strength of the interaction is given by the *triple Regge coupling*  $g_{ii j}$ . Using this picture the differential cross section is calculated as

$$\frac{d^2\sigma}{dt dM_Y^2} = \beta_j(0)\beta_i(t)^2 g_{ii j}(t) \left(\frac{s}{M_Y}\right)^{2[\alpha_i(t)-1]} \left(\frac{M_Y^2}{s_0}\right)^{\alpha_j(0)-1} \frac{1}{M_Y^2}. \quad (2.24)$$

The  $\beta$  functions correspond to the ones defined in Eq. (2.18) and describe the coupling of a trajectory to the proton. The variable  $s_0$  serves a normalisation factor. A derivation of above formula can be found in [120].

The  $\beta$  and triple Regge couplings are not known from theoretical calculations. Several approaches for  $\beta$  function exist and are usually chosen different for Reggeons and Pomerons.

<sup>(26)</sup>In the sense that all excited physical states are incorporated. Therefore this description does not reproduce the actual physical resonance states but recreates the main properties.

The standard approach for Reggeons is an exponential  $\beta(t) = e^{bt}$  with  $b$  as a free parameter. For the Pomeron exchange sometimes the isoscalar Dirac electromagnetic form factor is taken [104, 121] or a more generalised form like

$$\beta(t) = \frac{e^{0.5c_2 t}}{\left(1 - \frac{t}{c_1}\right)^2} \quad (2.25)$$

with free parameters  $c_1$  and  $c_2$ , as used in [122].

The triple Regge couplings and especially the triple Pomeron coupling needs to fulfill some constraints in order not to violate the Froissart-Martin limit. Several ideas have been proposed. In the *weak coupling* solution<sup>(27)</sup>, the cross section is approaching a constant value for  $s \rightarrow \infty$ , which requires that the vertex vanishes for  $t \rightarrow 0$  [80, 125, 126]. In the *strong coupling* solution [127] the triple Pomeron coupling is constant a low  $|t|$ . In this case the cross section is multiplied by the so called *rapidity gap survival factor*  $S^2$  (see below) which ensures the Froissart-Martin limit [126].

According to [80, 126] data favours the strong coupling solution. Therefore more recent analysis include rapidity gap survival factors into evaluation of the triple Regge analysis. An example of the global Regge fit from [80] to CERN-ISR and FNAL data is given in Fig. 2.14, which shows the double differential cross section  $d^2\sigma/dt d\xi$  as function of  $\xi \equiv M_Y^2/s$ . Also visible are the individual triple-Regge contributions.

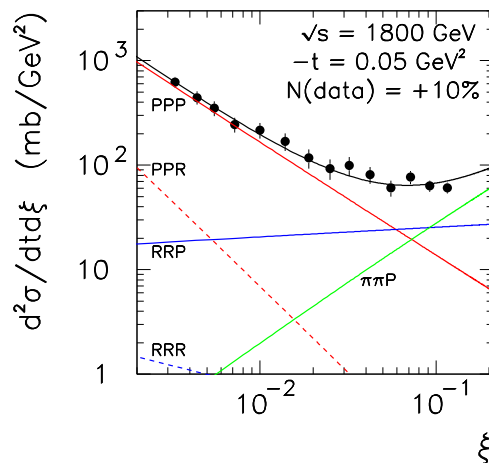


**Figure 2.14:** Triple Pomeron fit to FNAL data [121, 128, 129] taken from [80] with individual triple-Regge contributions as function of  $\xi = M_Y^2/s$ .

<sup>(27)</sup>Also a weak coupling solution with a vector like form exists. See for instance [123, 124] and references therein.

### 2.1.10 Screening effect

The exchange of a pomeron leads to a so called *rapidity*<sup>(28)</sup> *gap*, a region in rapidity in which no particles are found. This can be explained by the fact that the pomeron does not carry colour, because a colour field otherwise would fill up the gap with particles. Experimentally therefore the identification of a rapidity gap bears a good opportunity for selecting events in which a pomeron was exchanged.

Rescattering effects of the exchanged colour singlet object however can populate the rapidity gap with particles. The *rapidity gap survival probability* describes the likelihood of such a filling up of the gap, which is also called *screening effect*.

Including screening effects, such as the gap survival probability to be smaller than 1, leads in general to the evaluation of a larger *bare* soft Pomeron intercept  $\alpha_{\mathbb{P}}(0)$  in contrast to the *effective* value as seen in Sec. 2.1.8. In [80] a value of  $\alpha_{\mathbb{P}}(0) = 1.121 \pm 0.001$  is given. An even higher values of  $\alpha_{\mathbb{P}}(0) = 1.2$  is given in [130] and [122] lists a value range of 1.31 – 1.33. The listed values are given in chronological order, hence one cannot fail to observe that the estimates of the pomeron intercept is increasing.

In [131] the survival probability is calculated for  $pp$  interaction but also for  $J/\psi$  photo and DIS production. As pointed out in [80], the screening corrections in  $\gamma p \rightarrow J/\psi + Y$  are smaller. An observed pomeron intercept value in  $J/\psi$  production therefore is expected to be closer to the bare value<sup>(29)</sup>.

## 2.2 HERA Kinematics

### 2.2.1 Kinematics of electron proton scattering

The scattering process described in the preceding section is now applied to electron proton interactions at HERA. The two incoming particles are an electron<sup>(30)</sup> and a proton, as illustrated in Fig. 2.15, with four-momentum  $k$  and  $P$ , respectively. In this generic Feynman diagram the  $ep$  interaction is described by an exchange of a photon,  $\gamma$ , a  $Z^0$  or  $W^\pm$  gauge boson with four-momentum  $q$ . While a scattering process based on the former two bosons are called *neutral current*, containing in the final state the *scattered electron*, the exchange of a  $W^\pm$  boson is named *charge current* and produces an outgoing neutrino. The proton may

<sup>(28)</sup>Rapidity is defined as  $y \equiv 0.5 \log [(E + p_z) / (E - p_z)]$  with  $E$  and  $p_z$  the energy and the momentum component along the boost direction, respectively. Though the rapidity is a useful quantity because rapidity distributions  $dN/dy$  and rapidity differences are invariant under Lorentz boosts [58], experimentally more often the approximation called *pseudo rapidity*  $\eta \equiv -\log \tan(\theta/2)$  with  $\cos \theta = p_z/p$  is used.

<sup>(29)</sup>In case of  $J/\psi$  production traditionally two “kinds” of pomerons are used for description. A soft pomeron as given by DL with intercept close to 1 and rather large pomeron slope and a hard pomeron with larger pomeron intercept but smaller slope. In the tripple pomeron picture for  $J/\psi$  proton dissociative production, which is similar to the Fig. 2.13, where the protons at the top are replaced by the  $J/\psi$ . The upper two pomerons are then seen as hard pomerons, while the bottom pomeron at  $t = 0$  is a soft one. In [80] the connection between the soft and hard pomeron is explained by the large  $J/\psi$  mass, providing a higher scale which would require a DGLAP (Dokshitzer-Gribov-Lipatov-Altarelli-Parisi) evolution [132–135], causing then the hard pomeron. Since newer publication give larger bare pomeron intercept (and pomeron slopes  $\alpha_1 \sim 0$ ) the appearance of soft and hard pomerons is connected with the screening effects.

<sup>(30)</sup>HERA was operating alternatively with electrons and positrons, to lighten the text from unnecessary double statements only electrons are used for descriptions.

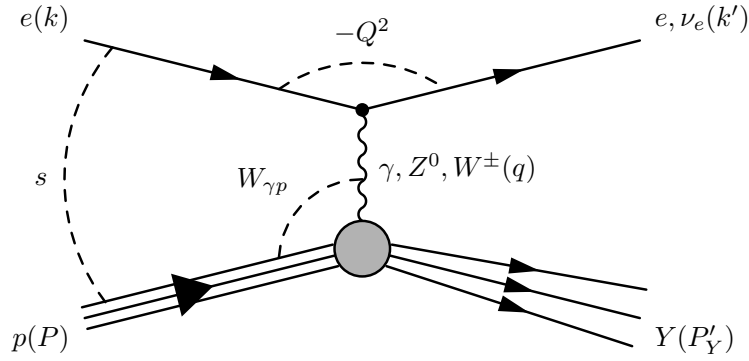


**Figure 2.15:** Generic (leading order) Feynman diagram for electron proton scattering.

stay intact or break up into a collection of particles, summarised as  $Y$  with momentum  $P'_Y$ . (Details are already discussed in Sec. 2.1.9.)

An  $ep$  interaction as shown in Fig. 2.15 has a set of variables characterising it. The most important ones are briefly explained in the following. The virtuality is defined as the inverse of the squared four-momentum of the exchanged gauge boson:

$$Q^2 \equiv -q^2 = -(k - k')^2. \quad (2.26)$$

In the limit  $Q^2 \rightarrow 0$  the photon becomes real and therefore the low  $Q^2$  limits is called *photoproduction*, while the regime of larger virtuality is called *electroproduction* or *deep inelastic scattering* (DIS). Since the measurement performed within this thesis is in the regime of photoproduction, the only relevant boson exchange is a virtual photon. Exchange of  $Z^0$  and  $W^\pm$  bosons are highly suppressed at low  $Q^2$  values due to their large masses.

The *squared centre of mass energy* is given by

$$s \equiv (P + k)^2 \quad (2.27)$$

and by neglecting the electron and proton masses, it can be written as  $s \simeq 4E_e E_P$ . The *squared centre of mass energy in the photon proton rest frame* is defined as

$$W_{\gamma p}^2 \equiv (P + q)^2. \quad (2.28)$$

Using the *inelasticity*

$$y \equiv \frac{(P \cdot q)}{(P \cdot k)} = \frac{\frac{1}{2}(W_{\gamma p}^2 - M_p^2 + Q^2)}{\frac{1}{2}(s - M_p^2 - M_e^2)} \quad (2.29)$$

and neglecting the mass contribution the photon proton energy can be written as

$$W_{\gamma p} \simeq \sqrt{ys - Q^2}. \quad (2.30)$$

The Björken  $x$  is in the leading order quark parton model the momentum fraction carried by

the proton constituent involved in the scattering process and is defined as

$$x \equiv \frac{Q^2}{2(P \cdot q)}. \quad (2.31)$$

The variables  $Q^2$ ,  $s$ ,  $x$  and  $y$  are not independent but fulfill the identity  $Q^2 = sxy$ .

### 2.2.2 From $ep$ to $\gamma p$ cross sections

The usual way to present cross sections for vector mesons production at HERA is not for  $ep$  interaction, though that is what is actually measured, but to present converted cross sections as they would appear in  $\gamma p$  interactions. This representation carries some advantages. First, it is easier to compare with non electron proton scattering experiments. Second, theoretical calculations are almost exclusively carried out for  $\gamma p$  interactions.

The standard approach to convert cross sections from  $ep$  to  $\gamma p$  is to use the *Weizsäcker-Williams approximation* [136–139]. It is an extension to the ultra relativistic case of Fermi's idea [139, 140], that if a charged particle passes the vicinity of an other particle it creates a variable electric field, which can be seen as flux of virtual photons. In photoproduction region the contribution from longitudinal polarised photons is suppressed by the transverse polarised photons. Therefore the electron proton cross section can be written as<sup>(31)</sup>

$$\sigma_{ep} \simeq \Phi_\gamma^T \sigma_{\gamma p} (\langle y \rangle, \langle Q^2 \rangle). \quad (2.32)$$

with  $\Phi_\gamma^T$  the transverse polarised photon flux, which is the integral over the phase space in  $Q^2$  and  $y$

$$\Phi_\gamma^T = \int_{y_{\min}}^{y_{\max}} dy \int_{Q_{\min}^2}^{Q_{\max}^2} dQ^2 \mathcal{F}_\gamma^T(y, Q^2), \quad (2.33)$$

with  $Q_{\min}^2 \simeq m_e^2 y^2 / (1 - y)$  and  $m_e$  the electron mass, see [141]. The differential transverse photon flux  $\mathcal{F}_\gamma^T$  can be expressed as

$$\mathcal{F}_\gamma^T(y, Q^2) = \frac{\alpha_{em}}{2\pi y Q^2} \left[ 1 + (1 - y)^2 - 2(1 - y) \frac{Q_{\min}^2}{Q^2} \right], \quad (2.34)$$

with  $\alpha_{em}$  the fine-structure constant.

## 2.3 Diffractive vector meson production in $ep$ interaction

### 2.3.1 Diffractive kinematics for vector meson production

The generic diagram for diffractive production of vector mesons in electron proton scattering is given in Fig. 2.16. In addition to the variable defined in Sec. 2.2.1 describing general  $ep$  interactions, for diffractive interactions in photoproduction two variables in addition are of interest:  $t$  and  $M_Y$ . The quantity  $t$  describes the squared momentum transfer in the

<sup>(31)</sup>A derivation is given in [141–143]. See also [144] for a summary of terms neglected in the original Weizsäcker-Williams approximation.

proton vertex, while in case of proton dissociation interaction  $M_Y$  is the invariant mass of the dissociated proton remnant.

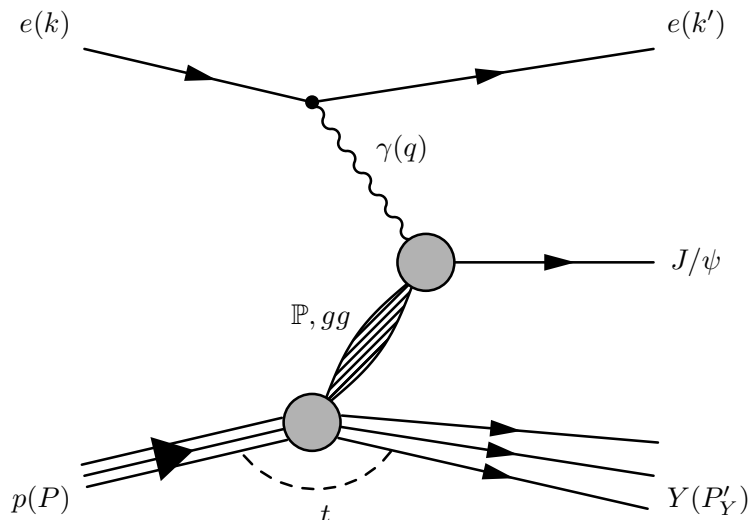


**Figure 2.16:** Generic diagram for diffractive  $J/\psi$  production in electron proton interaction with exchange of a Pomeron.

$J/\psi$  and in general vector mesons are diffractively produced by exchange of a Pomeron from the proton vertex which interacts with a photon originated from the electron vertex. As discussed in Sec. 2.1.7 in the QCD picture the Pomeron is described by a gluon ladder. In case of proton dissociation in addition to the triple pomeron PPP also the contribution of Pomeron-Pomeron-Reggeon PPR can contribute [80].

### 2.3.2 Diffractive vector meson production mechanisms

Different ideas exist how to describe the actual mechanism responsible for vector meson production in photon proton interaction. In the following sections two approaches will be briefly explained. However in both interaction “pictures” a large variety of actual models exists. A description of additional ideas can be found in [145].

#### 2.3.2.1 The vector dominance model

It was seen in early experiments that photons nuclei interaction resembles hadron nuclei interaction. In [146] the effect is called  $\rho$  photon analogy, since the photon scattering appears to behave like a  $\rho$  scattering. The same idea of a connection of amplitudes was found to exist in decays, e.g. in [147]  $\rho^0 \rightarrow \mu\mu$  and  $\pi^- \rightarrow \mu^- \bar{\nu}_\mu$  amplitudes could be related.

The idea ended in the *vector dominance model* (VDM) [148–152], in which electromagnetic interaction amplitudes are expressed as scattering amplitudes of light vector mesons.

The concept was later extended to also include heavier vector mesons such as the  $J/\psi$ <sup>(32)</sup>, which is referred to as *generalised vector dominance model*, more information can be found in [156, 157].

### 2.3.2.2 Dipole model

In more recent times the dipole model is used to describe vector meson production but also for describing general  $ep$  interactions. Instead seeing the incoming photon as composition of vector mesons, as done in the vector dominance model, in the dipole picture the photon is split into a quark antiquark pair before the actual interaction. A wide variety of different models within this ansatz exists, some are listed in [158], where also an introduction to the dipole model can be found. Global fits to exclusive vector meson production cross sections within the *colour glass condensate* [159] dipole model are performed in [160, 161]. In [162] exclusive vector mesons are described using the Golec-Biernat and Wüsthoff [163, 164] dipole approach in combination with the Balitsky-Kovchegov evolution [165–167].

---

<sup>(32)</sup>It is worth noticing that the anticipation formulated in [153] for requirement of heavier vector mesons in order to describe the inelastic electron proton scattering, was chronological before the discovery of the  $J/\psi$  particle [154, 155]. Though as stated in [153] indication existed already at that point that such higher vector mesons exists.

## HERA and the H1 detector

### 3.1 The HERA accelerator

Electron proton experiments have a long history in particle physics and date back to 1955 when the first such experiment was conducted at Stanford University by a group around Hofstadter [168]. The intention was to measure the form factors of the proton [169, 170] and later also for other nucleons [170].

But not until HERA (Hadron Elektron Ring Anlage) [171, 172], starting its operation in 1992, a collider using electron<sup>(1)</sup> and proton beams had been built. HERA was located at DESY (Deutsches Elektron Synchrotron) in Hamburg (Germany) until its shut down in 2007. The operation time is split in two phases called HERA I (1992 – 2000) and HERA II (2004 – 2007). The shut down time was used for a luminosity upgrade with a design luminosity for HERA II of  $7.6 \times 10^{31} \text{ cm}^{-2} \text{ s}^{-1}$ . This period was also used by the detector collaborations to upgrade and install new components in their experiments.

A schematic diagram of the HERA collider including its preaccelerators is shown in Fig. 3.1. The HERA tunnel, containing the electron and the proton accelerator beam pipes, had a circumference of 6.3 km. The clockwise operating electron beam was accelerated up to an energy of 27.6 GeV. The proton beam used super conducting magnets and reached an energy up to 920 GeV<sup>(2)</sup>, providing a centre of mass energy of  $\sqrt{s} \simeq 318 \text{ GeV}$  for the collider experiments.

The electrons and protons inside of the beams were localised in 210, so called, *bunches* [172], though not all bunches were filled with particles. Each filled bunch contained about  $10^{10} - 10^{11}$

<sup>(1)</sup>HERA was operating alternately with electrons and positrons beams. The term electron however will be used to refer to the lepton beam particle.

<sup>(2)</sup>A the end of HERA operation the proton beam energy was reduced to 460 GeV and 575 GeV primarily with the intention to measure the proton structure function  $F_L$ . But also the analysis presented in this thesis make use of these special running periods, as will be explained later.

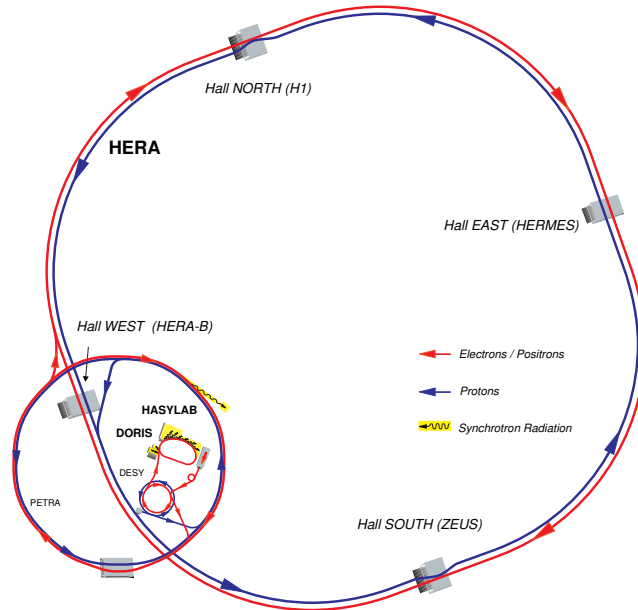


**Figure 3.1:** Schematic view of the HERA collider including its preaccelerators. The four interaction regions were equipped with the four experiments H1, HERMES, ZEUS and HERA-B. (Adapted from [173].)

particles and were separated by about 96 ns, defining the HERA clock frequency of about 10.4 MHz.

The counter rotating beams were either head-on colliding or used in combination with a fixed target in four uniformly distributed interaction regions, each containing a detector to study physical interactions. In the North and South hall, the H1 and ZEUS collider experiments were located. The East hall contained the fixed target experiment HERMES, which performed scattering of the electron beam on polarised and unpolarised hydrogen or deuterium targets in order to study the spin structure of nucleons. The HERA-B experiment, shut down in 2001, intended to measure CP violation [174] with B mesons.

## 3.2 The H1 experiment

The H1 detector [175, 176] located in the North hall of the HERA ring was designed as a multi purpose detector to measure the products of electron proton interactions.

The origin of the H1 coordinate system is set to the nominal beam *interaction point* (IP). The  $z$  axis is defined along the outgoing proton beam and defines the *forward* and *backward* region as  $z > 0$  and  $z < 0$ , respectively. The  $x$  direction points towards the centre of the HERA ring and hence the  $y$  axis direction is upwards. The polar  $\theta$  and azimuthal  $\varphi$  angle of a vector  $\mathbf{r}$  are defined according to the usual convention, as angle between  $\mathbf{r}$  and the  $z$  axis and the angle between the projection of  $\mathbf{r}$  in the  $xy$  plane and the  $x$  axis, respectively.

The main detector as shown in Fig. 3.2 covers almost the full solid angle, allowing therefore particles to be measured not only in the central, but also in forward and backward region.

The higher energy of the incoming proton beam with respect to the electron beam is reflected in the asymmetric detector design along the forward-backward direction.

The legend to the subdetector numbers as they appear in Fig. 3.2 is given in Table 3.1. A brief overview of the main detector systems important for this measurement will be given in the following, a more elaborate description can be found in [175, 176], including the detector components not described here.

### 3.2.1 Tracking detectors

The contra-rotating electron and proton beams cross each other at the *interaction point* (IP) [1]. The last focusing is performed by the superconducting magnets GO and GG [2], located inside the H1 detector, which produce the small transverse beam sizes at the IP. In case of the proton beam the horizontal and vertical beam size were  $\sigma_x = 112 \mu\text{m}$  and  $\sigma_y = 30 \mu\text{m}$  [177]<sup>(3)</sup>.

The elliptical BeAl beam pipe was surrounded by the *Central Silicon Tracker* (CST) [178–181] [2], which was built out of two double-sided (one side measuring along the  $z$ -direction, the other perpendicular to it) silicon strip layers, covering a polar angle region of  $30^\circ \leq \theta \leq 150^\circ$  [182] and a high enough resolution to identify secondary vertices. In forward direction the *Forward Silicon Tracker* (FST) [183] [3] was installed in the upgrade phase covering the region  $6.7^\circ \leq \theta \leq 18.8^\circ$ . The *Backward Silicon Tracker* (BST) [183, 184] [4] constructed from 12 planes perpendicular to the  $z$ -direction covering  $163^\circ \leq \theta \leq 174^\circ$  and helped identifying the scattered beam electron.

The next layer surrounding the silicon trackers is the *Central Inner Proportional Chamber* (CIP) [5], mainly responsible for background rejection during the online selection process (see Sec. 5.2.5). The *Central Jet Chambers* encapsulate the CIP and is composed of two concentric parts called CJC1 [7] and CJC2 [8], building the main H1 track detector. Between the CJC1 and CJC2 the *Central Outer Z-chamber* (COZ) and the *Central Outer Proportional chamber* (COP) [6] are installed.

In addition H1 is equipped with an additional forward and backward tracking devices called *Forward Tracker Detector* (FTD) [9] and *Backward Proportional Chamber* (BPC) [10].

#### 3.2.1.1 Central track reconstruction

Track hit information is gathered from the central tracker subdetectors. The main input is from the concentric drift chambers CJC1 and CJC2, with wires parallel to the beam axis and tilted drifted cells with respect to the radial direction to compensate for the Lorentz angle [176, 185]. In addition information are included from the COZ, which provides a good resolution in  $z$  direction of about  $300 \mu\text{m}$  [176] and from the CST. The  $p_t$  resolution of the CJC combined with CST is  $1.5\% \oplus 0.17\% \cdot p_t$  [GeV] [186].

The collected hit information is used by the H1 reconstruction software to perform a so called *broken line fit* [187, 188], which means that the fit is allowed to have an offset in the transition from CJC1 to CJC2. Such an offset can be caused by scattering, due the to increased amount of material of the COZ and COP both located between the CJC1 and CJC2.

<sup>(3)</sup>A small transverse beam size is crucial for a collider experiment, since the luminosity is inverse proportional to the beam size, i.e.  $\mathcal{L} \propto 1/(\sigma_x \sigma_y)$ . Hence the smaller the beam size, the larger the luminosity will be.

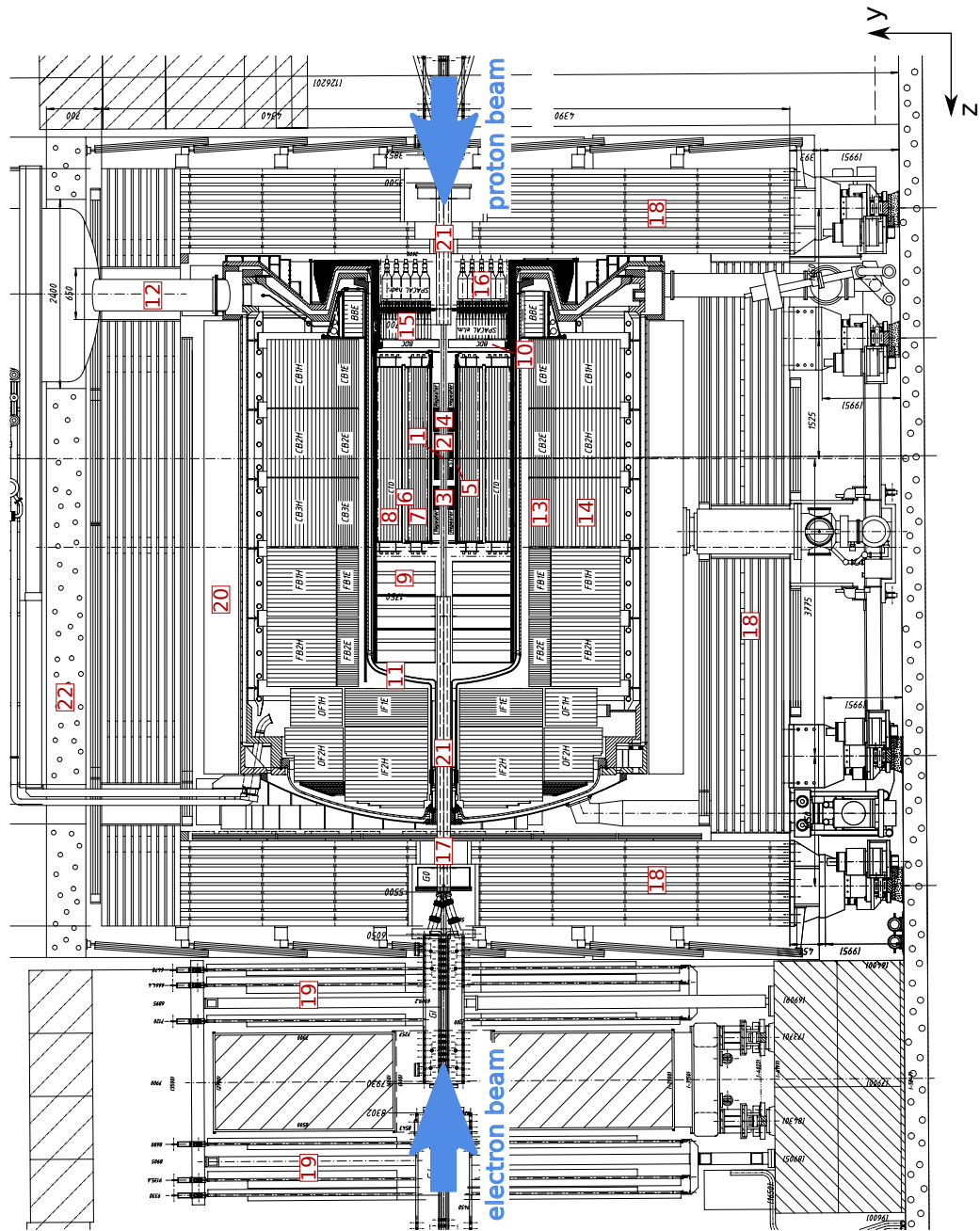


**Figure 3.2:** A schematic drawing of the H1 detector setup for the HERA II run periods. The detector components are listed in Table. 3.1 and further description is given in the text.

Number	Abbreviation	Detector component name
1	IP	Interaction Point
Tracking detectors components		
2	CST	Central Silicon Tracker
3	FST	Forward Silicon Tracker
4	BST	Backward Silicon Tracker
5	CIP(2k)	Central Inner Proportional Chamber (2000)
6	COZ	Central Outer Z-chamber
	COP	Central Outer Proportional chamber
7	CJC1	Inner Central Jet Chamber
8	CJC2	Outer Central Jet Chamber
9	FTD	Forward Tracker Detector
10	BPC	Backward Proportional Chamber
Calorimeter detectors components		
11		Liquid argon vessel
12		Liquid argon cryostat
13	LAr (elm.), ECal	Electromagnetic Liquid Argon calorimeter
14	LAr (had.), HCal	Hadronic Liquid Argon calorimeter
15	SpaCal (elm.)	Electromagnetic Spaghetti Calorimeter
16	SpaCal (had.)	Hadronic Spaghetti Calorimeter
17	PLUG	PLUG calorimeter
Muon detector components		
18	CMD	Central Muon Detector (embedded in the iron return yoke of the magnet)
19	FMD	Forward Muon Detector
Miscellaneous detector components		
20		Superconducting solenoid coil
21	GO / GG	Beam focusing magnets
22		Concrete shielding

**Table 3.1:** Listing of the main H1 detector components present during the HERA II running period. The location of the detector components is shown in Fig. 3.2 and are referred to by the numbers given in the first column.

### 3.2.2 The H1 calorimeter detectors

The *Liquid Argon Calorimeter* (LAr) [189] is composed of two detector parts. The *electromagnetic LAr calorimeter* (ECal) [13] is intended to measure the energy deposition of electrons and photons and the *hadronic LAr calorimeter* (HCal) [14] measures hadrons, which mostly penetrate the ECal with only a small amount of energy loss. The LAr system covers a polar angle region of  $3^\circ \lesssim \theta \lesssim 153^\circ$ .

In the backward direction H1 is equipped with the *SpaCal* calorimeter. Similar to LAr calorimeter also the SpaCal detector is composed of an electromagnetic [15] and hadronic [16] part. Its main design purpose is to detect the scattered beam electron as efficient as possible and covers a polar angle region of  $155^\circ \leq \theta \leq 175^\circ$ .

### 3.2.3 The H1 central muon detector

The H1 main solenoid magnet [20] is surrounded by the magnet's return yoke [18], shaped as octagon in the barrel, running parallel to the beam axis, and flat end caps. Figure 3.3 shows in the upper part a front view of the H1 detector with opened southern and northern shells. The barrel, forward and backward end cap cover a polar region of about  $35^\circ \lesssim \theta \lesssim 130^\circ$ ,  $5^\circ \lesssim \theta \lesssim 35^\circ$  and  $130^\circ \lesssim \theta \lesssim 175^\circ$ , respectively.

The lower part of the figure shows an enhancement of the iron yoke structure, which is interlaced with slits, equipped with *limited streamer tubes* (LST) in 8 single layers and 1 double layer. In front and behind the yoke 3 layers of LST's are installed, called *inner* and *outer muon box*. The purpose of the LST is not only to return information of particle passing through the muon system, but also serves as tail catcher for the hadronic LAr calorimeter.

The layers of LST are built of several pairs of fire-retardant Luranyl [190] blocks, each block containing 8 chambers with a silver coated Cu-Be wire with diameter of  $100 \mu\text{m}$ . The blocks are composed from U-profiles which are painted with graphite to ensure low surface resistance and are closed by a Luranyl plate with high surface resistance, which prohibits an immediate discharge. The localised charge is measured by strips or pads glued on top of the blocks, providing information of a passing particle in transverse direction of the wires [176, 191].

Muon track reconstruction is based mainly on the digital read out information of the 16 wire and the 5 strip layers with resolutions of  $3 - 4 \text{ mm}$  and  $10 - 15 \text{ mm}$ , respectively. The 11 pad layers, providing only coarse information, are used to resolve ambiguities [192] <sup>(4)</sup>.

### 3.2.4 The H1 forward detectors

#### 3.2.4.1 PLUG calorimeter

The PLUG calorimeter [176, 193] [17] is built of four scintillating planes with a azimuthal substructure of 8 so called tiles. They are read out by 8 photo multiplier tubes (PMT) for measuring the deposited energy, plus 4 additional PMT's for collecting timing information. A side view is shown in Fig. 3.4.

The timing information is used for background suppression caused by beam gas and beam wall scattering [194, 195]. The PLUG calorimeter is located in the forward direction at

<sup>(4)</sup>The pad layers are read out analog as well and structured in towers used as information for the tail catcher.

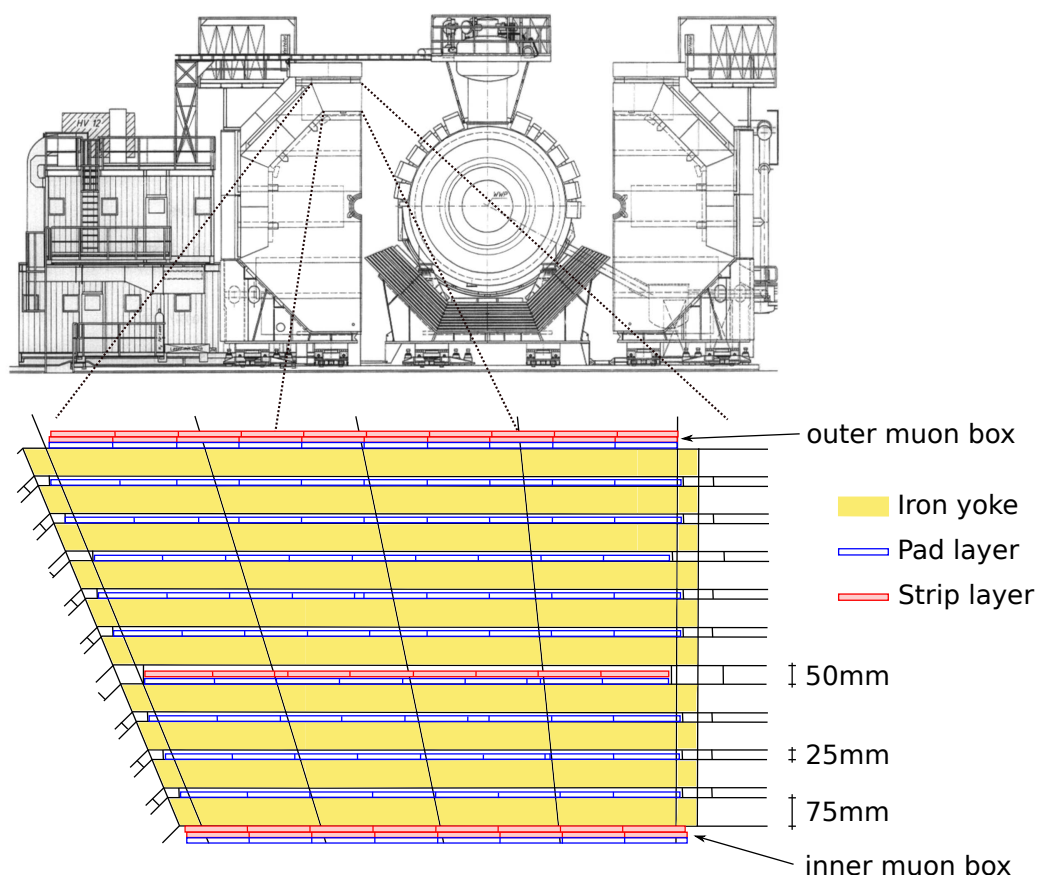


**Figure 3.3:** Illustration of the H1 front view with open southern and northern iron yoke (upper part, taken from [175]) and a sketch of the equipped iron yoke with limited streamer tubes (lower part).

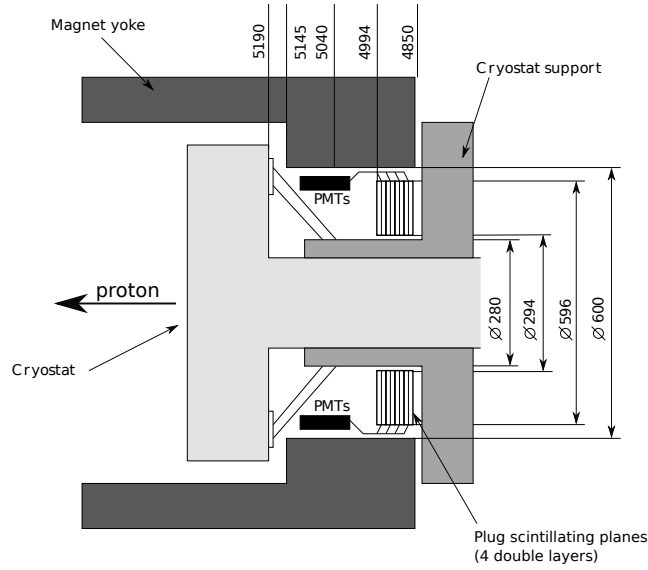


**Figure 3.4:** Schematic illustration of side view of the PLUG detector.

$z = 4.9\text{m}$  close to the beam pipe, covering the polar angle region of about  $2.3^\circ - 3.2^\circ$ . It therefore extends the  $\theta$  angle covered by the LAr calorimeter system.

The particles of the proton remnant in proton dissociative events are mainly produced in forward direction close to the beam pipe. Hence the PLUG calorimeter is at an optimal position to detect these particles, which is used in this analysis, as will be explained later.

### 3.2.4.2 Forward tagger system

The *Forward Tagger System* (FTS) is composed of four layers, each located at different positions along the beam pipe in forward direction at 26, 28, 53 and 92 m from the nominal interaction point. Each layer plane contains four scintillating counters mounted transversely to the beam direction. The four scintillators are positioned around the beam pipe as close as possible. An illustration of the organisation of the scintillator plates in the layer at  $z = 28\text{m}$  is given in Fig. 3.5. It covers a polar angle region of about  $0.08^\circ - 0.6^\circ$ . To protect the scintillators from synchrotron radiation each is shielded by 1 mm of lead.

The position of the FTS counters close to the beam pipe and far away from the nominal interaction point, combined with a reasonable efficiency for registering proton remnant particles, makes it an ideal detector for tagging proton dissociative events.

### 3.2.4.3 The forward muon detector

The forward muon detector (FMD) is located outside the forward end cap of the central muon detector. It covers a polar angle region of about  $3^\circ \leq \theta \leq 18^\circ$  and is composed of 6 layers. Due to its large acceptance region in forward direction it would be a preferable detector for measuring proton remnant particles. However for the considered data periods it

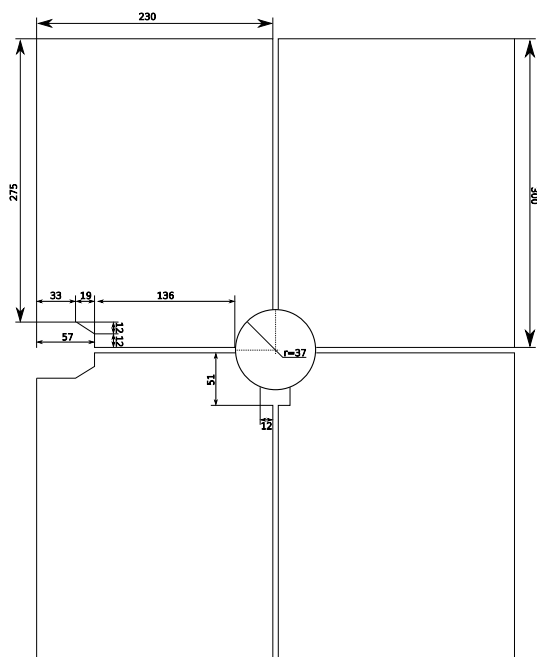


**Figure 3.5:** Schematic drawing of scintillator plates in forward tagging station at  $z = 28$  m.

was seen during this work that the description of the simulation is not sufficient, leading to the decision not to include the FMD in the analysis.



## Monte Carlo Simulations

*Monte Carlo* (MC) simulations are widely used within the field of particles physics. The reasons vary but usually they are inevitable for extracting certain information otherwise not accessible. Simulations are used to create theoretical predictions, which can be compared to measurements, to extrapolated measured quantities into other regions of phase space or for calculating detector effects such as acceptance and efficiency quantities.

Producing a final MC sample basically involves two steps. First events are dived according to a physical model or theoretical distributions by use of random generators. The software responsible for this step is called a *generator*. The variety of different ideas and models is immense, an overview of different MC generators for electron proton interactions can be found in [196]. On whatever model a generator is built, the output remains the same: four-vectors of all stable particles contained in an event.

From an experimentalist point of view the four-vectors of particles, as they are produced by a generator, are not very useful. The response of the detector is not yet contained in the simulation. Therefore the next step contains the conversion from bare four-vectors of particles to their response in a detector. In contrast to the generator, which is independent of a specific detector, the detector response simulation depends on the actual detector design.

In H1 the conversion from MC generated four-vectors to the actual response of the detector is performed in three main steps. First, the interaction of the particles with each detector subsystem is simulated by the *H1SIM* software. It contains a realistic model of the H1 detector, of each subsystem including material compounds and geometrical orientation, built within the GEANT 3 framework [197], which simulates the interaction of particles with the detector material. Afterwards the output of H1SIM is fed into *HIREC* the H1 reconstruction software, which is identical for MC generated events and real data events. It recreates the physical events, i.e. track, momentum and energy reconstruction of particles contained in a event, out of the information returned by the detector subsystems. A last step involves the simulation of the H1 track trigger system called Fast Track Trigger by use of the *FTTEMU* software. More information can be found in in Sec. 5.2.

In the following a description of the MC generators used in this thesis is given.

## 4.1 The DiffVM Monte Carlo generator

The  $J/\psi$  signal events and the background contribution of  $J/\psi$  produced by feed downs of the  $\psi(2S)$  resonance are simulated by using the DiffVM [198, 199] generator. It simulates diffractive vector meson production in electron proton interaction in the framework of the vector dominance model (VDM) and Regge theory (see Chapter 2).

### 4.1.1 $J/\psi$ production

To produce elastic  $ep \rightarrow J/\psi p$  and proton dissociative  $ep \rightarrow J/\psi Y$  signal events the DiffVM Monte Carlo generator is used. In order to perform the cross section measurements for both decay channels  $J/\psi \rightarrow ee$  and  $J/\psi \rightarrow \mu\mu$ , MC samples for both channels are produced.

The models for elastic and proton dissociative event creation are not varying with respect to the photon creation but for the pomeron interaction with the proton leading to the different final states. Therefore first a short description of the photon creation treatment within DiffVM is given. Afterwards elastic and proton dissociation implementation is discussed.

#### 4.1.1.1 Simulation of photon exchange in DiffVM

At the very beginning of each event DiffVM generates an electron and a proton with momenta as defined in the steering card provided to the generator. From the incoming electron the exchange of a virtual photon is simulated according to the Weizsäcker-Williams approximation, discussed in Sec. 2.2.2.

The transition of the virtual radiated photon to the vector meson is performed in the VDM picture. The parametrisation of the  $Q^2$  dependence of the transverse polarised photon cross section is given by

$$\sigma_{\gamma^*p}^T = \sigma_{\gamma p} \left( \frac{1}{1 + \frac{Q^2}{\Lambda^2}} \right)^{n_q} \quad (4.1)$$

with  $\sigma_{\gamma p}$  the photon proton cross section<sup>(1)</sup>. The free parameters  $\Lambda$  and  $n_q$  can be freely chosen. The default value for  $\Lambda$  is the mass of the produced vector meson, i.e. in case of this measurement the  $J/\psi$  mass  $M_{J/\psi} \simeq 3.097$  GeV. The parameter  $n_q$  is set to 2.5 in agreement with the value of  $2.486 \pm 0.080(\text{stat.}) \pm 0.068(\text{syst.})$  given in [29].

The ratio  $R_{LT}$  of longitudinal to transverse cross section is in DiffVM parametrised as

$$R_{LT}(Q^2) \equiv \frac{\sigma_{\gamma^*p}^L}{\sigma_{\gamma^*p}^T} = \frac{\xi \frac{Q^2}{\Lambda^2}}{1 + \chi \xi \frac{Q^2}{\Lambda^2}}. \quad (4.2)$$

---

<sup>(1)</sup>The transverse cross section in the VDM picture as given in [151] is  $\sigma_T \propto 1/(1 + Q^2/\Lambda)^{n_q}$  with  $n_q = 2$ . A former version of DiffVM therefore was using this exact expression, but was later extended to allow varying also  $n_q$ , in order to increase the description of data by DiffVM.

The variable  $\chi$  is a phenomenological parameter without theoretical background. In case of  $\chi = 0$  the above formula simplifies to

$$R_{LT} = \xi \frac{Q^2}{\Lambda^2} \quad (4.3)$$

with  $\xi$  controlling the rise of  $R_{LT}$  with  $Q^2$ <sup>(2)</sup>. In order to have a realistic estimate for generating events, the  $R_{LT}$  distribution was fitted to H1 [29] and ZEUS [35] data, as displayed in Fig. 4.1, using the parametrisation with  $\chi = 0$ . The H1 data are shown as

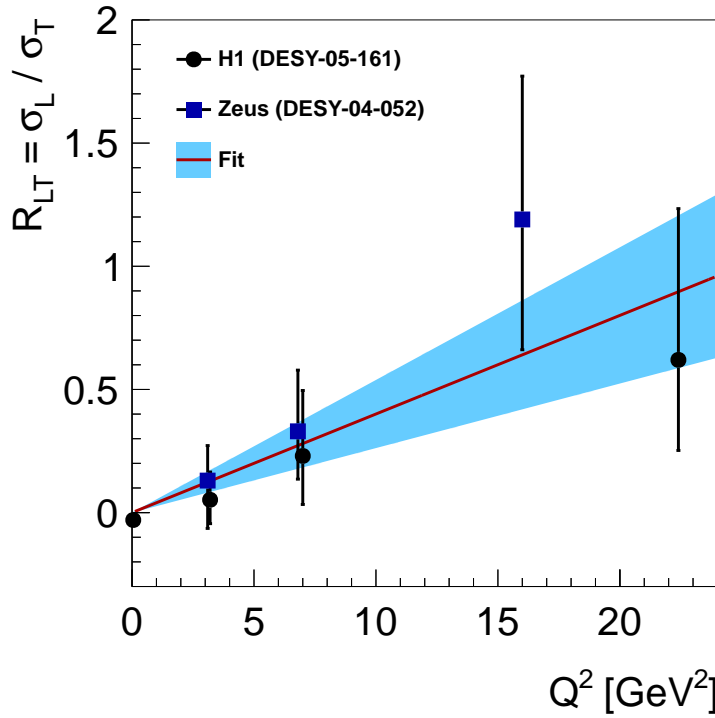


**Figure 4.1:** The ratio  $R_{LT}$  of longitudinal to transverse cross section is shown as function of  $Q^2$ . The black circles and blue squares represent H1 [29] and ZEUS [35] data. The red line shows the performed fit with the function  $R_{LT}(Q^2) = \xi Q^2 / M_{J/\psi}^2$  including error band.

black circles and the ZEUS data as blue squares. The fit function is taken as Eq. (4.3) with  $\Lambda = M_{J/\psi}$  and obtained is the parameter value  $\xi = 0.38 \pm 0.13$ <sup>(3)</sup>.

<sup>(2)</sup>The dependence  $R_{LT} \propto Q^2 / \Lambda^2$  is given by the VDM model [151, 153]. As stated in [153], the  $R_{LT}$  dependence on  $Q^2$  is weaker than expected, which can be simulated by the parametrisation shown in Eq. (4.2), which allows with  $\chi > 0$  a damping of the increase of  $R_{LT}$  with  $Q^2$ .

<sup>(3)</sup>In addition a fit with  $\chi$  as free parameter was performed, giving a negative value, which would create a singularity in  $Q^2$ . Since for trigger efficiency studies (see Sec. 7.1) a DIS sample is required, this ansatz was dropped and the phenomenological parameter  $\chi$  was fixed to 0.

#### 4.1.1.2 Elastic $J/\psi$ production

The interaction of the vector meson with the proton is implemented in DiffVM as exchange of a single pomeron. DiffVM offers the possibility to either produce elastic or proton dissociative events.

As can be seen from Eq. (2.18) and (2.20) the differential cross section in  $T \equiv -t > 0$  can be expressed in Regge theory with single pomeron exchange as

$$\frac{d\sigma}{dT} \propto [\beta_{p\mathbb{P}}(T)\beta_{J/\psi\mathbb{P}}(T)]^2 W^{4[\alpha(T)-1]} \quad (4.4)$$

with  $W \equiv W_{\gamma p}$ . Experimental data show that for elastic interactions at low  $T$  a good description is achieved by using an exponential function for the  $\beta$  couplings<sup>(4)</sup>. This seems to be independent of the actual interaction, for  $pp$  see for instance [201] or for  $J/\psi$  production in  $ep$  scattering [29].

The implementation in DiffVM is similar to Eq. (4.4) and uses a linear trajectory  $\tilde{\alpha}_{\text{el}}(T) = 1 + \tilde{\varepsilon}_{\text{el}} - \tilde{\alpha}_{1,\text{el}}T$  and has the form

$$\frac{d\sigma}{dT} = \left. \frac{d\sigma}{dT} \right|_{W=W_0, T=0} e^{-bT} \left( \frac{W}{W_0} \right)^{4\tilde{\varepsilon}_{\text{el}}} \quad (4.5)$$

with a so called effective  $b$  of

$$b = b(W; \tilde{b}_{\text{el}}, \tilde{\alpha}_{1,\text{el}}, W_0) = \tilde{b}_{\text{el}} + 4\tilde{\alpha}_{1,\text{el}} \log \left( \frac{W}{W_0} \right). \quad (4.6)$$

The variable  $W_0$  serves as normalisation parameter and must be provided as input together with  $d\sigma/dT|_{W=W_0, T=0}$ ,  $\tilde{b}_{\text{el}}$ ,  $\tilde{\varepsilon}_{\text{el}}$  and  $\tilde{\alpha}_{1,\text{el}}$  to DiffVM. The pomeron slope is set to 0, while the parameter  $\tilde{b}_{\text{el}}$  is knowingly set to a smaller value in order to increase statistics at larger  $T$  values. A summary of the parameters can be found in Table 4.1.

#### 4.1.1.3 Proton dissociation $J/\psi$ production

For the proton dissociative  $J/\psi$  production the pure  $T$ -dependence is not sufficient anymore. Also the proton remnant has to be modelled within DiffVM. The double differential cross section is parametrised as

$$\frac{d\sigma}{dT dM_Y^2} = \left. \frac{d\sigma}{dT dM_Y^2} \right|_0 \left( 1 + \frac{\tilde{b}_{\text{pd}}}{\tilde{n}_{\text{pd}}} T \right)^{-\tilde{n}_{\text{pd}}} \left( \frac{W}{W_0} \right)^{4(\tilde{\varepsilon}_{\text{pd}} - \tilde{\alpha}_{1,\text{pd}}T)} \frac{f(M_Y^2)}{\left( \frac{M_Y^2}{M_{Y,0}^2} \right)^{1+\tilde{\varepsilon}_M}}, \quad (4.7)$$

<sup>(4)</sup>Due to proportionality of the differential cross section to the  $\beta$  couplings, sometimes  $d\sigma/dT \propto e^{-bT}$  is written with  $b = b_p + b_V$ . The transverse size of the proton is characterised by  $b_p$  and  $b_V \propto 1/(Q^2 + M_V^2)$  with  $M_V$  the mass of the vector meson. It can then be shown that  $b(Q^2 + M_V^2)$  has a universal behaviour for all vector mesons (see for instance Fig. 22 in [8]). At large scales one obtains  $b_V \sim 0$  and therefore  $b \sim b_p$  which gives a value of  $b_p$  of about  $5 \text{ GeV}^{-2}$ . Since the  $b$ -slope is related to the averaged squared transverse radius of the proton by  $\langle r^2 \rangle = 2b_p$  and to the gluonic proton radius (assuming also Gaussian behaviour in the 3<sup>rd</sup> dimension)  $R_p = \sqrt{3b_p}$  [160], i.e.  $R_p \simeq 0.76 \text{ fm}$ . This value is slightly smaller than the proton rms charged radius of about  $0.88 \text{ fm}$  [200].

inspired by the triple Regge model, as introduced in Sec. 2.1.9.2. The  $J/\psi$  pomeron coupling is now simulated by the function  $(1 + \tilde{b}_{\text{pd}}T/\tilde{n}_{\text{pd}})^{-\tilde{n}_{\text{pd}}}$ , which behaves like an exponential ( $e^{-\tilde{b}_{\text{pd}}T}$ ) for  $\tilde{b}_{\text{pd}}T/\tilde{n}_{\text{pd}} \ll 1$ , but follows a power law ( $T^{-\tilde{n}_{\text{pd}}}$ ) at large  $T$  values. As in the elastic case the parameters controlling the  $T$  spectrum are chosen in order to increase statistics at large  $T$  values. The parameter values are given in Table 4.1. The  $W$  dependence is chosen to be identical to the elastic case.

The last factor in Eq. (4.7) models the  $M_Y$  distribution with normalisation factor  $M_{Y,0} = 1$  GeV. The pomeron intercept of the soft pomeron coupling to the proton is set to the value obtained by the Donnachie and Landshoff fit to total hadronic cross sections, i.e.  $\tilde{\epsilon}_M = 0.0808$ , as seen in Sec. 2.1.8. The  $f$  function takes into account the resonance states for low  $M_Y$  and is defined as

$$f(M_Y) = \begin{cases} 1, & M_Y \geq 2 \text{ GeV} \\ \text{resonances,} & M_Y < 2 \text{ GeV.} \end{cases} \quad (4.8)$$

In case of low masses  $M_Y < 1.9$  GeV the  $N$  resonances ( $N(1440)$ ,  $N(1520)$ ,  $N(1680)$ ,  $N(1700)$  and  $N(1710)$ ) are produced. For larger  $M_Y$  values the incoming proton is seen as a quark-diquark system, in which the quark couples to the pomeron. The system then is hadronised by the use of JETSET [202, 203].

#### 4.1.1.4 Parameters of generated MC samples

All parameters relevant for generating the elastic and proton dissociative signal MC samples are given in Table 4.1.

Parameter	Value
$\xi$	0.38
$\eta$	0
$W_0$	95 GeV
$\tilde{b}_{\text{el}}$	$2 \text{ GeV}^{-2}$
$\tilde{\epsilon}_{\text{el}}$	0.224
$\tilde{\alpha}_{1,\text{el}}$	0
$\tilde{b}_{\text{pd}}$	$1.3 \text{ GeV}^{-2}$
$\tilde{n}_{\text{pd}}$	2.0
$\tilde{\epsilon}_{\text{pd}}$	0.224
$\tilde{\epsilon}_M$	0.0808
$\tilde{\alpha}_{1,\text{pd}}$	0

**Table 4.1:** Parameters used for generating the elastic and proton dissociative DiffVM MC samples.

#### 4.1.2 QED corrections with PHOTOS

The DiffVM generator is extended by the PHOTOS generator [204–206], which simulates the correction due to QED (quantum electrodynamics) radiation in the final state. This is required

especially for the  $J/\psi \rightarrow ee$  decay channel, since the electron radiation is substantial.

The measured ratio of events with  $J/\psi \rightarrow ee\gamma$  to  $J/\psi \rightarrow ee$  is  $(15 \pm 2)\%$  with photon energies  $E_\gamma > 100 \text{ MeV}$  [207]. This is in good agreement with PHOTOS which gives a ratio of about 16.5% in case of single photon radiation and about 2% in case of double photon radiation.

The branching ratios  $\mathcal{B}(J/\psi \rightarrow ee) = (5.94 \pm 0.06)\%$  and  $\mathcal{B}(J/\psi \rightarrow \mu\mu) = (5.93 \pm 0.06)\%$  listed in [58] are dominated by the measurements performed by the CLEO collaboration [208]. After consulting with an expert from the CLEO collaboration [209], it became clear that the listed branching ratios do in fact include these radiative  $J/\psi \rightarrow ee\gamma$  contributions.

Hence the  $J/\psi \rightarrow ee\gamma$  decay should not be seen as separate decay channel of the  $J/\psi$ , but simply as radiation of the electrons in the final state, as it is implemented in PHOTOS, i.e. there is no need to increase the branching ratios by 15%.

### 4.1.3 $\psi(2S)$ background production

The first radial excited state of the  $J/\psi$  the  $\psi(2S)$ , also called  $\psi'$ , decays dominantly ( $\sim 60\%$ ) into a  $J/\psi$  and something else. It is expected therefore that a sample selected for a  $J/\psi$  analysis also contains feed downs from  $\psi(2S)$ .

This background is simulated using DiffVM producing  $\psi(2S)$  events. All  $\psi(2S)$  decay channels as implemented in JETSET are used. The elastic and the proton dissociative MC samples are both created with an exponential  $T$  spectrum  $d\sigma/dT \propto e^{-\tilde{b}T}$  with  $\tilde{b}_{\text{el}} = 4.31$  and  $\tilde{b}_{\text{pd}} = 0.59$  as measured in [40]. The  $W_{\gamma p}$  dependance is generated with an  $\tilde{\varepsilon} = \tilde{\varepsilon}(J/\psi) + \frac{1}{4}\Delta\tilde{\delta} = 0.284$ , with  $\tilde{\varepsilon}(J/\psi) = 0.224$  taken from [29] and  $\Delta\tilde{\delta} = 0.24$  taken from [40]. The pomeron slope in both cases is set to 0.

The DiffVM generator requires from the user to provide the absolute cross section  $\sigma_0 \equiv \sigma(W = W_0)$  of the process to generate. (In case of elastic vector meson production  $\sigma_0$  is  $d\sigma/dT|_{W=W_0, T=0}$  as it appears in Eq. (4.5).) But the absolute diffractive  $\psi(2S)$  cross section was – to the knowledge of the author – never measured. In order therefore to determine  $\sigma_0$  for elastic and proton dissociative  $\psi(2S)$  production, first the  $J/\psi$  cross section measurement was performed. The cross section ratio of  $\psi(2S)$  to  $J/\psi$   $R = 0.166 \pm 0.007(\text{stat.}) \pm 0.008(\text{sys.}) \pm 0.007(\text{BR})$  [40] in combination with the  $J/\psi$  cross section measurement from the first step is used to determine a realistic estimate of the absolute  $\psi(2S)$  cross section  $\sigma_0$ . In the last step  $\sigma_0$  is provided to DiffVM to generate the  $\psi(2S)$  MC samples.

The expected correction for this measurement due to  $\psi(2S)$  contribution is about 4%, as an evaluation in [210] shows. The actual determined corrections for this measurement are discussed in Sec. 9.2.3.3.

## 4.2 GRAPE – Dilepton Generator

GRAPE [211–213] is a Monte Carlo event generator for non-resonant di-lepton production in electron proton scattering. Several types of process are included in the generator. The main process, most dominant in the largest part of the phase space, is the two-photon Bethe Heitler process. In addition also QED-Compton type diagrams, where a radiative photon from the beam electron converts into a lepton pair, is considered. Further  $Z^0$  on/off-shell production type diagrams are taken into account. In case of producing electron-positron pairs in the final

state also interference terms with the scattered electron are simulated. The calculations are performed at tree level using exact matrix elements in electroweak theory. The contributing amplitudes are calculated by auto generated code produced by GRACE [214–216].

To cover the full kinematic phase space three regions are distinguished: elastic, quasi-elastic and inelastic. An illustration is given in Fig. 4.2 showing the kinematical regions in  $(M_Y, -t)$  plane<sup>(5)</sup>. The blue vertical line at  $M_Y = M_p$ , with  $M_p$  the proton mass, indicates the elastic ( $ep \rightarrow ep\ell\ell$ ) process with  $\ell\ell$  either electron-positron or muon-antimuon pair. The quasi-elastic<sup>(6)</sup> process is shown in two parts because GRAPE does produce events only for one part at a time<sup>(7)</sup>. The ranges of the quasi-elastic region 1 is  $M_p + M_\pi \leq M_Y \leq M_Y^{\max}$  (with  $M_\pi$  the pion mass) and for region 2 it is  $M_Y > M_Y^{\max}$  &&  $-t < -t^{\max}$ . The parameters are set to  $M_Y^{\max} = 5$  GeV and  $-t^{\max} = 1$  GeV<sup>2</sup> as recommended in [211] and also used in [219]. In the inelastic region parton-density-functions are used for generating DIS events.

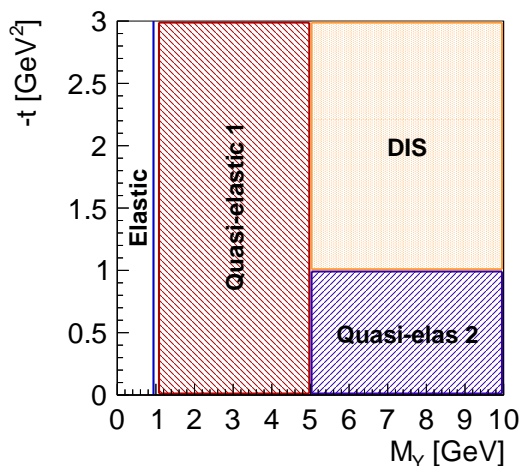


**Figure 4.2:** Illustration of composition used to generated events in GRAPE to cover the whole kinematical phase space.

### 4.3 The CASCADE generator

In addition to diffractive vector meson production also the so called *inelastic* production is possible. Seen in the leading order QCD picture, inelastic  $J/\psi$  are produced by exchange of

<sup>(5)</sup>The notation used within GRAPE differs from what is used in this analysis. In GRAPE  $M_Y$  and  $-t$  are called  $M_{\text{had}}$  and  $Q_p^2$ , respectively.

<sup>(6)</sup>For quasi-elastic event generation in the resonance region  $M_Y < 2$  GeV the Brass et al. [217] parametrisation is used, while for  $M_Y > 2$  GeV the ALLM97 [218] is description is used.

<sup>(7)</sup>Seven separate runs are performed one for the elastic, two for the quasi-elastic and four for the inelastic process, each generated with the same luminosity. Afterwards all events from the seven runs are randomised and combined, resembling the output of a generator producing events for the whole kinematic phase space.

only one gluon between the proton vertex and the incoming  $c\bar{c}$  system. The CASCADE MC generator [220] can be used to produce a MC sample modeling the inelastic  $J/\psi$  production.

To check the contribution of inelastic produced  $J/\psi$  events in the selected data sample, the same CASCADE MC sample is used as in the measurement [221].

## Trigger and data periods

The more general ideas, as discussed so far, must face reality at some point. The focus in this chapter is turned to the online selection of data performed with a trigger system. The first two sections discuss the necessity for a trigger system and its specific implementation in H1. The next section explains in more detail the trigger conditions required for this analysis, while the last section describes the used data periods.

### 5.1 What is a trigger and why is it needed?

A detector in the environment of today's particle accelerators often faces a series of problems connected with selecting data. Generally speaking, the interesting interactions, caused by the processes intended to be measured, often have small cross sections<sup>(1)</sup>. In an ideal setup all those events of interest could just be recorded and stored on disk or tape for the offline data analysis. But events not connected to the process of interest are also present, contaminating the sample. The bulk of these events, regardless of their origin, is called background. As long as the background is non-dominant this seems not to be an issue, but usually the contribution of non-signal events are orders of magnitude higher. For example the background event rate for HERA II, typically caused by proton collisions with the beam pipe or gas, was expected post-upgrade to be in the order of 500 kHz [222] compared to the frequency of good  $ep$  events stored to tape in the order of 10 Hz.

At this point a trigger system is taking its place. Its only job is to decide during the data recording, if an event is considered of any interest or not. A positive decision should lead to a record of the event, a negative outcome to its rejection.

---

<sup>(1)</sup>Cross section  $\sigma$  is defined as ratio of number of events,  $N$ , over integrated luminosity,  $\mathcal{L}$ , of the process of interest or more formalised:  $\sigma = N/\mathcal{L}$ .

Ideally a trigger system should only reject those events, for which a reasonable amount of doubt exist that the event signatures in the detector is connected to a process of interest. The filtering of events unfortunately also rejects events of interest, therefore not only its background rejection must be high, but also its efficiency for selecting events of interest should be as large as possible.

The hardware and/or software implementation of the trigger system<sup>(2)</sup> requires a finite time for deriving the keep-reject-decision for an event. While an event is processed by the trigger system, a possible next event may not be analysed and therefore is lost. The time duration for which the trigger system is not capable to handle a next event is called *dead time*, which is preferred to be as small as possible, in order to loose as less events as possible.

## 5.2 The H1 trigger system

As discussed in the previous section, the H1 trigger system should return an online decision statement, either to rejected an event or to record and permanently store it. The H1 trigger system is based on event signatures in the detector, such as hits and energy depositions from the various detector subsystems, left by the produced particles of the *ep* interaction. The quality of such a decision is strongly depending on the amount of information available, which itself is related to the obtainable time for collecting these information.

The HERA bunch crossing rate of 10.4 MHz gives the maximal observable event rate, though *ep* interactions only occur with a rate of about 1 kHz. The H1 readout frequency is about 50 Hz and the rate of events stored to tape is about 10 - 40 Hz. Therefore a rate reduction in the order of one million must be achieved.

The problem of achieving this high reduction rate is solved by dividing it into stages in time, called *trigger levels*, organized in H1 in four levels, abbreviated as *L1* to *L4*. A higher trigger level only examines an event, if all preceding levels accepted it, giving each new level more time for deriving a decision. After successfully passing all levels the event quantities are stored on disk, ready for the offline data analysis.

A sketch of the H1 trigger system is given in Fig.5.1 and will be discussed in the following subsections.

### 5.2.1 The level 1 trigger

The first level trigger [225] is designed without dead time, in order to maximise the online selection of interesting events. The available decision time for the first level trigger is  $2.3 \mu\text{s}$ . To achieve the no dead time requirement, all bunch crosses within  $2.3 \mu\text{s}$  are stored in a pipeline, providing the first level triggers enough time to analyse each bunch cross and forming a decision.

On this level 256 *trigger elements* are defined, each using information from a single H1 subdetector system. By logic combination of these elements in the *central trigger logic* (CTL) 128 L1 *raw subtriggers* are formed, which build the basic concept for decision on L1.

---

<sup>(2)</sup>Most trigger system design use a setup with hardware and software components, an early example for such a design in multipurpose detectors are the Super Proton Synchrotron (SPS) experiments UA1 and UA2 [223]. On the other side the planned trigger systems for the International Linear Collider (ILC) detectors tend to be composed only from software components [224].

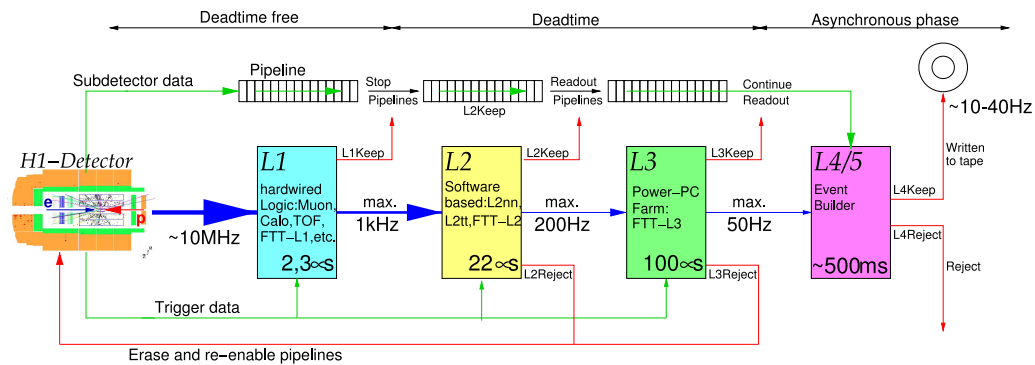


**Figure 5.1:** Overview of the H1 trigger system showing the four trigger levels L1 to L4. (Figure adapted from [182].)

All trigger levels share the same two-sided problem. On the one hand they must select the physical process of interest, which is done for L1 on the basis of the subtriggers. On the other side the output rate may still be too high for the next level to be handled. Therefore on L1 an additional statistical reduction mechanism is introduced, with so called *prescale factors*, which are adjustable integral numbers. The mechanism works in the following way: A prescale factor  $n_i$  is defined for every subtrigger  $i$  and only every  $n_i$ -th time a specific subtrigger is fulfilled, it is flagged as *actual*. If an event has at least one *actual subtrigger* condition fulfilled, it is passed on to the second level trigger.

The maximal L2 input rate is fixed to 1 kHz. Due to changing beam condition and delivered luminosity<sup>(3)</sup> the prescale factors for each subtrigger are adjusted by reevaluation of the trigger rates during data recording [226].

If an event is accepted by at least one sub trigger, the *L1Keep* signal is formed and the event is transferred to the second level. The L1 pipelines are frozen and the dead time begins.

### 5.2.2 The level 2 trigger

The second level trigger [227] is formed by three systems, each defining their own level 2 trigger elements.

The L2 neural network trigger system [228–230] uses an offline trained feed-forward neural network to interpret the available information and exploit the parallel computation features available with this method. The topological trigger system [231, 232] compares correlation of information from calorimeter, tracker and muon system in a  $16 \times 16$  binned  $(\theta, \phi)$  space with offline calculated tables to select events. The third system, the *L2 Fast Track Trigger* (FTT), reconstructs online tracks and reaches a high spatial track resolution, comparable with the information available after the full event reconstruction. More details about the full FTT system are provided in Sec. 5.2.5.

<sup>(3)</sup>During a typical fill of HERA lasting about 10 hours, usually defined by the electron beam lifetime, the luminosity decreases by about a factor of 3 or more [226].

The three L2 trigger systems define in total 56 L2 trigger elements. Although it would be possible to combine L2 trigger elements it is usually not needed. Not all subtrigger define a requirement on L2. In such a case an event is automatically passed on to the next level.

The maximal decision time available on this level is  $20\ \mu\text{s}$ , which contributes to the dead time. A negative decision restarts the L1 pipeline filling. A positive answer starts the full detector read out, which can require up to 2 ms. The L2 output rate can maximally be about 200 Hz.

### 5.2.3 The level 3 trigger

The read out, started after a positive decision from L2 trigger, is largely responsible for the total dead time. The decision time available on L3 is  $100\ \mu\text{s}$ , which is compared to the total read out time small. If a negative answer is formed for a subtrigger with an L3 condition, the detector read out is stopped and the data taking is restarted. Therefore the verification of L3 (if such a condition is defined for the specific subtrigger), can minimize the dead time.

The implementation of the L3 trigger is done in the third level of the FTT [182, 233, 234] using in addition to the FTT L2 track information also quantities provided by the muon and the calorimeter system. The decision calculations are performed solely on a PowerPC equipped PC-farm.

### 5.2.4 The level 4 trigger

After an event is passed to the L4 trigger level, the L1 pipeline filling is restarted. The fourth level trigger is operating asynchronous to the HERA clock and does not contribute to the dead time. The maximal input rate is about 50 Hz and the output rate is set to about 10 – 40 Hz.

Compared to the other trigger levels, L4 is handled by a commercially available Linux computer farm [235] running the H1 reconstruction software *H1Rec* on the complete read out detector information. A filter software afterwards labels events according to predefined event classes, in order to reject background events. Giving some classes a down scaling weight, called *L4 Weights*, reduces the amount of data further to fulfill the bandwidth requirements. Events passed the L4 are written to tape and saved permanently.

### 5.2.5 HERA II trigger upgrade

The HERA upgrade, taking place in the years 2000/2001, had the goal to increase the luminosity<sup>(4)</sup> by a factor of 3 [236]. The increase in luminosity however also leads to more background, which must be filtered by the trigger system in order to profit from the higher luminosity.

In H1 three main trigger system where upgraded. The *CIP2k*<sup>(5)</sup> [222, 237–240] provides a high efficiency for rejecting non-*ep* events caused by beam gas and proton wall scattering.

---

<sup>(4)</sup>In addition also longitudinal polarized lepton beams could be provided for the ZEUS and H1 detectors.

<sup>(5)</sup>In HERA I a CIP was existing already, therefore the suffix *2k* is added for the new CIP after the HERA upgrade. Since this analysis uses only HERA II data, the liberty is taken to call the CIP2k from now on CIP without introducing any ambiguities.

The *Jet Trigger* [241–244] builds its decision on the ability to locate energy deposition in the LAr calorimeter. The third new trigger system is the *Fast Track Trigger* (FTT) [142, 182, 234, 245–251], which provides trigger elements for the first three trigger levels with increasing precision for higher levels. While DIS events are selected by the calorimeter triggers, exclusive final state triggers, especially at low transverse momentum, are more challenging. The FTT offers a satisfactory solution to these challenges by online reconstruction of tracks and on third level also by partial event reconstruction.

### 5.2.5.1 The Fast Track Trigger (FTT)

Since the FTT is of special importance for this measurement a brief description of the FTT working flow is given, details can be found in the references given above. From the 56 *wire layers* of the CJC1 and CJC2 are 12 used by the FTT and are grouped into 4, so called *trigger layers*, each with 3 wires, see Fig. 5.2. The deposited charges in these 4 trigger

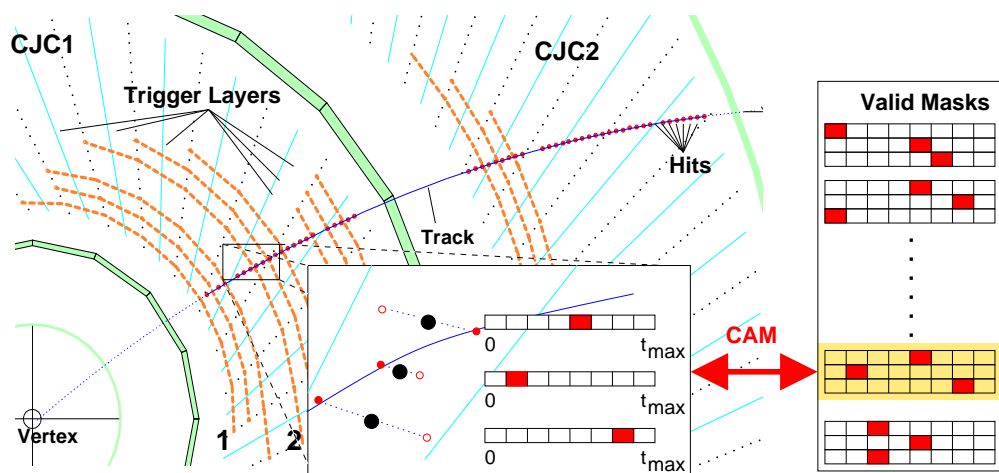


**Figure 5.2:** Sketch of the radial view of the H1 central tracker, illustrating the Fast Track Trigger (FTT) track finding, taken from [142]. A description is given in the text.

layers with in total 450 wires are digitalised and with time information, at a sampling rate of 20 MHz on L1, stored in hit registers. For each trigger layer the hit patterns are then compared with precalculated 3072 hit pattern masks to identify tracks originated from the vertex and to reconstruct the azimuthal angle  $\varphi$  and  $\kappa$ , the signed curvature (defined as the signed inverse of the transverse momentum<sup>(6)</sup>), for this track segment. On level 1 only poor information about the  $z$  coordinate is obtained. Afterwards a merging of the four track segments is performed producing the  $(\kappa, \varphi)$  information for this track. In case the segments do not fit together, they are rejected.

On L2 the same procedure as for level 1 is repeated but the hit registers are produced with an increased sampling rate of 80 MHz providing better precision. Subsequently, fits in the

<sup>(6)</sup>In [176]  $\kappa$  is defined as the signed inverse of the track radius,  $r$ , but due to Lorentz force  $r$  is proportional to the transverse momentum.

$(r, \varphi)$  and  $(r, z)$  planes are performed to derive the  $(\kappa, \varphi, \theta)$  properties of a track. FTT L2 tracks reach a high precision comparable to offline evaluated tracks.

On the third trigger level the FTT extends its knowledge beyond track information, performing a partial event reconstruction and deriving information about invariant masses and particle identification. This is possible due to the increase decision time available on L3. In addition it also takes into account information from other trigger systems to produce its decisions.

A high efficient trigger is unavoidable for selecting rare events in an environment dominated by background. But for performing a measurement with this selected events in addition also a simulation must exist to process MC events. The simulation for the FTT system is called *FTT emulation software* (FTTEMU) [250], which is run as a post processing step after the main H1 reconstruction software.

### 5.3 Trigger conditions

After the general introduction of trigger systems and the specific implementation in H1, this section discusses the subtrigger used for this analysis. The goal is to measure the elastic and proton dissociative  $J/\psi$  cross sections in the untagged photoproduction region using the two accessible reconstruction channels  $J/\psi \rightarrow ee$  and  $J/\psi \rightarrow \mu\mu$ . Therefore the final state detector signature to select these elastic and proton dissociative  $J/\psi$  events consists of two tracks in the central detector and an undetected scattered beam electron.

A trigger based on the scattered beam electron, as is standard for DIS selection, cannot be used. A successful trigger for online selection of  $J/\psi$  events therefore must be based on the  $J/\psi$  decay products, i.e. the two electron or the two muons. Due to the different nature of both lepton species regarding interaction with material in the detector, triggering of both decay channels can be achieved by using the online track information as provided by the FTT. This is done in the subtrigger *s59*, which is the trigger used for this analysis.

The used subtrigger *s59* has conditions on the first two trigger levels. The main conditions are the online reconstruction of exactly two tracks, each with a minimal transverse momentum of 800 MeV and opposite charge. In addition the subtrigger contains some background suppression conditions based on the H1 *time-of-flight system* [176], which will not further be described.

In Table 5.1 a detailed overview of the trigger elements is given. Two subtrigger systems are contributing. As already explained the CIP elements are mainly responsible for background rejection. The FTT elements are selecting the signature to look for two  $J/\psi$  daughter particles.

Trigger level	Condition
L1	$(\text{CIP}_{\text{sig}} > 1) \ \&\& \ (\text{CIP}_{\text{mul}} < 6) \ \&\& \ (\text{FTT}_{\text{mul T}_a} < 5) \ \&\& \ (\text{FTT}_{\text{mul T}_d} > 0)$
L2	$(\text{FTT}_{\text{mul T}_e} = 2) \ \&\& \ (\text{FTT}_{\text{Qtot}} = 4)$

**Table 5.1:** Description of trigger elements for subtrigger *s59*.

The first trigger element  $\text{CIP}_{\text{sig}} > 1$  has the meaning that the number of central CIP tracks must be larger than the number of forward and backwards CIP tracks together. The second CIP trigger element  $\text{CIP}_{\text{mul}} < 6$  requires events to have less than 30 CIP tracks. Table 5.2 gives a more detailed explanation of the CIP trigger elements.

Element	Description																																
$\text{CIP}_{\text{sig}}$	<p>Defines the balance between central, forward and backward CIP tracks. It is used for background suppression. The actual formula can be written as <math>n_{\text{cent}} &gt; k \cdot (n_{\text{fwd}} + n_{\text{bwd}})</math>, where <math>n_{\text{cent}}</math>, <math>n_{\text{fwd}}</math> and <math>n_{\text{bwd}}</math> denote the number of central, forward and backward tracks, respectively. The connection between parameter <math>k</math> and the <math>\text{CIP}_{\text{sig}}</math> condition is given in the following table:</p> <table border="1" style="margin-left: auto; margin-right: auto;"> <thead> <tr> <th><math>\text{CIP}_{\text{sig}}</math></th> <th><math>k</math></th> </tr> </thead> <tbody> <tr> <td>1</td> <td>1</td> </tr> <tr> <td>2</td> <td>2</td> </tr> <tr> <td>3</td> <td>4</td> </tr> </tbody> </table>	$\text{CIP}_{\text{sig}}$	$k$	1	1	2	2	3	4																								
$\text{CIP}_{\text{sig}}$	$k$																																
1	1																																
2	2																																
3	4																																
$\text{CIP}_{\text{mul}}$	<p>States the maximum number of allowed tracks, <math>n</math>, in central, forward and backward direction. In the table below a summary of <math>\text{CIP}_{\text{mul}}</math> values and the actual cut on the number of tracks <math>n</math> is given<sup>(7)</sup>.</p> <table border="1" style="margin-left: auto; margin-right: auto;"> <thead> <tr> <th><math>\text{CIP}_{\text{mul}}</math></th> <th><math>n</math></th> <th><math>\text{CIP}_{\text{mul}}</math></th> <th><math>n</math></th> </tr> </thead> <tbody> <tr> <td>0</td> <td>= 0</td> <td>7</td> <td>&gt; 65</td> </tr> <tr> <td>1</td> <td>&gt; 0</td> <td>8</td> <td>&gt; 100</td> </tr> <tr> <td>2</td> <td>&gt; 2</td> <td>9</td> <td>&gt; 130</td> </tr> <tr> <td>3</td> <td>&gt; 6</td> <td>10</td> <td>&gt; 160</td> </tr> <tr> <td>4</td> <td>&gt; 10</td> <td>11</td> <td>&gt; 190</td> </tr> <tr> <td>5</td> <td>&gt; 20</td> <td>12</td> <td>&gt; 220</td> </tr> <tr> <td>6</td> <td>&gt; 30</td> <td></td> <td></td> </tr> </tbody> </table>	$\text{CIP}_{\text{mul}}$	$n$	$\text{CIP}_{\text{mul}}$	$n$	0	= 0	7	> 65	1	> 0	8	> 100	2	> 2	9	> 130	3	> 6	10	> 160	4	> 10	11	> 190	5	> 20	12	> 220	6	> 30		
$\text{CIP}_{\text{mul}}$	$n$	$\text{CIP}_{\text{mul}}$	$n$																														
0	= 0	7	> 65																														
1	> 0	8	> 100																														
2	> 2	9	> 130																														
3	> 6	10	> 160																														
4	> 10	11	> 190																														
5	> 20	12	> 220																														
6	> 30																																

**Table 5.2:** Description of single CIP trigger elements contributing to the subtrigger  $s59$ .

The  $\text{FTT}_{\text{mul}}$  trigger elements define conditions on FTT track multiplicities. The additional suffixes Ta, Td and Te define the minimal transverse momentum threshold required such that the tracks are counted. The thresholds, though might have the same suffix, are different for first and second FTT trigger level. The actual thresholds are listed in Table 5.3. The subtrigger  $s59$  requests therefore on L1 at least one track with  $p_t$  of 900 MeV, but not more than 4 tracks with  $p_t$  of 100 MeV and on L2 that exactly two tracks exist with  $p_t \geq 800$  MeV.

The last condition  $\text{FTT}_{\text{Qtot}}$ , states a requirement on the total charge of all FTT tracks with  $p_t > 100$  MeV. A value of 4 demands the sum of all FTT tracks above the threshold to be

<sup>(7)</sup>The values  $n = 13 - 15$  are dropped because they define some special conditions unimportant for this analysis.

Level 1		Level 2	
Element	$p_t$ threshold	Element	$p_t$ threshold
FTT <sub>mul, Ta</sub>	100 MeV	FTT <sub>mul, Te</sub>	800 MeV
FTT <sub>mul, Td</sub>	900 MeV		

**Table 5.3:** Description of the used first and second FTT trigger level multiplicity thresholds.

equal to zero.

## 5.4 Data periods

This analysis covers two data periods, both recorded in the years 2006 and 2007. The lepton<sup>(8)</sup> beam had an energy of 27.6 GeV. The first running period contains data taken with HERA operating at a nominal proton energy of 920 GeV, resulting in a centre of mass energy,  $\sqrt{s}$ , of 320 GeV. In the other data period the accelerator was operating with a reduced proton energy of 460 GeV, which corresponds to  $\sqrt{s} = 225$  GeV<sup>(9)</sup>.

The former running period, due to the higher proton energy, will be referred to as *high energy running period* (HER), while the latter will be denoted as *low energy running period* (LER).

The integrated luminosities in the two periods are different by about one order of magnitude, as specified in Table 5.4. The additional statistics gained with adding the low energy data period is therefore small compared to the higher energy data period. But, as discussed in Chapter 2, the important gain is based in the fact that, due to the lower proton energy in LER, a lower  $W_{\gamma p}$  range can be accessed.

For both data sets only runs with at least  $0.1 \text{ nb}^{-1}$  and good or medium run conditions are taken into account. A small amount of runs is ignored, due to known problems of single detector subsystems during recording of these runs. In addition, it is requested that the central jet chambers, central inner chamber, Fast Track Trigger, liquid argon, SpaCal

<sup>(8)</sup>HERA was operating alternately with electron and positron beams. In both data periods considered in this analysis positrons were used. However, for clarity reasons in the following the incoming and outgoing lepton will be referred to as electron.

<sup>(9)</sup>The data taken at the reduced proton energy had the physical goal to measure the structure function  $F_L$  in a model independent way, which requires to measure the inclusive cross section at different centre of mass energies  $s$  [252]. The reason is best seen in the dependence of the inclusive cross section

$$\frac{d^2\sigma}{dx dQ^2} = \frac{2\pi\alpha^2}{xQ^4} \left\{ [1 + (1-y)^2] F_2 - y^2 F_L \right\}$$

on  $F_2$  and  $F_L$  structure functions. In order to see the difference between the two structure functions, which are unknown, the differential cross section needs to be measured at fixed  $(x, Q^2)$  and at different values of  $y$ , because then the dependence of  $F_2$  and  $F_L$ , weighted with  $(1-y)^2$  and  $-y^2$ , respectively, show their contributions [253]. Because  $x$  and  $Q^2$  are fixed and due to the relation  $Q^2 = xys$ , measuring at  $y$  translates in determination of the differential cross section at different  $\sqrt{s}$ .

Also the measurement of  $F_L^D$ , the equivalent to  $F_L$  for inclusive diffractive process only, is using these data sets [254]. A third running period with a nominal proton energy of 575 GeV was considered in the  $F_L$  and  $F_L^D$  measurement, but is left out in this analysis, due to the limited statistics available in this data period of only about  $6 \text{ pb}^{-1}$ .

Data Period	run range	Prescale factor	$\mathcal{L}$ [pb <sup>-1</sup> ]
HER	468530–500917	1.09	130
LER	500918–507824	1.01	10.81

**Table 5.4:** Overview of integrated luminosities for both data periods used in this analysis. HER and LER denote the high and low energy data periods operating with a nominal proton energy of 920 and 460 GeV, respectively. The prescale corrected integrated luminosities are denoted as  $\mathcal{L}$ .

and PLUG calorimeters, forward tagger, forward muon, time-of-flight, veto and luminosity detector components were fully operational.



## Data Analysis

This chapter describes all selection cuts applied to derive the sample of  $J/\psi$  candidates. A large fraction of this measurement uses this sample as starting point, sometimes with small modifications.

The first section describes the methods used for reconstructing the needed kinematic quantities. Section 6.3 discusses the track selection, which the  $J/\psi$  decay particles must fulfill, while the next part gives the basic event selection cuts. Afterwards follows the description of handling and rejection of large  $M_Y$  events on reconstruction side. Section 6.6.2.1 explains for the  $J/\psi \rightarrow \mu\mu$  reconstruction channel the rejection of cosmic muons. It is followed by the description of the electron and muon identification for the two reconstruction channels  $J/\psi \rightarrow ee$  and  $J/\psi \rightarrow \mu\mu$ , needed in order to reject di-pion background. Finally, in the last section the kinematic phase space is summarised.

### 6.1 Reconstruction of kinematic variables

The kinematic variables described in Sec. 2.2 in terms of four-vectors need to be reconstructed from measurable quantities. In general there are five standard reconstruction schemes for the kinematic variables relevant for DIS. An overview can be found in [255]. In this section only the used methods for the needed variables are explained. In addition also reconstruction of the diffractive variable  $t$  is discussed.

#### 6.1.1 Photoproduction region

In deep inelastic scattering events the virtuality  $Q^2$ , the momentum transfer at the electron vertex, is reconstructed using measured properties of the scattered beam electron. The

virtuality is calculated by the formula<sup>(1)</sup>

$$(Q_e^2)^{\text{rec}} = 4E_e (E'_e)^{\text{rec}} \cos^2 \left( \frac{\theta_e^{\text{rec}}}{2} \right). \quad (6.1)$$

The variables  $E_e$ ,  $(E'_e)^{\text{rec}}$  and  $\theta_e^{\text{rec}}$  denote the beam electron energy before and after interaction with a proton, and the scattering angle of the beam electron, respectively. For the HERA II running period the backward calorimeter, SpaCal, is able to detect electrons down to an angle of about  $175.5^\circ$  [142], which corresponds in  $Q^2$  to a lower threshold of about  $2.5 \text{ GeV}^2$ . Vice versa: the bulk of  $ep$  interactions with a undetected scattered beam electron corresponds to a virtuality region of  $Q^2 \lesssim 2.5 \text{ GeV}^2$ . In this analysis this phase space regime is called *photoproduction* region and is identified on reconstruction level with an undetected scattered beam electron.

### 6.1.2 Reconstruction of the $J/\psi$ four-momentum

The four-momentum of a  $J/\psi$  is reconstructed by use of the four-momentum of  $J/\psi$  decay products, i.e. either of the two electrons or muons by

$$p_{J/\psi}^{\text{rec}} = p_1^{\text{rec}} + p_2^{\text{rec}} \quad (6.2)$$

with  $p_i$  denoting the four-momentum of the two  $J/\psi$  daughter particles. The momentum of the electrons and muons are determined from the track measurement. A precise track measurement, as provided by the CJC and CST, is therefore crucial. The energy of the daughter particles are calculated by use of the momentum and the mass of the electrons or muons. The electron (muon) mass is taken for the measurement in the  $J/\psi \rightarrow ee$  ( $J/\psi \rightarrow \mu\mu$ ) decay channel<sup>(2)</sup>. The lepton identification (see Sec. 6.6) uses in addition to the momentum also information provided by the calorimeter and in case of muon identification also quantities measured with the muon system.

### 6.1.3 Reconstruction of the di-lepton mass

The reconstruction of the di-lepton mass  $m_{ll}$ , usually denoted by the variables  $m_{ee}$  and  $m_{\mu\mu}$  for the di-electron and di-muon masses, are a direct consequence of the  $J/\psi$  four-momentum measurement as given above and is obtained by

$$m_{ll}^2 = (p_1^{\text{rec}} + p_2^{\text{rec}})^2, \quad (6.3)$$

with  $p_i^{\text{rec}}$ ,  $i = \{1, 2\}$  as defined in Sec. 6.1.2.

### 6.1.4 Reconstruction of $W_{\gamma p}$

Starting with the approximation of the centre of mass energy in the photon proton rest frame,  $W_{\gamma p}$ , as given in Eq. (2.30), which only assumed that the electron and proton masses are small

<sup>(1)</sup>The subscript  $e$  in  $Q_e^2$  indicates that the electron method [255] is used. In the following text this specification is dropped.

<sup>(2)</sup>The influence however of the mass taken to calculate the energy is negligible small due to the large momenta compared to the masses.

compared to the corresponding particle momenta and applying it to the photoproduction region with  $Q^2 \sim 0 \text{ GeV}^2$ , the reconstruction of  $W_{\gamma p}$  can be written as

$$W_{\gamma p}^{\text{rec}} = \sqrt{s \cdot y^{\text{rec}}}. \quad (6.4)$$

With  $s$  the squared electron proton center of mass energy and  $y^{\text{rec}}$  the reconstructed inelasticity. (Definitions are given in Sec. 2.2.1.)

A modified Jacquet Blondel method is used to reconstruct the process inelasticity,  $y^{\text{rec}}$ , from  $J/\psi$  quantities

$$y_{mh}^{\text{rec}} = \frac{(E - p_z)_{\psi}^{\text{rec}}}{2E_e}, \quad (6.5)$$

whereas  $E$  and  $p_z$  denote the reconstructed energy and  $z$  momentum component of the  $J/\psi$ . A derivation is given in Appendix A.1.

### 6.1.5 Reconstruction of $t$

The squared momentum transfer in the proton vertex,  $t$ , is reconstructed by the formula

$$t^{\text{rec}} = -p_{t,\psi}^2, \quad (6.6)$$

with  $p_{t,\psi}$  being the transverse momentum of the  $J/\psi$ <sup>(3)</sup>. A derivation of the formula can be found in Appendix A.2.

Whenever  $t^{\text{rec}}$  is used, it has the meaning of Eq. (6.6). But  $t^{\text{gen}}$  *always* has the meaning of the true squared momentum transfer in the proton vertex and *never* refers to the inverse of the transverse momentum of the  $J/\psi$  on generator level.

## 6.2 Kinematic phase space definition

The focus of this analysis is on the low virtuality region in the regime of almost real photon exchange, called photoproduction. Due to the restrictions given by the backward SpaCal calorimeter to veto high  $Q^2$  events, the photoproduction phase space for HERA II period is  $Q^2 \lesssim 2.5 \text{ GeV}^2$ .

The phase space of elastic and proton dissociative process as function of  $|t|$  must be chosen differently, due to the individual behaviour of the two processes. In the elastic case a very hard spectrum is expected, whereas in the proton dissociative case only a moderate slope of the cross section is predicted. In addition also the statistics of the two data periods must be considered.

A summary of the phase space is given in the Table 6.1. The lower edge of  $W_{\gamma p}$  region is smaller for the low energy running period (LER), since  $W_{\gamma p} \propto \sqrt{E_p}$  with  $E_p$  the proton energy. This gives the possibility to reach lower  $W_{\gamma p}$  values, which otherwise are not accessible using only events from the high energy running period (HER)<sup>(4)</sup>.

<sup>(3)</sup>As can be seen in Eq. (6.6)  $t^{\text{rec}}$  is always negative. For equations and displaying distributions as function of  $t$ , positive values are more comfortable. Often therefore  $-t$  is used instead, especially in plots. Because the syntax  $-t$  is unhandy in formulae, usually either  $|t|$  or sometimes  $T \equiv -t$  is used. But whenever this

Variable	Data period	Process	Range
$Q^2$	HER, LER	elas, pdis	$\lesssim 2.5 \text{ GeV}^2$
$ t $	HER	elas	$< 1.2 \text{ GeV}^2$
		pdis	$< 6 \text{ GeV}^2$
	LER	elas	$< 1.2 \text{ GeV}^2$
		pdis	$< 5 \text{ GeV}^2$
$W_{\gamma p}$	HER	elas, pdis	40 – 110 GeV
	LER	elas, pdis	25 – 110 GeV

**Table 6.1:** Phase space overview for variables: virtuality  $Q^2$ , squared transverse momentum in the proton vertex  $|t|$  and the center of mass energy in the proton photon rest frame  $W_{\gamma p}$ . HER and LER denote the high and low energy running period. The two  $J/\psi$  production processes elastic and proton dissociative are abbreviated as elas and pdis, respectively.

## 6.3 Track selection

The two tracks used to reconstruct a  $J/\psi$  are based on the standard H1 Lee West track selection. The cuts applied in this selection are given in Sec. 6.3.1. Further some additional cuts are applied, which are discussed in Sec. 6.3.2. An overview of all applied cuts to the used tracks is given in Table 6.2.

### 6.3.1 Standard H1 Lee West track

The Lee west track selection, implemented in the *H100* analysis framework [256], starts with the sample of tracks, reconstructed as described in Sec. 3.2.1.1, with the additional constraint that the tracks must be connected to a vertex, so called *vertex fitted tracks*. On this sample of tracks cuts are applied to ensure a good quality. A polar angle,  $\theta$ , between  $1^\circ$  and  $179^\circ$  and a minimum transverse momentum,  $p_t$ , of 70 MeV is required. A minimum track length cut of 10 cm or 5 cm depending on the polar angle and transverse momentum is applied. In addition a Lee West track must have a start radius below 50 cm, to ensure a track starts before the CJC2. The  $d'_{ca}$ , the absolute value of the distance to closest approach in the transverse  $r\phi$  plane, corrected for the polar angle, must be smaller than 2 cm.

### 6.3.2 $J/\psi$ daughter particles track selection

On the basis of Lee West tracks some further cuts are applied. The implementation is contained in the  $J/\psi$  *finder*, which is part of the H100 analysis framework [256]. The polar region is restricted to  $20^\circ$  -  $165^\circ$ , which ensures a good quality and resolution of the tracks. A second reason is that the FTT tracks, built on information from the CJC, cover this polar angle region. A trigger based on the FTT hence is restricting tracks to this region.

---

is the case, close by the definition will be provided again to reduce possible confusion.

<sup>(4)</sup>This assumes no changes in the detector acceptance. E.g. smaller polar angles would as well give access to a lower  $W_{\gamma p}$  region, so would smaller transverse momentum.

On L2 the used subtrigger *s59* requires a minimal transverse momentum for the FTT tracks of 800 MeV. Therefore this cut is also applied in the offline selection and supersede the loose  $p_t > 70$  MeV cut from the standard selection.

A summary of the final vertex fitted track requirements is given in Table 6.2.

Lee West track	
Description	Cut
transverse momentum $p_t$	$p_t > 70$ MeV
polar angle $\theta$	$1^\circ < \theta < 179^\circ$
track length $L$	
$\theta < 150^\circ$	
$p_t > 150$ MeV	$L \geq 10$ cm
$p_t < 150$ MeV	$L \geq 5$ cm
$\theta > 150^\circ$	$L \geq 5$ cm
start radius $R$	$R \leq 50$ cm
track fit quality	$ d_{ca}  \sin \theta \leq 2$ cm
Additional selection cuts (H1 $J/\psi$ finder)	
transverse momentum $p_t$	$p_t > 800$ MeV
polar angle $\theta$	$20^\circ < \theta < 165^\circ$

**Table 6.2:** Overview of the vertex fitted track selection requirements.

## 6.4 Basic event selection

A selection of photoproduction events ( $Q^2 \lesssim 2.5 \text{ GeV}^2$ ) is achieved by requesting the absence of a detected scattered beam electron in the backward SpaCal calorimeter<sup>(5)</sup>. A cut on the  $z$ -component of the reconstructed vertex of  $|z_{\text{vtx}}| < 35$  cm is applied, such that events with a large distance to the nominal interaction point are rejected. The cut corresponds to about 2 standard deviations of the proton punch length of about 20 cm [257] and reduces the non- $ep$  background caused by beam interactions with the beam pipe, the collimators or the rest gas.

Diffractive  $J/\psi$  events, decaying into an electron-positron or a muon-antimuon pair, are selected by requesting exactly two tracks in an event, both fulfilling the cuts given in Table 6.2. In addition, the two tracks must have opposite charge to ensure decay of a neutral particle.

Background composed from di-pion events survive these cuts to some part as well. This contamination can only be reduced by a positive identification of the tracks as electrons or muons, which is the subject of Sec. 6.6.

<sup>(5)</sup>DIS events with  $Q^2 \gtrsim 100 \text{ GeV}^2$  are expected to be found in the LAr rather than in the SpaCal calorimeter and are therefore not rejected by an empty SpaCal condition. Real  $J/\psi$  events at such large  $Q^2$  are highly suppressed since the cross section is falling with  $\sigma \propto 1/(M_\psi^2 + Q^2)^{2.5}$  [29]. A background process in this  $Q^2$  region could only appear, when a second track is reconstructed, such that the di-lepton mass of the scattered beam electron and the track is around the nominal  $J/\psi$  mass, which is impossible due to  $p$  balance.

## 6.5 Low $M_Y^{\text{gen}}$ restriction

For this analysis a  $M_Y^{\text{gen}} < 10 \text{ GeV}$  region was chosen in order to satisfy  $M_Y^{\text{gen}}/W_{\gamma p}^{\text{gen}} \lesssim 0.15$  with a  $\langle W_{\gamma p}^{\text{gen}} \rangle \sim 70 \text{ GeV}$ . This requirement ensures that the phase space is restricted to a region without significant contribution of inelastic  $J/\psi$  production<sup>(6)</sup>.

To suppress the high  $M_Y^{\text{gen}}$  contribution a cut on reconstruction level was invented. The squared sum of all liquid argon clusters with at least 400 MeV energy and unassociated to the  $J/\psi$  daughter tracks is built. It is required that this sum is not larger than  $2.5 \text{ GeV}^2$ . In terms of a formula it can be written as

$$\sum_{\text{LAr clusters}} E^2(E > 400 \text{ MeV, unassociated}) < 2.5 \text{ GeV}^2. \quad (6.7)$$

A cluster is *unassociated* to a  $J/\psi$  daughter particle, if the distance<sup>(7)</sup> in the  $\eta - \phi$  plane is larger than  $10^\circ$ .

This cut will be referred to as *empty calorimeter* (EC) cut<sup>(8)</sup>.

### 6.5.1 Performance of the empty calorimeter cut

The effect of this cut on the  $M_Y^{\text{gen}}$  distribution can be seen in Fig. 6.1. The left plot (a) shows as solid blue line the efficiency

$$\varepsilon = \frac{N(M_Y^{\text{gen}} < 10 \text{ GeV} \ \&\& \ \text{EC})}{N(M_Y^{\text{gen}} < 10 \text{ GeV})} \quad (6.8)$$

and as dashed red line the rejection

$$\delta = \frac{N(M_Y^{\text{gen}} \geq 10 \text{ GeV} \ \&\& \ \text{EC})}{N(M_Y^{\text{gen}} \geq 10 \text{ GeV})} \quad (6.9)$$

as function of the empty calo(rimeter) cut. The expression  $N(C)$  means number of events with fulfilled condition  $C$ . In the right plot (b) the contamination

$$c = \frac{N(M_Y^{\text{gen}} \geq 10 \text{ GeV} \ \&\& \ \text{EC})}{N(\text{EC})} \quad (6.10)$$

in the final sample, after applying the empty calorimeter cut, is estimated<sup>(9)</sup>. A cut value of  $2.5 \text{ GeV}^2$ , as indicated by the dashed vertical line, corresponds to  $\varepsilon = 78 \%$ ,  $\delta = 0.93 \%$  and  $c = 1.8 \%$ . The cut value was chosen such that the contamination is below  $2 \%$ .

<sup>(6)</sup>Inelastic  $J/\psi$  production occurs in leading order with exchange of a single gluon, instead of a pomeron or two gluons.

<sup>(7)</sup>The norm of objects in eta-phi is defined as  $\sqrt{\Delta\eta^2 + \Delta\phi^2}$ , with  $\Delta\phi$  the difference in the azimuth angles and  $\Delta\eta$  the difference in pseudo rapidity of the objects. The pseudo rapidity is defined as  $\eta = -\ln[\tan(\theta/2)]$  with  $\theta$  the polar angle.

<sup>(8)</sup>Different ideas of variables were tried, including the reconstruction of  $M_Y$  as suggested in [258]. But the described variable shows the best performance with respect to efficiency and rejection.

<sup>(9)</sup>The used proton dissociative MC simulation is reweighted to describe data as explained in Sec. 8.2

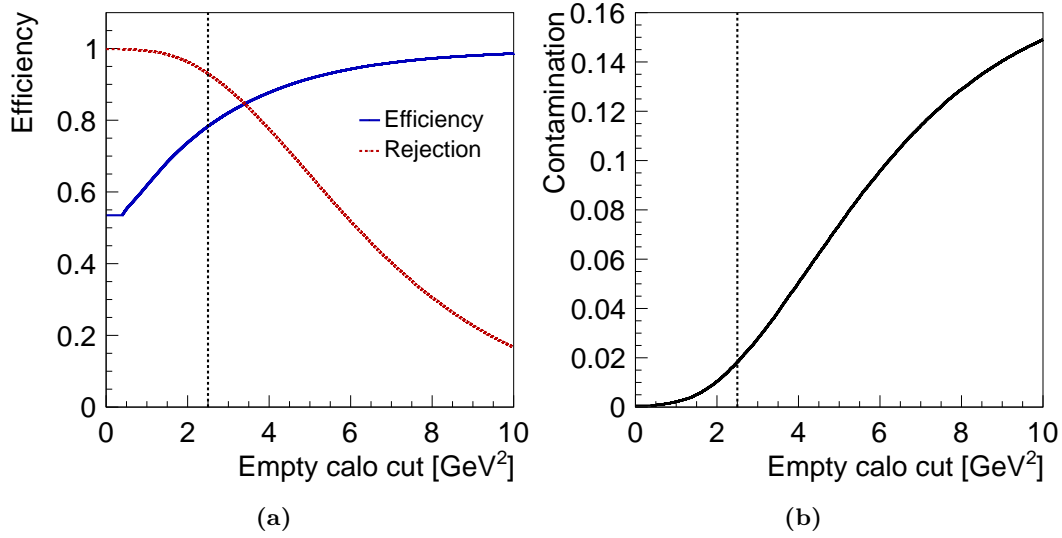


**Figure 6.1:** Effect of applying a cut on the sum of squared,  $J/\psi$  unassociated liquid argon cluster energies above threshold of 400 MeV, to reduce high  $M_Y^{\text{gen}}$  contribution. In (a) the solid blue line shows the efficiency for  $M_Y^{\text{gen}} < 10$  GeV as function of the empty calorimeter cut. The dashed red line represents the rejection efficiency of events with  $M_Y^{\text{gen}} \geq 10$  GeV. Figure (b) Shows the contamination of events with  $M_Y^{\text{gen}} \geq 10$  GeV in the analysis sample. The vertical dashed black line indicates the used cut value of 2.5 GeV<sup>2</sup>.

## 6.5.2 Contamination of inelastic $J/\psi$ process

Figure 6.2 shows the number of data events as red circles, while the blue histogram represents the inelastic  $J/\psi$  CASCADE [220] MC simulation, both as function of the empty calorimeter cut. The Monte Carlo is normalised to the data luminosity. The dashed line represents the

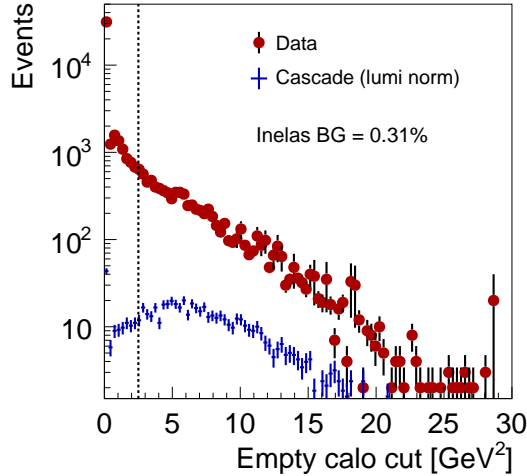


**Figure 6.2:** Inelastic contamination. The red points indicate data, the blue histogram the inelastic  $J/\psi$  CASCADE [220] MC simulation normalised to data luminosity as function of the empty calo(rimeter) cut. The dashed line represents the position of the cut at  $2.5 \text{ GeV}^2$  as used in the analysis.

position of the empty calo cut at  $2.5 \text{ GeV}^2$ . The level of contamination, due to inelastic  $J/\psi$  events after applying the cut, is evaluated to be of the order of 0.3%. Due to this very small contamination, the contribution of inelastic  $J/\psi$  events in data is neglected.

## 6.6 Lepton identification

Until this point both decay channels are treated equally. As discussed in Sec. 6.4 a non-resonant di-pion background may still be present, which calls for the need of identifying the two possible  $J/\psi$  daughter particles. In the following subsections the methods for identification of electrons and muons are explained.

### 6.6.1 Electron identification

This analysis uses the same electron identification as in [221]. The identifier will be referred to as  $D_{\text{ele}}$  and is distributed between 0 and 1, where a value closer to 1 enriches electrons. Figure 6.3 shows the  $D_{\text{ele}}$  discriminator for one of the two tracks, were a cut is applied on the other track to enrich the electron sample.

The  $D_{\text{ele}}$  discriminator is constructed from two independent identifiers. The former is based on a neural network using the LAr calorimeter and track input information. A detailed

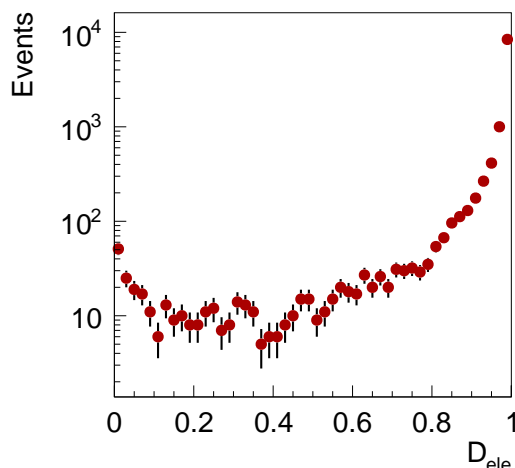


**Figure 6.3:** Electron discriminator  $D_{\text{ele}}$  distribution for one track of the two tracks in the sample. A cut  $D_{\text{ele}} > 0.99$  is applied on the other track to enrich the electron and to suppress the di- $\pi$  background.

description can be found in [234]. The latter is based on the measurement of the specific energy loss,  $dE/dx$ , of particles in the CJC tracking chambers. The energy loss treatment, especially the calibration and applied corrections, within H1 can be found in [259, 260].

An event passes the electron identification selection cut, if one track fulfills the requirement  $D_{\text{ele}} > 0.8$  and lies within the LAr calorimeter polar angle acceptance of  $\theta < 140^\circ$ , guaranteeing an optimal performance of the electron identifier<sup>(10)</sup>. The other track must fulfill the weak constraint that the likelihood of the particle, constructed from energy loss measurement of the track, is larger to be an electron than a pion.

### 6.6.2 Muon identification

Muons in this analysis are identified in two different parts of the detector, in the LAr calorimeter and in the central muon detector (CMD). Given the place of identification the names are chosen accordingly. The identified muons in the LAr calorimeter are called *calorimeter muons*, while muons identified in the muon system are labeled as *iron muons*.

In order for the muon system to identify a particle as muon, the particle must reach the muon system in the outer part of the detector, which is in the barrel part of the central detector (corresponding to a polar angle region of about  $35^\circ < \theta < 130^\circ$ ) only possible, if the particle has at least a transverse momentum,  $p_t$ , of about 2 GeV. However, a particle does not need a  $p_t$  of 2 GeV to reach the muon system in the forward or backward end cap. This increases the amount of identified muons in the forward and backward direction and contributes to the wide acceptance of the muon identification.

<sup>(10)</sup>The actual acceptance of the LAr calorimeter in backward direction is larger than  $140^\circ$ , but the amount of sensitive material is dropping in this area, which leads to a worse resolution and therefore to suboptimal working of the discriminator.

On the other side low  $p_t$  muons can be identified in the LAr calorimeter system rather well. A combination of both identification mechanisms by a logical *or* operation, therefore increases the accessible kinematic region. One well identified muon, either as iron or calorimeter muon, is sufficient for an event to be accepted.

To reject the small background contribution from misidentified electrons as muons a cut is added, which requires that the likelihood of the particle is larger to be a muon than an electron. The used likelihood is constructed from the energy loss measurement of the track.

But even if the muon identification is done to a satisfactory level, the sample may still contain muons produced as decay products of secondary particles created by incoming cosmic rays (about 90% protons [58]) in the atmosphere, usually called *cosmic muons*. Section 6.6.2.1 therefore first describes the rejection of these cosmic muons, while the following two sections explain the muon identification in the central muon detector and in the calorimeter. The last section discusses the quality of the identification and the applied efficiency corrections for the muon identification.

### 6.6.2.1 Cosmic muon rejection

The signature of cosmic muons appear as straight tracks crossing the detector from top to bottom, mimic the  $J/\psi$  decay particles. Figure 6.4 shows an example of such an event, where a particle passes the H1 detector from top to bottom depositing energy in the calorimeter and the muon system.

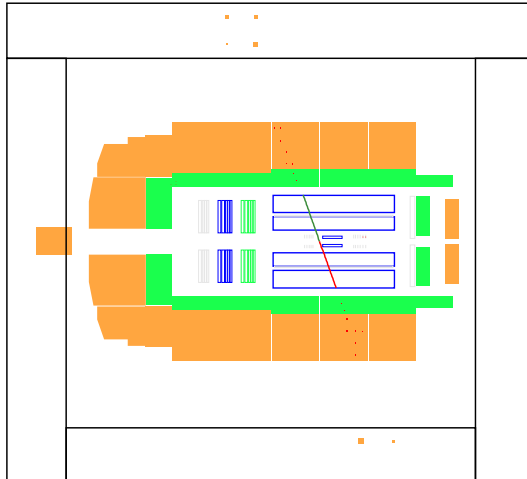


**Figure 6.4:** Example of a cosmic muon passing the H1 detector, shown in  $rz$  view.

should be kept in mind for the following discussion.

#### 6.6.2.1.1 Cut compositions for cosmic muon rejection

The background rejection is achieved by a cut composition of three conditions connected with Boolean *or* operations. The following list gives a description of the three conditions, which are standard cosmic rejection cuts in H1.

- A cosmic muon is only by chance crossing the detector at the same time, as a real interaction takes place. Therefore a timing cut, like

$$T_1^0 > 0 \quad \&\& \quad T_2^0 > 0 \quad \&\& \quad |T_1^0 - T_2^0| > 12$$

can reduce this background. With  $T^0$  representing the time difference to the bunch cross in units of ticks, whereas 500 ticks = 96 ns. The subscripts 1 and 2 indicate the first and second track, respectively.

- A cut on the distance-to-closest approach to the primary vertex  $d'_{ca}$  for both tracks may be able to identify cosmic muons because on average they are not passing the detector close to the vertex. In a formula the cut is expressed as

$$d'_{ca,1} > 0.1 \text{ cm} \quad \&\& \quad d'_{ca,2} > 0.1 \text{ cm}.$$

- The third cut is built on the idea that a cosmic muon produces fake  $J/\psi$  decay particle tracks in the detector with a back-to-back signature. A cut on the quality that both tracks are caused by just one cosmic muon can be used for rejection. The actual cut is done on the  $\chi^2$  of a fit assuming both tracks can be combined into a single track.

$$\chi^2 < 10.$$

#### 6.6.2.1.2 Effect of cosmic muon rejection cut

If the two daughter tracks of a  $J/\psi$  candidate are originated by a cosmic muon, a direct dependence between the photon proton centre of mass energy  $W_{\gamma p}$  and the reconstructed di-muon mass  $m_{\mu\mu}$  can be derived, due to the back-to-back signature of the tracks. The dependence is

$$W_{\gamma p} \simeq \sqrt{2m_{\mu\mu}E_p}$$

with  $E_p$  the proton energy. A derivation of the formula can be found in [210]. This dependence is shown in Fig. 6.5(a) as diagonal line, while the vertical line is caused by real  $J/\psi \rightarrow \mu\mu$  events peaking around the nominal  $J/\psi$  mass of about 3.097 GeV. The second weakly visible vertical line represents events reconstructed around the nominal  $\psi(2S)$  mass. The more uniformly distributed events at low  $m_{\mu\mu}$  and low  $W_{\gamma p}$  are non-resonant background mostly caused by Bethe-Heitler type processes. In fig 6.5(b) the same plot is given with applied cosmic rejection cut. A clear extinction of non- $J/\psi$  events caused by cosmic muons is visible.

#### 6.6.2.2 Muon identification in the CMD

A particle must survive a series of cuts, such that it is identified as a muon in the central muon system and labeled as *iron muon*. This section describes this set of applied cuts.

The H1 reconstruction software performs a linking between two kind of tracks and returns a probability of compatibility  $p$  that both tracks originate from the same particle. The first kind are tracks reconstructed by use of information from the central tracker, as described in Sec. 3.2.1.1. The second group of tracks are reconstructed on information from the CMD, see

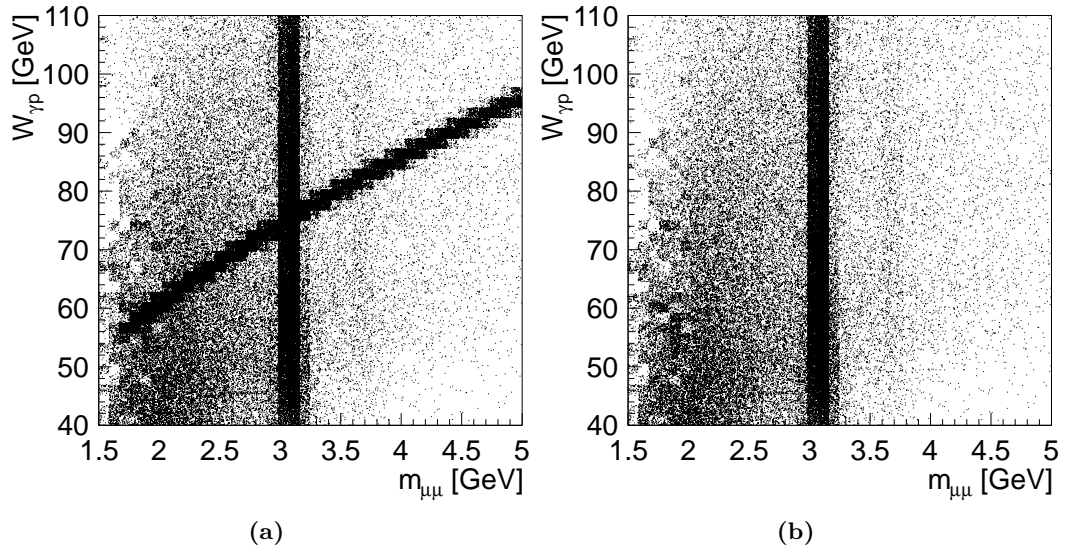


**Figure 6.5:** Scatter plot of the reconstructed mass  $m_{\mu\mu}$  versus the center of mass energy in the proton photon rest frame  $W_{\gamma p}$ . Plot (a) before and (b) after applying the cosmic rejection cuts.

Sec. 3.2.3. The probability is set to  $p < 5 \cdot 10^{-3}$ , which is slightly stronger than the standard H1 cut of  $10^{-4}$ .

In addition quality cuts on the iron tracks are applied depending on the geometric position of a track in the detector. Three regions in the detector are separated: the barrel, the forward and backward end caps. A summary of the applied cuts can be found in Table 6.3. The

Description	Barrel	Forward end cap	Backward end cap
Lee West - iron track link prob. $p$	$p > 5 \cdot 10^{-3}$	$p > 5 \cdot 10^{-3}$	$p > 5 \cdot 10^{-3}$
Number of layers $N_{\text{lay}}$	$N_{\text{lay}} > 3$	$N_{\text{lay}} \geq 6$	$N_{\text{lay}} > 4$
Layer number of first hit $N_{\text{lay}0}$	$N_{\text{lay}0} \leq 5$	$N_{\text{lay}0} \leq 5$	$N_{\text{lay}0} \leq 8$
Layer number of last hit $N_{\text{lay}1}$	$N_{\text{lay}1} \geq 2$	$N_{\text{lay}1} \geq 6$	$N_{\text{lay}1} \geq 3$
Distance of first to last layer $D_{\text{lay}}$	$D_{\text{lay}} > 4$	$D_{\text{lay}} > 4$	$D_{\text{lay}} > 6$
Track quality on $d'_{ca}$	$\rho \leq 100 \text{ cm},$ $z \leq 100 \text{ cm}$	$x \leq 100 \text{ cm},$ $y \leq 100 \text{ cm}$	$x \leq 100 \text{ cm},$ $y \leq 100 \text{ cm}$

**Table 6.3:** Summary of additional applied cuts for muon identification based on track information using the central muon detector (CMD). The cuts vary depending on the region of a track in the detector. The three region coincide with the CMD barrel, forward and backward end caps. A description of the variables is given in the text.

variables  $N_{\text{lay}}$ ,  $N_{\text{lay}0}$  and  $N_{\text{lay}1}$  denote the total number of wire layers and the wire layer number of the first and last hit in the instrumented iron system (i.e. without counting the inner and outer muon boxes) with a response above threshold. The quantity  $D_{\text{lay}}$  represents the distance of the first to the last associated hit:  $D_{\text{lay}} = N_{\text{lay}1} - N_{\text{lay}0}$ . The last cut in the

table is a track quality cut on the  $d'_{ca}$  obtained by the CMD. The cuts are given in cylindrical coordinates.

The used cuts are taken from [261] and are identical to those used in [262].

The description of the simulation is further improved by rejecting regions of rapidly falling efficiencies. Therefore the polar angle ranges  $122.5^\circ - 145^\circ$  and  $\theta > 162.5^\circ$  are excluded.

### 6.6.2.3 Muon identification in the calorimeter

The calorimeter muon identification in H1 is called KALEP. It combines several estimator quantities, compares them with reference curves and returns a single quantity, the *KALEP muon identification probability*<sup>(11)</sup>  $p_{\text{KALEP}}$ .

As estimator input variables are used

- the deposited energy in the electromagnetic calorimeter  $E_{\text{em}}$ ,
- the total energy (electromagnetic plus hadronic part)  $E_{\text{tot}}$ ,
- the track length inside the calorimeter  $L_{\text{max}}$  and
- the summed distances of all track associated cells to the calorimeter impact point of the track  $S_{\text{len}}$ .

These quantities are compared to reference curves and the weighted deviations of the four estimators are combined to form a single variable distributed between 0 and 1. Values close to 0 enriches muons, while values around 1 mostly contain non-muon particles. Within H1 three standard cut position on the KALEP probability are defined: *sloppy*, *medium* and *good*. A *medium* KALEP muon corresponds to  $p_{\text{KALEP}} < 0.1$  and a *good* to  $p_{\text{KALEP}} < 0.015$ . For further information see [263–266].

The KALEP selected muons need further to fulfill the acceptance cut  $\theta < 125^\circ$ , due to a fast falling efficiency at larger polar angles, where a description of data is difficult. To reject electrons contaminating the sample an additional cut is applied on the likelihood ratio, built from energy loss  $dE/dx$ , of a particle to be an electron or a muon.

The default identified muons in the calorimeter system, will be called *calorimeter muons*. They are defined as particles identified as medium KALEP muons with the additional cuts, as given above, applied.

#### 6.6.2.3.1 Creation of performance plots for muon identification

The idea is to produce a sample composed purely from muons, then derive muon identification efficiency plots and finally compare these plots created from data with the ones created from the simulation.

The creation of the pure muon sample uses a so called tag and probe method. The tagged sample is composed from the  $J/\psi$  candidates selection with restriction of the di-muon mass

---

<sup>(11)</sup>The additional information about muons is sometimes specified to prevent ambiguities, since a KALEP electron identifier exists in H1, too. Since it is not used in the present analysis, in the rest of the text *KALEP probability* is taken for referencing to this identifier.

$m_{\mu\mu}$  to the window  $2.8 < m_{\mu\mu} < 3.4$  GeV in the vicinity of the nominal  $J/\psi$  mass, which reduces background contamination. Further it is required that one of the  $J/\psi$  daughter particles are identified as a good KALEP muon or as an iron muon. The not already identified  $J/\psi$  daughter tracks build then the probe sample. Applying the muon identification to this sample reveals the actual efficiency of the identifier.

The remaining background in the data sample is corrected by a side band subtraction. A description of the side band method to subtract background can be found in [266]. On the simulation side both signal MC's, elastic and proton dissociative, are added assuming a ratio of one-to-one.

The MC conditional muon identification efficiencies  $\varepsilon(\text{probe}|\text{tag})$  from the described tag and probe method are differentially compared to real MC efficiencies. Deviations are in all bins smaller than 0.5%. I.e the distortion in MC simulation due to the applied method is small. Therefore comparing on the conditional rather on the real efficiencies, which are not accessible in data, reflects the true situation rather well.

#### 6.6.2.3.2 KALEP estimator input quantities

The KALEP estimator input quantities are plotted in Fig. 6.6 for the probe sample. The red points show the background corrected data distributions. The blue and green histograms represent the elastic and proton dissociative MC simulation distributions, respectively. To compare the shapes all histograms are normalised to a unit integral. The description is clearly suboptimal, indicating a possible problem in the efficiency description of the simulations.

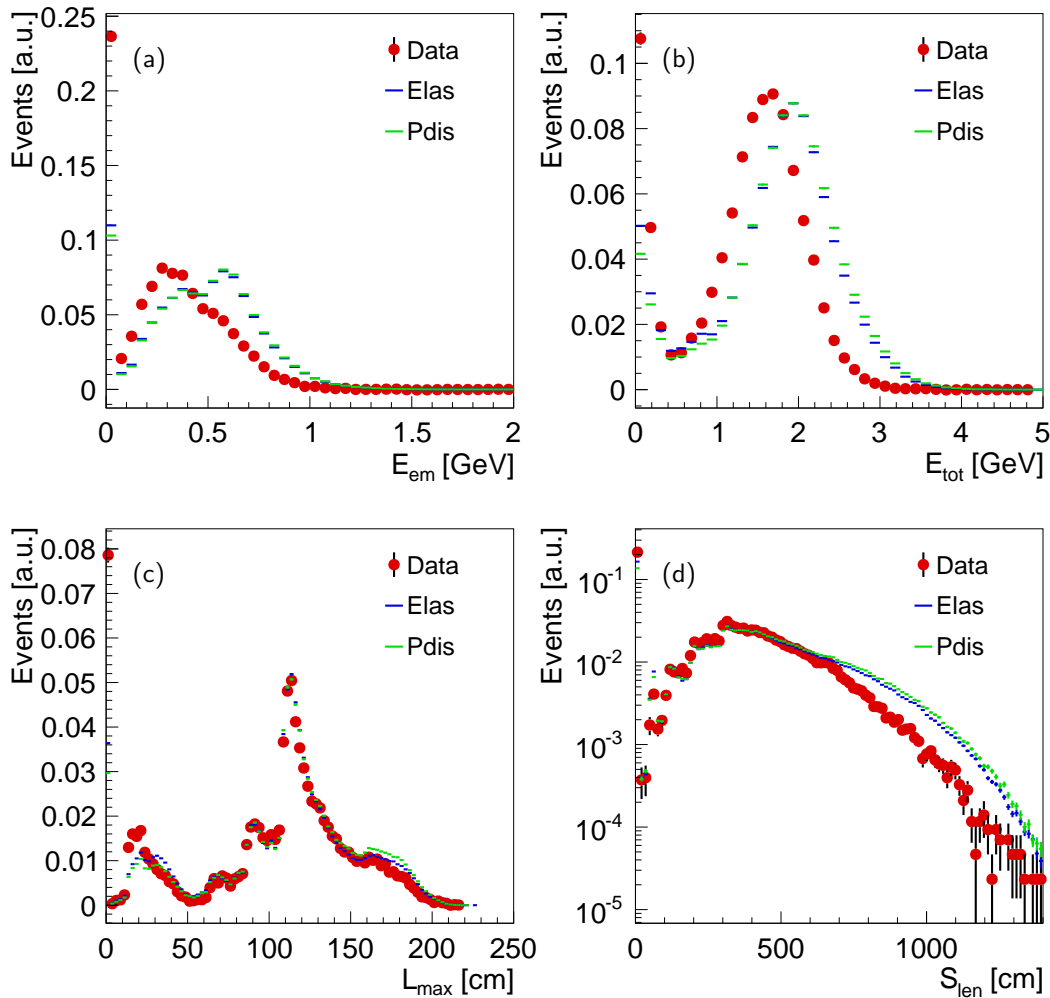
#### 6.6.2.4 Muon identification correction

Figure 6.7 shows efficiency distributions for the standard muon identification used in this analysis: a medium KALEP or an iron muon. The efficiencies are given as function of the polar angle  $\theta$  in (a) and of the momentum  $p$  in (b). The red points represent data. The MC simulation without any efficiency correction is shown as blue histogram. Clearly the description is rather poor and requires a correction.

The nuisance of badly described efficiencies are cured by efficiency reweighting. Because KALEP operates in  $(p, \theta)$  coordinates and the contribution of KALEP identified muons is larger than the contribution from muons identified in the CMD, due to high moment  $p \gtrsim 2$  GeV needed to reach the iron system, reweighting is done in bins of  $(p, \theta)$ . In consequence of detector topology the  $\theta$  efficiency distribution includes large dips. The correction therefore has to have a fine granularity to resolve these structures.

A correction must take into account that a track can be identified as iron muon, as KALEP muon, or as iron and KALEP muon. Further a correction must take into account that an event is accepted, if at least one track is identified as muon. In order to cope with this two level problem, first weights are calculated in bins of  $(p, \theta)$  according to the formula

$$w_i(p, \theta) = \frac{w_i^K(p, \theta)\varepsilon_i^K(p, \theta) + w_i^I(p, \theta)\varepsilon_i^I(p, \theta) - w_i^K(p, \theta)w_i^I(p, \theta)\varepsilon_i^K(p, \theta)\varepsilon_i^I(p, \theta)}{\varepsilon_i^K(p, \theta) + \varepsilon_i^I(p, \theta) - \varepsilon_i^K(p, \theta)\varepsilon_i^I(p, \theta)} \quad (6.11)$$



**Figure 6.6:** The KALEP estimator input quantities: the electromagnetic  $E_{em}$  and total energy deposition  $E_{tot}$ , the maximal track length inside the calorimeter  $L_{tot}$  and the summed distances of all track associated cells to the calorimeter impact point of the track  $S_{len}$ . Red points represent the background subtracted data, the blue (green) histogram indicates the elastic (proton dissociative) MC simulation. The histograms are normalised to 1.

for each track  $i$ . Whereas  $\varepsilon_i^K$  and  $\varepsilon_i^I$  are the MC simulation efficiencies for identifying a KALEP muon and an iron muon, respectively. The weights  $w_i^K$  and  $w_i^I$  are given by

$$w_i^K(p, \theta) = \varepsilon_i^{K,D}(p, \theta) / \varepsilon_i^K(p, \theta) \quad \text{and} \quad (6.12)$$

$$w_i^I(p, \theta) = \varepsilon_i^{I,D}(p, \theta) / \varepsilon_i^I(p, \theta) \quad (6.13)$$

with  $\varepsilon_i^{K,D}$  and  $\varepsilon_i^{I,D}$  the data efficiencies.

In a second step, the event efficiency correction for the Boolean *or* combination of the muon identification for the two tracks is calculated as

$$w(p, \theta) = \frac{w_1(p, \theta)\varepsilon_1(p, \theta) + w_2(p, \theta)\varepsilon_2(p, \theta) - w_1(p, \theta)w_2(p, \theta)\varepsilon_1(p, \theta)\varepsilon_2(p, \theta)}{\varepsilon_1(p, \theta) + \varepsilon_2(p, \theta) - \varepsilon_1(p, \theta)\varepsilon_2(p, \theta)} \quad (6.14)$$

with  $\varepsilon_i = \varepsilon_i^K(p, \theta) + \varepsilon_i^I(p, \theta) - \varepsilon_i^K(p, \theta)\varepsilon_i^I(p, \theta)$ .

The reweighted efficiencies are shown in Fig. 6.7 as orange histograms. A rather well description is achieved.

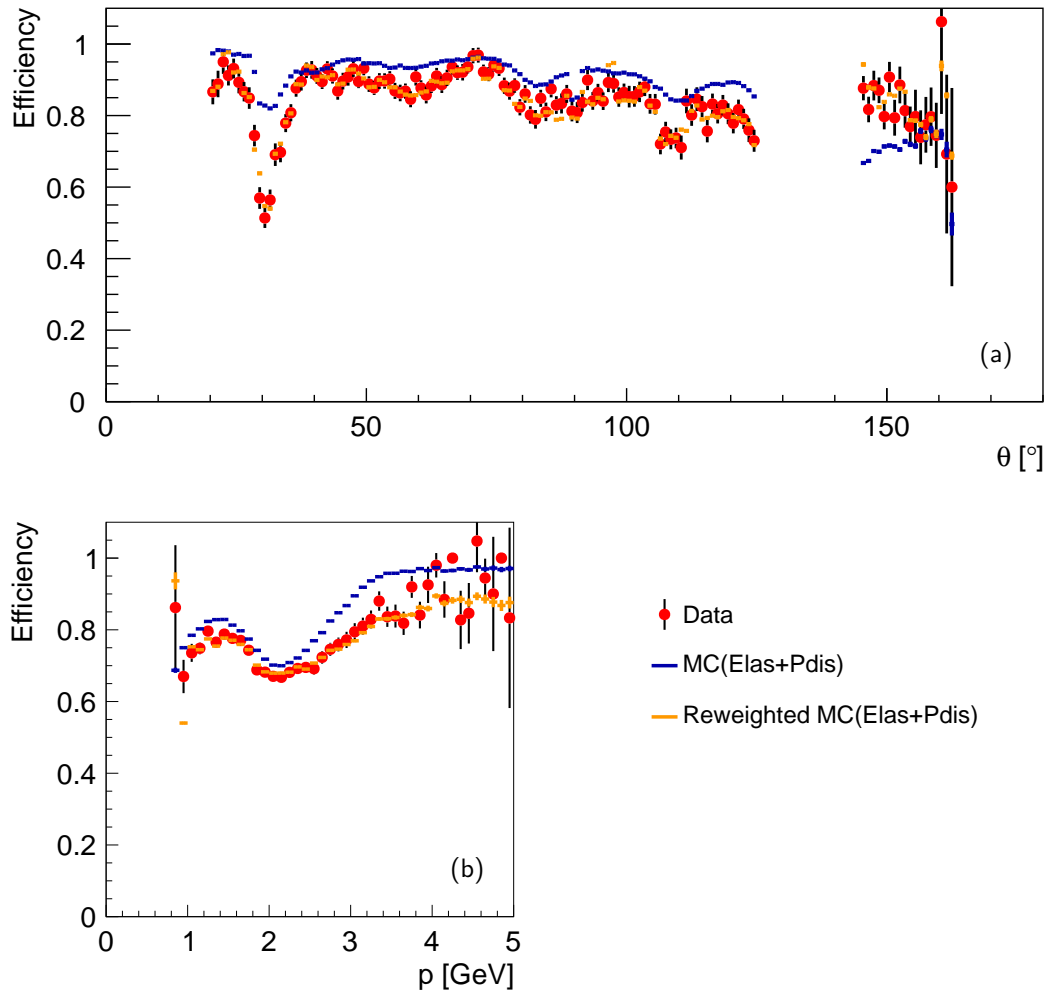
#### 6.6.2.4.1 Remaining systematic uncertainty after correction

Figure 6.8 shows the efficiencies as function of  $t$  (a) and  $W_{\gamma p}$  (c). The notation of the distributions are the same as used in Fig. 6.7. In Fig. 6.8(b) and (d) the ratios of the efficiency corrected MC simulations to data are given. The bands indicate the remaining uncertainties. They are evaluated by taking the statistical errors of each bin in a histogram and add in quadrature in all bins a constant value. A fit is done with a constant fit function, returning a  $\chi^2/\text{ndf}$ . Now the constant value is increased and the new histograms are refitted until the condition  $\chi^2/\text{ndf} = 1$  is reached.

The constant value for which the condition is fulfilled then is taken as remaining systematic uncertainty. It is evaluated to be 4% in  $t$  and 1.7% in  $W_{\gamma p}$ .

## 6.7 Mass window cut

After applying all selection cuts, still some small background is present. A further background suppression in the electron and muon sample is achieved by using a mass window cut of  $m_{ee} = 2.3 - 3.3 \text{ GeV}$  and  $m_{\mu\mu} = 2.8 - 3.3 \text{ GeV}$ , respectively. The lower cut edge in the electron decay channel accounts for the larger radiative tail.



**Figure 6.7:** Combined muon identification efficiencies for a medium calorimeter muon or an iron muon as function of the polar angle  $\theta$  (a) and momentum  $p$  (b). Data are displayed as red points, the uncorrected MC simulation as blue and the corrected as orange histogram.

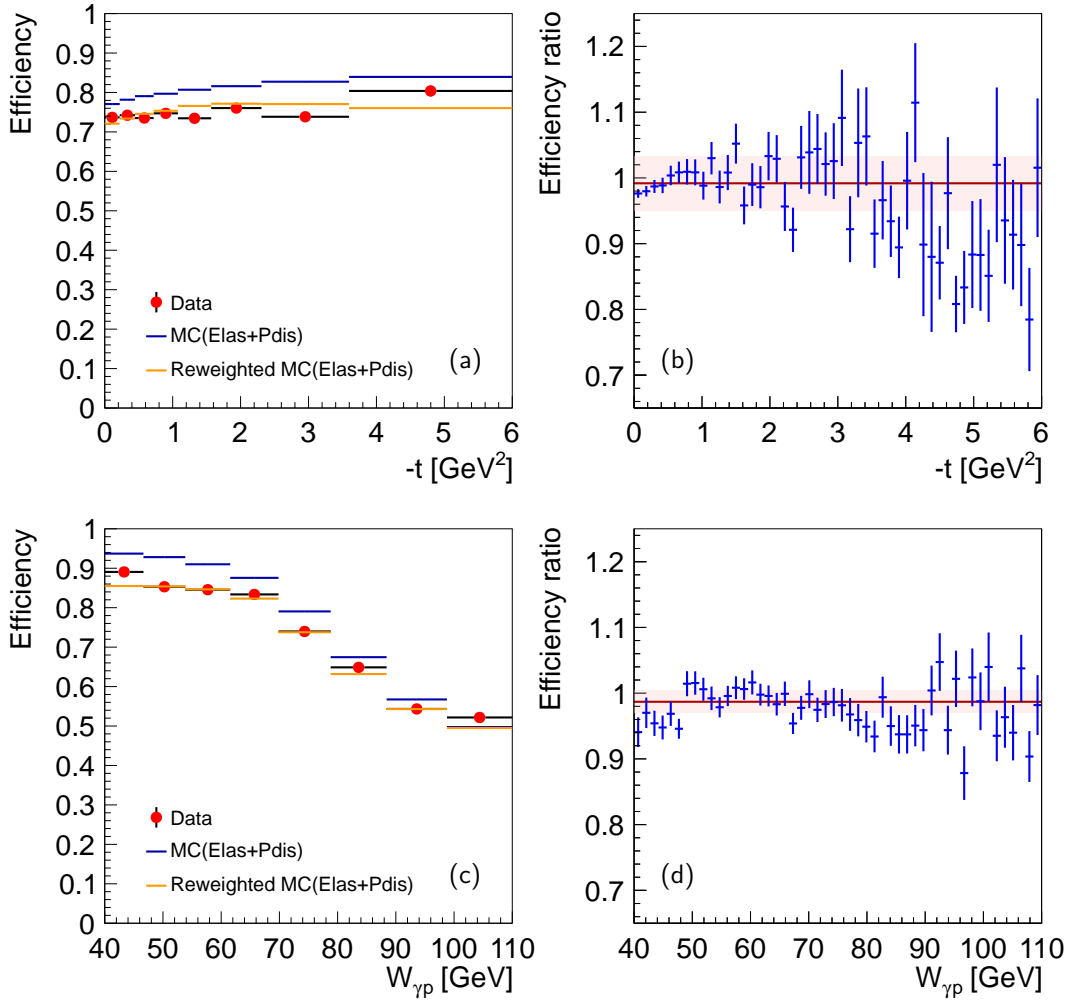


**Figure 6.8:** Muon identification efficiencies for a medium calorimeter muon or an iron muon as function of  $-t$  (a) and  $W_{\gamma p}$  (c). Data are displayed as red points, the efficiency uncorrected MC simulation as blue and the corrected as orange histogram. The plots in the right column show the ratios of efficiency corrected MC simulation to data for the distributions  $-t$  (b) and  $W_{\gamma p}$  (d). The pink band indicates the remaining uncertainty.

## Efficiencies

The focus in this chapter is put on the description of efficiencies or rather inefficiencies resulting from applying the selection cuts. The first section deals with trigger efficiencies, while the second explains the acceptance and selection efficiencies. Section 7.3 will briefly discuss the resolution of kinematic quantities.

### 7.1 Trigger efficiencies

Cross section calculations for this analysis depend upon various parts, in particular on a proper correction for trigger inefficiencies. A derivation of the trigger efficiencies built exclusively from data is preferable due to independence from any simulation. Such a construction however requires an independent, so called, *reference* or *monitor trigger* to select an independent reference sample, relative to which the trigger efficiency is determined. For the photoproduction subtrigger used in this analysis, it is – unfortunately – not possible to extract the trigger efficiency only from data, due to a missing independent reference sample in data. Hence the trigger simulation is used.

Because the used subtrigger *s59* is mainly built from FTT trigger elements (see Sec. 5.3), the FTT emulation software, FTTEMU, (see Sec. 5.2.5) builds the crucial part of the trigger simulation of subtrigger *s59*. Performance analyses for various FTT subtriggers were carried out [142,143,234,259,266–270] showing that FTTEMU is in general working very well.

However good the simulation’s description for other subtriggers may be, it cannot be omitted to check FTTEMU also for the subtrigger *s59*. To serve this purpose, efficiencies of data and the simulation are studied in a phase space region where comparison is possible.

Determination of trigger efficiencies in data requires an independent reference sample recorded by an independent monitor trigger. Because FTT conditions are contained in most H1

subtriggers, the only partially overlapping subtriggers of *s59*, which do not depend on any FTT trigger elements and select a sample with enough statistics, are the subtriggers *s0 – s3*, which reconstruct the scattered beam electron from DIS events in the SpaCal calorimeter.

These DIS monitor triggers depend on reconstructing energy deposited by the scattered beam electron. But the standard selection, as it is used for the analysis, is selecting photoproduction events. An adaption of the selection from photoproduction to a DIS events is therefore necessary. For all trigger efficiency studies the following changes to the selection, as described in Chapter 6, are assigned:

- The cut on the scattered beam electron’s absence is replaced by the requirement  $Q_e^2 > 2.5 \text{ GeV}$ .
- The track multiplicity cut is relaxed from less than three to less than four, to allow an additional track, due to the scattered beam electron, in the selection.
- For the electron decay channel  $J/\psi \rightarrow ee$  an additional polar angle cut to electron tracks of  $\theta < 140^\circ$  is used. This suppresses events in the reference sample, where an electron from a  $J/\psi$  decay, instead of the scattered beam electron, is responsible for the SpaCal triggering.

Though the selection results in a sample usable to test the subtrigger *s59* with the DIS monitor triggers *s0 – s3*, the statistics of the sample is in both decay channel approximately 600 events for the high energy data period and only about 40 events for the low energy data period. This is less than desirable, but enough for a cross check.

### 7.1.1 Trigger efficiency distributions

Trigger efficiency<sup>(1)</sup> comparisons between the data and the simulation for the high energy data period are given in Fig 7.1 and 7.2 for the  $J/\psi \rightarrow ee$  and  $J/\psi \rightarrow \mu\mu$  decay channels, respectively. Data are represented by the red circles, the solid blue and dotted green histograms show the elastic and proton dissociative DIS MC simulations<sup>(2)(3)</sup>.

Within the given limited statistics the simulation describes the data. However, a small normalisation difference exists. The total trigger efficiencies are for the electron channel  $(81.7 \pm 0.3) \%$  in the simulation<sup>(4)</sup> and  $(82.3 \pm 1.7) \%$  in data. For the muon reconstruction channel the simulation obtains  $(78.4 \pm 0.3) \%$ , while in data  $(81.1 \pm 1.5) \%$  is estimated. To correct for this small difference in the muon decay channel sample the simulated MC efficiencies are globally shifted upwards by 3%.

In Fig. 7.3 and 7.4 the trigger comparison plots for the low energy data period are shown. The representation of the data and MC simulations are the same as in the plots for the high energy data period. Since the number of events in the reference sample is small, the statistical errors are rather large.

<sup>(1)</sup>The asymmetric error on the trigger efficiency in data are calculated using the Wilson confidence interval for binomial statistics, as suggested in [271]. The implementation in ROOT [272] is used.

<sup>(2)</sup>The elastic and proton dissociative DIS simulations used for the trigger studies are the same as are used for the main analysis. They were generated without any  $Q^2$  cut to allow this kind of studies.

<sup>(3)</sup>The bin centre for the simulations are artificially shifted to increase visibility of the histograms.

<sup>(4)</sup>The given total trigger efficiency in the simulation is the arithmetic mean from the elastic and proton dissociative MC simulation. Both agree within their statistical uncertainty with each other.

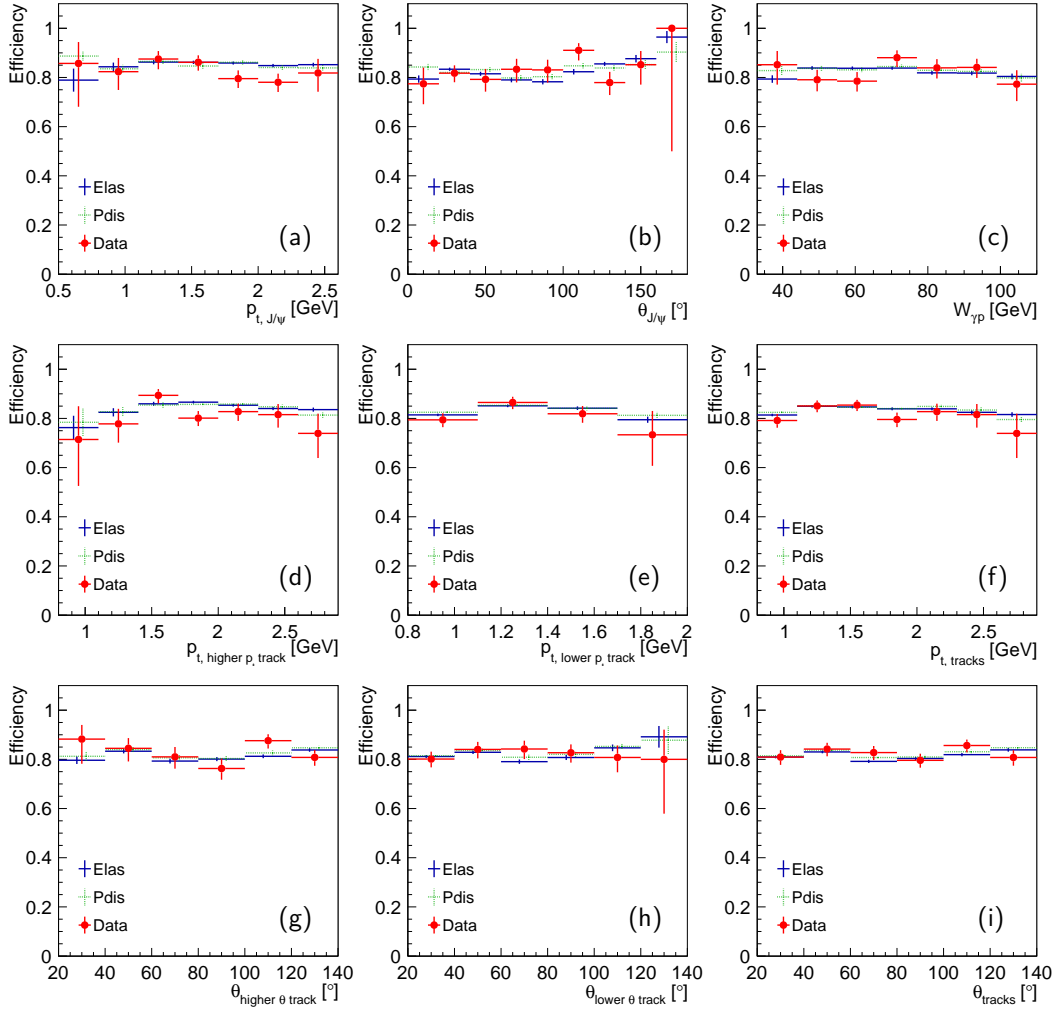


**Figure 7.1:** Trigger efficiency comparison for DIS of MC simulation to data for the high energy data period in the decay channel  $J/\psi \rightarrow ee$ . The red points represent data using the DIS monitor triggers  $s0 - s3$  as reference sample. The elastic (Elas) and proton dissociative (Pdis) simulations are shown as solid blue and dotted green histograms, respectively. The efficiencies are presented as functions of the transverse momentum  $p_{t,J/\psi}$  (a) and polar angle  $\theta_{J/\psi}$  (b) of the  $J/\psi$ . Subfigure (c) gives the efficiency as function of the centre of mass energy in the photon proton rest frame  $W_{\gamma p}$ . Plots (d) – (f) show the efficiency dependence as function of  $p_t$  of the two selected tracks with lower and higher transverse momentum ( $p_{t,lower p_t \text{ track}}$ ,  $p_{t,higher p_t \text{ track}}$ ) and the combination of both  $p_{t,tracks}$ . Plots (g) – (i) give the efficiency as function of the polar angle of the track with lower and higher angle ( $\theta_{lower \theta \text{ track}}$ ,  $\theta_{higher \theta \text{ track}}$ ) and the combination  $\theta_{tracks}$ .

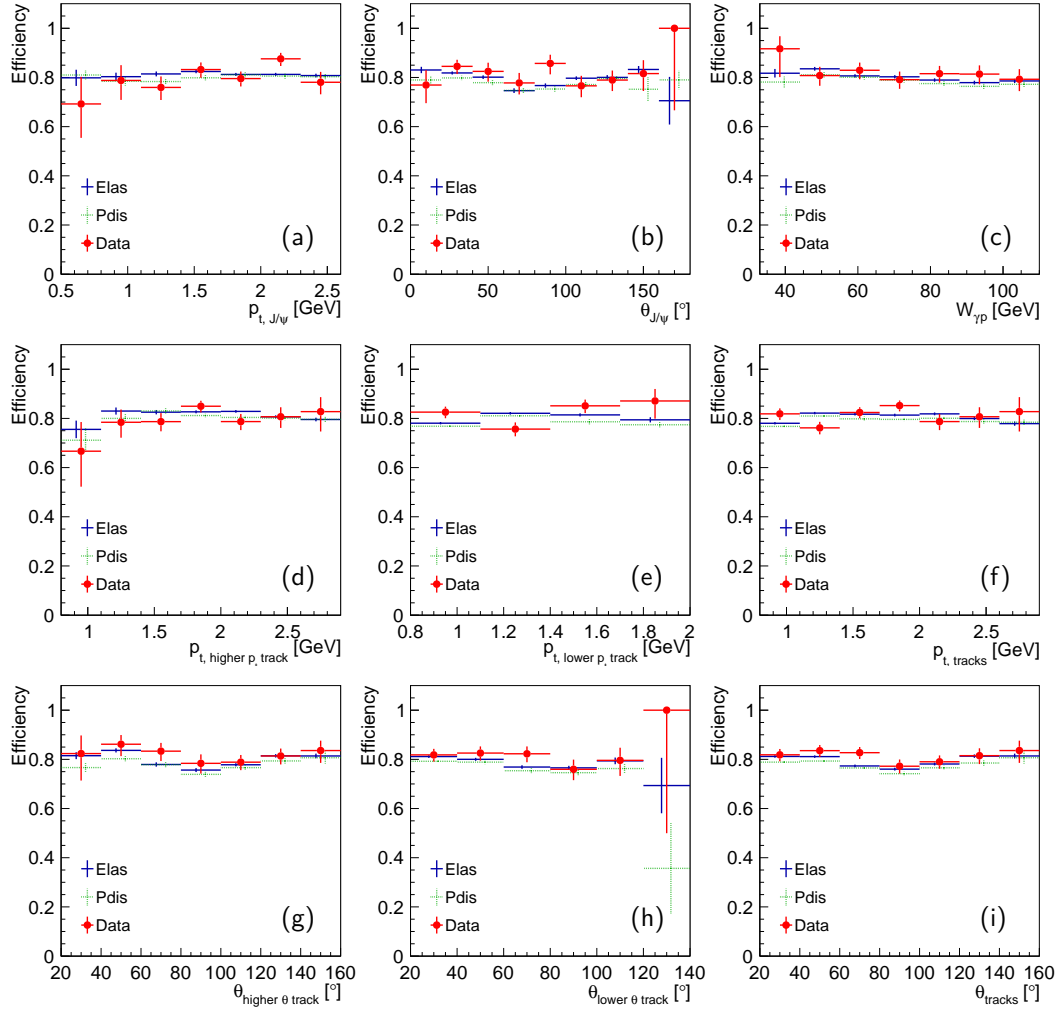


**Figure 7.2:** Trigger efficiency comparison for DIS of MC simulation to data for the high energy data period in the decay channel  $J/\psi \rightarrow \mu\mu$ . The red points represent data using the DIS monitor triggers  $s0 - s3$  as reference sample. The elastic (Elas) and proton dissociative (Pdis) simulations are shown as solid blue and dotted green histograms, respectively. The efficiencies are presented as functions of the transverse momentum  $p_{t,J/\psi}$  (a) and polar angle  $\theta_{J/\psi}$  (b) of the  $J/\psi$ . Subfigure (c) gives the efficiency as function of the centre of mass energy in the photon proton rest frame  $W_{\gamma p}$ . Plots (d) – (f) show the efficiency dependence as function of  $p_t$  of the two selected tracks with lower and higher transverse momentum ( $p_{t,lower p_t \text{ track}}$ ,  $p_{t,higher p_t \text{ track}}$ ) and the combination of both  $p_{t,tracks}$ . Plots (g) – (i) give the efficiency as function of the polar angle of the track with lower and higher angle ( $\theta_{lower \theta \text{ track}}$ ,  $\theta_{higher \theta \text{ track}}$ ) and the combination  $\theta_{tracks}$ .

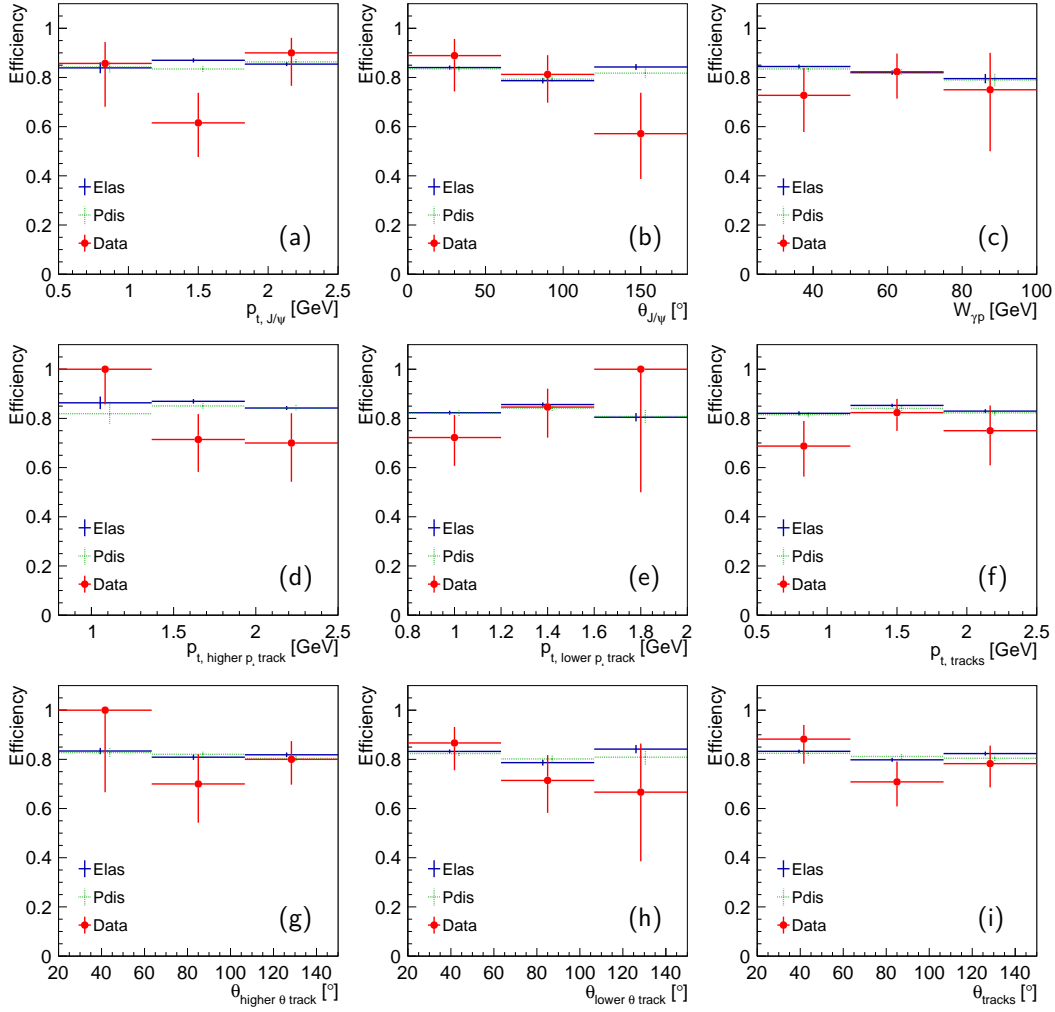


**Figure 7.3:** Trigger efficiency comparison for DIS of MC simulation to data for the low energy data period in the decay channel  $J/\psi \rightarrow ee$ . The red points represent data using the DIS monitor triggers  $s0 - s3$  as reference sample. The elastic (Elas) and proton dissociative (Pdis) simulations are shown as solid blue and dotted green histograms, respectively. The efficiencies are presented as functions of the transverse momentum  $p_{t,J/\psi}$  (a) and polar angle  $\theta_{J/\psi}$  (b) of the  $J/\psi$ . Subfigure (c) gives the efficiency as function of the centre of mass energy in the photon proton rest frame  $W_{\gamma p}$ . Plots (d) – (f) show the efficiency dependence as function of  $p_t$  of the two selected tracks with lower and higher transverse momentum ( $p_{t,lower p_t \text{ track}}$ ,  $p_{t,higher p_t \text{ track}}$ ) and the combination of both  $p_{t,tracks}$ . Plots (g) – (i) give the efficiency as function of the polar angle of the track with lower and higher angle ( $\theta_{lower \theta \text{ track}}$ ,  $\theta_{higher \theta \text{ track}}$ ) and the combination  $\theta_{tracks}$ .

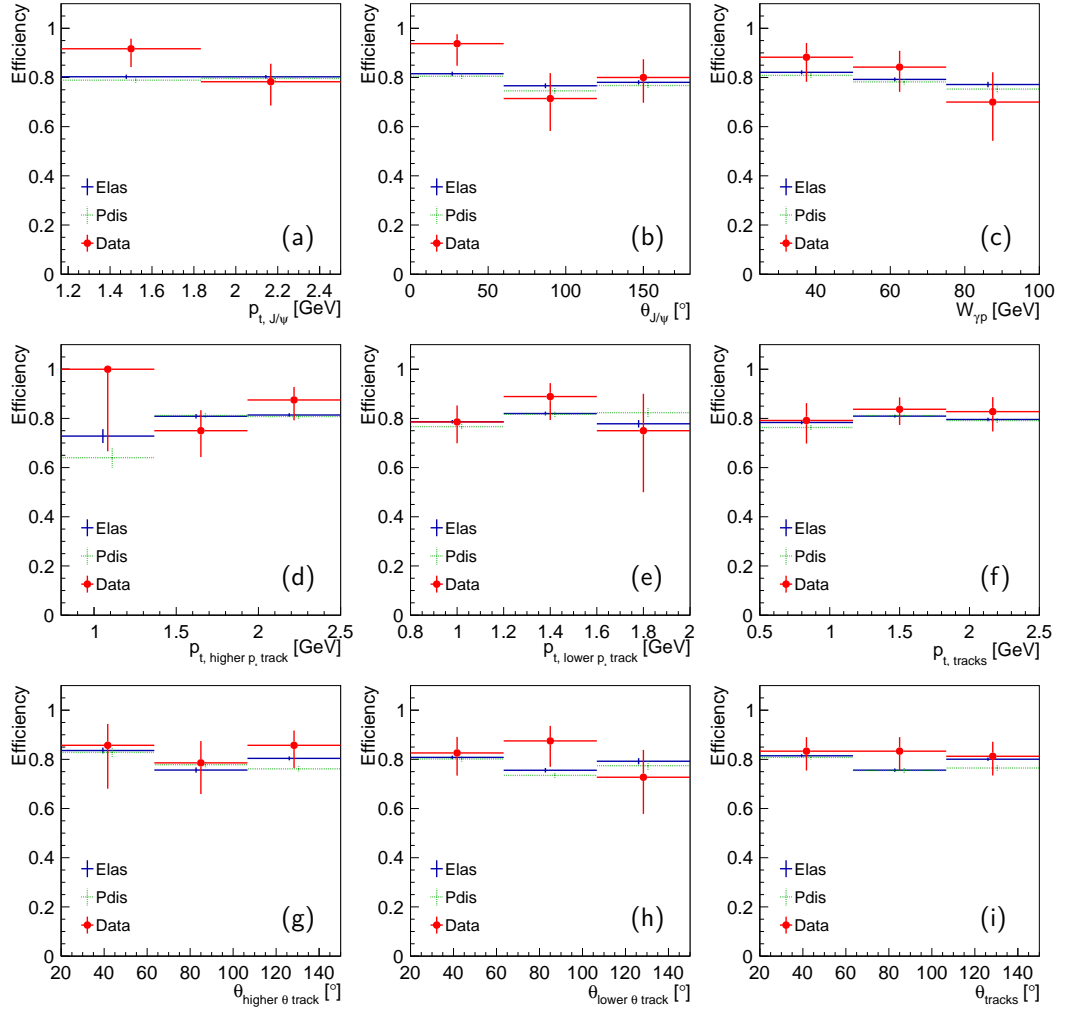


**Figure 7.4:** Trigger efficiency comparison for DIS of MC simulation to data for the low energy data period in the decay channel  $J/\psi \rightarrow \mu\mu$ . The red points represent data using the DIS monitor triggers  $s0 - s3$  as reference sample. The elastic (Elas) and proton dissociative (Pdis) simulations are shown as solid blue and dotted green histograms, respectively. The efficiencies are presented as functions of the transverse momentum  $p_{t,J/\psi}$  (a) and polar angle  $\theta_{J/\psi}$  (b) of the  $J/\psi$ . Subfigure (c) gives the efficiency as function of the centre of mass energy in the photon proton rest frame  $W_{\gamma p}$ . Plots (d) – (f) show the efficiency dependence as function of  $p_t$  of the two selected tracks with lower and higher transverse momentum ( $p_{t,lower p_t \text{ track}}$ ,  $p_{t,higher p_t \text{ track}}$ ) and the combination of both  $p_{t,tracks}$ . Plots (g) – (i) give the efficiency as function of the polar angle of the track with lower and higher angle ( $\theta_{lower \theta \text{ track}}$ ,  $\theta_{higher \theta \text{ track}}$ ) and the combination  $\theta_{tracks}$ .

Within the errors the simulation is able to describe the data for both reconstruction channels. Due to statistical reasons, the same normalisation correction in the  $\mu\mu$  sample, as evaluated in the high energy data period, is used for the low energy sample.

## 7.2 Acceptance and selection efficiencies

This section describes all other efficiencies except those caused by the trigger. The acceptance (efficiency) is defined here as

$$\varepsilon_{\text{acc}} = \frac{N_{\text{gen}} \left[ \text{PS} \ \&\& \ (20^\circ < \theta_{\text{gen}}^{1,2} < 165^\circ) \ \&\& \ (p_{t,\text{gen}}^{1,2} > 0.8 \text{ GeV}) \right]}{N_{\text{gen}}(\text{PS})} \quad (7.1)$$

with  $N_{\text{gen}}(\text{PS})$  representing the number of generated events in the kinematic phase space (PS), see Table 6.1. The variables  $\theta_{\text{gen}}^{1,2}$  and  $p_{t,\text{gen}}^{1,2}$  denote the generated polar angle and the transverse momentum of the  $J/\psi$  daughter particles, i.e. the two electrons or the two muons.

The selection efficiency is defined without trigger condition and can be expressed in a formula as

$$\varepsilon_{\text{sel}} = \frac{N_{\text{rec}}(\text{selection cuts w/o trigger})}{N_{\text{gen}} \left[ \text{PS} \ \&\& \ (20^\circ < \theta_{\text{gen}}^{1,2} < 165^\circ) \ \&\& \ (p_{t,\text{gen}}^{1,2} > 0.8 \text{ GeV}) \right]}, \quad (7.2)$$

where  $N_{\text{rec}}(\text{selection cuts w/o trigger})$  means the number of reconstructed events after applying all selection cuts but the trigger requirement, as given in Chapter 6.

The total reconstruction efficiency combines all effects of acceptance, selection and trigger efficiency. Expressed in an equation it takes the form:

$$\varepsilon_{\text{rec}} = \frac{N_{\text{rec}}(\text{selection cuts w/ trigger})}{N_{\text{gen}}(\text{PS})}. \quad (7.3)$$

An example of the efficiencies is given in Fig 7.5 for the high energy data period in the decay channel  $J/\psi \rightarrow ee$ . The solid black, dashed blue and dotted red histogram indicate the acceptance, selection and reconstruction efficiency as defined above. Plot (a) and (b) show the efficiencies as function of  $W_{\gamma p}$  and figures (c) and (d) as function of  $-t$  for elastic and proton dissociative processes, respectively.

### 7.2.1 Discussion of the selection efficiency

The selection efficiency as given in Fig. 7.5(c) reaches efficiencies above 100 % in the highest  $|t|$  bins. This is clearly an unexpected behaviour and needs to be explained. To investigate the

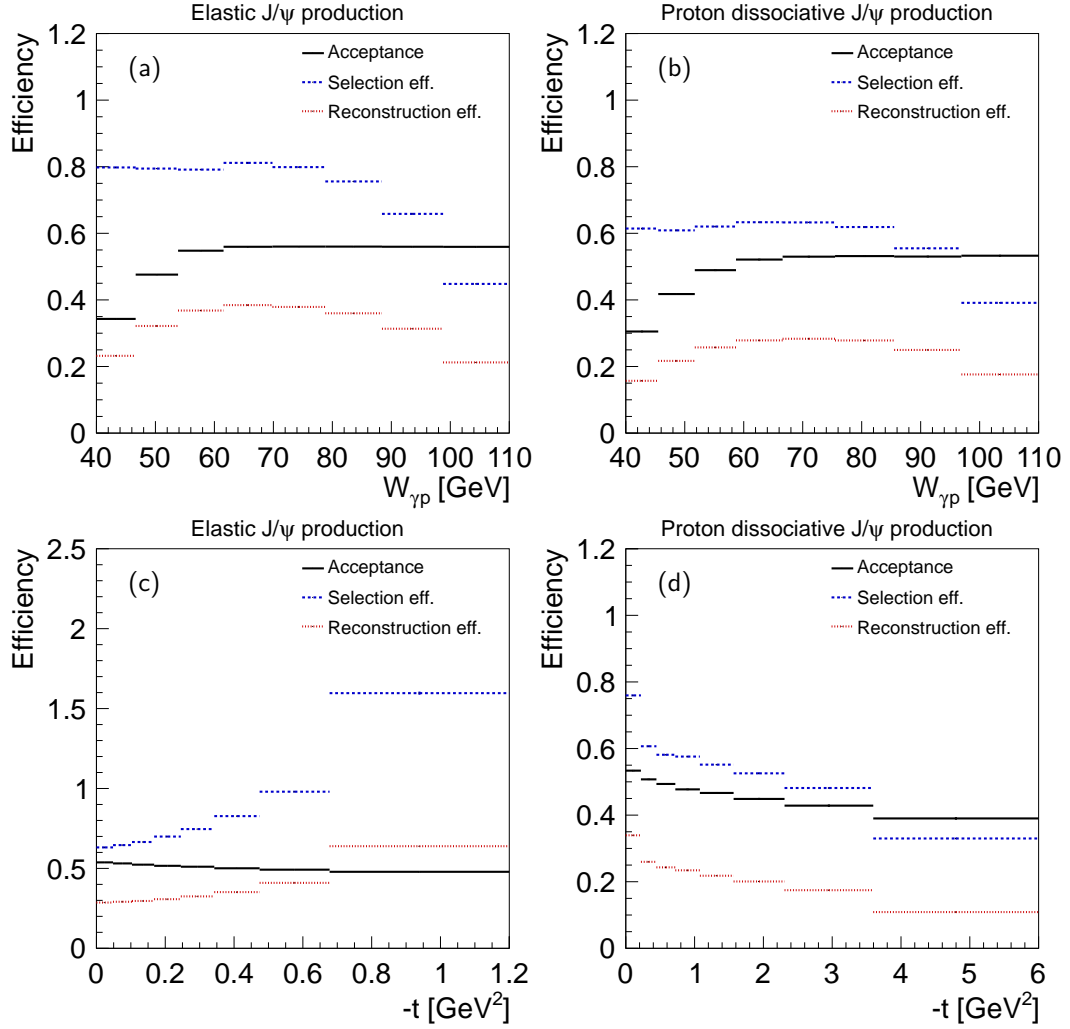


**Figure 7.5:** Overview of efficiencies for the high energy data period in the  $ee$  decay channel. The solid black, dashed blue and dotted red histogram represent the acceptance, selection and reconstruction efficiency as defined in Eq. (7.1) - (7.3). Figure (a) and (b) show the efficiencies as function of  $W_{\gamma p}$ , (c) and (d) as function of  $-t$  for the elastic and the proton dissociative process, respectively.

characteristics of the selection efficiency, it is better to separate generator from reconstruction level. The selection efficiency as function of  $t$  can be rewritten as

$$\varepsilon_{\text{sel}} = \frac{N(t_{\text{rec}}; \text{selection cuts w/o trigger})}{N(t_{\text{gen}}; \text{PS \&\& acceptance})} \quad (7.4)$$

$$= \underbrace{\frac{N(t_{\text{rec}}; \text{selection cuts w/o trigger})}{N(p_{t,\psi,\text{gen}}^2; \text{PS \&\& acceptance})}}_{\varepsilon_1} \cdot \underbrace{\frac{N(p_{t,\psi,\text{gen}}^2; \text{PS \&\& acceptance})}{N(t_{\text{gen}}; \text{PS \&\& acceptance})}}_{\varepsilon_2}, \quad (7.5)$$

with  $\varepsilon_2$  depending only on generated quantities. The term *acceptance* is used to abbreviate the acceptance cuts as shown in the denominator of Eq. (7.2). As defined in Sec. 6.1.5  $t_{\text{rec}}$  is approximated by  $p_{t,\psi,\text{rec}}^2$ ,  $t_{\text{rec}} \equiv -p_{t,\psi,\text{rec}}^2$ , the expansion of the selection efficiency via  $p_{t,\psi,\text{gen}}^2$  is therefore quite natural. In Fig. 7.6(a) the selection efficiency is plotted again, while in Fig. 7.6(b) the  $\varepsilon_1$  efficiency is given. The  $x$ -axis are labeled with  $-t_{\text{gen}}$  and  $p_{t,\psi,\text{gen}}^2$  to clearly indicate the difference of the denominator for the given efficiencies but one should not forget that the nominator depends on the reconstructed quantity  $p_{t,\psi,\text{rec}}^2$ . The  $\varepsilon_1$  efficiency shows a reasonable behaviour, which does not exceed 100 %.

The reconstruction of  $p_{t,\psi,\text{gen}}^2$  with  $p_{t,\psi,\text{rec}}^2$  does not cause the problem of efficiencies above 100 %. It is located in  $\varepsilon_2$ , i.e. in the transition from  $-p_{t,\psi,\text{gen}}^2$  to  $t_{\text{gen}}$ , as can be seen in Fig. 7.6(c).

The  $\varepsilon_2$  behaviour can also be investigated by plotting its fraction components separately, as it is done in Fig. 7.7 using the elastic  $J/\psi \rightarrow ee$  MC simulation. The red circles and the blue squares show the number of events as function of  $-t_{\text{gen}}$  and  $p_{t,\psi,\text{gen}}^2$ , respectively<sup>(5)</sup>. A ratio of them would be equal to  $\varepsilon_2$  with the blue squares represent the nominator and the red circles the denominator, which produces, due to more events at high  $p_{t,\psi,\text{gen}}^2$  than at high  $-t_{\text{gen}}$ , an  $\varepsilon_2$  which rises at high values and therefore a selection efficiency exceeding a 100 %.

The reason for the odd behaviour of the selection efficiency can be explained, simply by the needed approximation of  $t_{\text{gen}}$  with  $-p_{t,\psi,\text{gen}}^2$ . One could stop at this point, but it seems natural to ask, if there is not a more sophisticated approach for expressing  $t_{\text{gen}}$ .

A better attempt would be the approximation  $t_{\text{gen}} \simeq -(p_{t,\psi,\text{gen}}^2 - Q_{\text{gen}}^2)$ , taking into account also the leading  $Q^2$  dependence<sup>(6)</sup>, as can be seen in Fig. 7.7, which shows the elastic<sup>(7)</sup> distribution as function of  $p_{t,\psi,\text{gen}}^2 - Q_{\text{gen}}^2$  as green triangles. Clearly it would work better than using only  $p_{t,\psi,\text{gen}}^2$ . Unfortunately on reconstruction side an expression for the virtuality would be required, which is not possible since this analysis operates in photoproduction region. No other choice therefore remains than reconstruct  $t$  with  $-p_{t,\psi,\text{rec}}^2$ .

To summaries this discussion, the effect of a selection efficiency exceeding 100 % is explained and it was shown that is not unphysical, but simply caused due to a variable change from  $t$

<sup>(5)</sup>The plot labeling is slightly unusual and needs to be explained. The abscissa of the plot shows a dependence on the variable  $x$ , while  $x$  is defined differently for each single distribution. Therefore the three plots actually depend on three different variables. This representation was chosen to better indicate the different behaviour of the distributions, especially at high values.

<sup>(6)</sup>In the derivation of  $t_{\text{rec}}$  in Appendix A.2 it can be seen that the leading  $Q^2$  dependence is simply an additive term.

<sup>(7)</sup>No proton dissociative distributions are shown because the effect is much smaller, since the derivative in  $t$  of the elastic cross section is much larger than in the proton dissociative case.

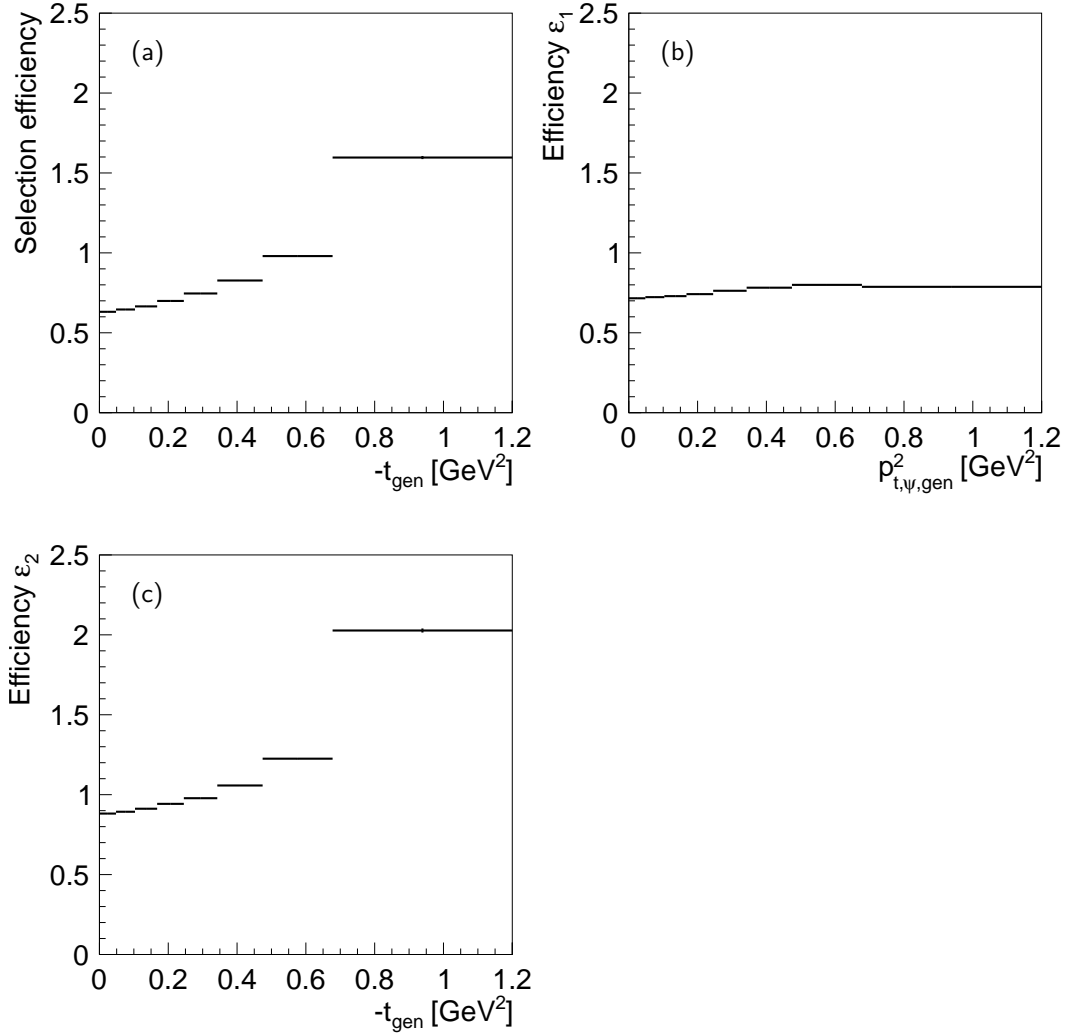


**Figure 7.6:** Plot (a) shows the selection efficiency of the elastic MC simulation as function of  $-t_{\text{gen}}$  and (b) gives the efficiency  $\varepsilon_1$ , as defined in the text, as function of  $p_{t,\psi,\text{gen}}^2$ . It can be regarded as selection efficiency where  $t_{\text{gen}}$  is replaced by  $-p_{t,\psi,\text{gen}}^2$ . Figure (c) shows the efficiency  $\varepsilon_2$  as function of  $-t_{\text{gen}}$ .

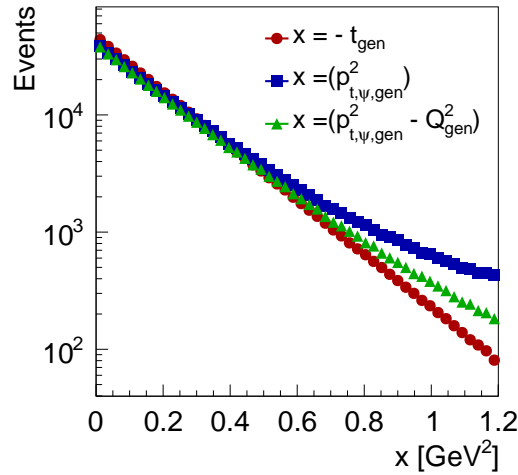


**Figure 7.7:** The figure shows the number of elastic MC events as function of  $x = -t_{\text{gen}}$ ,  $p_{t,\psi,\text{gen}}^2$  and  $p_{t,\psi,\text{gen}}^2 - Q_{\text{gen}}^2$ , represented by the red circles, the blue squares and green triangles, respectively.

to  $p_{t,\psi}^2$ , which is only an approximation, but needed to be able to reconstruct  $t$ . However, a change of this size in the selection efficiency already indicates a different expected result of the cross section as function of  $p_{t,\psi}^2$  instead of  $|t|$ . This issue will be discussed again later in this text.

### 7.3 Resolutions

To finalise this chapter the reconstruction resolutions are discussed. Figure 7.8 shows the resolutions for the photon proton centre of mass energy,  $W \equiv W_{\gamma p}$ , for elastic and proton dissociative produced  $J/\psi$  events in the upper and lower row, respectively. The two decay channels  $J/\psi \rightarrow ee$  and  $J/\psi \rightarrow \mu\mu$  are given in the left and right pairs, respectively. For each process and decay channel two plots are provided, the former shows absolute, the latter relative resolutions. The resolution distributions for the negative squared four-momentum transfer at the proton vertex,  $T \equiv -t$ , are presented in Fig. 7.10 in the same plot representation as used in Fig. 7.8.

In general the resolutions for the  $J/\psi \rightarrow \mu\mu$  decay channel are smaller and more symmetric than for the  $J/\psi \rightarrow ee$  channel, due to QED final state radiation, which is more prominent in the electron than in the muon decay channel.

More precise information are provided in Fig. 7.9 and 7.11, which show differential resolutions<sup>(8)</sup> as function of  $W_{\gamma p}$  and  $-t$  for the two decay channels  $J/\psi \rightarrow ee$  and  $J/\psi \rightarrow \mu\mu$  as solid black and dashed red lines, respectively, for elastic (left pairs) and proton dissociative

<sup>(8)</sup>Because the distributions are asymmetric, the resolution values, given in each bin, are the width formed by one-sigma (68%) symmetric confidence interval.

(right pairs) process. For each pair the first plot shows the absolute and the second the relative differential resolution.

The relative resolution for  $W_{\gamma p}$  is quite good, about 5 – 7 % and 2 – 3 % in the electron and muon decay channel, respectively. In both channels the distribution is flat over the whole range.

Unfortunately the situation in case of the reconstruction resolution in  $t$  is worse. Not only are the relative resolutions large, at best level about 50 % and 30 % for the two decay channels  $J/\psi \rightarrow ee$  and  $J/\psi \rightarrow \mu\mu$ , respectively, also they strongly vary over the range in  $t$ . This size of the reconstruction resolution causes large migrations, fortunately a *cure* exist for such kind of problems, which will be discussed later.

As in the previous section it is interesting to know how much of the bad resolution is due to reconstruction of  $|t_{\text{gen}}|$  with  $p_{t,\psi,\text{rec}}^2$ , instead of reconstructing  $p_{t,\psi,\text{gen}}^2$ . For this purpose Fig. 7.12 shows the resolution and Fig. 7.13 the differential resolutions for  $p_{t,\psi}^2$ . Again, the muon decay channel has smaller resolutions than the electron channel, due to lower QED photon radiation. Probably not surprising is the fact that the resolutions for  $p_{t,\psi}^2$  are smaller than for  $|t|$ , however even for  $p_{t,\psi}^2$  they sill are large, especially at low  $|t|$ .

The final conclusion from this section can only be that the large migrations, caused by the broad resolutions of the quantities for which cross section are measured, need to be properly accounted for, in order for a measurement to reflect the true situation. The method used in this analysis is based on an unfolding technique as will be explained in Chapter 9.

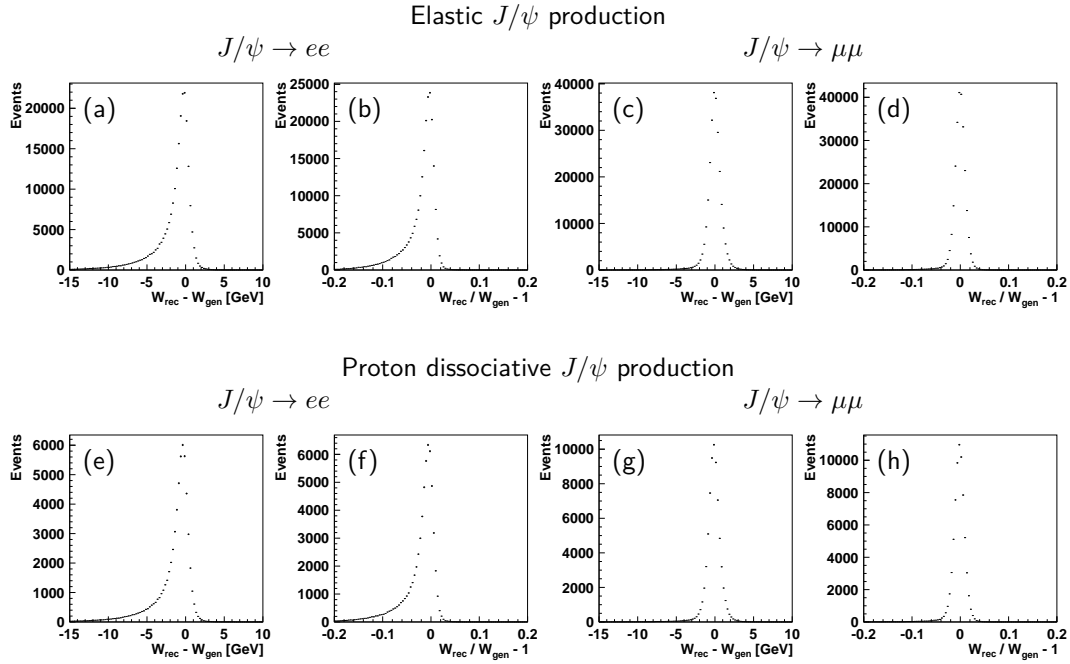


**Figure 7.8:** Absolute and relative resolution of  $W_{\gamma p}$  for the high energy data period in the  $J/\psi \rightarrow ee$  (left pairs) and  $J/\psi \rightarrow \mu\mu$  (right pairs) decay channel. The upper row shows the resolutions derived from elastic, the lower from proton dissociative MC simulation.

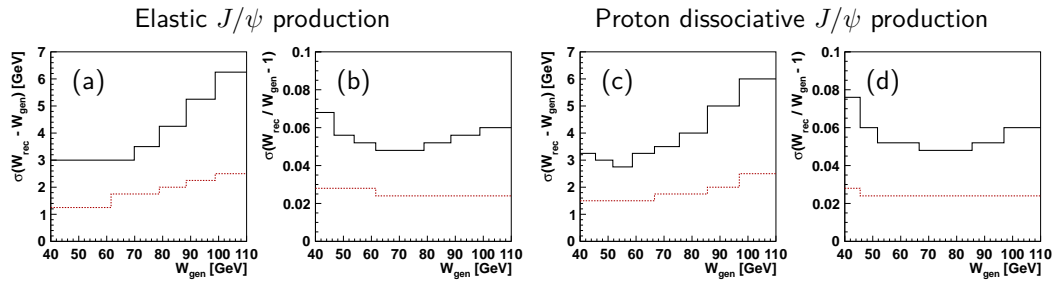


**Figure 7.9:** Absolute and relative differential resolution of  $W_{\gamma p}$  for the high energy data period for elastic (left pair) and proton dissociative (right pair) MC simulation. The resolutions for the  $J/\psi \rightarrow ee$  and  $J/\psi \rightarrow \mu\mu$  decay channel are represented by the solid black and dashed red lines, respectively.

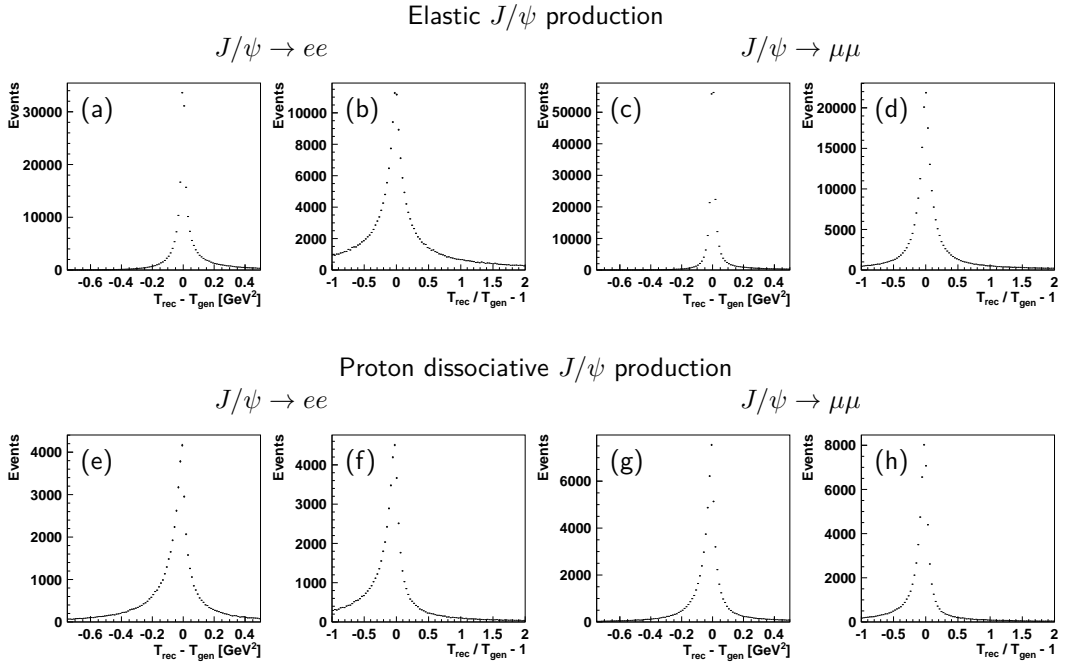


**Figure 7.10:** Absolute and relative resolution of  $T \equiv -t$  for the high energy data period in the  $J/\psi \rightarrow ee$  (left pairs) and  $J/\psi \rightarrow \mu\mu$  (right pairs) decay channel. The upper row shows the resolutions derived from elastic, the lower from proton dissociative MC simulation.

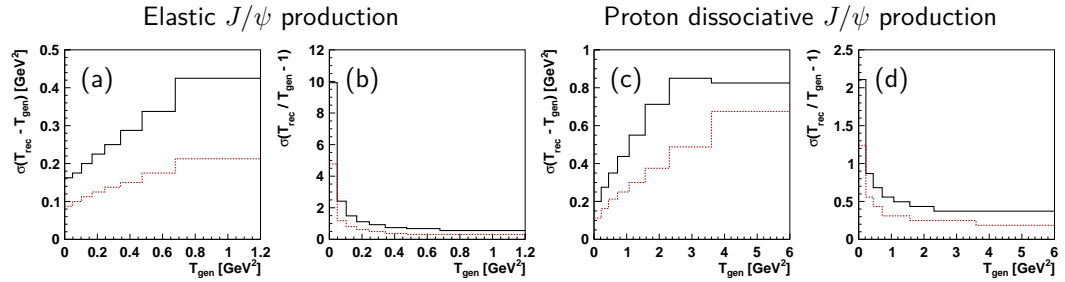


**Figure 7.11:** Absolute and relative differential resolution of  $T \equiv -t$  for the high energy data period for elastic (left pair) and proton dissociative (right pair) MC simulation. The resolutions for the  $J/\psi \rightarrow ee$  and  $J/\psi \rightarrow \mu\mu$  decay channel are represented by the solid black and dashed red lines, respectively.

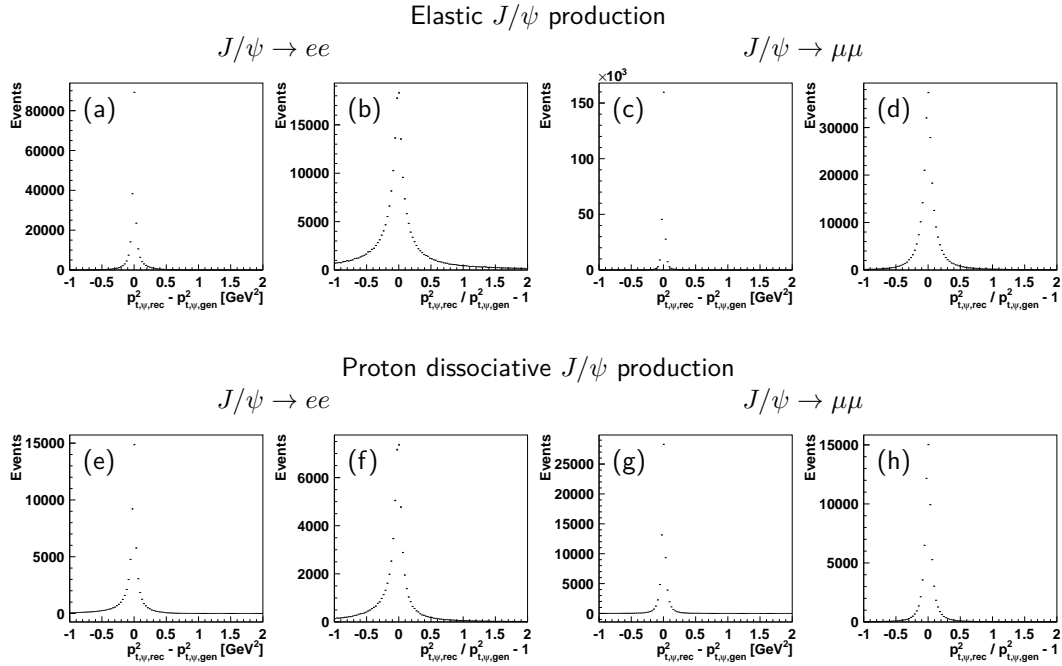


**Figure 7.12:** Absolute and relative resolution of  $p_{t,\psi}^2$  for the high energy data period in the  $J/\psi \rightarrow ee$  (left pairs) and  $J/\psi \rightarrow \mu\mu$  (right pairs) decay channel. The upper row shows the resolutions derived from elastic, the lower from proton dissociative MC simulation.

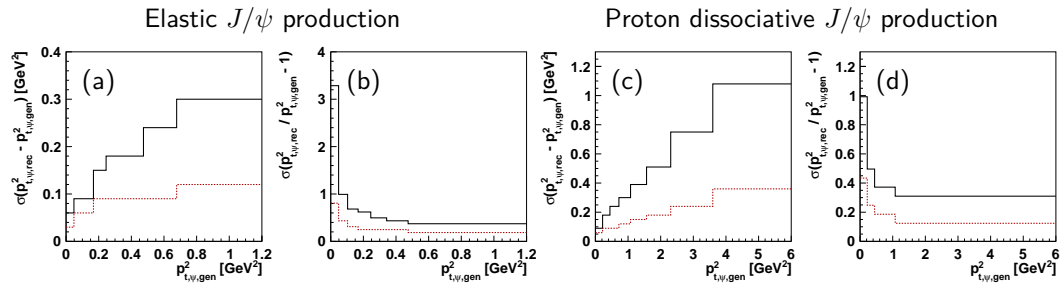


**Figure 7.13:** Absolute and relative differential resolution of  $p_{t,\psi}^2$  for the high energy data period for elastic (left pair) and proton dissociative (right pair) MC simulation. The resolutions for the  $J/\psi \rightarrow ee$  and  $J/\psi \rightarrow \mu\mu$  decay channel are represented by the solid black and dashed red lines, respectively.



## Experimental tagging of proton dissociative events and modeling of forward energy flow

After applying all selection cuts (see Chapter 6) the sample contains mainly diffractive  $J/\psi$  events produced in elastic and proton dissociative processes. In addition also a small fraction of non-resonant background is present. In order to extract elastic and proton dissociative cross sections from data, the measured contribution of both signal processes<sup>(1)</sup> have to be disentangled. The actual separation and cross section determination is performed with an unfolding procedure as discussed in Chapter 9. The focus of this chapter is put on the reconstructed input quantity to the unfolding procedure, which is essential for the separation of elastic and proton dissociative process. Without this quantity the disentanglement of the processes could not be performed.

This input quantity on reconstruction level is in the following called *tagging of proton dissociative events* and abbreviated with *tagging*. It is based upon the response of the used H1 forward detectors. The construction of this tagging quantity is discussed in the first section of this chapter.

A proper separation of the elastic and proton dissociative cross section is only possible with a correct description of the response behaviour of the H1 forward detectors, which depends strongly on the modelling of the forward energy flow. Finding an optimal parametrisation for the forward energy flow is however not straight forward. Several ideas were investigated in the course of this thesis and the final successful procedure is explained in the Sec. 8.2.

---

<sup>(1)</sup>The separation of signal from the remaining background is discussed in Sec. 9.2.3.

## 8.1 Proton dissociative tagging quantity

### 8.1.1 Why are elastic and proton dissociative events overlapping on reconstruction level?

In a naive picture the expectation would be that only a proton dissociative event would cause a certain signal<sup>(2)</sup> in the forward detectors. But the outgoing proton in case of an elastic event may scatter with the beam pipe, beam gas or collimators, inducing a signal as well. Furthermore, a signal in the forward detectors can be caused by electronic noise accidentally occurring in the same time window as the online selection. These effects are overall small but nevertheless relevant, since, depending on the region of the phase space (especially at low  $|t|$  values), the number of elastic events is about an order of magnitude larger than the number of proton dissociative events, which produces a non-negligible contribution from elastic events to the total amount of occurring signals in the forward detectors.

On the other hand, a proton dissociative event may not necessarily produce a measurable signal in the forward detectors, due to detector inefficiencies. This circumstance is tightened because of limited acceptance of the forward detectors. In both situations the decay products of an excited proton from a proton dissociative event remain undetected in the forward detectors and therefore mimic an elastic event.

This mixture of both processes needs a proper treatment on reconstruction level.

### 8.1.2 Forward detector quantities

Dissociative protons occur prominently in the forward direction, making the H1 forward detectors best suited for detecting traces of their remnants. Three subdetectors, situated at different locations, are used to cover the acceptance of the forward direction as much as possible. Considered is the liquid argon calorimeter detector, where only clusters in forward direction, satisfying the polar angle restriction of  $\theta < 10^\circ$ , are taken into account. It will be referred to as *LAr10* in the following. The PLUG calorimeter and the forward tagging station FTS<sup>(3)</sup> at  $z = 28$  m are included as well.

The forward muon detector (FMD), though perfectly fitted for tagging of proton remnants due to its large acceptance, is not used in the present analysis. It was shown during the work of this thesis that the hit distribution of the FMD layers are poorly described by the simulation in the run periods considered in this analysis.

Improving the calorimeter cluster energy description and reducing dependence on the LAr calorimeter noise is achieved by requiring a minimal energy threshold for LAr10 clusters of 400 MeV. For the PLUG calorimeter clusters the threshold is set to 1.2 GeV.

The calorimeter cluster energy distribution are given in Fig. 8.1 for LAr10 in (a) and for PLUG in (b) for the electron sample in the high energy data period. Data are shown as red

---

<sup>(2)</sup>The actual definition of what is called *signal* in this analysis is defined below. For the moment the actual definition is unimportant.

<sup>(3)</sup>The FTS station at  $z = 26$  m was broken for about half of the run time considered in this analysis. Therefore this station is neglected for all periods. The contribution of the FTS stations at  $z = 53$  m and 92 m is small due to acceptance and is not considered. Without ambiguity therefore FTS is referring only to the station at 28 m in the subsequent text.

points and the proton dissociative, elastic and the GRAPE background contribution are given as green, blue and magenta coloured stacked histograms. The combined MC simulations are normalised to data. The two distributions are well described, however a few remarks are needed. It was necessary in order to present this distributions to apply the parametrisation of the forward energy flow as described in Sec. 8.2, otherwise the simulation would not be able to describe the data. The ratio of elastic to proton dissociative contributions is taken from this determination as well. The background contribution from GRAPE MC simulation is normalised as described in Sec. 9.5.1.2.

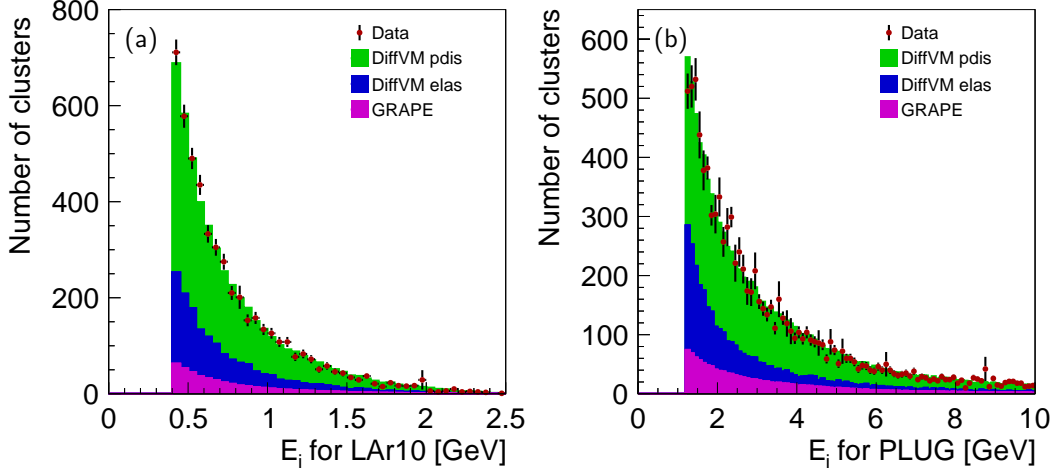


**Figure 8.1:** Calorimeter cluster energy distribution for electron sample in high energy data period. Sub figure (a) shows liquid argon clusters in forward directions with  $\theta < 10^\circ$  and (b) the energy distribution for PLUG. Only clusters above threshold as defined in the text are shown. The red points represent data. The green, blue and magenta coloured stacked histograms show the proton dissociative, elastic and GRAPE background contribution. The relative normalisation of elastic and proton dissociative process are taken from the forward energy flow parametrisation determination (see Sec. 8.2), while the absolute background normalisation is determined as described in Sec. 9.5.1.2. The combined MC simulations are normalised to data.

The clusters above the threshold are separately summed for LAr10 and PLUG to get the total deposited energies  $E_{\text{LAr10}}$  and  $E_{\text{PLUG}}$ , respectively. Written in a formula they take the form

$$E_{\text{LAr10}} = \sum_{i=1}^{N_{\text{LAr cluster}}} E_i(E_i > 400 \text{ MeV} \ \&\& \ \theta_i < 10^\circ) \quad \text{and} \quad (8.1)$$

$$E_{\text{PLUG}} = \sum_{i=1}^{N_{\text{PLUG cluster}}} E_i(E_i > 1.2 \text{ GeV}), \quad (8.2)$$

with  $N_{\text{LAr cluster}}$  and  $N_{\text{PLUG cluster}}$  the number of LAr and PLUG clusters, respectively.

For FTS only hit information is stored in the data record. It is denoted by  $N_{\text{FTS}}^{\text{hits}}$  and distributed between 0 – 4 hits.

### 8.1.3 Converting information from forward detectors into Boolean statements

Each response of the forward detectors is converted into a Boolean true-or-false statement by requiring a minimum deposited energy in the LAr10 and PLUG or a minimum number of hits in the FTS. The exact conditions are given in Table 8.1. Each derived Boolean statement

Detector	Condition
LAr10	$E_{\text{LAr10}} > 400 \text{ MeV}$
PLUG	$E_{\text{PLUG}} > 4 \text{ GeV}$
FTS	$N_{\text{FTS}}^{\text{hits}} \geq 1$

**Table 8.1:** Requirements for Boolean true-or-false statement for each forward detector quantity. The summed cluster energy above threshold for LAr10 is referenced as  $E_{\text{LAr10}}$  and for PLUG as  $E_{\text{PLUG}}$ . The number of FTS hits is denoted as  $N_{\text{FTS}}^{\text{hits}}$ .

from the three forward detectors will be referred to as *single tagging*, i.e. meaning a tag information extracted from only one of the forward detectors.

The single tagging information can now be used for deriving efficiency plots incorporating the acceptances of the forward detectors. Because each detector covers a different polar angle region of about  $3^\circ - 10^\circ$  [176, 189]<sup>(4)</sup>,  $2.4^\circ - 2.8^\circ$ <sup>(5)</sup> and  $0.08^\circ - 0.6^\circ$  for LAr10, PLUG and FTS, respectively, the response probability function depends on  $M_Y$  and also on  $t$ , due to dependence of the forward energy flow on these variables.

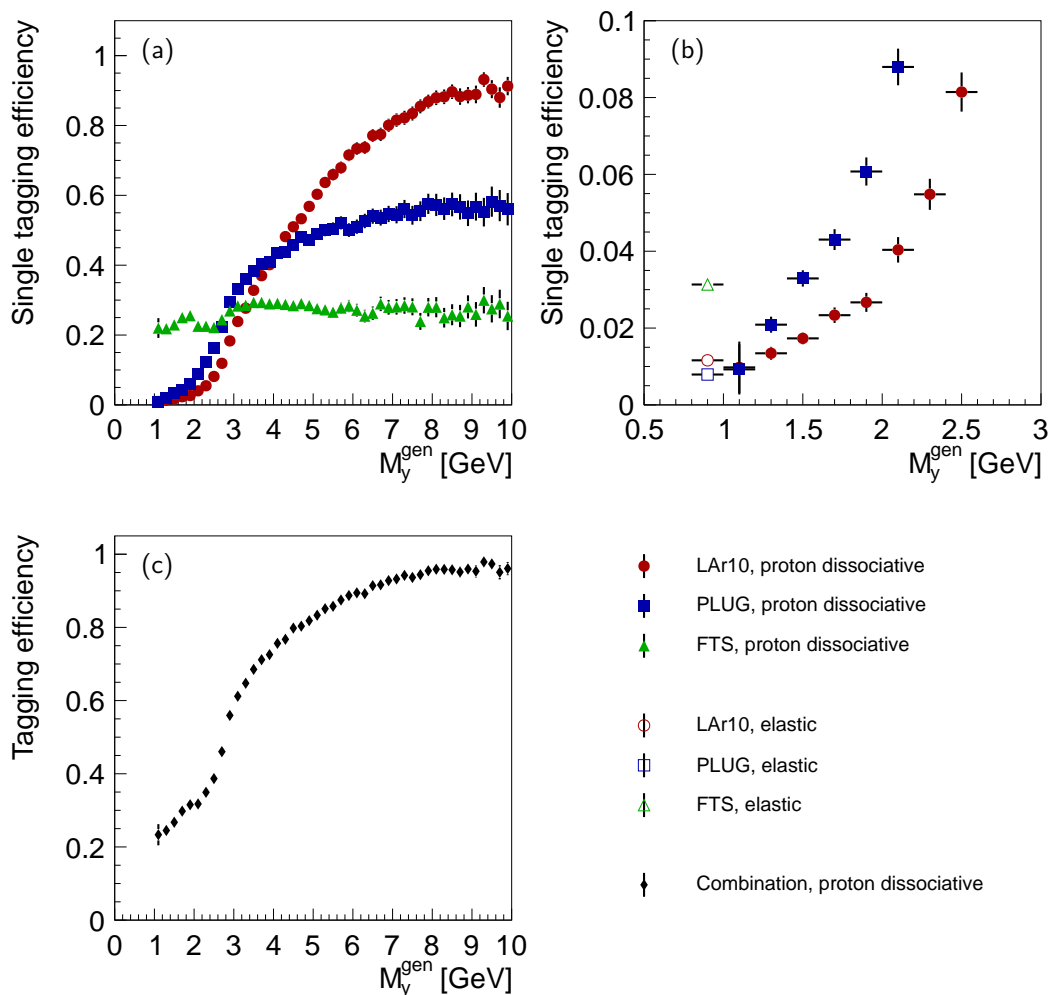
The single tagging efficiency for the individual detectors as function of  $M_Y^{\text{gen}}$  for the proton dissociative MC simulation is given in Fig. 8.2(a). It is worth noticing that FTS is rather flat over the whole  $M_Y^{\text{gen}}$  region and can tag events down to the limit<sup>(6)</sup> of  $M_p + M_\pi$ , with  $M_p$  and  $M_\pi$  the proton and pion mass, respectively. The LAr10 and PLUG single tagging efficiency rise with  $M_Y^{\text{gen}}$  and in case of the LAr10 reach about 90 % at high  $M_Y$  values.

Figure 8.2(b) shows a zoomed in version of Fig. 8.2(a) including the single tagging efficiencies for the elastic process. Compared to the proton dissociative process the single tagging efficiency for the elastic process is small. However, as mentioned above, the contribution of tagged events from elastic process is not negligible at small  $|t|$  due to a larger cross section with respect to proton dissociative process.

<sup>(4)</sup>The acceptance region of the whole liquid argon detector is  $3^\circ - 153^\circ$ , however for experimental tagging of proton dissociative events the maximal polar angle of  $10^\circ$  was chosen as described above.

<sup>(5)</sup>The polar angle acceptance of the PLUG detector as stated in Sec. 3.2.4.1 of  $2.3^\circ - 3.2^\circ$  is reduced to the given range, due to the applied cuts.

<sup>(6)</sup>The  $\Delta$  resonances can also decay into a proton and a photon which allows a lower  $M_Y$  in the final state. But because the decay is electromagnetic it is suppressed with respect to a strong decay. The PDG [58] lists the branching ratio of  $\Delta(1232) \rightarrow N\gamma$  as 0.52 – 0.60 %. Hence it can safely be ignored here.



**Figure 8.2:** The single tagging efficiency as function of  $M_Y^{\text{gen}}$  for proton dissociative MC simulation (a) and a zoomed in version showing also the elastic single tagging efficiencies (b). The LAr10, PLUG and FTS are represented by the red circles, the blue squares and the green triangle, respectively, with filled markers for proton dissociative and open symbols for elastic process. Figure (c) shows the combined tagging efficiency for proton dissociative process as function of  $M_Y^{\text{gen}}$ .

### 8.1.4 Combination of single tagging information

The information on the forward detector responses is used in the separation of elastic and proton dissociative process. For this purpose the single tagging information are combined into just one Boolean statement, called *tag*, by applying a simple logical *or* operation. This reduces the dependence on the noise description of the single detectors and, more important, increases the tagging efficiency compared to the single tagging efficiencies. The combined tagging efficiency as function of  $M_Y^{\text{gen}}$  is shown in Fig. 8.2(c). The tagging efficiency at low  $M_Y^{\text{gen}}$  starts about at the level given by the single tagging fraction of the FTS and follows with increasing  $M_Y^{\text{gen}}$  the shape of the single LAr10 and PLUG efficiency.

The overall number of tagged events expected in data might be misled by Fig. 8.2(c) without keeping in mind that the proton dissociative cross section  $d\sigma/dM_Y^2$  is proportional to  $1/M_Y^{2(1+\varepsilon)}$  (see Chapter 2), i.e. steeply decreasing with  $M_Y$ . The actual number of tagged events is the product of the tagging efficiency distribution and the rapidly falling cross section.

## 8.2 Parameter estimation for forward energy flow

A description of the tagging efficiency in the MC simulation is crucial for separating elastic and proton dissociative processes. As seen above the tagging efficiency depends strongly on  $M_Y$ , hence it would be reasonable to compare the tagging efficiencies as function of the reconstructed  $M_Y^{\text{ec}}$  between data and the simulation. So far only tagging fractions produced from proton dissociative and elastic MC simulations were shown, but none in data. The reason is based on the fact that a proper reconstruction of  $M_Y$  is not possible. This automatically means that all experimentally accessible distributions always show the integral over the  $M_Y$  distribution.

A cross check of the tagging efficiency therefore cannot be made easily and a more complicated setup is needed.

### 8.2.1 Procedure description for parameter determination

Due to the interplay of  $M_Y$  with  $t$  and  $W_{\gamma p}$  a successful approach to determine the forward energy flow must take all three variables into account. The basic idea is to perform a fit to determine all free parameters of the triple pomeron model (see Chapter 2), describing the proton dissociative process, and also the parameters responsible for the elastic process characterisation. The actual cross section dependencies for elastic and proton dissociative processes are hence not different than what is implemented in the DiffVM generator<sup>(7)</sup> (see Sec. 4.1), but a realistic determination of the parameters is achieved with this procedure<sup>(8)</sup>.

<sup>(7)</sup>Different parametrisations of the proton dissociative cross section were studied in addition but no improvements in the data description could be achieved.

<sup>(8)</sup>A direct comparison of parameters determined with this procedure and values used for generating proton dissociative and elastic events should not be made because the generated MC simulations are intentionally produced to populate regions of the phase space with enough events which otherwise, by use of realistic parameters, would suffer from statistics.

For this evaluation only the electron data sample is used<sup>(9)</sup>. The di-electron background simulated by GRAPE is normalised to the data sample by means of the side band method in the high di-electron mass region as described in more details in Sec. 9.2.3.2 and added to the elastic and proton dissociative MC simulations.

To evaluate all model parameters the proton dissociative and elastic MC simulation are reweighted on generator level quantities ( $t$ ,  $W$  and  $M_Y$ )<sup>(10)</sup>, until reconstructed tagged and non-tagged distributions as function of  $t_{\text{rec}}$  and  $W_{\text{rec}}$  show the best agreement between data and the combined (elastic, proton dissociative and background) MC simulation<sup>(11)</sup>. The quality of agreement is evaluated by using a  $\chi^2$  test to compare data with the combined MC simulation. The used  $\chi^2$  test to compare two equally binned histograms  $h$  and  $H$  is

$$\chi_H^2 \equiv \sum_{i=0}^{N_{\text{bins}}} \frac{(h_i - H_i)^2}{\sigma(h)_i^2 + \sigma(H)_i^2}, \quad (8.3)$$

whereas  $N_{\text{bins}}$  is the number of bins. The contents of bin  $i$  of the histograms are represented by  $h_i$  and  $H_i$ , while the errors in bin  $i$  are given as  $\sigma(h)_i$  and  $\sigma(H)_i$ .

The applied reweighting functions are motivated by the forward energy flow model described in Chapter 2. The used formula to reweight the proton dissociative MC simulation is

$$w_{\text{pdis}}(T, W, M) = N_{\text{pd}} \frac{\frac{e^{-2c_2 T}}{\left(1 + \frac{T}{c_1}\right)^4} \left(\frac{W}{M}\right)^{4(\varepsilon_{\text{pd}} - \alpha_{1,\text{pd}} T)} \left(\frac{M}{W_0}\right)^{2\varepsilon_M} \frac{1}{M^2}}{\left(1 + \frac{\tilde{b}_{\text{pd}} T}{\tilde{n}_{\text{pd}}}\right)^{-\tilde{n}_{\text{pd}}} \left(\frac{W}{W_0}\right)^{4\tilde{\varepsilon}_{\text{pd}}} \left(\frac{1}{M}\right)^{2(1+\tilde{\varepsilon})}} \quad (8.4)$$

and for the elastic process

$$w_{\text{elas}}(T, W) = N_{\text{elas}} \frac{\exp\left[-b_{\text{el}} + 4\alpha_{1,\text{el}} \log\left(\frac{W}{W_0}\right) T\right] \left(\frac{W}{W_0}\right)^{4\varepsilon_{\text{el}}}}{\exp\left(-\tilde{b}_{\text{el}} T\right) \left(\frac{W}{W_0}\right)^{4\tilde{\varepsilon}_{\text{el}}}} \quad (8.5)$$

with  $T \equiv |t^{\text{gen}}|$ ,  $W \equiv W_{\gamma p}^{\text{gen}}$  and  $M \equiv M_Y^{\text{gen}}$ .

The denominator in both equations represent the normalisation to the distribution actually used to generate the events in the MC simulations (see Sec. 4.1). The parameters used in DiffVM for generating events can be found in Table 4.1. The constant parameter  $W_0 = 90$  GeV

<sup>(9)</sup>The MC simulation description of the background in the muon data sample is not complete because the di-pion background, still present in data, is not simulated. For the  $ee$  data set the di-pion background is negligible due to the strong background rejection of the electron discriminator  $D_{\text{ele}}$ .

<sup>(10)</sup>A word about notation in this section: Generated quantities do not carry a subscript *gen*, but are blank. To ensure clear distinction to generated quantities, reconstructed variables are written with a subscript *rec*. The subscript  $\gamma p$  for  $W_{\gamma p}$  is dropped for readability.

<sup>(11)</sup>This procedure can be seen as an evaluation performed in the opposite direction of an unfolding strategy. In unfolding the true distribution is extracted from a measured distribution using realistic detector information for unsmearing. As pointed out in [273]: "... it is not necessary to unfold the measured distribution, in particular if the goal is to compare the result with the prediction of an existing theory". Here the goal is to compare on detector level, hence the simulation has to be folded by the detector simulation. In some sense this is easier than an unfolding procedure (the reasons can be found in Chapter 9). On the other side it carries its own problems, which are in this case mostly technical, due to the heavy data handling of the MC events which have to be processed for each point in the parameter space.

is only present for normalising the  $W$  and  $M_Y$  quantities and can be chosen arbitrarily, though the taken value is the most common, e.g. [29, 37].

The fit contains in total 8 free parameters:  $N_{\text{pd}}, N_{\text{elas}}, n_{\text{pd}}, \varepsilon_{\text{pd}}, \alpha_{1,\text{pd}}, \varepsilon_M, b_{\text{el}}$  and  $\varepsilon_{\text{el}}$ . The parameters  $N_{\text{pd}}$  and  $N_{\text{el}}$  contain all normalisation factors appearing in the actual cross section formulae (see Sec. 4.1), but incorporate also the statistics contained in the MC simulations, since no luminosity normalisation is applied. Their actual size is unimportant in the context of this fit. The parameter  $\alpha_{1,\text{el}}$  is fixed to  $0.164 \text{ GeV}^{-2}$ , as given in [29], because of poor sensitivity to this parameter in the fit<sup>(12)</sup>. A more detailed description of the other parameters can be found in Chapter 2.

## 8.2.2 Reconstructed distributions after determination of the optimal parameter set

Figure 8.3 shows the four reconstructed distributions contributing to the  $\chi^2$  used to determine the best parameter set, at the point of minimal  $\chi^2$ . The  $\chi^2$  is the sum of the  $\chi_H^2$ , as defined in Eq. (8.3), for each of the four contribution distributions. Sub figure (a) and (b) show the non-tagged and tagged distributions divided by the bin width as function of  $-t_{\text{rec}}$ . In sub figure (c) and (b) the non-tagged and tagged distributions as function of  $W_{\text{rec}}$  are given. The overall description is rather good and leads to a reasonable

$$\chi^2/\text{ndf} = 78.2/63 \simeq 1.2.$$

Figure 8.4 shows the tagging efficiencies as function of  $W_{\text{rec}}$  (a) and  $-t_{\text{rec}}$  (b), which are equally good described as the tagged and non-tagged distributions. The tagging fraction as function of  $W_{\text{rec}}$  for the combined MC and data sample is about 20% and flat over the whole range. The tagging efficiency for only the proton dissociative process is about 50%, which is satisfying for separation of the two processes  $ep \rightarrow J/\psi p$  and  $ep \rightarrow J/\psi Y$ . On the other side, the tagging efficiency is strongly depending on  $-t_{\text{rec}}$  and reaches its maximum of about 65% at large  $|t_{\text{rec}}|$ .

## 8.2.3 Discussion of fit result

Table 8.2 lists the fit parameter values including MINOS [274] errors. Though the values are interesting and worth being discussed, it is not claimed to be a measurement. Also do the parameter errors not include any systematic uncertainties. The goal of this evaluation and the applied reweighting are solely to have a better description especially of the  $M_Y$  distribution in order to get a reasonable description of the tagging efficiencies of the forward detectors.

A few remarks however can be made about the parameter values. The slope parameter  $b_{\text{el}}$  is rather large compared to  $4.630 \pm 0.060^{+0.043}_{-0.163}$  [29] and  $4.15 \pm 0.05^{+0.30}_{-0.18}$  [37]. A possible explanation could be the use of  $-p_{t,\psi,\text{gen}}^2$  instead of  $t_{\text{gen}}$ , which could lead to a larger  $b$  value.

<sup>(12)</sup>In a modified version of the fit two-dimensional distributions in  $(t_{\text{rec}}, W_{\text{rec}})$  are used for comparing data with the MC simulation. This improves sensitivity to  $\alpha_{1,\text{el}}$  and leads to a fit value of  $0.03 \pm 0.19 \text{ GeV}^{-2}$ , which is consistent with the used value, although the uncertainties are still large.

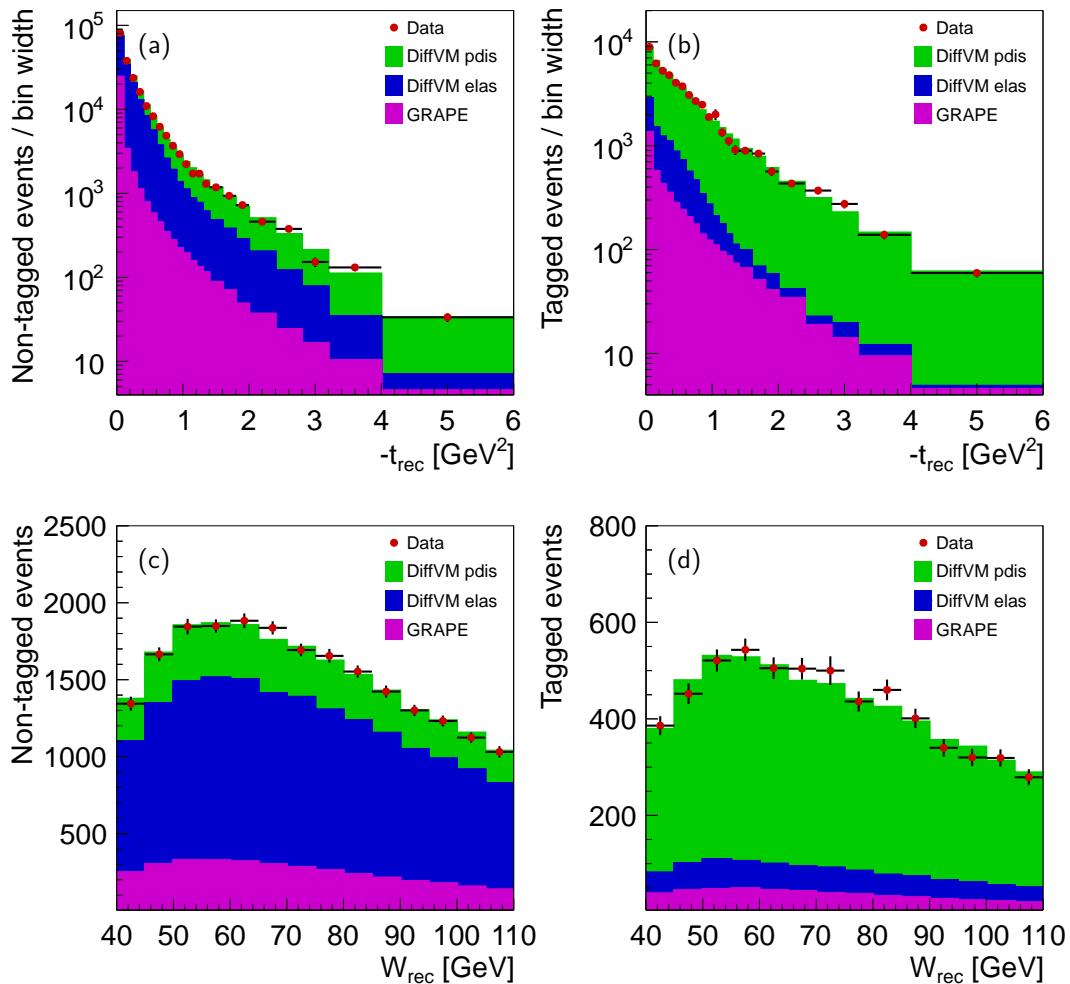


**Figure 8.3:** Distributions used for the forward energy flow parameter evaluation. Figure (a) and (b) show the non-tagged and tagged distributions divided by the bin width as function of  $-t_{\text{rec}}$ . In (c) and (d) the non-tagged and tagged distribution as function of  $W_{\text{rec}} \equiv W_{\gamma p}^{\text{rec}}$  are displayed. The red points represent data. The green, blue and violet histograms show the contributions from proton dissociative, elastic and QED background processes.

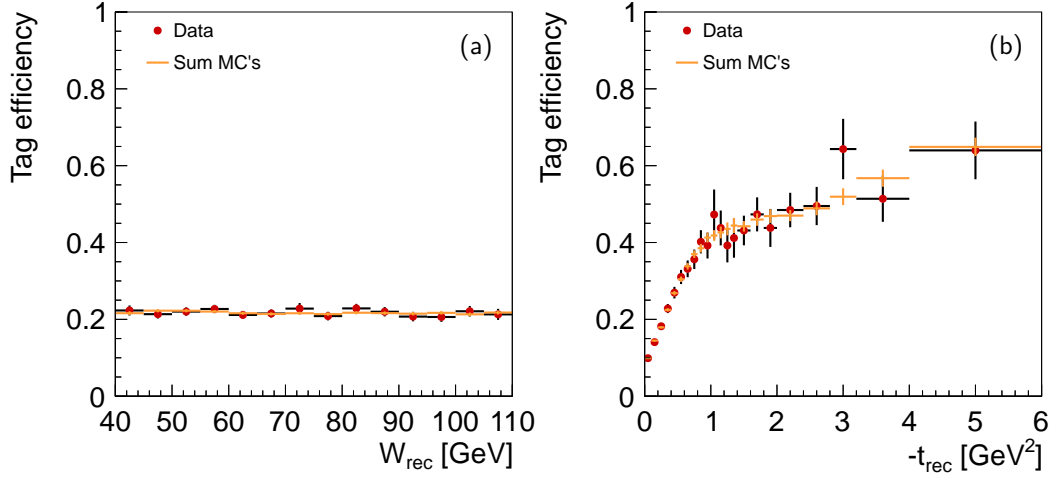


**Figure 8.4:** Tagging efficiencies as function of  $-t_{\text{rec}}$  (a) and  $W_{\text{rec}} \equiv W_{\gamma p}^{\text{rec}}$  (b). The red points represent data. The combination of the three MC simulations (DiffVM elastic and proton dissociative, and QED background) is given as orange histogram.

Parameter	Fit value
$b_{\text{el}}$	$5.25^{+0.19}_{-0.18}$
$\varepsilon_{\text{el}}$	$0.195^{+0.013}_{-0.014}$
$c_1$	$3.3^{+0.6}_{-0.4}$
$c_2$	$-0.47^{+0.13}_{-0.12}$
$\varepsilon_{\text{pd}}$	$0.21 \pm 0.03$
$\alpha_{1,\text{pd}}$	$0.10^{+0.03}_{-0.02}$
$\varepsilon_M$	$0.27 \pm 0.08$

**Table 8.2:** Parameter set from fit to tagged and non-tagged distributions.

For the proton dissociative case a comparison of the parameters  $c_1$  and  $c_2$  with published values for the *pure*<sup>(13)</sup>  $|t|$  spectrum is impossible since it was never measured.

The pomeron intercept ( $\alpha(0) = 1 + \varepsilon$ ) in the elastic case seems to be in agreement with  $1.224 \pm 0.010 \pm 0.012$  [29] and  $1.200 \pm 0.009^{+0.004}_{-0.010}$  [37]. For the proton dissociative case the intercept is in agreement with  $1.167 \pm 0.048 \pm 0.024$  [30], but far off from  $1.084 \pm 0.31^{+0.025}_{-0.018}$  [34]. Both measurement however only measure the proton dissociative cross section in the high  $|t|$  region with  $|t| > 2 \text{ GeV}^2$  where the elastic contribution is negligible.

By comparing the proton dissociative pomeron slope  $\alpha_1$  with values from the high  $|t|$  measurements  $-0.0135 \pm 0.0074 \pm 0.0051 \text{ GeV}^{-2}$  [30] and  $-0.014 \pm 0.007^{+0.004}_{-0.005} \text{ GeV}^{-2}$  [34], a clear disagreement is visible. The phase space in  $M_Y$  of  $M_Y < 30 \text{ GeV}$  in both measurements differs to the definition used in this evaluation, though it is doubtful that this is the reason for the deviation. In the end no satisfying explanation can be given here and this issue must remain unanswered.

The obtained value of  $\varepsilon_M$  is interesting. It appears to be larger than the well known value of 0.0808 from the Donnachie and Landshoff (DL) fits [110,275] to hadron-hadron data (see also Sec. 2.1.8). But as discussed in Sec. 2.1.10, the parameter value of DL is only an effective power and more recent analysis taking into account screening effects tend to obtain larger values. An  $\varepsilon_M$  value as extracted from the fit seems therefore plausible.

A check for sensitivity to a pomeron-pomeron-reggeon, PPR, exchange was performed, by adding an additional term to the proton dissociative weighting function, reflecting a PPR contribution. It was found that the additional term is consistent with 0. Hence the parameter value of  $\varepsilon_M$  must be understood as effective value incorporating the dominant pomeron-pomeron-pomeron and subleading PPR contribution.

The evaluated set of parameters is used for reweighting the elastic and proton dissociative MC simulations in all following distributions.

---

<sup>(13)</sup>Pure meaning in this case that usually the differential cross sections are measured integrated over  $M_Y$ , which of course would give different parameter values.



## Cross section determination with $t$ and $W_{\gamma p}$ unfolding

The goal of this analysis is to measure differential cross sections for elastic and proton dissociative  $J/\psi$  production as function of the squared transfer momentum at the proton vertex  $t$  and as function of the photon proton centre of mass energy  $W_{\gamma p}$ . The common approach followed in previous analyses within H1 is to define for each analysis bin a two-by-two matrix filled with information from reconstruction level about the proton remnant and by inversion solve the problem of separation of elastic and proton dissociative processes (see e.g. [142, 143, 210, 276]). This procedure however neglects the treatment of migrations. A further neglect of previous analyses was to determine cross sections not as function of  $t$  but as function of  $-p_{t,J/\psi}^2$  (see for instance [29, 37]). These shortcomings are addressed in this analysis by a combined technique involving an unfolding procedure, which is explained in this chapter.

It was seen in Sec. 7.3 that the resolutions of  $t$  and  $W_{\gamma p}$  for which cross section are intended to be evaluated can be large, producing inevitably large migrations between bins on reconstruction level. Even if the migrations are small, the question remains to quantify the effect. To account for this problem, an unfolding procedure is used. A general overview of the concepts involved within unfolding is given in the first section. It is not claimed, however, to be complete, since the subject itself is almost limitless, but describes the ideas relevant to this analysis. The second section assembles the elements for a proper unfolding procedure for separating elastic and proton dissociative processes. It is followed by Sec. 9.3 discussing how the unfolding output is transformed into differential cross sections.

At this stage cross sections could be presented but only with statistical errors, which is only half the battle because the systematic uncertainties are missing. Hence Sec. 9.4 presents all the systematic sources, their treatment and the resulting effects on the unfolding output. The subsequent section presents control plots and explains their construction.

## 9.1 Introduction to unfolding

A distribution  $f(x)$ , for reason of distinction called *true* distribution, intended to be determined, be only indirectly accessible by a reconstructed distribution  $g(y)$ . Detector effects like acceptance restrictions, efficiencies and migration between bins, produced by broad reconstruction resolutions of quantities, affect these reconstructed quantities. The relation between the measured distribution  $g(y)$  and the underlying true distribution  $f(x)$  can be expressed by a Fredholm integral equation of the first kind:

$$g(y) = \int dx A(x, y) f(x). \quad (9.1)$$

The kernel  $A(x, y)$ , within physical applications usually called *response function*, does incorporate and quantify the mentioned distortion effects. If no acceptance and efficiency effects are present, then the kernel satisfies the requirement<sup>(1)</sup>  $\int dy A(x, y) = 1, \forall x$ .

The task of unfolding is now to extract the true distribution  $f(x)$  for the known function  $g(y)$  and kernel  $A(x, y)$ , which is in general, for any kernel, an ill-posed problem<sup>(2)</sup> [278].

In discrete notation the Eq. 9.1 can be approximated as<sup>(3)</sup>

$$y_i = A_{ij} x_j, \quad (9.2)$$

whereas  $A_{ij}$  is called response matrix, which is in high energy physics usually constructed from MC events passed through a realistic detector simulation. The variable  $y_i$  represents the number of reconstructed events in the chosen binning. The number of true, i.e. efficiency and acceptance corrected, events is referred to as  $x_i$ .

If the resolution of the quantity in focus is narrow, the migration effects are small, which is reflected in small off-diagonal entries in the response matrix  $A_{ij}$ . In this situation the use of the simple approach of an approximated, diagonal response matrix  $A_{ij} = \varepsilon_i \delta_{ij}$  can be justified. The true distribution is then calculated as  $x_i = y_i / \varepsilon_i$  with  $\varepsilon_i$  taking the role of the reconstruction efficiency. However neglecting these off-diagonal entries produce in general a wrong shape and a wrong error estimate, which usually is not quantified [279].

A more complete approach is to work with the full response matrix. In case of an  $n \times n$  matrix, an inversion in the form

$$x_i = (A^{-1})_{ij} y_j \quad (9.3)$$

could be thought of. This can produce large oscillation in  $x_i$ , caused by statistical fluctuation in  $y_j$ , see also [280, 281]. Although neither result nor uncertainty estimate is mathematically wrong, the result looks unphysical [282].

<sup>(1)</sup>With the assumption that no migration in or out of the phase space exists.

<sup>(2)</sup>The subsequent text is focusing on experimental aspects only and will leave out – with the exception of this note – the mathematical finesses. This descriptions follow the explanations given in [277, 278] and are repeated, because it provides a clearer understanding of the text below.

Let  $g_n \equiv \int dx A(x, y) \sin nx \rightarrow 0$  for  $n \rightarrow \infty$  (Riemann-Lebesgue Lemma) be added to  $g(y)$  of Eq. (9.1), which means that for a large  $n$  the change in data  $g$  can be small but the corresponding change in the true distribution  $f$  might be much larger. This is the origin why this kind of problems are called ill-posed.

<sup>(3)</sup>In general expressions for physical purposes often a background contribution is added, the equation takes then the form  $y_i = A_{ij} x_j + b_i$ , with  $b_i$  representing the background. In this analysis the background signal separation is performed separately from the unfolding process, therefore this general introduction assumes no background contribution  $b_i$ .

The recommendation found in literature is not to use the same amount of reconstructed and generated bins. For example as stated in [283–285], by using  $n = m$ , “... the numerical methods contain features that effectively render the inverse problem less ill-posed than it actually is, thus yielding unrealistically optimistic results.” Better is to work with a response matrix  $A_{ij}$  with  $i = 1, \dots, n$  and  $j = 1, \dots, m$  where  $n \leq m$  is fulfilled, or even better  $2n \leq m$ . Following this recommendation,  $m = 2n$  is always taken in this analysis.

In order to solve the overdetermined problem given in Eq. (9.2) with an  $n \times m$  response matrix  $A$ , a  $\chi^2$  minimisation can be used. The standard  $\chi^2$  expression [282, 286–288] takes the form

$$\chi^2 = (y - Ax)^\top V_y^{-1} (y - Ax) \quad (9.4)$$

with  $V_y$  the covariance matrix of the measured quantity  $y$ . Due to the linear nature of the problem, an analytical solution exists:

$$x = (A^\top V_y^{-1} A)^{-1} A^\top V_y^{-1} y. \quad (9.5)$$

Unfortunately also this solution often suffers from large oscillation as the simple matrix inversion in Eq. (9.3). To cope with this issue an additional term is added to Eq. (9.4), called *regularisation*, ensuring smooth results. Because unfolding has a long history, a wide variety of different ideas of regularisation have been proposed over time (see [282, 289, 290] for methods suggested for particle physics purposes).

The software package used in this analysis for the unfolding is *TUnfold* [291], which uses a Tikhonov type regularisation, independently proposed [282] by Phillips [277] and Tikhonov. The  $\chi^2$  expression including the additional term takes the form<sup>(4)</sup>

$$\chi^2 = (y - Ax)_i (V_y^{-1})_{ij} (y - Ax)_j + \tau^2 \|Lx\|_2^2 \quad (9.6)$$

with the norm operator  $\|a\|_2 = \sqrt{a^\top a}$ . The matrix  $L$  describes the introduced *connection* between the  $x$  bins. Due to a physical process a certain smoothness of the  $x$  distribution can be assumed. Usually  $L$  takes the form of a discrete derivative first or second order. In this analysis an  $L$  is chosen for regularising the curvature of  $x$ , i.e.  $L$  is the discrete second derivative.

The solution to the  $\chi^2$  defined in Eq. (9.6) incorporating also the regularisation is

$$x = \underbrace{(A^\top V_y^{-1} A + \tau^2 L^2)^{-1}}_{\equiv B} A^\top V_y^{-1} y. \quad (9.7)$$

The parameter  $\tau$  acts as the strength of the regularisation. It is desirable to have a small  $\tau$  parameter, otherwise the result becomes largely biased. On the other hand it should be strong enough to damp large oscillations. Finding a suitable  $\tau$  value for a given problem is “the most difficult task” [277] within the unfolding procedure. To cope with the situation several methods for finding an optimal  $\tau$  are proposed in literature, for an overview consult [281, 282].

TUnfold offers an automatic mode for finding the optimal  $\tau$  using the *L-curve* method [292]. In this analysis a different method is used, following the recommendation given in [281]. The

---

<sup>(4)</sup>Least square methods in general do not conserve the total number of events [282]. TUnfold introduces an option for area preservation by adding a penalty term  $[\sum_i y_i - \sum_i (Ax)_i]^2$  to the  $\chi^2$  expression. For this analysis no difference was visible with or without the option turned on.

method chooses  $\tau$  to be at the point with smallest *averaged global correlation*

$$\bar{\rho} = \frac{1}{n} \sum_{k=1}^{k \leq n} \rho_k, \quad (9.8)$$

with  $\rho_k$  being the *global correlation coefficient* [287], defined as

$$\rho_k = \sqrt{1 - [(V_x)_{kk} \cdot (V_x^{-1})_{kk}]^{-1}}, \quad (9.9)$$

whereas  $V_x$  denotes the covariance matrix of the true unfolding output vector  $x$ , calculated by standard error propagation, i.e.  $V_x = BV_y B^\top$  [291].

## 9.2 Collection of unfolding constituents

The last section summarised the unfolding concepts as far as they are used in this analysis from a general point of view. This section now concentrates on collecting all ingredients required to perform an unfolding procedure within this analysis, namely the response matrix, the measured data input vector and the regularisation matrix. But before discussing this topics a short description of the chosen binning procedure is given.

### 9.2.1 Binning

#### 9.2.1.1 Binning on generator level

The binning for the true distribution  $x$  is mainly driven by requirements of the regularisation condition. The curvature regularisation as implemented in TUnfold smooths the second derivative of the bin integrated cross sections. The generated binning must be chosen accordingly, meaning that the difference in contained events of adjacent bins must be constant. This is illustrated in Fig. 9.1 for the example of the chosen proton dissociative binning in the variable  $-t$  for the high energy data period sample. Plot (a) shows the generated differential distribution as blue histogram. The bins are indicated by the red vertical lines. In the right plot (b) the integrated number of events per bin normalised to the total number of events in the sample is given as function of the bin number. The chosen linear behaviour is clearly visible.

Depending on the general behaviour of the differential distribution for which the binning is evaluated, the slope of the integral fraction is chosen accordingly. For the  $W_{\gamma p}$  distribution binning a constant slope is used.

The binnings for the true distributions, evaluated with the described procedure, are given in Appendix D.

#### 9.2.1.2 Binning on reconstruction level

Following the discussed recommendation in Sec. 9.1 to use more bins for the reconstructed unfolding input vector  $y$ , than for the true vector  $x$ , this analysis uses for all distributions two times more bins in  $y$  than in  $x$ . In order to be independent of the actual data distribution

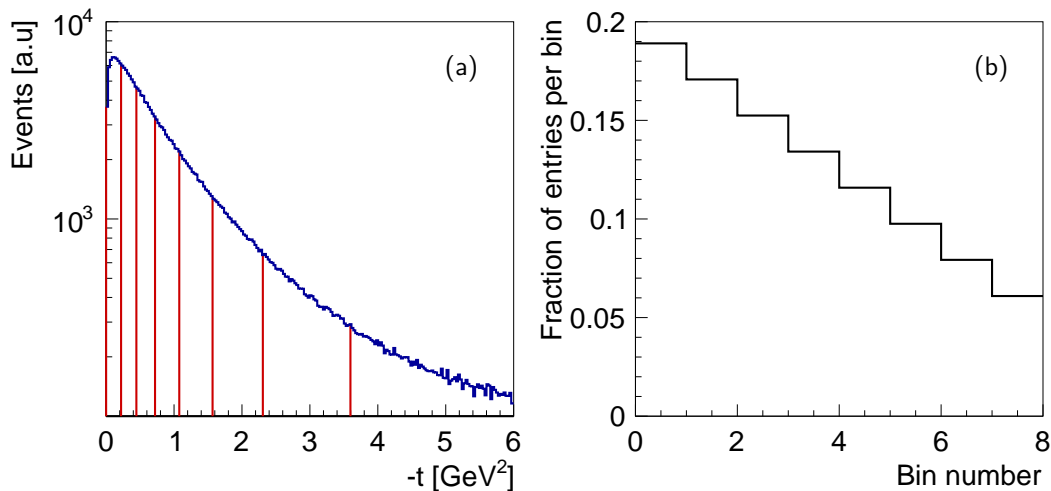


**Figure 9.1:** Illustration of the binning determination for the true vector  $x$ . Plot (a) shows as blue histogram the generated differential distribution as function of  $-t$  for the high energy data sample in the  $J/\psi \rightarrow ee$  decay channel for the proton dissociative MC simulation. The evaluated bin edges for the true vector  $x$  are indicated by the red vertical lines. Plot (b) shows the integrated number of events per bin normalised to the total number of events in the sample as function of the bin number.

and not introducing any artefacts, each generated bin is split centrally to create the binning on reconstruction level.

## 9.2.2 Response matrix

The response matrix must not only incorporate resolution, migration and efficiency effects but also be defined such that the contributions from elastic and proton dissociative  $J/\psi$  production can be separated. For the cross section determination for each data period, decay channel and variable a separate response matrix is calculated from MC simulated events.

In the following subsections a description of the response matrix definitions for unfolding in the variables  $t$  and  $W_{\gamma p}$  is given. The structure of the response matrices used for unfolding cross sections as function of either  $t$  or  $W_{\gamma p}$  for the two decay channel samples are identical. The response matrices differ however in the used MC simulation from which they are computed. The response matrix structure for the different data periods are similar, they only vary in the number of used generated and reconstructed bins.

### 9.2.2.1 Response matrix definition for unfolding the differential cross sections in $|t|$

An illustration of the response matrix structure used to obtain differential cross sections in  $t$  is shown in Fig. 9.2. Response matrices in this text are always given with abscissae representing the generated and the ordinates showing the reconstructed quantities.

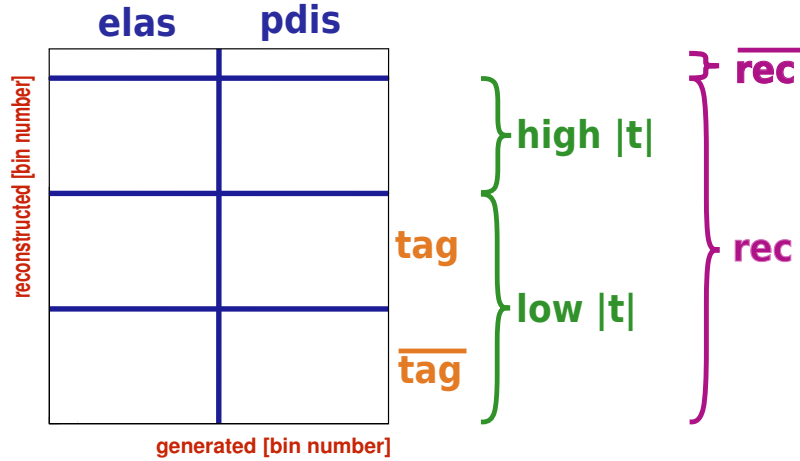


**Figure 9.2:** Illustration of the response matrix structure used for unfolding to obtain the differential cross section as function of  $|t|$ .

The structure of the response matrices are constructed by two blocks located next to each other on the generated axis, representing the contribution from the elastic (elas) and the proton dissociative (pdis) process. The true vector  $x$  will therefore be composed from an elastic and proton dissociative part, i.e.  $x = \{x^{\text{el}}, x^{\text{pd}}\}$ . In this setup there is no need for additional columns, for example for background processes.

On reconstruction level the sample from each process is split into four blocks of which each has several bins. The not reconstructed and not selected DiffVM MC events are filled in the top row marked as  $\overline{\text{rec}}$  and are used for a proper normalisation of the response matrix. All other, reconstructed events are contained in the part labeled as  $\text{rec}$ . They are separated into a low and high  $|t|$  region. Because the elastic cross section is steeply falling as function of  $|t|$ , a transition point  $T_{\text{low-high}}$  above  $1.2 \text{ GeV}^2$  ensures only a negligible small contamination (below per-mill level) from elastic process in the high  $|t|$  region, which therefore only contains proton dissociative events. The actual position of the transition points are chosen at the bin edges of the generated  $t$  binnings and therefore rely on the binning construction as described in Sec. 9.2.1. For the high energy data period  $T_{\text{low-high}} = 1.50 \text{ GeV}^2$  and for the low energy data period  $T_{\text{low-high}} = 2.12 \text{ GeV}^2$  are taken. The low  $|t|$  sample is further split into a (proton dissociative) tagged and non-tagged sample, indicated with  $\text{tag}$  and  $\overline{\text{tag}}$ , respectively, in the illustration. For this separation the definition of the experimental tagging as discussed in Sec. 8.1.4 is used. All three reconstructed blocks are then split into bins of  $|t|$  as described in Sec 9.2.1.2.

### 9.2.2.2 Response matrix definition for unfolding the cross sections in $W_{\gamma p}$

The response matrices for the cross section determination as function of  $W_{\gamma p}$  have the same general form as the ones used for the cross section determination as function of  $|t|$ . An illustration is displayed in Fig.9.3. Two blocks account for the elastic and proton dissociative process similar to the response matrix setup given in the last section. They are filled with DiffVM  $J/\psi$  elastic and proton dissociative signal MC events.

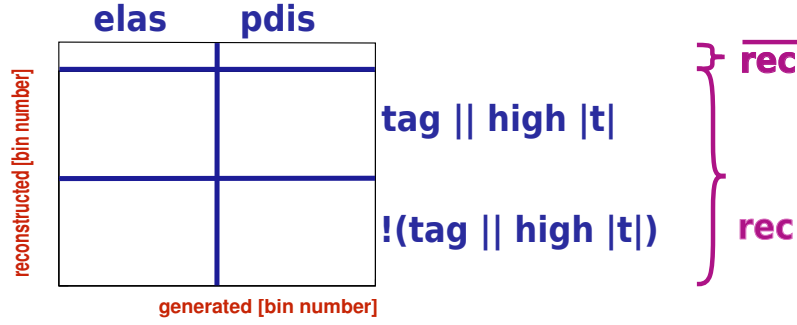


**Figure 9.3:** Illustration of the response matrix structure used for unfolding to obtain the cross section as function of  $W_{\gamma p}$ .

The row at the very top, labeled with  $\overline{rec}$ , can also be found for response matrices used to create cross sections as function of  $|t|$ , it contains all non-reconstructed events. It follows the block filled with reconstructed MC events, split into two parts. The condition for splitting the sample of reconstructed events requires either a proton dissociative tag (as described in Sec. 8.1.4) or a high  $|t|$  tag. Events with a reconstructed  $|t|$  above a transition point  $T_{\text{low-high}}$  are labeled as *high*  $|t|$  tag. The transition point  $T_{\text{low-high}}$  between high and low  $|t|$  region is chosen identically as described in Sec. 9.2.2.1<sup>(5)</sup>.

The term  $tag_W$  will be used to refer to the combined tag condition on reconstruction level as defined above. Written in a formula it takes the form

$$tag_W \equiv tag \ || \ high \ |t|. \quad (9.10)$$

### 9.2.3 Determination of the reconstructed input vectors $y$

The subject of this subsection is the second piece necessary for an unfolding procedure: the determination of the data vectors  $y_{ee}$  and  $y_{\mu\mu}$  containing the number of  $J/\psi$  events in the electron-electron and muon-muon data sets, evaluated in the chosen  $t$  and  $W_{\gamma p}$  binning on reconstruction level.

The determination of the number of  $J/\psi$  events must deal with background, still contained in the data sample obtained with the selection discussed in Chapter 6. As the background is non-resonant, it can best be seen in a di-lepton mass distribution plot. The di-lepton mass is reconstructed from the two tracks as discussed in Sec. 6.1.3. Figure 9.4 shows in the left column the di-electron,  $m_{ee}$ , distributions in the  $J/\psi \rightarrow ee$  decay channel for the high (a) and low energy (c) data periods. The corresponding plots for the  $J/\psi \rightarrow \mu\mu$  decay channel as function  $m_{\mu\mu}$  are given in the right column.

The di-lepton mass distributions for the two decay channels show a different general behaviour. In the  $J/\psi \rightarrow ee$  decay channel a large tail is visible, caused by final state QED radiation of the electrons and positrons. The low energy radiated photons are not well measurable in the H1 detector and are therefore not reconstructed. The missing momentum information

<sup>(5)</sup>As stated, the transition point  $T_{\text{low-high}}$  is chosen according to the evaluated generated binning in  $|t|$ . There is no general restriction where to set it in case of unfolding to determine the cross section as function of  $W_{\gamma p}$ . It seems however natural to choose the same transition point as is used in the case of unfolding to extract the differential cross section in  $|t|$ .

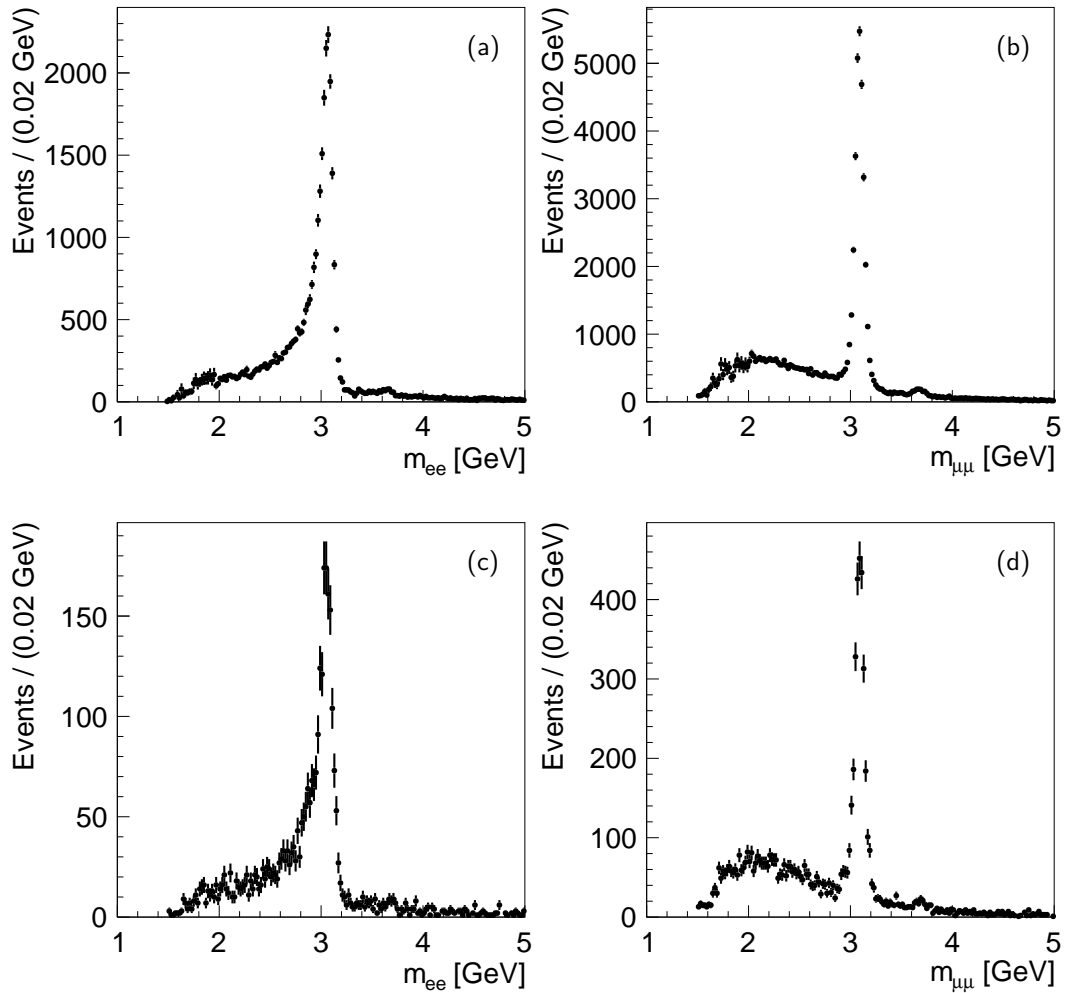


**Figure 9.4:** Di-lepton mass distributions for the high energy data period in  $J/\psi \rightarrow ee$  (a) and  $J/\psi \rightarrow \mu\mu$  (b) decay channel and for the low energy data period in  $J/\psi \rightarrow ee$  (c) and  $J/\psi \rightarrow \mu\mu$  (d) decay channel.

of these photons decreases the track momentum resolution of the electrons and positrons, ultimately causing a smeared invariant mass peak. The  $J/\psi \rightarrow \mu\mu$  decay channel, due to the higher mass of the muons, is almost not affected by the QED radiation, resulting in a higher track momentum resolution and hence narrower mass peaks.

The number of the  $J/\psi$  signal events in case of the  $J/\psi \rightarrow \mu\mu$  sample are obtained by simultaneous signal and background fits to the di-muon mass distributions. For the  $J/\psi \rightarrow ee$  decay channel such a fit is difficult, due to the radiative tail. Therefore a different procedure based on background subtraction is applied. Details are discussed below.

The number of  $J/\psi$  signal events are evaluated in bins of  $t$  and  $W_{\gamma p}$  in order to determine differential cross sections. For the separation of elastic and proton dissociative process a further split of the sample into tagged and non-tagged events is done (see Sec. 9.2.2). The steps of extracting the numbers of  $J/\psi$  signal events, the results and uncertainties are described in the following two subsections.

### 9.2.3.1 The muon channel

This subsection describes the determination of the number of  $J/\psi$  signal events from the di-muon mass distributions. First the method is described, then the results are presented and in the last part the evaluation of the systematic uncertainties is discussed.

#### 9.2.3.1.1 Fit model

The number of  $J/\psi$  events in the  $J/\psi \rightarrow \mu\mu$  decay channel are determined from combined fits of signal and background to the di-muon mass distributions. For the signal a Student's  $t$  function and for the background an exponential distribution are chosen. The fit model has the form

$$f(m_{\mu\mu}; \mu, \sigma, n, c) = N_{\text{sig}} p_{\text{sig}}(m_{\mu\mu}; \mu, \sigma, n) + N_{\text{BG}} p_{\text{BG}}(m_{\mu\mu}; c) \quad (9.11)$$

with free shape parameters  $\mu$ ,  $\sigma$ ,  $n$  and  $c$ . The number of signal and background events are represented by  $N_{\text{sig}}$  and  $N_{\text{BG}}$ , respectively. The probability density functions (pdf) are defined as

$$p_{\text{sig}}(m) = n_{\text{sig}} \left( 1 + \frac{t^2}{n} \right)^{-0.5(n+1)}, \quad t = (m - \mu)/\sigma, \quad n > 0 \quad \text{and} \quad (9.12)$$

$$p_{\text{BG}}(m) = n_{\text{BG}} e^{-c \cdot m}. \quad (9.13)$$

The factors  $n_{\text{sig}}$  and  $n_{\text{BG}}$  are chosen, such that the densities are normalised, i.e.

$$\int dm p(m) = 1$$

for  $p = p_{\text{sig}}$  and  $p = p_{\text{BG}}$ .

## 9.2.3.1.2 Data fits

The combined signal and background fits are performed using an extended binned maximum likelihood minimisation [286] using the *RooFit* [293] software package. It was tested and seen that no significant difference of the result to an unbinned extended likelihood fit exists. For computing time performance reason the binned version is chosen.

The di-muon mass distribution fits in bins of  $|t|$  for the tagged, non-tagged and high  $|t|$  sample and in bins of  $W_{\gamma p}$  for the  $\text{tag}_W$  [definition given in Eq. (9.10)] and  $\overline{\text{tag}_W}$  sample can be found in Appendix B.1. In general the data description by the fits are rather good as can be seen in the  $\chi^2/\text{ndf}$  values from the  $\chi^2$  goodness of fit test, given for the different samples in the tables B.1 and B.2.

## 9.2.3.1.3 Bias study

A fit – in general – can always produce biased results. To ensure a correct estimate of the true parameter values, the fit procedure should be tested for a possible bias. For this purpose a toy MC study is performed and discussed in the following.

The idea behind a toy study is to create realistic replicas similar to data. Then apply the same procedure, as was applied to the data sample, to each replica in order to obtain for each of them the same information as in the case of data. In the end, a set of information from replicas is available and ready for additional analysis, which otherwise would not be possible, since only one version of the information is present, the one from the real data.

Here replicas of the di-muon mass distributions are created. Each replica is then fitted by the same model [Eq. (9.11)] as used for the data di-muon mass distribution fits and the number of signal  $J/\psi$  events for each replica is extracted. Allowing then to perform on statistical basis an analysis of a possible bias.

The replica di-muon mass distributions are generated from a pdf model  $p_{\text{toy}}^{\text{gen}}(m)$ , whereas for simplicity here  $m \equiv m_{\mu\mu}$  is used. The model itself is not given as an analytical function but constructed from high statistics histograms of *real* signal and background MC samples. In this context *real* refers to MC events produced by DiffVM for the signal and GRAPE<sup>(6)</sup> for the background contribution, which were processed by the full H1 reconstruction software. The term *real* is used in contrast the to toy MC simulation to distinguish both sets and reduce confusion.

The  $p_{\text{toy}}^{\text{gen}}(m)$  model is defined as

$$p_{\text{toy}}^{\text{gen}}(m) = f k_{\text{sig}}(m) + (1 - f) k_{\text{BG}}(m), \quad (9.14)$$

with  $k_{\text{sig}}(m)$  and  $k_{\text{BG}}(m)$  representing the signal and background pdf's. They are obtained by interpolating<sup>(7)</sup> the di-muon mass distributions of the high statistics real signal and

<sup>(6)</sup>The data sample contains besides the di-muon events also a small contribution of di-pion events. The GRAPE generator produces only di-muon MC events, hence the replicas do not include the di-pion background contribution. This however is not a problem, since the bias study has to evaluate the quality of estimating fit parameters and not how good the MC simulation describes the data. As long as the shape of the di-muon mass distribution from GRAPE resembles the true background shape, the bias study can be performed. The number of events generated for the background contribution is discussed below and is not taken from the simulation.

<sup>(7)</sup>Different orders of the interpolating polynomials were tried without seeing a significant difference on the obtained bias.

background MC simulations. The final model  $p_{\text{toy}}^{\text{gen}}(m)$  then serves as shape template from which toy histograms, are dived by means of a random number generator. These histograms serve as the replicas for the bias study.

The contribution of the signal and background pdf to the final model is given by the fraction  $f$ . Because the actual value of  $f$  is unknown, it is taken from the data fit, but is varied within  $2 \cdot \Delta f$  to minimise the influence from the data input. The  $\Delta f$  corresponds to the size of the error on the number of signal events from the data fit. Expressed in formulae it can be written as

$$f_c = \frac{N_{\text{sig}}^{\text{data}}}{N_{\text{sig}}^{\text{data}} + N_{\text{BG}}^{\text{data}}} \quad \text{and} \quad \Delta f = \frac{\Delta N_{\text{sig}}^{\text{data}}}{N_{\text{sig}}^{\text{data}} + N_{\text{BG}}^{\text{data}}}, \quad (9.15)$$

with  $f_c$  meaning the central  $f$ , whereas  $N_{\text{sig}}^{\text{data}} \pm \Delta N_{\text{sig}}^{\text{data}}$  and  $N_{\text{BG}}^{\text{data}}$  are the number (and error) of the  $J/\psi$  and background events from the data fit.

For each reconstructed  $|t|$  and  $W_{\gamma p}$  bin 750 replicas are dived according to the pdf model  $p_{\text{toy}}^{\text{gen}}(m)$  for five different fractions of  $f$  ( $f_c$ ,  $f_c \pm \Delta f$  and  $f_c \pm 2\Delta f$ ). Each generated toy histogram contains the same statistics as the corresponding data histogram in the same  $|t|$  or  $W_{\gamma p}$  bin.

In a second step, all replicas are fitted with the same fit function as is used to fit the data mass distributions [see Eq. (9.11)] and the number of signal events  $N_{\text{sig}}^{\text{fit}}$  is extracted.

Then for each  $|t|$  and  $W_{\gamma p}$  bin and each fraction  $f$  the relative difference of fitted signal events,  $N_{\text{sig}}^{\text{fit}}$ , to generated events<sup>(8)</sup>,  $N_{\text{sig}}^{\text{gen}}$ , for the 750 toy MC simulations are plotted. Figure 9.5 shows an example of such a bias distribution, which is taken from the first  $W_{\gamma p}$  bin in the tag<sub>W</sub> sample for fraction  $f = f_c$ . These bias distributions are then fitted with a Gaussian

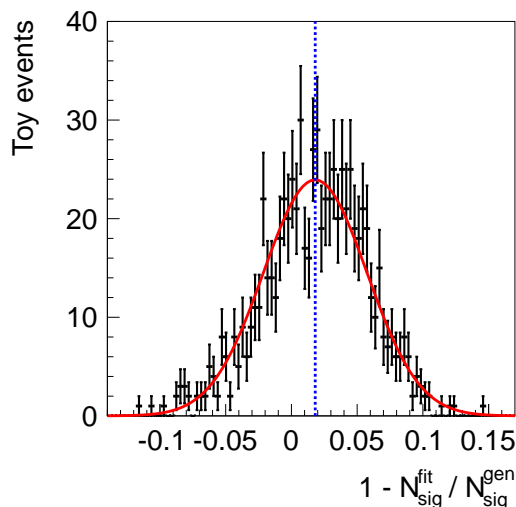


**Figure 9.5:** Example of bias distribution obtained from generating and fitting of 750 toy MC simulations. The red line indicates a Gaussian fit to determine the mean of the relative bias.

<sup>(8)</sup>The mass distribution fits are extended likelihood fits, therefore they contain an additional Poisson factor for the number of events (see [286]). To account for this on toy generating level, the number of events are also Poisson distributed with the mean taken from the number of events in data. The comparison of generated with fitted number of signal events in each toy is done using the actual values in each histogram.

as indicated in Fig. 9.5 by the red line. The mean of the fit, illustrated by the left vertical dashed blue line, is used as relative bias.

For each bin the relative bias is only weakly depending on the fraction  $f$ . Therefore in the following only the central fraction  $f_c$  is further considered.

Figure 9.6 gives a summary of the estimated bias for the  $\overline{\text{tag}_W}$  (a) and  $\text{tag}_W$  (b) sample in bins of  $W_{\gamma p}$  and plots (c) – (d) for bins of  $|t|$  for non-tagged, tagged and high  $|t|$  sample, respectively. In general the biases are small and the variation is centred around 0. Only for the low  $W_{\gamma p}$  bins in the  $\text{tag}_W$  sample it reaches a level of about  $-9\%$ <sup>(9)</sup>. However the bias is still in the order of the statistical error from the data fits.

Performing the same study with replaced Student’s  $t$  signal distribution in Eq. (9.12) by a Gaussian function, shows a common underestimation of the number of  $J/\psi$  signal events extracted from the fit. However, especially where the study shows large biases for the Students’  $t$  signal function, the Gaussian alternative is performing better. The overall picture still favours the Students’  $t$  distribution, which is the reason for its use.

The evaluated biases on the fit procedure to determine the number of  $J/\psi$  signal events are not corrected in the analysis but taken into account as source of systematic uncertainty. Its treatment will be discussed later.

### 9.2.3.2 The electron channel

The extraction of the number of  $J/\psi$  events in the  $J/\psi \rightarrow ee$  decay channel is more challenging due to the large radiative tails in the di-electron mass distribution plots. The same approach of a combined signal and background fit, as done in the  $J/\psi \rightarrow \mu\mu$  channel, was tried, but no stable fitting procedure could be established, which would not lead to large biases. Therefore a different ansatz is chosen.

In data the di-pion background is negligibly small due to the good rejection of pions in the electron identification. The remaining background is therefore the Bethe-Heitler type processes (see Sec. 4.2), simulated by the GRAPE MC generator. The uncertainty on the calculation used by GRAPE is about  $3\%$ <sup>(10)</sup>. Figure 9.7(a) shows the di-electron mass distribution in data for the high energy data period and the GRAPE background MC simulation, normalised to the data luminosity. A statistical subtraction of the background from data using the GRAPE MC samples results in  $J/\psi$  peaks only, as illustrated in Fig. 9.7(b). After the background subtraction the remaining events are counted within a window of  $m_{ee} = 2.3 - 3.3 \text{ GeV}$  around the nominal  $J/\psi$  mass, represented as orange area in Fig. 9.7(b), to determine the number of  $J/\psi$  signal events. The additional, small inefficiency, due to the counting window, is corrected by using the MC simulation and reduces the uncertainties introduced by the large radiative tail.

The di-electron mass distributions as simulated by the GRAPE MC generator are mostly depending on QED calculation, which are well known. However to further adapt the GRAPE

<sup>(9)</sup>It could be shown that the large bias in these two bins is reduced to a couple of percent, if the statistics in the di-muon mass distribution replicas is artificially increased. I.e. the estimator of the number of signal events is asymptotically almost unbiased. (This however may not be a surprise since as stated in [286] “. . . they [maximum likelihood estimators] are, in general, biased. This is not mentioned every often, partly because the bias becomes small as the sample size gets reasonably large”.)

<sup>(10)</sup>As stated in [294] the uncertainty on the calculations implemented in GRAPE for lepton pair production is about  $3\%$ . In [295] the contribution from elastic process is given as less than  $1\%$  and for quasi-elastic and deep inelastic scattering, due to uncertainty on the proton structure function, less than  $5\%$ .

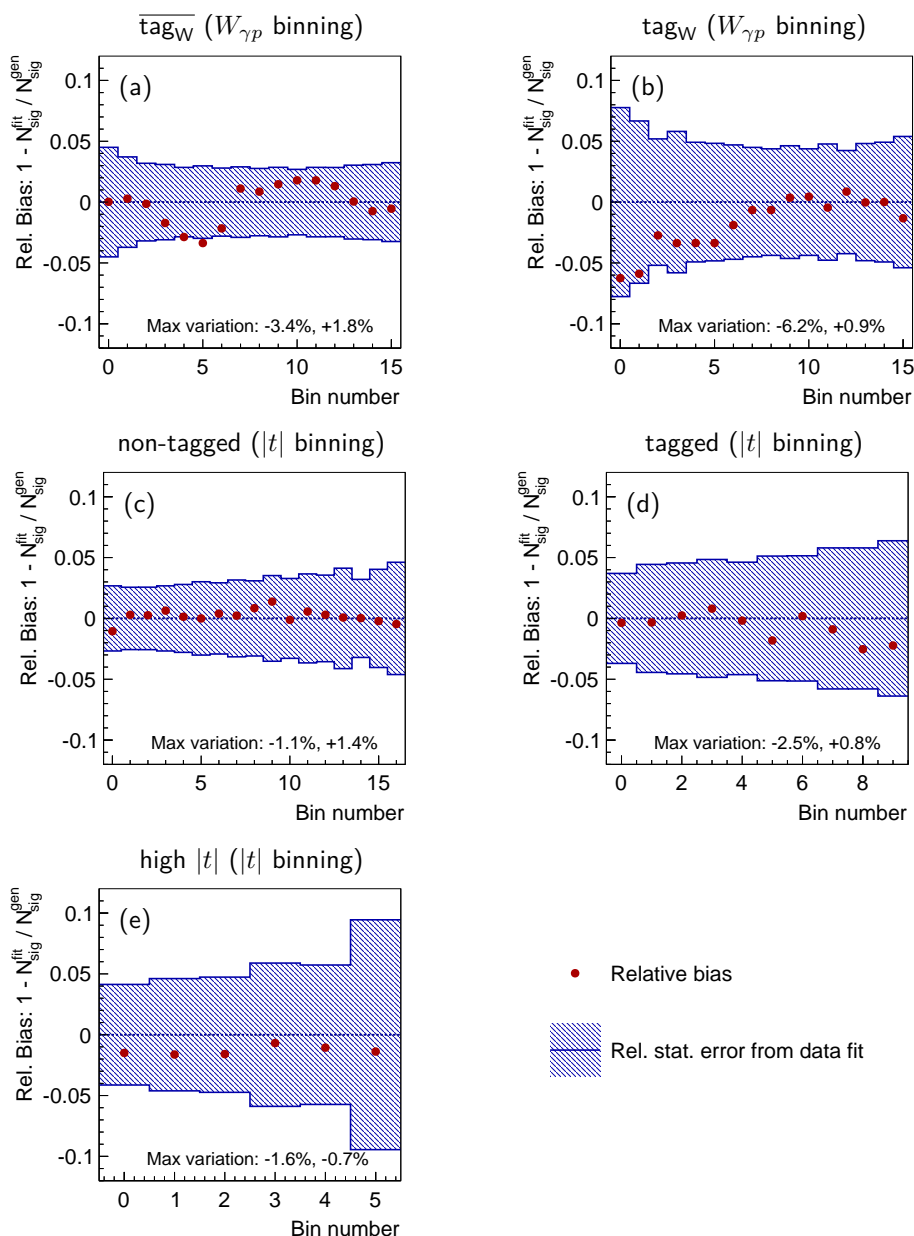


**Figure 9.6:** Summary plots of toy studies to evaluate the relative bias of fits to extract the number of  $J/\psi$  events. Red points represent the evaluated relative bias. The blue hatched area indicates the relative statistical uncertainty from the data fits. The Plot (a) and (b) show the relative bias as function of the reconstructed bin numbers in  $W_{\gamma p}$  for the  $\overline{\text{tag}}_W$  and  $\text{tag}_W$  samples, respectively. The figures (c) – (e) give the estimation as function of the reconstructed bins in  $|t|$  for the non-tagged, tagged and high  $|t|$  sample, respectively. The blue band indicate the maximal range of the bias in each sample.

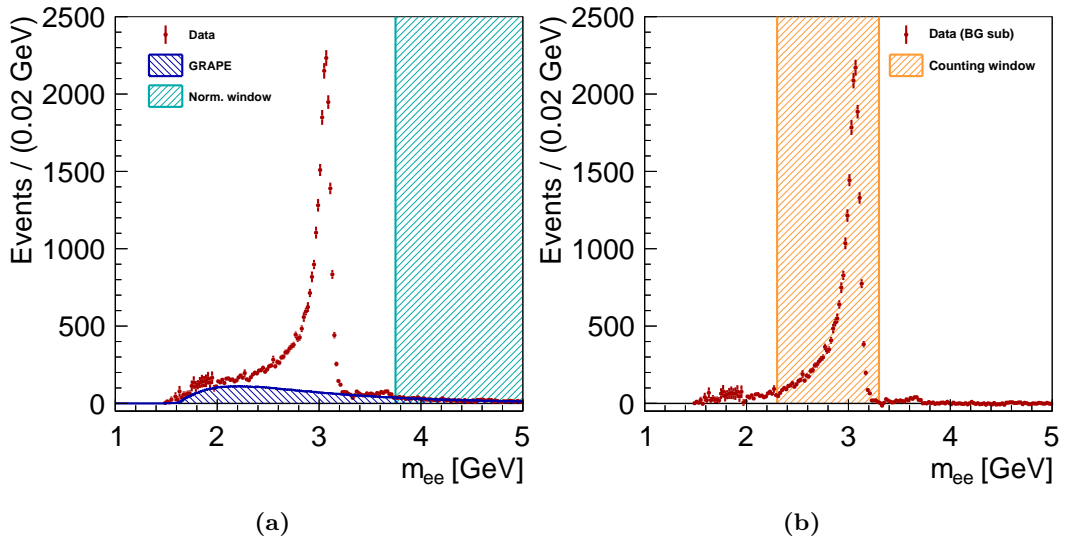


**Figure 9.7:** Illustration of the background subtraction technique used to evaluate the number of  $J/\psi$  signal events. Figure (a) shows the di-electron mass distribution for the high energy data period with the red points representing data and the blue, shaded histogram the GRAPE background MC simulation. The turquoise shaded area indicates the region used for normalisation determination. Figure (b) shows data after statistical background subtraction using the GRAPE MC simulation. The orange shaded area shows the region used for event counting to determine the number of  $J/\psi$  events.

background MC samples to data, a normalisation correction is added in form of a scaling factor  $s$ . Three methods are used to determine  $s$ . The first method is to calculate the factor directly from the ratio of data to the generated GRAPE luminosity. The factor obtained with this method will be referred to as  $s_{\text{lumi}}$ .

The other two methods estimate the scale factor in the high di-electron mass region above the  $\psi(2S)$  peak, where only the background contribution is present [see Fig. 9.7(a)]. The scale factor  $s$  is defined as

$$s = \frac{N_{\text{data}}(m_{ee} = 3.75 - 5 \text{ GeV})}{N_{\text{GRAPE}}(m_{ee} = 3.75 - 5 \text{ GeV})} \quad (9.16)$$

with  $N_{\text{data}}$  and  $N_{\text{GRAPE}}$  being the number of events in the given mass window for the data sample and for the GRAPE MC simulation. The second method uses the full data sample for each data period and estimates a *global* factor, called  $s_{\text{global}}$ . The third method determines the scale factor for each reconstructed analysis bin in  $|t|$  and  $W_{\gamma p}$  separately, giving a set of factors  $\{s_i\}$ .

Figure 9.8 shows the different scale factors normalised to  $s_{\text{lumi}}$  for the high energy data sample. The subfigures (a) and (b) show the  $\overline{\text{tag}_W}$  and  $\text{tag}_W$  sample as function of  $W_{\gamma p}$ . In (c) – (e) the non-tagged, tagged and high  $|t|$  sample are given as function of  $-t$ .

The difference between  $s_{\text{global}}$  and  $s_{\text{lumi}}$  of 2.5% is within the uncertainty on the extraction of  $s_{\text{global}}$  which is about 2.5%. The partial fluctuation of the scale factors extracted by using only the events in each bin, is caused by the reduced amount of statistics, especially in the tagged samples. Because of the more stable result expected by using  $s_{\text{global}}$  this method is used to extract the  $J/\psi$  events.

For evaluation of the systematic uncertainty of the signal extraction, the  $s_i$  factors are used as an alternative method. (For further details see Sec. 9.4.3.) An additional alteration using the scale factor  $s_{\text{lumi}}$  instead of  $s_{\text{global}}$  is not performed, due the agreement of the size of both factors, which would result in a smaller systematic uncertainty and not reflecting the situation properly.

The di-electron mass distributions after background subtraction are given in Appendix B.3. The number of extracted  $J/\psi$  signal events in the mass window can be found in Appendix B.4 for both data periods.

### 9.2.3.3 $\psi(2S)$ background

The used di-electron and di-mass distributions to extract the number of  $J/\psi$  events contain also a small amount of so called feed-downs from  $\psi(2S)$  decays, which dominantly decay into a  $J/\psi$  and something else. To correct for the  $\psi(2S)$  contribution a realistic MC sample is used as described in Sec. 4.1.3.

To illustrate the size of the applied  $\psi(2S)$  subtraction correction Fig. 9.9 shows as an example the ratio of the number of  $\psi(2S)$  events over the number of data events for the high energy data sample in the  $J/\psi \rightarrow \mu\mu$  decay channel for the  $\overline{\text{tag}_W}$  (a) and  $\text{tag}_W$  (b) sample as function of  $W_{\gamma p}$  and the tagged (c), non-tagged (d) and high  $|t|$  (e) sample as function of  $-t$ .

The final number of  $J/\psi$  events subtracted from the data sample is the sum of  $J/\psi$  feed-downs from the elastic and proton dissociative  $\psi(2S)$  simulations.

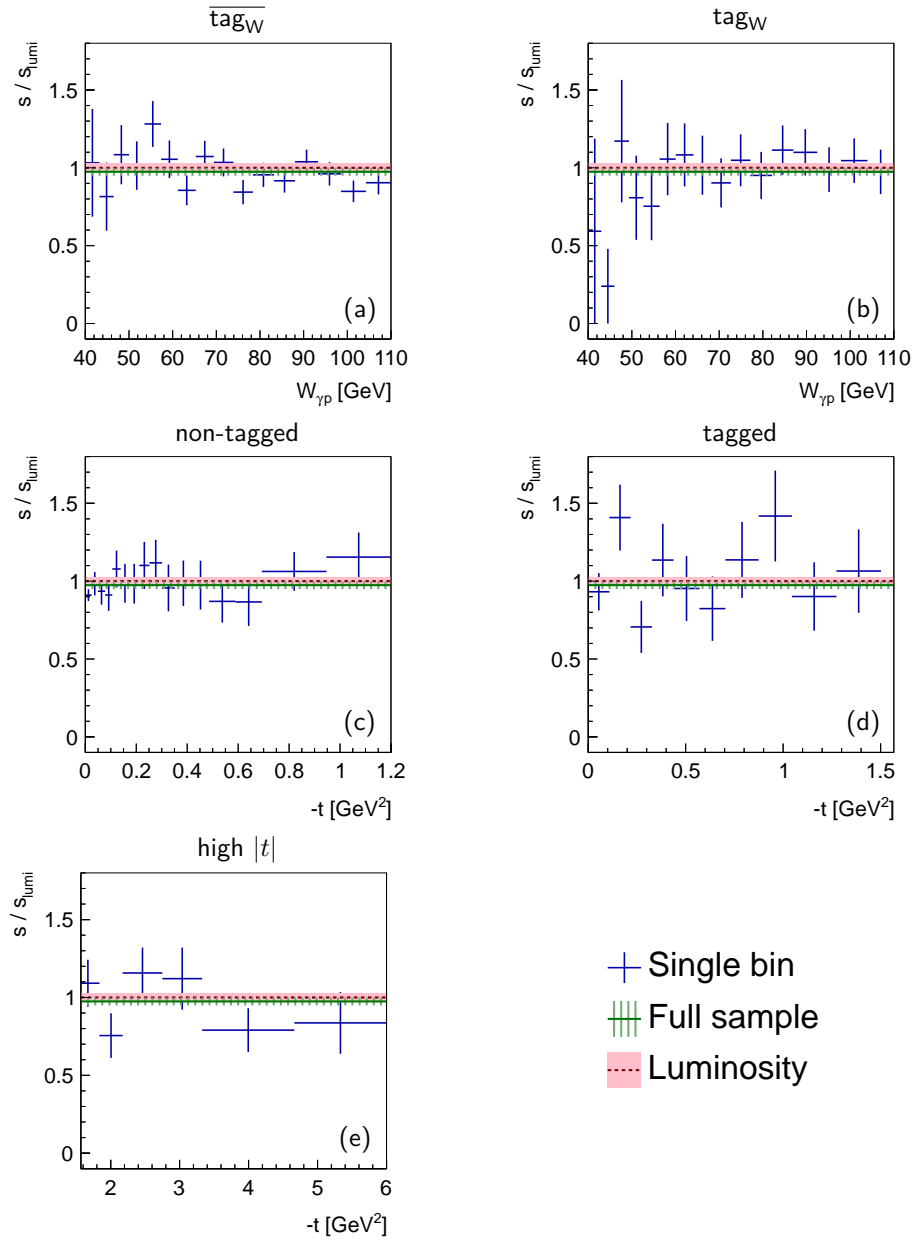


**Figure 9.8:** Background scale factors  $s$  normalised to the factor determined using the data and GRAPE MC simulation luminosities  $s_{\text{lumi}}$  are shown using different methods for determination. Figure (a) and (b) show the factors for the  $\overline{\text{tag}}_W$  and  $\text{tag}_W$  sample as function of  $W_{\gamma p}$  and (c) – (e) as function of  $-t$  for the non-tagged, tagged and high  $|t|$  sample. The blue histograms show the results for evaluating the factors for each bin separately in the high mass region  $m_{ee} = 3.75 - 5$  GeV, while the green solid line is derived using the same technique applied to the full sample. The red dashed line indicates the factor calculated from data and GRAPE MC simulation luminosities.

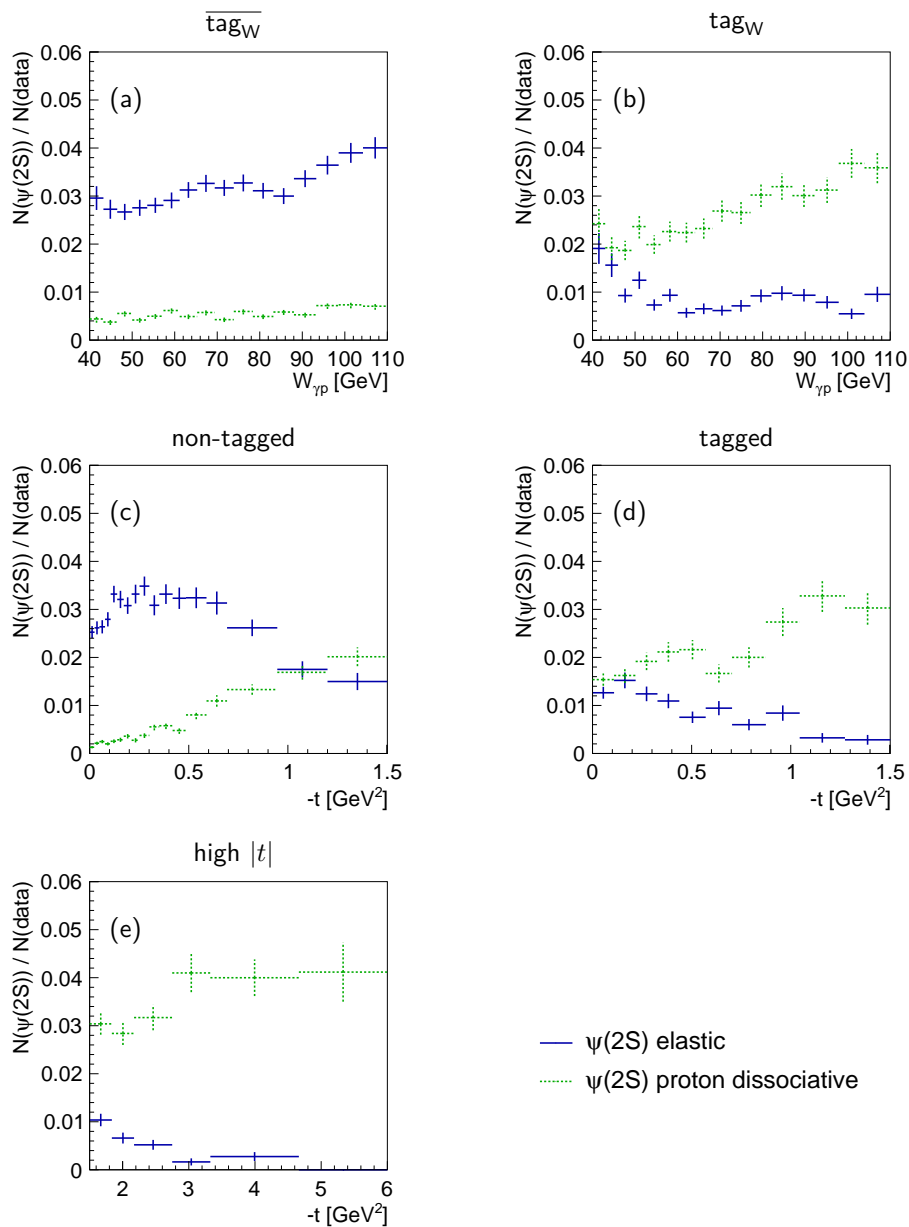


**Figure 9.9:** Examples of relative contribution of  $J/\psi$  feed-downs from  $\psi(2S)$  events contained in the data sample. The plots show the ratio of number of  $\psi(2S)$  events normalised to the number of data events for the high energy data sample in the  $J/\psi \rightarrow \mu\mu$  decay channel for the  $\overline{\text{tag}}_W$  (a) and  $\text{tag}_W$  (b) sample as function of  $W_{\gamma p}$  and the tagged (c), non-tagged (d) and high  $|t|$  (e) sample as function of  $-t$ . The solid blue and dashed green histograms represent the relative contribution due to elastic and proton dissociative  $\psi(2S)$  production.

## 9.2.4 Regularisation

### 9.2.4.1 An example for the regularisation matrix $L^2$

The composition of the two independent processes, elastic and proton dissociative, produce a regularisation matrix  $L$  containing two blocks, similar to the response matrix definition given in Sec. 9.2.2. Each block is regularising exactly one process. Since there is no connection between the blocks, no additional constraint is added between the elastic and proton dissociative regularising blocks, i.e. each process is regularised by itself. An illustration of the form of  $L^2$  is given in Fig. 9.10 taken from  $W_{\gamma p}$  unfolding of the high energy data period in the  $J/\psi \rightarrow ee$  decay channel. The  $L^2$  used in case of unfolding of cross section as function of  $|t|$  looks similar.

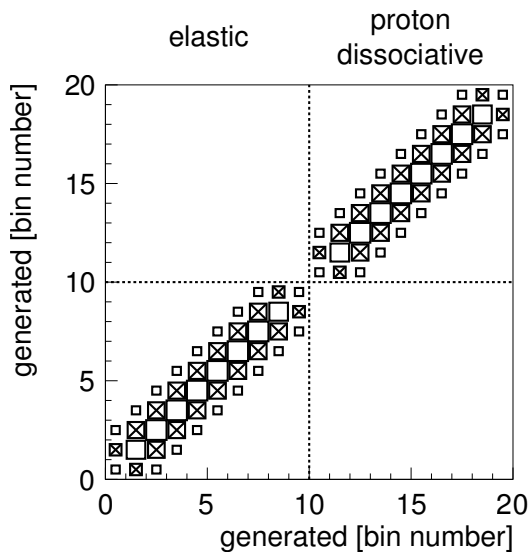


**Figure 9.10:** Illustration of the squared regularisation matrix  $L^2$ , taken from  $W_{\gamma p}$  unfolding of the high energy data period in  $J/\psi \rightarrow ee$  decay channel. The first and second blocks are regularising the true vector  $x$  for the elastic and proton dissociative processes, respectively. The size of the contents in each bin is represented by the area of the square in the bin; a negative entry is represented by a crossed square.

### 9.2.4.2 Example for estimation of $\tau$ parameter

For each data period, decay channel and variable a series of unfolding evaluations are performed, each with different  $\tau$  value. The result in form of the true vector  $x$  are not of importance for the determination of the optimal  $\tau$  values, the interest solely rests on the global correlation  $\bar{\rho}$  as defined in Eq. (9.8). Such an evaluation is given in Fig. 9.11, taken from the unfolding in the variable  $t$  for the high energy data period in the  $J/\psi \rightarrow ee$  decay channel. Because a result is preferable in which the correlations between the different bins of the true distribution  $x$  are minimal (see Sec. 9.1), the optimal working point is taken where the averaged global correlation is minimal, in Fig. 9.11 marked with a red star.

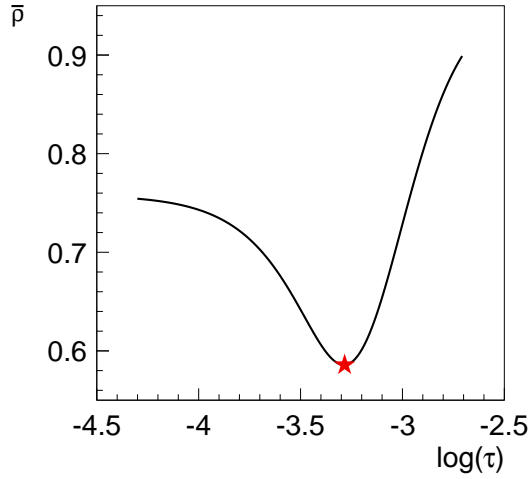


**Figure 9.11:** Determination of optimal  $\tau$  value, taken from the unfolding in the variable  $t$  for the high energy data period in the  $J/\psi \rightarrow ee$  decay channel. The line represents the averaged global correlation  $\bar{\rho}$  for different values of  $\tau$ . The optimal  $\tau$  value, represented as red star, is defined at the minimal  $\bar{\rho}$ .

### 9.3 Cross section construction with unfolding

The point is reached where all parts needed for a proper unfolding procedure are assembled. The output of this unfolding procedure is the true vector  $x$ , it is composed of two parts  $x = \{x^{\text{el}}, x^{\text{pd}}\}$  containing the number of true elastic and true proton dissociative  $J/\psi$  events in the former and latter part, respectively. It is straight forward to calculate from the  $x$  vector the cross section because all efficiencies corrections are already applied within the unfolding procedure.

The cross section points  $\sigma_{i_t}(\gamma p \rightarrow J/\psi)$  for both processes in  $t$  are calculated by

$$\frac{\Delta\sigma_{i_t}}{\Delta t} = \frac{1}{\Phi_\gamma^T \mathcal{L} \cdot \mathcal{B} \cdot \Delta t_i} \tilde{x}_{i_t}, \quad (9.17)$$

with  $\Phi_\gamma^T$  the transverse polarised photon flux factor (see Sec. 2.2.2), which is constant in  $|t|$ ,  $\mathcal{L}$  the prescaled corrected, integrated luminosity,  $\mathcal{B}$  the branching ratio and  $\Delta t_i$  the  $i$ -th bin width. The  $\tilde{x}$  reference either to  $x^{\text{el}}$  or  $x^{\text{pd}}$ .

For  $W_{\gamma p}$  it takes a slightly different form

$$\sigma_{i_W}(\gamma p \rightarrow J/\psi) = \frac{1}{\Phi_\gamma^{T,i} \mathcal{L} \cdot \mathcal{B}} \tilde{x}_{i_W}. \quad (9.18)$$

The photon fluxes  $\Phi_\gamma^{T,i}$  depend in this case on the actual ranges of the  $W_{\gamma p}$  bins, as given in Sec. 2.2.2.

Before the results in form of cross sections are presented a detour to two important subjects are made. The former discusses the sources and effects of the systematic uncertainty, the

latter describes the control plots of this measurement.

## 9.4 Systematic uncertainties

The subject of this section is the discussion of all systematic sources. Because of the formal way of treatment they are split into three different groups. The first contains non-differential contribution which affect therefore only the normalisation. The second group is populated with effects, treated in creating alternative response matrices which are propagated through the unfolding to get the effect on the cross sections. The last group deals with uncertainties related to the input vector.

### 9.4.1 Normalisation uncertainty

A summary of the single effects contributing to the total normalisation uncertainty is given in Table 9.1 for both reconstruction channels in each data period. The uncertainty on the trigger efficiency is evaluated from the control plots of data and MC simulation and is estimated to be 4% (see control plots shown in Sec. 7.1). The uncertainty on the track finding and vertex fit is different for the electron and muon channel. A value of 2% per electron and 1% per muon tracks is used, resulting in 4% and 2% uncertainty for the  $J/\psi \rightarrow ee$  and  $J/\psi \rightarrow \mu\mu$  decay channel. The uncertainty on the luminosity is set to 2.7% in the high energy data period and a value of 5% is used for the low energy data period<sup>(11)</sup>. An uncertainty of 1.5% on the  $\psi(2S)$  background and 1% on the branching ratio [58] is used. All effects are added in quadrature leading to a total normalisation uncertainty of 6.5% and 5.5% for the  $J/\psi \rightarrow ee$  and  $J/\psi \rightarrow \mu\mu$  decay channel for the high energy period and to 7.8% and 6.9% for the two decay channels for the low energy data period.

Effect	Uncertainty [%]			
	High energy data period		Low energy data period	
	$ee$ channel	$\mu\mu$ channel	$ee$ channel	$\mu\mu$ channel
Trigger efficiency	4.0	4.0	4.0	4.0
Track/vertex fit	4.0	2.0	4.0	2.0
Luminosity	2.7	2.7	5.0	5.0
$\psi(2S)$	1.5	1.5	1.5	1.5
Branching ratio	1.0	1.0	1.0	1.0
Total	6.5	5.5	7.8	6.9

**Table 9.1:** Overview of contributions to the normalisation uncertainty for both used decay channels  $J/\psi \rightarrow ee$  and  $J/\psi \rightarrow \mu\mu$  in each data period. Total represents the sum in quadrature of the given sources.

<sup>(11)</sup>The precision of the luminosity measurement was substantially increased with the measurement [296], producing smaller uncertainties for the high energy data period. The low energy data period however is not covered by this measurement, leading to larger uncertainties.

## 9.4.2 Response matrix variations

The various systematic sources discussed in the following give not directly an estimate on how much the differential cross sections are affected by them. Therefore each effect needs to be propagated to the output vector  $x$  in order to see the size of the effect on the cross section. For this purpose first alternative response matrices for each systematic source are created. Then the difference of each alternative matrix to the default matrix is, by use of standard error propagation, forwarded to the output vector  $x$ , in order to obtain the uncertainty  $\Delta x$  due to a specific systematic source.

Some systematic sources are treated in an up-down variation approach, producing two separate alternative response matrices. The averaging mechanism used to combine the up and down variation into one alternative response matrix is described in the next sub section. In Sec. 9.4.2.2 the standard error propagation of the alternative response matrix to the  $x$  vector as implemented in TUnfold is explained. Afterwards in Sec. 9.4.2.3 a list of the considered systematic sources is given. Finally in last sub section the relative differences  $\Delta x/x$  for each systematic source in each data period, decay channel and variable are presented.

### 9.4.2.1 Averaging mechanism for response matrix variations

For each of the sources described below alternative response matrices are produced. Usually one for an up and one for a down variation, but for some effects only a one-sided variation is performed.

In the case of up-down-variation, the difference of each element to the default response matrix  $A$  of the two alternatives are averaged by keeping the relative sign of the first variation. Expressed in a formula it takes the form

$$A_{ij}^{\text{avg}} = A_{ij} + \text{sgn}(A_{ij}^1 - A_{ij}) \frac{1}{2} \sum_{k=1}^2 |A_{ij}^k - A_{ij}|, \quad (9.19)$$

with  $A^k$  the alternative response matrices and  $A^{\text{avg}}$  the averaged matrix.

### 9.4.2.2 Calculating the effect of alternative response matrices on the $x$ vector

The one-sided or averaged variation are then fed to TUnfold, where for each source the shift  $\Delta x$  on the true output vector  $x$  is calculated by the formula<sup>(12)</sup>

$$\Delta x = E \Delta A^T V_y^{-1} (y - Ax) - B \Delta Ax. \quad (9.20)$$

A derivation is given in Appendix A.4.

Further an error matrix for each source  $s$  is calculated by the rank-1 matrix  $V_s^{\text{sys}} = \Delta x_s \Delta x_s^T$ . The total systematic covariance matrix of all sources is then the sum of the individual error matrices  $V_s^{\text{sys}}$ , i.e.

$$V^{\text{sys}} = \sum_s V_s^{\text{sys}}. \quad (9.21)$$

<sup>(12)</sup>The given formula does not take into account the area preservation. It was left out for simplicity.

In the following subsection the different sources are described, the actual uncertainty effect of the uncertainty sources on the true vector  $x$  are given in Sec. 9.4.2.4.

### 9.4.2.3 Systematic sources

#### 9.4.2.3.1 Forward tagging

A one-sided tagging efficiency variation is performed for each forward detector separately. The size of the variation is extracted from the difference of the single tagging efficiency between the simulation and data. The construction of the efficiency for the simulation are equal to the control plot construction (see Sec. 9.5.1). The relative efficiency variation for each data period, decay channel and variable is given in Table. 9.2.

Period	Channel	Variable	Variation [%]		
			LAr	PLUG	FTS
HER	$ee$	$t$	$-23 \pm 2$	$5 \pm 2$	$-1 \pm 2$
		$W_{\gamma p}$	$-24 \pm 2$	$4 \pm 2$	$-2 \pm 2$
	$\mu\mu$	$t$	$-23 \pm 3$	$4 \pm 2$	$0 \pm 2$
		$W_{\gamma p}$	$-24 \pm 3$	$3 \pm 2$	$0 \pm 2$
LER	$ee$	$t$	$-38 \pm 8$	$3 \pm 6$	$8 \pm 7$
		$W_{\gamma p}$	$-37 \pm 8$	$3 \pm 6$	$11 \pm 7$
	$\mu\mu$	$t$	$-31 \pm 9$	$0 \pm 8$	$3 \pm 8$
		$W_{\gamma p}$	$-31 \pm 9$	$-1 \pm 8$	$6 \pm 8$
Used variation			-24	4	-1

**Table 9.2:** Overview of single tagging efficiency variations for all data periods, channels and variables used in this analysis are given. HER and LER denote the high and low energy data period, respectively. They are applied to produce alternative response matrices to quantify the effect on the forward tagging uncertainty on the cross sections.

The relative tagging variation values for each forward detector are in general in agreement between the different data periods, decay channels and variables. The errors on the relative difference are in the order of 2% for the high energy sample and about 8% for the low energy sample, due to the lower statistics contained in this sample.

All produced variations for a single forward detector for each data period, decay channel and variable are chosen to be equal, due to the agreement of the relative tagging variation differences. The used variation values are listed in the last row of Table 9.2.

#### 9.4.2.3.2 Forward energy flow

The two parameters relevant for the forward energy flow modeling  $\alpha_{1,pd}$  and  $\varepsilon_M$  are up and down varied within the uncertainty evaluated in the fit described in Chapter 8. The actual values of the variation are given in Table 8.2.

## 9.4.2.3.3 Elastic slope

The trajectory slope  $\alpha_{1,el} = 0.164 \pm 0.04$  is taken from Ref. [29] and the variation is performed within the given total (statistical and systematic) error.

## 9.4.2.3.4 Muon identification

The variation are taken from the remaining difference of the simulation compared to data after the efficiency reweighting is applied (cf. Sec. 6.6.2.4.1). The size of the up and down variations are 4% in  $t$  and 1.7% in  $W_{\gamma p}$ .

## 9.4.2.3.5 Electron identification

The same method as described in [234] is used but was evaluated for a different cut position of the electron identification.

Briefly summarised the method looks at the  $\chi^2$  value, calculated from data and the MC simulation, in a window around the cut position as function of the shift in the electron identifier variable  $D_{ele}$  of the MC simulation. By a fit on this distribution the minimum is determined. Figure 9.12 shows minima as function of the shift  $\Delta D_{ele}$  for different  $D_{ele}$  values around the nominal cut position of 0.8. As can be seen the maximal deviation in  $\Delta D_{ele}$  is around 0.04, therefore a variation of 0.04 is used for the systematic uncertainty evaluation.

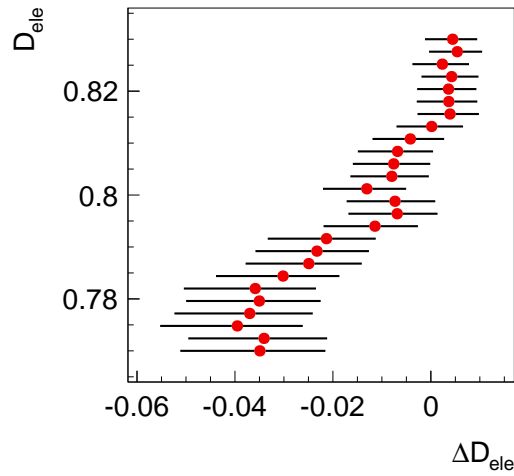


**Figure 9.12:** Summary plot for variation evaluation used for creating alternative response matrices to propagate the effect on the electron identification through the unfolding to the cross section. The details are given in the text.

#### 9.4.2.3.6 Empty calorimeter cut (EC)

In order to get an idea of the influence on the cut position of the empty calorimeter cut a variation of  $\pm 0.25 \text{ GeV}^2$  around the cut value of  $2.5 \text{ GeV}^2$  is done.

#### 9.4.2.3.7 $Q^2$ and $R_{LT}$ dependence

The influence of the  $Q^2$  dependence is expected to be small for a photo production analysis. However to take this uncertainty into account the slope  $n_q$  in Eq. (4.1) is varied by  $\pm 0.09$ . This reflects the total uncertainty of the measurement [29] giving a value  $n_q = 2.486 \pm 0.080(\text{stat.}) \pm 0.068(\text{sys.})$ .

The uncertainty on the variable  $R_{LT}$ , the ratio of longitudinal to transverse cross section, is taken into account by variation of the  $\xi$  parameter in Eq. (4.3) by  $\pm 0.13$  as estimated in Sec. 4.1.1.1.

#### 9.4.2.4 Propagated errors on true vector $x$

After having explained all systematic effects treated in creating alternative response matrices and propagate the result to the true  $x$  vector, the next step is to look at the size of the resulting uncertainties caused by the discussed systematic sources. The relative error on the true unfolded output vector  $\Delta x/x$  for the single systematic variations are given in Fig. 9.13 and 9.14 for the  $J/\psi \rightarrow ee$  decay channel data set in the high energy data period as function of the bin numbers for bins in  $|t|$  and  $W_{\gamma p}$ , respectively. The same is given for the  $J/\psi \rightarrow \mu\mu$  decay channel in Fig. 9.15 and 9.16. The Figures 9.17 - 9.20 show the same plots for the low energy data period. The two blocks (low and high bin numbers) in each plot refer to elastic and proton dissociative process and are separated by empty bins.

In general the systematic uncertainties are rather flat as function of  $W_{\gamma p}$  bins, but depend and usually increase with higher  $|t|$  bins. The largest uncertainty is found to be the result of the tagging variations, especially the LAr variation. Because the tagging conditions are responsible for the separation of elastic and proton dissociative contribution, the variation in the tagging efficiency causes anti-correlated changes on  $\Delta x/x$  with respect to elastic and proton dissociative bins.

For  $|t|$  unfolding also the forward energy flow parameters  $\alpha_{1,\text{pd}}$  and  $\varepsilon_M$ , and the empty calorimeter cut lead to larger uncertainties at high  $|t|$  values. Generally this are the second largest sources also for  $W_{\gamma p}$ . All other sources seem to be negligibly small compared to these three effects.

### 9.4.3 Input vector variations

The systematic uncertainty on the input vector is handled differently because it does not change the response matrix. The systematic errors  $S_y$  on  $y$  are propagated to the unfolding output vector  $x$  as uncorrelated errors, therefore the covariance matrix on  $x$ , due to this error source is given by standard error propagation

$$V_x = BV_y B^T, \quad \text{with } (V_y)_{ij} = \delta_{ij} S_y^2 \quad \text{and} \quad (9.22)$$

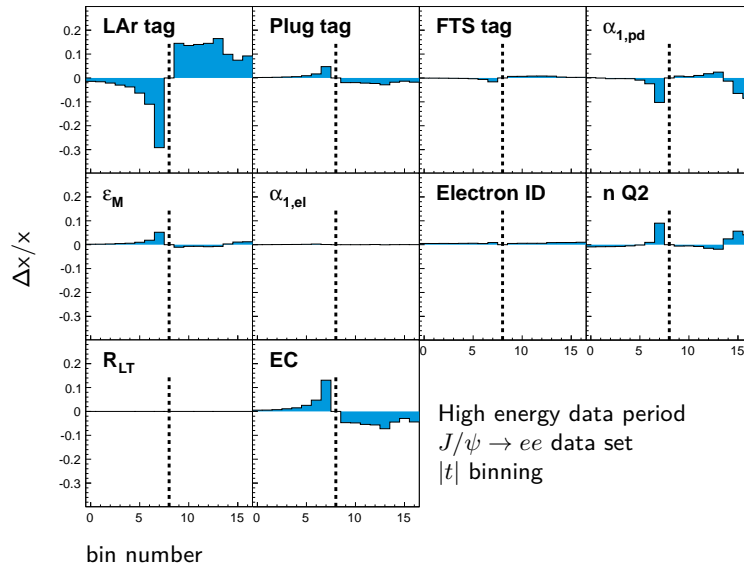


**Figure 9.13:** Relative error on true vector  $x$  as function of bins in  $|t|$  for the different systematic sources for  $J/\psi \rightarrow ee$  decay channel data set in the high energy data period. The first block in each figure represents elastic, the second proton dissociative bins.

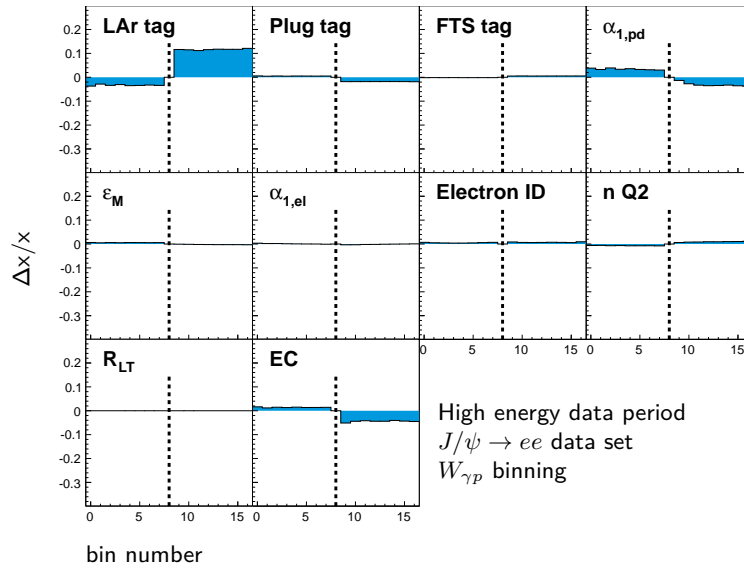


**Figure 9.14:** Relative error on true vector  $x$  as function of bins in  $W_{\gamma p}$  for the different systematic sources for  $J/\psi \rightarrow ee$  decay channel data set in the high energy data period. The first block in each figure represents elastic, the second proton dissociative bins.

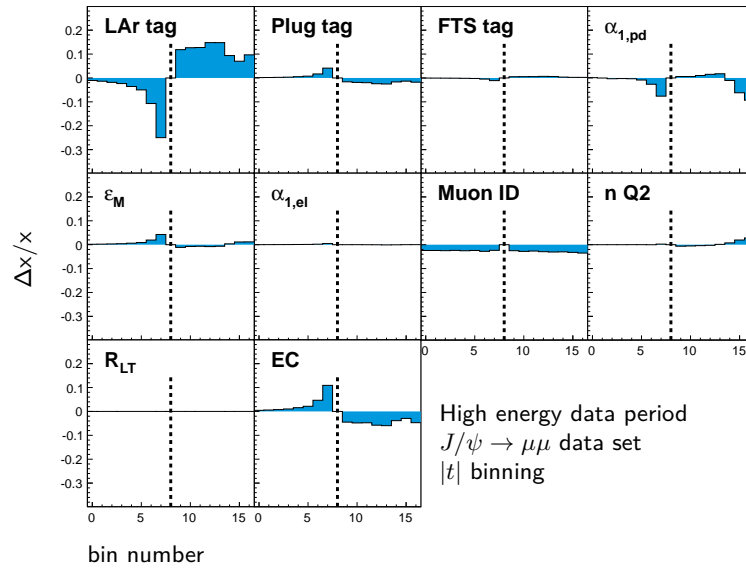


**Figure 9.15:** Relative error on true vector  $x$  as function of bins in  $|t|$  for the different systematic sources for  $J/\psi \rightarrow \mu\mu$  decay channel data set in the high energy data period. The first block in each figure represents elastic, the second proton dissociative bins.

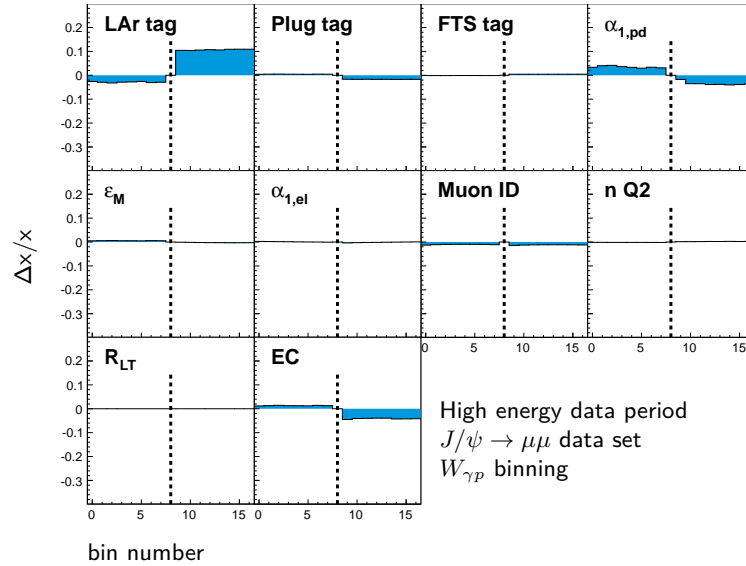


**Figure 9.16:** Relative error on true vector  $x$  as function of bins in  $W_{\gamma p}$  for the different systematic sources for  $J/\psi \rightarrow \mu\mu$  decay channel data set in the high energy data period. The first block in each figure represents elastic, the second proton dissociative bins.

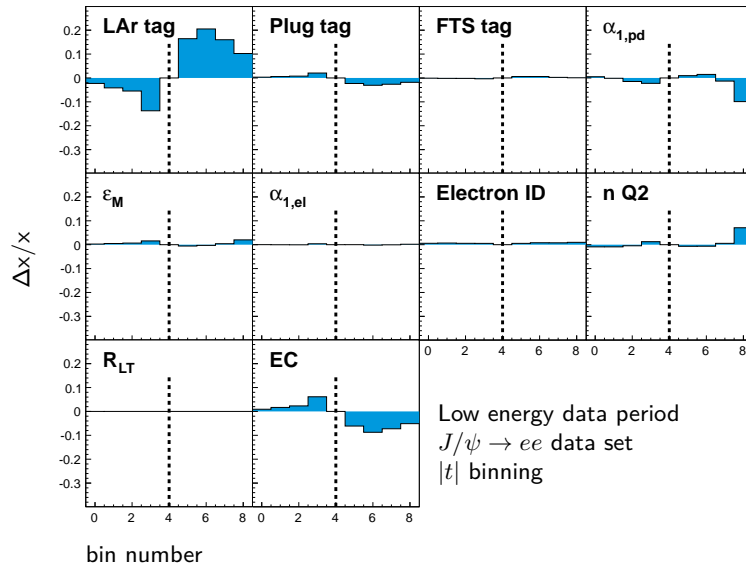


**Figure 9.17:** Relative error on true vector  $x$  as function of bins in  $|t|$  for the different systematic sources for  $J/\psi \rightarrow ee$  decay channel data set in the low energy data period. The first block in each figure represents elastic, the second proton dissociative bins.

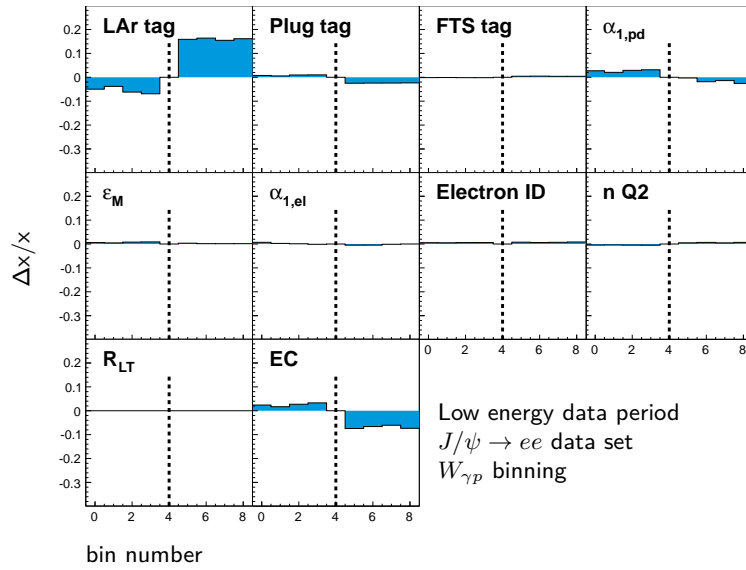


**Figure 9.18:** Relative error on true vector  $x$  as function of bins in  $W_{\gamma p}$  for the different systematic sources for  $J/\psi \rightarrow ee$  decay channel data set in the low energy data period. The first block in each figure represents elastic, the second proton dissociative bins.

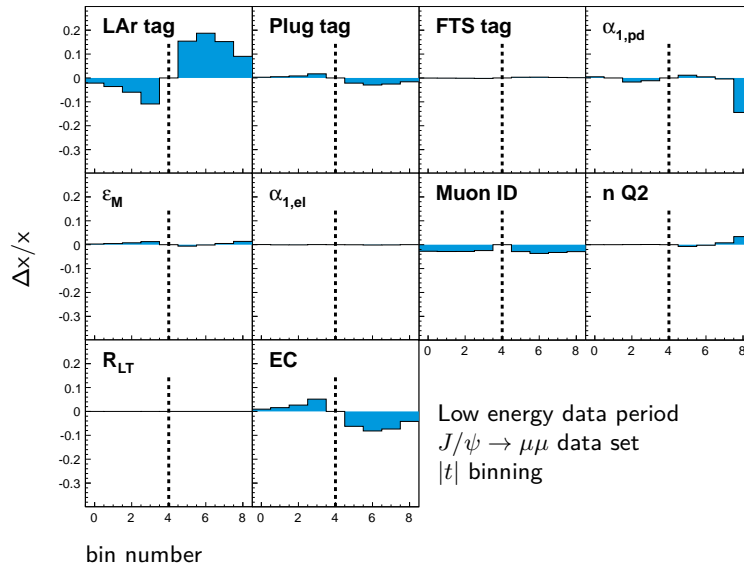


**Figure 9.19:** Relative error on true vector  $x$  as function of bins in  $|t|$  for the different systematic sources for  $J/\psi \rightarrow \mu\mu$  decay channel data set in the low energy data period. The first block in each figure represents elastic, the second proton dissociative bins.

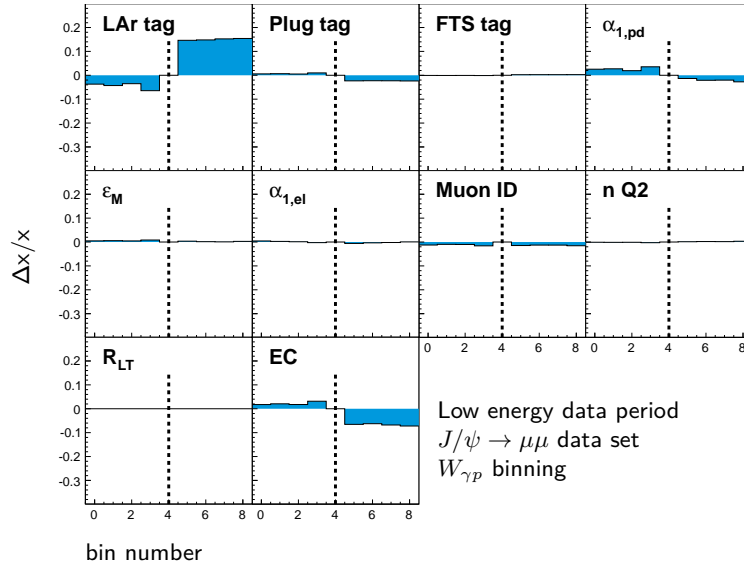


**Figure 9.20:** Relative error on true vector  $x$  as function of bins in  $W_{\gamma p}$  for the different systematic sources for  $J/\psi \rightarrow \mu\mu$  decay channel data set in the low energy data period. The first block in each figure represents elastic, the second proton dissociative bins.

with  $B$  as defined in Eq. (9.7).

The size of  $S_y$  in the muon channel is taken from the bias study described in Sec. 9.2.3.1.3. For the electron channel an alternative estimation of the number of  $J/\psi$  events in each bin was performed. Instead of using a normalisation for the background MC simulation evaluated on the full sample, it is determined in each bin separately as described in Sec. 9.2.3.2.

The resulting uncertainties on the square root of the diagonal elements,  $d_i \equiv \sqrt{(V_x)_{ii}}$  due to the input vector variations, divided by  $x$  are shown in Fig. 9.21 as function of bins in  $|t|$  for the high energy data period in the decay channel  $J/\psi \rightarrow ee$  (a) and  $J/\psi \rightarrow \mu\mu$  (b), and for the low energy data period in the decay channel  $J/\psi \rightarrow ee$  (c) and  $J/\psi \rightarrow \mu\mu$  (d). The relative uncertainties due to the input vector variations  $d_i/x$  as function of bins in  $W_{\gamma p}$  are given in Fig. 9.22 shown in the same setup as used for Fit. 9.21.

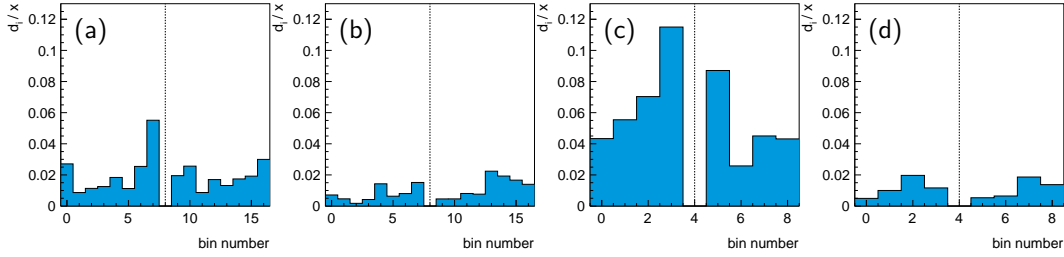


**Figure 9.21:** Uncertainties on the square root of the diagonal elements,  $d_i \equiv \sqrt{(V_x)_{ii}}$ , caused by the input vector variation, divided by  $x$ , are shown as function of bins in  $|t|$  for the high energy data period in the decay channel  $J/\psi \rightarrow ee$  (a) and  $J/\psi \rightarrow \mu\mu$  (b), and for the low energy data period in the decay channel  $J/\psi \rightarrow ee$  (c) and  $J/\psi \rightarrow \mu\mu$  (d).

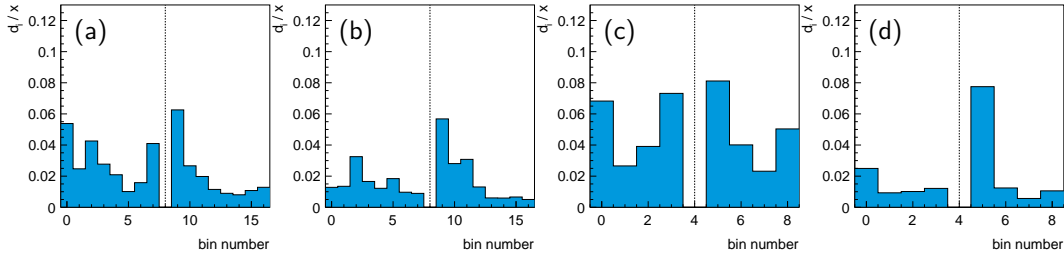


**Figure 9.22:** Uncertainties on the square root of the diagonal elements,  $d_i \equiv \sqrt{(V_x)_{ii}}$ , caused by the input vector variation, divided by  $x$ , are shown as function of bins in  $W_{\gamma p}$  for the high energy data period in the decay channel  $J/\psi \rightarrow ee$  (a) and  $J/\psi \rightarrow \mu\mu$  (b), and for the low energy data period in the decay channel  $J/\psi \rightarrow ee$  (c) and  $J/\psi \rightarrow \mu\mu$  (d).

## 9.5 Control plot distributions

One set of control plots is created for each unfolding result. All control plots show distributions restricted to a window in the di-lepton mass distribution around the nominal  $J/\psi$  mass, in

order to suppress background contribution. The applied cuts are equal to the mass window restriction used in the determination of the number of  $J/\psi$  signal events in Sec 9.2.3.

## 9.5.1 Control plot construction

The construction of the control plots is in the following briefly explained. The first subsection discusses the construction of the signal contribution, while the second subsection explains the treatment of the background contribution.

### 9.5.1.1 Signal contribution

The construction of the signal distribution  $H_{\text{sig}}$  of a certain control plot is done separately for the elastic and proton dissociative part. To obtain the  $H_{\text{sig}}$  histogram, the elastic and proton dissociative distributions,  $H_{\text{elas}}$  and  $H_{\text{pdis}}$ , are summed, i.e.

$$H_{\text{sig}} = H_{\text{elas}} + H_{\text{pdis}}. \quad (9.23)$$

In the following the construction of the elastic and proton dissociative part is given in a general manner, applicable for both signal contributions.

The elastic and proton dissociative  $J/\psi$  MC samples are split into  $N^{\text{bin}}$  bins of the generated unfolding quantity, i.e.  $t_{\text{gen}}$  or  $W_{\text{gen}}$ , with the same binning as used for the response matrix construction. The bins will be referenced by the index  $i = 1, \dots, N^{\text{bin}}$ . In each generated bin  $i$  the reconstructed distribution, for which the control plot should be constructed, is drawn, producing the histogram  $h_i$ . These histograms are then normalised to unity integral, which will be represented by  $\hat{h}_i$ , and serve as templates.

Each template  $\hat{h}_i$  is weighted by the number of reconstructed data events of the corresponding bin  $N_i^{\text{data,rec}}$ . Summed up one obtains the signal part distribution (elastic or proton dissociative)

$$H = \sum_i^{N^{\text{bin}}} \hat{h}_i N_i^{\text{data,rec}}. \quad (9.24)$$

The  $N_i^{\text{data,rec}}$  are obtained from the unfolded true number of  $J/\psi$  events  $x_i$  and the reconstruction efficiency in the bin  $i$ ,  $\varepsilon_i$ , by  $N_i^{\text{data,rec}} = \varepsilon_i x_i$ .

### 9.5.1.2 Background contribution

The good description of the background MC simulation in the electron channel, allows to use the simulation directly. The GRAPE background MC sample is normalised by the same technique used to determine the number of  $J/\psi$  signal events, described in Sec. 9.2.3.2.

The construction of control plots in the muon decay channel was chosen differently, because the background distribution cannot be described by the GRAPE simulation only, due to additional processes contained in the data sample. Instead of adding the background contribution in the control plot, the data sample is subtracted from the background contribution using the side band method. A good description of the side band subtraction method can be found in [266]. Therefore control plots produced for the  $J/\psi \rightarrow \mu\mu$  decay channel only contain the signal (elastic and proton dissociative) contribution and the background subtracted data.

The contribution from the  $\psi(2S)$  elastic and proton dissociative simulation are normalised to data luminosity.

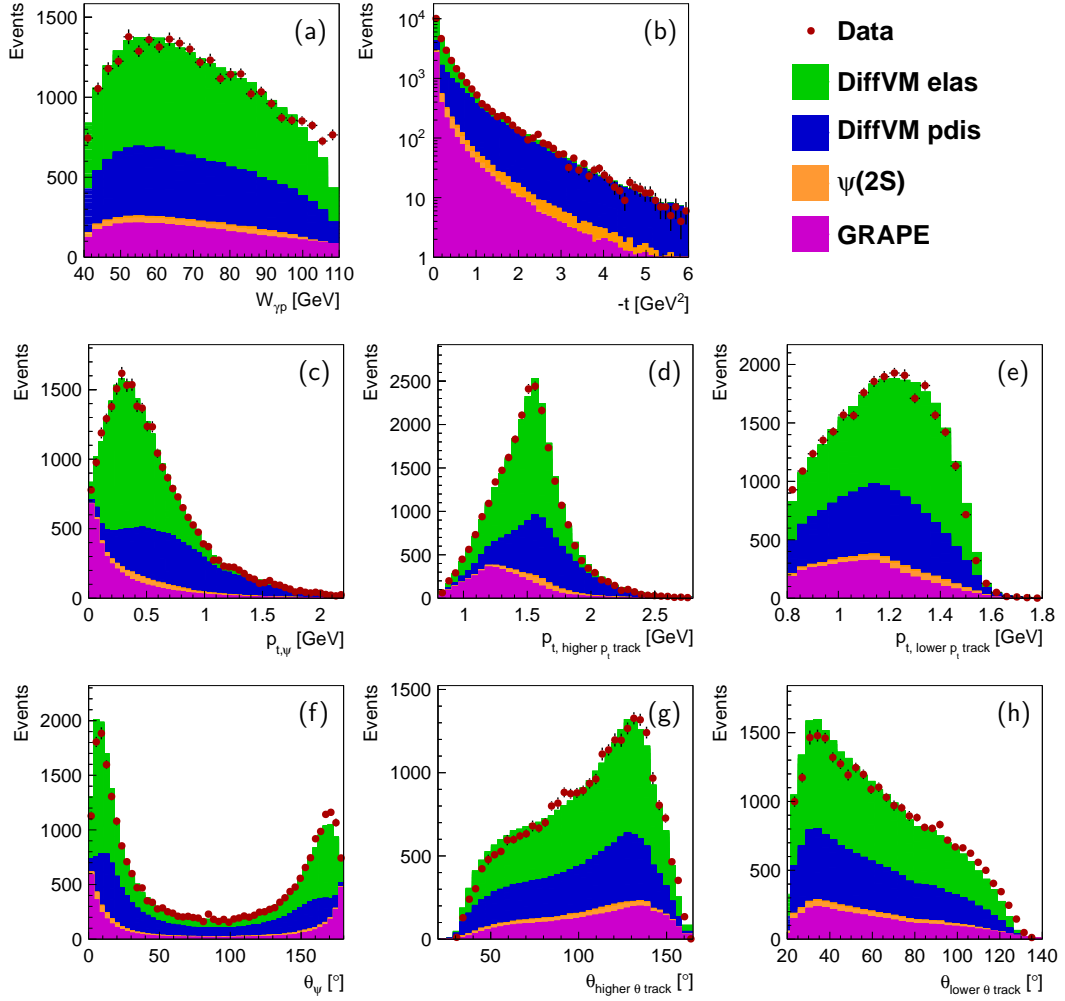
A final remark before the control plots are shown and discussed: The control plots do not include any systematic uncertainties but only incorporate the statistical error. A comparison of the simulation with data therefore should not leave out this aspect.

### 9.5.2 Control plot discussion

Figure 9.23 and 9.24 show the control plot distributions for unfolding in  $t$  and  $W_{\gamma p}$  in the decay channel  $J/\psi \rightarrow ee$  for the high energy data period. Figure (a) and (b) show the  $W_{\gamma p}$  and  $t$  distribution. The transverse momentum  $p_t$  of the  $J/\psi$  is shown in figure (c), while in plot (d) and (e) the transverse momentum of the  $J/\psi$  decay particles with the higher and lower  $p_t$  are given. The last row shows the polar angle  $\theta$  of the  $J/\psi$  (f) and the polar angle of the  $J/\psi$  decay particles with higher (g) and lower (h)  $\theta$  angle. The description in general is rather good. In the control distribution for  $W_{\gamma p}$  9.23(a), produced for unfolding in  $t$ , however some difference of data to the combined MC sample at larger  $W_{\gamma p}$  values are visible. Since the  $t$  and  $W_{\gamma p}$  variable are rather orthogonal to each other it is not expected that the used template method weighting in the variable  $t$  can also describe the  $W_{\gamma p}$  dependant distributions. In Fig. 9.24(a) which does the weighting with unfolded bins in  $W_{\gamma p}$  the differences are not visible anymore. Since the polar angle of the  $J/\psi$ ,  $\theta_{J/\psi}$ , is depending on  $W_{\gamma p}$  roughly as  $\cos \theta_{J/\psi} + 1 \propto 1/W_{\gamma p}^2$ , it also explains the better description of this variable for the control plots created for the  $W_{\gamma p}$  unfolding then for the  $t$  unfolding.

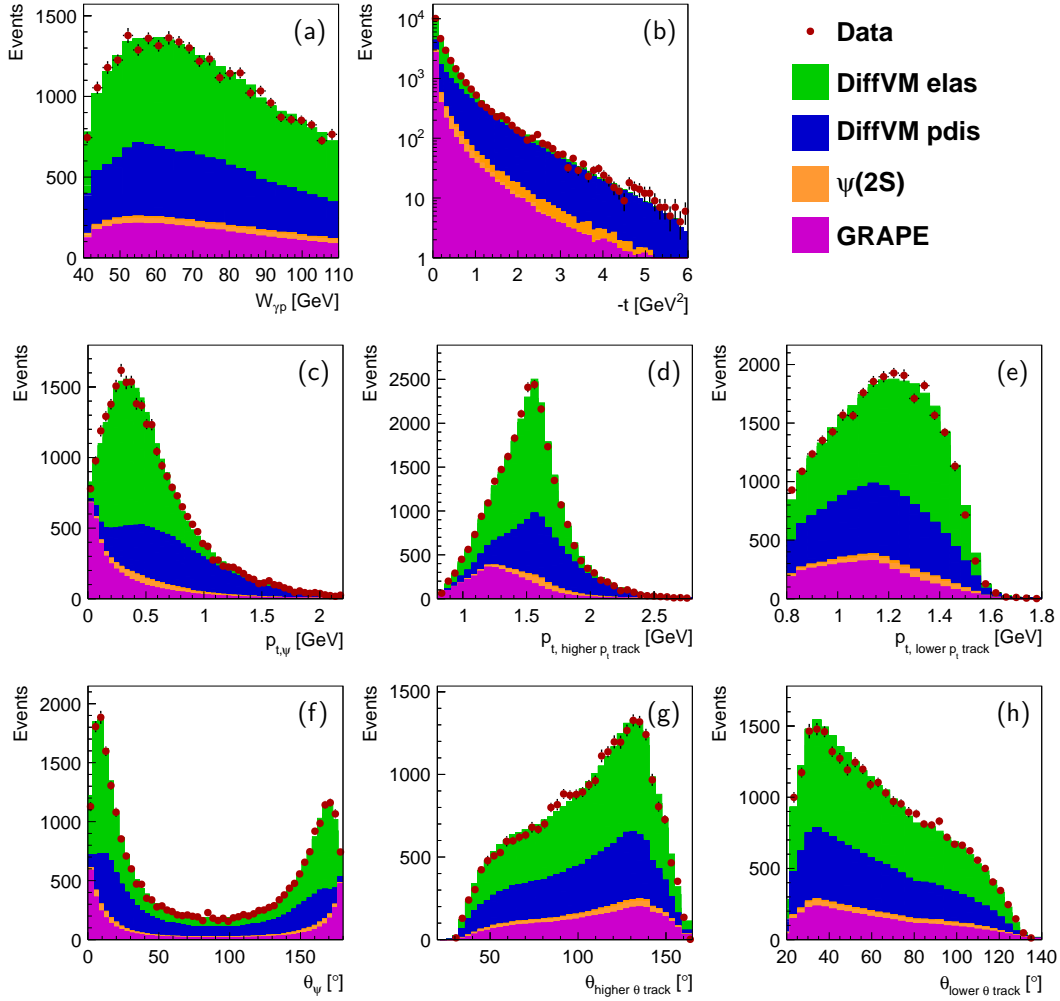
In Fig. 9.25 and 9.26 the control distributions are shown for the high energy data period in the decay channel  $J/\psi \rightarrow \mu\mu$ . Data, the elastic and the proton dissociative MC samples are represented similar to the Fig. 9.23 and 9.24. Due to the construction of the control plots data are background subtracted by use of the side band method, further details are given in 9.5.1.2. A background contribution as in the case of the  $J/\psi \rightarrow ee$  decay channel is therefore superfluous. The  $p_t$  distribution for the  $J/\psi$  decay particle track with lower  $p_t$ , Fig. 9.25(e) and 9.26(e), shows some difference between data and the simulation, which is most probably due to background subtraction.

The control plots for the low energy data period are given in the Fig. 9.27 and 9.28 for the  $J/\psi \rightarrow ee$  decay channel for the unfolding in  $t$  and  $W_{\gamma p}$ . The plots for the  $J/\psi \rightarrow \mu\mu$  decay channel can be found in Fig. 9.29 and 9.30 also for the two variables. Within the available statistics the distributions are well described.

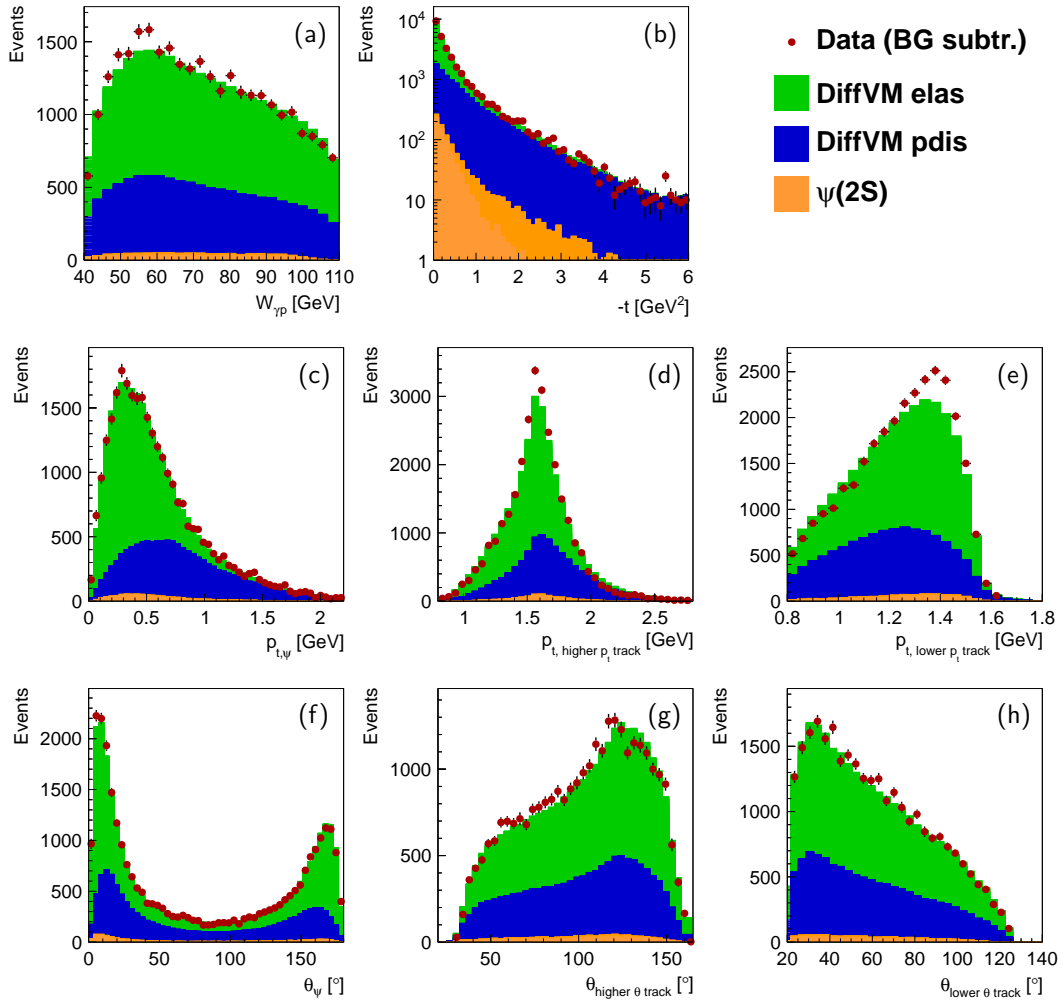
Control plots: high energy data period,  $t$  unfolding,  $J/\psi \rightarrow ee$  decay channel


**Figure 9.23:** Control plot distributions in the di-electron mass window  $m_{ee} = (2.3 - 3.3)$  GeV for the high energy data period in the  $J/\psi \rightarrow ee$  decay channel for unfolding in the variable  $t$ . Data are shown as red circles. The green and blue coloured stacked histograms represent the contribution from elastic and proton dissociative  $J/\psi$  production. The orange histogram gives the contribution from elastic and proton dissociative  $\psi(2S)$  production. The background process contribution simulated by GRAPE is given as magenta histogram. Figure (a) and (b) show the  $W_{\gamma p}$  and  $t$  distribution. The transverse momentum  $p_t$  of the  $J/\psi$  is shown in figure (c), while in plot (d) and (e) the transverse momentum of the  $J/\psi$  decay particles with the higher and lower  $p_t$  are given. The last row shows the polar angle  $\theta$  of the  $J/\psi$  (f) and the polar angle of the  $J/\psi$  decay particles with higher (g) and lower (h)  $\theta$  angle.

Control plots: high energy data period,  $W_{\gamma p}$  unfolding,  $J/\psi \rightarrow ee$  decay channel

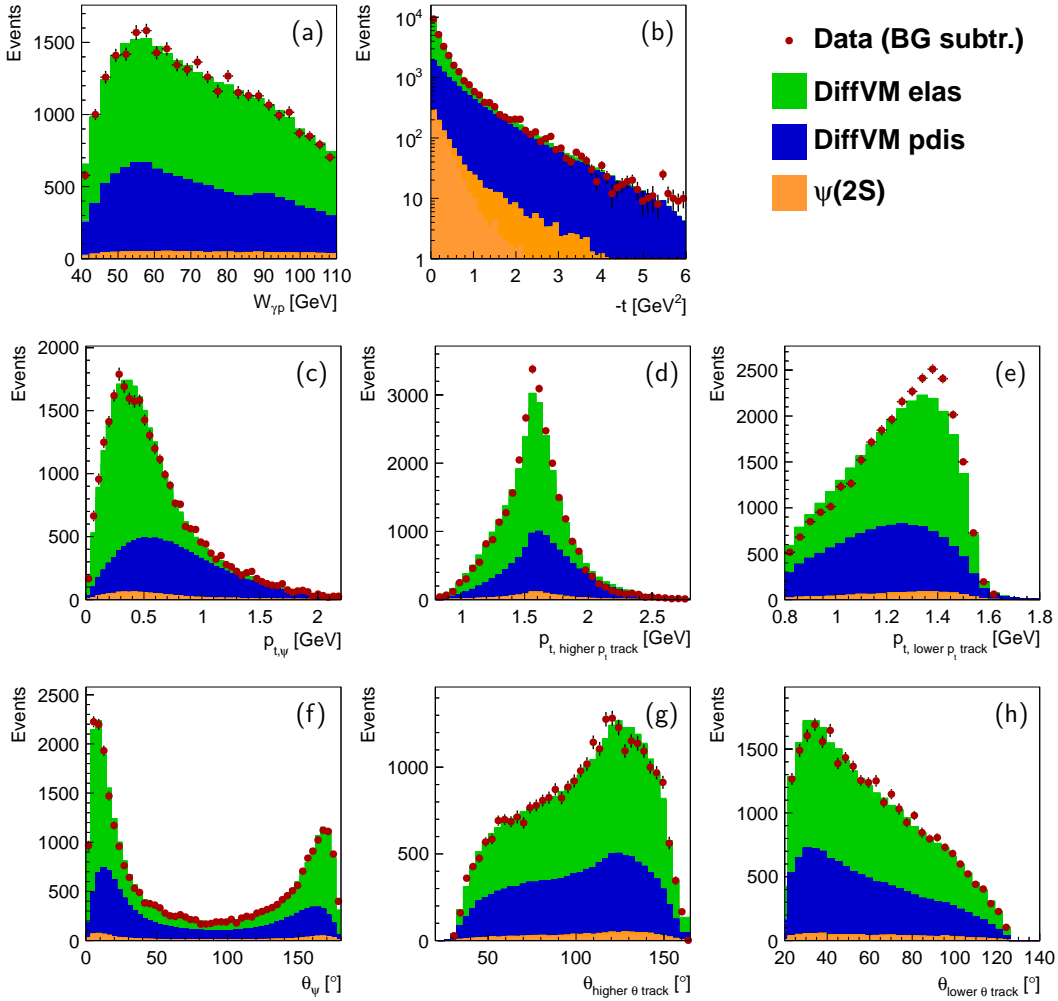


**Figure 9.24:** Control plot distributions in the di-electron mass window  $m_{ee} = (2.3-3.3)$  GeV for the high energy data period in the  $J/\psi \rightarrow ee$  decay channel for unfolding in the variable  $W_{\gamma p}$ . Data are shown as red circles. The green and blue coloured stacked histograms represent the contribution from elastic and proton dissociative  $J/\psi$  production. The orange histogram gives the contribution from elastic and proton dissociative  $\psi(2S)$  production. The background process contribution simulated by GRAPE is given as magenta histogram. Figure (a) and (b) show the  $W_{\gamma p}$  and  $t$  distribution. The transverse momentum  $p_t$  of the  $J/\psi$  is shown in figure (c), while in plot (d) and (e) the transverse momentum of the  $J/\psi$  decay particles with the higher and lower  $p_t$  are given. The last row shows the polar angle  $\theta$  of the  $J/\psi$  (f) and the polar angle of the  $J/\psi$  decay particles with higher (g) and lower (h)  $\theta$  angle.

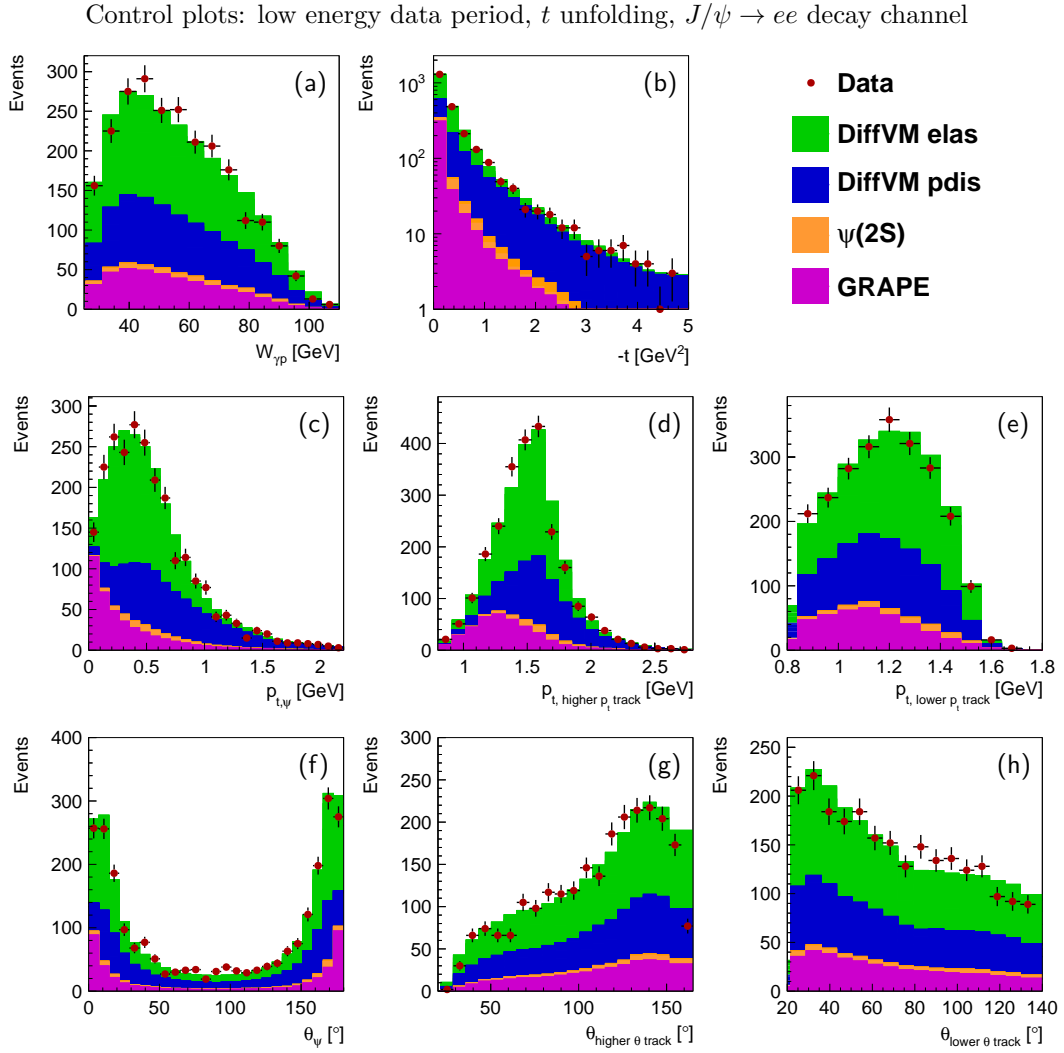
Control plots: high energy data period,  $t$  unfolding,  $J/\psi \rightarrow \mu\mu$  decay channel


**Figure 9.25:** Control plot distributions in the di-muon mass window  $m_{\mu\mu} = (2.8 - 3.3)$  GeV for the high energy data period in the  $J/\psi \rightarrow \mu\mu$  decay channel for unfolding in the variable  $t$ . The background subtracted data are shown as red circles. The green and blue coloured stacked histograms represent the contribution from elastic and proton dissociative  $J/\psi$  production. The orange histogram gives the contribution from elastic and proton dissociative  $\psi(2S)$  production. Figure (a) and (b) show the  $W_{\gamma p}$  and  $t$  distribution. The transverse momentum  $p_t$  of the  $J/\psi$  is shown in figure (c), while in plot (d) and (e) the transverse momentum of the  $J/\psi$  decay particles with the higher and lower  $p_t$  are given. The last row shows the polar angle  $\theta$  of the  $J/\psi$  (f) and the polar angle of the  $J/\psi$  decay particles with higher (g) and lower (h)  $\theta$  angle.

Control plots: high energy data period,  $W_{\gamma p}$  unfolding,  $J/\psi \rightarrow \mu\mu$  decay channel

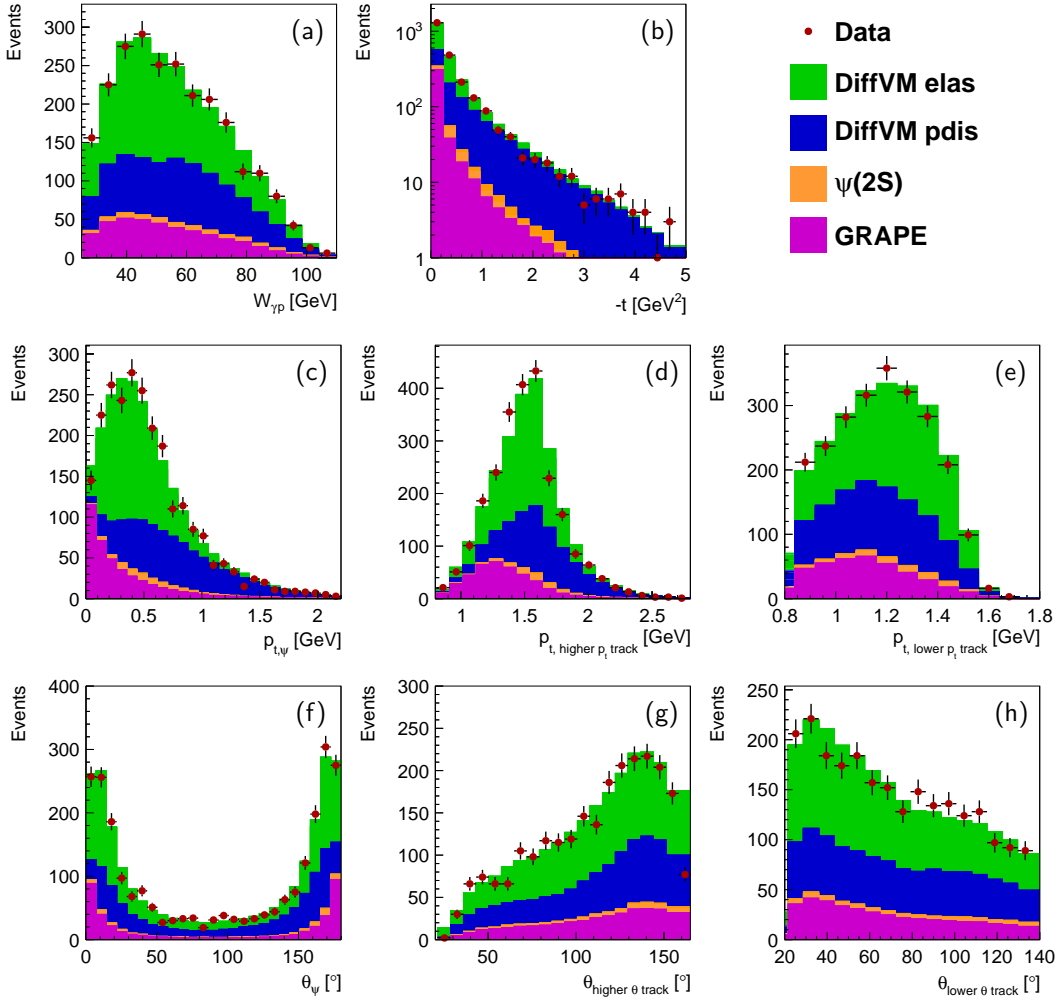


**Figure 9.26:** Control plot distributions in the di-muon mass window  $m_{\mu\mu} = (2.8 - 3.3)$  GeV for the high energy data period in the  $J/\psi \rightarrow \mu\mu$  decay channel for unfolding in the variable  $W_{\gamma p}$ . The background subtracted data are shown as red circles. The green and blue coloured stacked histograms represent the contribution from elastic and proton dissociative  $J/\psi$  production. The orange histogram gives the contribution from elastic and proton dissociative  $\psi(2S)$  production. Figure (a) and (b) show the  $W_{\gamma p}$  and  $t$  distribution. The transverse momentum  $p_t$  of the  $J/\psi$  is shown in figure (c), while in plot (d) and (e) the transverse momentum of the  $J/\psi$  decay particles with the higher and lower  $p_t$  are given. The last row shows the polar angle  $\theta$  of the  $J/\psi$  (f) and the polar angle of the  $J/\psi$  decay particles with higher (g) and lower (h)  $\theta$  angle.

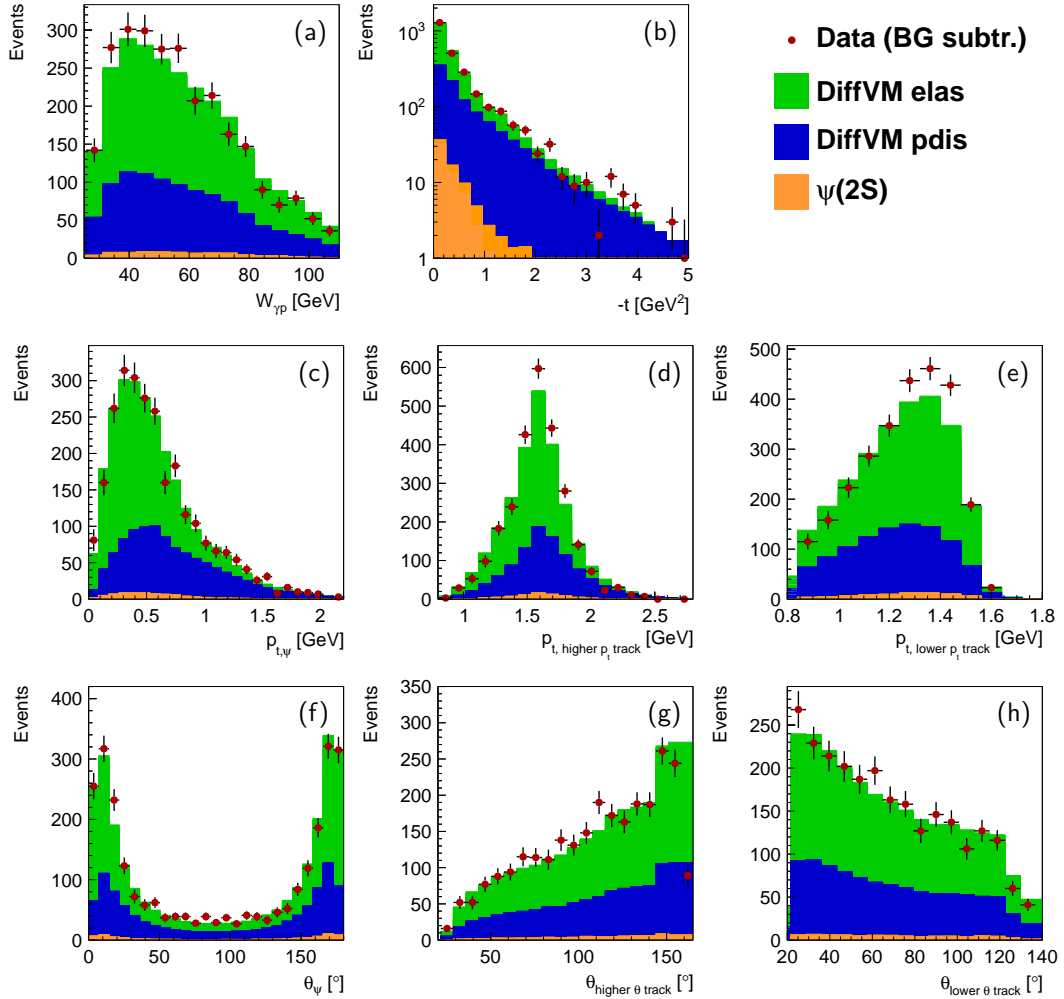


**Figure 9.27:** Control plot distributions in the di-electron mass window  $m_{ee} = (2.3 - 3.3)$  GeV for the low energy data period in the  $J/\psi \rightarrow ee$  decay channel for unfolding in the variable  $t$ . Data are shown as red circles. The green and blue coloured stacked histograms represent the contribution from elastic and proton dissociative  $J/\psi$  production. The orange histogram gives the contribution from elastic and proton dissociative  $\psi(2S)$  production. The background process contribution simulated by GRAPE is given as magenta histogram. Figure (a) and (b) show the  $W_{\gamma p}$  and  $t$  distribution. The transverse momentum  $p_t$  of the  $J/\psi$  is shown in figure (c), while in plot (d) and (e) the transverse momentum of the  $J/\psi$  decay particles with the higher and lower  $p_t$  are given. The last row shows the polar angle  $\theta$  of the  $J/\psi$  (f) and the polar angle of the  $J/\psi$  decay particles with higher (g) and lower (h)  $\theta$  angle.

Control plots: low energy data period,  $W_{\gamma p}$  unfolding,  $J/\psi \rightarrow ee$  decay channel



**Figure 9.28:** Control plot distributions in the di-electron mass window  $m_{ee} = (2.3-3.3)$  GeV for the low energy data period in the  $J/\psi \rightarrow ee$  decay channel for unfolding in the variable  $W_{\gamma p}$ . Data are shown as red circles. The green and blue coloured stacked histograms represent the contribution from elastic and proton dissociative  $J/\psi$  production. The orange histogram gives the contribution from elastic and proton dissociative  $\psi(2S)$  production. The background process contribution simulated by GRAPE is given as magenta histogram. Figure (a) and (b) show the  $W_{\gamma p}$  and  $t$  distribution. The transverse momentum  $p_t$  of the  $J/\psi$  is shown in figure (c), while in plot (d) and (e) the transverse momentum of the  $J/\psi$  decay particles with the higher and lower  $p_t$  are given. The last row shows the polar angle  $\theta$  of the  $J/\psi$  (f) and the polar angle of the  $J/\psi$  decay particles with higher (g) and lower (h)  $\theta$  angle.

Control plots: low energy data period,  $t$  unfolding,  $J/\psi \rightarrow \mu\mu$  decay channel


**Figure 9.29:** Control plot distributions in the di-muon mass window  $m_{\mu\mu} = (2.8 - 3.3)$  GeV for the low energy data period in the  $J/\psi \rightarrow \mu\mu$  decay channel for unfolding in the variable  $t$ . The background subtracted data are shown as red circles. The green and blue coloured stacked histograms represent the contribution from elastic and proton dissociative  $J/\psi$  production. The orange histogram gives the contribution from elastic and proton dissociative  $\psi(2S)$  production. Figure (a) and (b) show the  $W_{\gamma p}$  and  $t$  distribution. The transverse momentum  $p_t$  of the  $J/\psi$  is shown in figure (c), while in plot (d) and (e) the transverse momentum of the  $J/\psi$  decay particles with the higher and lower  $p_t$  are given. The last row shows the polar angle  $\theta$  of the  $J/\psi$  (f) and the polar angle of the  $J/\psi$  decay particles with higher (g) and lower (h)  $\theta$  angle.

Control plots: low energy data period,  $W_{\gamma p}$  unfolding,  $J/\psi \rightarrow \mu\mu$  decay channel

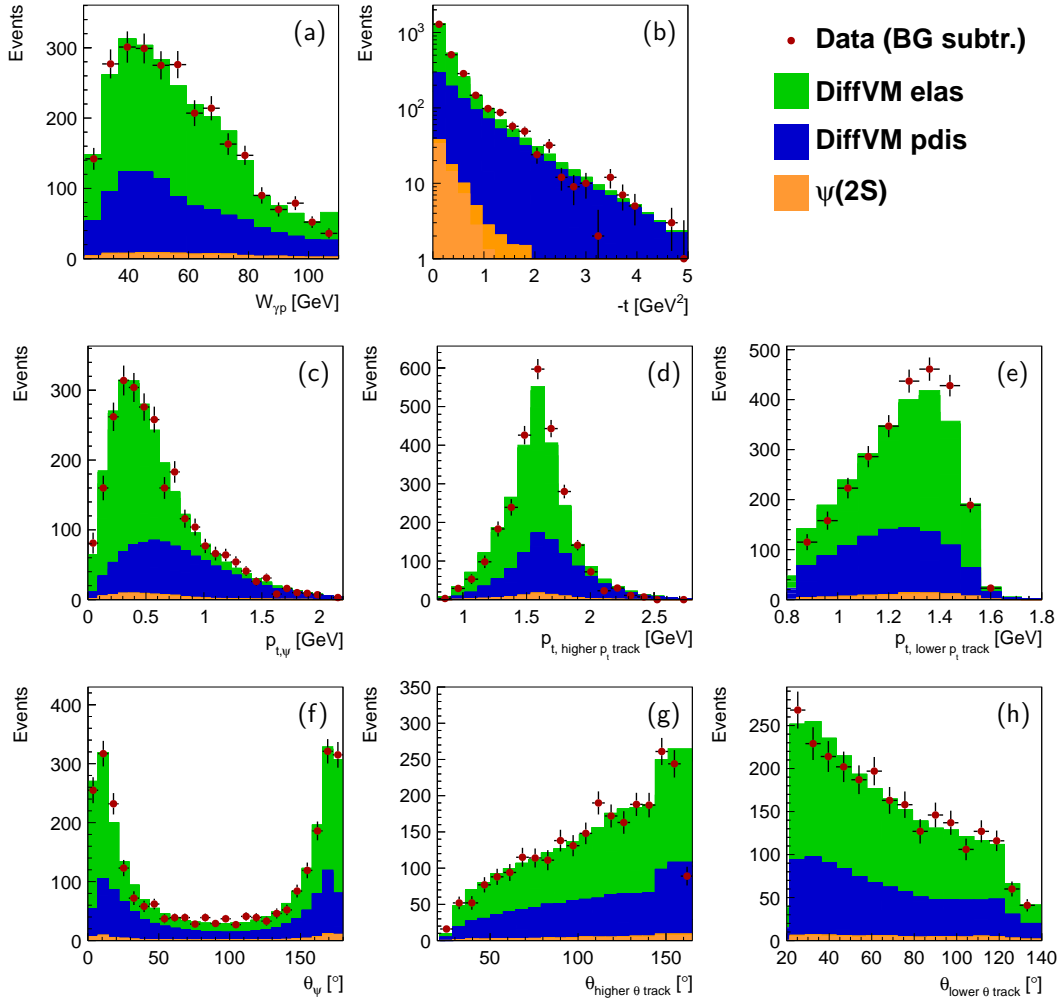


**Figure 9.30:** Control plot distributions in the di-muon mass window  $m_{\mu\mu} = (2.8 - 3.3)$  GeV for the low energy data period in the  $J/\psi \rightarrow \mu\mu$  decay channel for unfolding in the variable  $W_{\gamma p}$ . The background subtracted data are shown as red circles. The green and blue coloured stacked histograms represent the contribution from elastic and proton dissociative  $J/\psi$  production. The orange histogram gives the contribution from elastic and proton dissociative  $\psi(2S)$  production. Figure (a) and (b) show the  $W_{\gamma p}$  and  $t$  distribution. The transverse momentum  $p_t$  of the  $J/\psi$  is shown in figure (c), while in plot (d) and (e) the transverse momentum of the  $J/\psi$  decay particles with the higher and lower  $p_t$  are given. The last row shows the polar angle  $\theta$  of the  $J/\psi$  (f) and the polar angle of the  $J/\psi$  decay particles with higher (g) and lower (h)  $\theta$  angle.



C H A P T E R

# 10

## Results

This chapter presents the results of this measurement in form of differential cross sections as function of  $-t$  and  $W_{\gamma p}$  for the elastic,  $\gamma p \rightarrow J/\psi p$ , and proton dissociative,  $\gamma p \rightarrow J/\psi Y$ , produced  $J/\psi$  in the photoproduction region of  $Q^2 \lesssim 2.5 \text{ GeV}^2$ . Results for the high and low energy data periods with a centre of mass energy  $\sqrt{s}$  of 318 GeV and 225 GeV are presented for the two decay channels  $J/\psi \rightarrow ee$  and  $J/\psi \rightarrow \mu\mu$ .

### 10.1 Differential cross sections as function of $-t$ for the high energy data period

Figure 10.1 shows the unfolded differential cross section as function of  $-t$  for the elastic (left) and proton dissociative (right) process, both measured in the range of  $40 < W_{\gamma p} < 110 \text{ GeV}$  and in case of proton dissociation for the invariant proton remnant mass of  $M_P + M_\pi < M_Y < 10 \text{ GeV}$  with  $M_P$  and  $M_\pi$  the proton and pion masses.

In Table D.1 the cross section values for each point are listed including the systematic uncertainties. The bin correlation coefficients of the statistical covariance matrix for the  $J/\psi \rightarrow ee$  and  $J/\psi \rightarrow \mu\mu$  data sets are given in Table D.4 and Table D.5, respectively. The combined unfolding applied causes not only the bins within the elastic and proton dissociative sample to be correlated, but also creates correlation between bins of the two samples. This correlation is a natural consequence of the procedure applied for extracting the contribution of the two processes and reflects the true situation.

The general agreement between the two measurements performed in the different decay channels is rather good. Some small deviations are visible, which however could be caused by the unfolding process correlating the unfolded bins in the elastic and proton dissociative part. Also possible is a small oscillation of the data points due to unfolding procedure which is not fully suppressed by the regularisation.

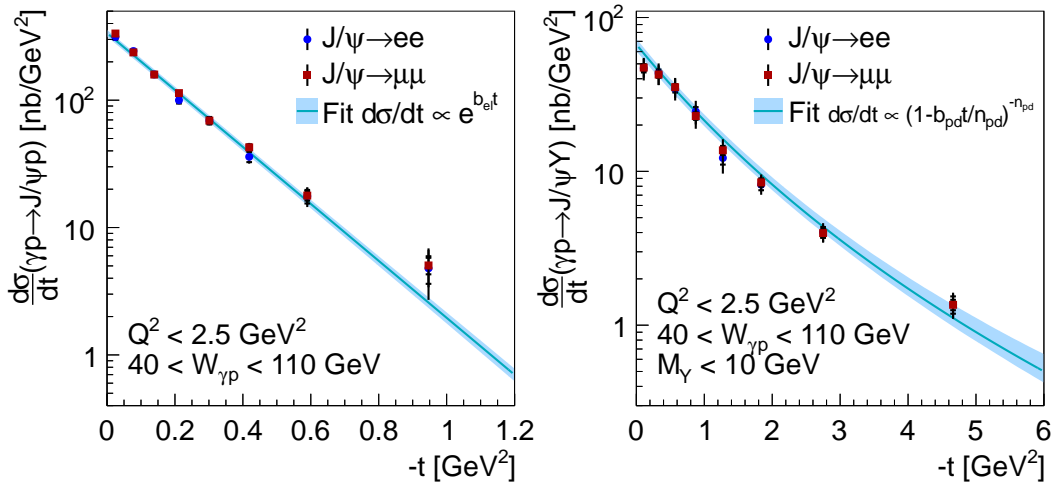


**Figure 10.1:** Differential cross section as function of  $-t$  for elastic  $\gamma p \rightarrow J/\psi p$  (left) and proton dissociative  $\gamma p \rightarrow J/\psi Y$  (right) process for the high energy data period obtained at a centre of mass energy of 318 GeV. The red circles and blue squares represent the cross sections measured in the decay channels  $J/\psi \rightarrow ee$  and  $J/\psi \rightarrow \mu\mu$ , respectively. The turquoise solid line represents the combined fits to both data sets. The inner and outer error bars reflect the square root of the diagonal elements in the covariance matrix  $\sqrt{V_{ii}}$  for only statistical and statistical plus systematic uncertainties. The normalisation uncertainties as given in Table 9.1 are not included in the systematic uncertainty representation of the data points.

## 10.1 Differential cross sections as function of $-t$ for the high energy data period

The elastic and proton dissociative cross sections for both reconstruction channels are fitted in a combined minimisation procedure using the full information from the statistical covariance matrix and all systematic sources. A detailed discussion on the  $\chi^2$  definition used to perform the fit is given in Appendix C. The normalisation uncertainties are split in three parts each with its own nuisance parameter. The first covers all normalisation effects except the track and vertex fit uncertainties, combined 5.2 %, and affects both data sets. The second and third part are the track and vertex fit uncertainties for the electron and muon decay channel only. All systematic sources, except the lepton identifications, are treated as totally correlated between the two data sets and each source gets its own nuisance parameter.

As fit function in the elastic case an exponential

$$\frac{d\sigma}{d|t|} = N_{\text{el}} \exp(-b_{\text{el}}|t|) \quad (10.1)$$

is used, with  $b_{\text{el}}$  the slope parameter. The proton dissociative cross section does not follow a pure exponential behaviour over the whole  $|t|$  range. Therefore the fit function

$$\frac{d\sigma}{d|t|} = N_{\text{pd}} \left(1 + \frac{b_{\text{pd}}}{n_{\text{pd}}} |t|\right)^{-n_{\text{pd}}} \quad (10.2)$$

is chosen. This function behaves like an exponential  $e^{-b_{\text{pd}}|t|}$  for  $\frac{b_{\text{pd}}}{n_{\text{pd}}} |t| \ll 1$  and follows a power-law  $|t|^{-n_{\text{pd}}}$  at high  $|t|$ . The additional uncertainties caused by normalisation are correctly taken into account by the fit, as described in Appendix C.

The  $|t|$  positions of the data points are bin centre corrected, following the approach given in [297]. The actual procedure applied for the bin centre determination does iteratively first perform the fit, then calculate the bin centre correction, until the relative change in position is less than 1 %. The stable condition is reached within a few iteration steps. The bin centres are listed in Table D.1.

The results of the fit parameters are listed in Table 10.1 and the correlation of the parameters is given in Table 10.2. In order to separate the statistical error from the systematic uncertainty on the fit parameters, two fits are performed. One fit uses the full information including statistical covariance matrix and systematic sources, the second makes use only of the statistical information. The first error of the parameter values given in Table 10.1 represents the uncertainty from the fit using only the statistical error information. The second is the square root subtraction of the fit parameter error from the first and second fit and represents the uncertainty due to the systematic sources.

In general the fit function describe the data well. It appears however that the fit function in case of the proton dissociative differential cross section is not optimal at low  $|t|$  values. A function with a smaller derivative at low  $|t|$  values would describe the data better, however a theoretical motivated function capable of such a behaviour is – to the knowledge of the author – not existing.

### 10.1.1 Comparison with published results

The fitted  $b$ -slope of the elastic differential cross section was determined to be  $5.15 \pm 0.07 \pm 0.05 \text{ GeV}^{-2}$ . This is larger than  $4.630 \pm 0.060^{+0.043}_{-0.163} \text{ GeV}^{-2}$  given in [29] and  $4.15 \pm 0.05^{+0.30}_{-0.18} \text{ GeV}^{-2}$  stated in [37]. However both cited analysis determine  $b$  at  $W_{\gamma p} = 90 \text{ GeV}$

performed in a double differential analysis. Still, the influence of the non-zero slope parameter of the trajectory as measured in both publications combined with the lower range in  $W_{\gamma p}$  of this analysis cannot explain the difference of the  $b$ -slope value<sup>(1)</sup>.

A more probable explanation for the difference of the elastic  $b$  slope of this measurement with the published values is that the definition of  $t$  is not identical. The definition of  $t$  in [29] is “The variable  $t$  is approximated as  $t \simeq -p_{t,\psi}^2 \dots$ ” and in [37] “The squared four-momentum transfer at the proton vertex is given by  $t \approx -p_T^2$ , the transverse-momentum squared of the dilepton system”. There is no explicit statement that this approximation is only applied on reconstruction level, but not on generator level. It seems therefore that the shown cross sections in these publication should more be understood as function of the squared transverse momentum of the  $J/\psi$ ,  $p_{t,J/\psi}^2$ , rather than of the actual  $t$ .

Hence comparing with the cited publication is only meaningful if the  $b$  slope is extracted from the differential cross section  $d\sigma/dp_{t,J/\psi}^2$  instead of  $d\sigma/dt$ . Creating the elastic differential cross section as function of  $p_{t,J/\psi}^2$  and fitting it, gives a  $b$  slope of  $4.30 \pm 0.07(\text{stat.}) \text{ GeV}^{-2}$ <sup>(2)</sup>, which is in good agreement with the published values.

Comparing the fit parameters in case of the proton dissociative differential cross section is difficult, because most analysis measuring only in the phasespace  $|t| \geq 2 \text{ GeV}^2$  in order to suppress the elastic contribution. In Fig. 10.2 the differential proton dissociative cross section as function of  $-t$  is given again, in addition the measurements at large  $|t|$  values of [30, 34] are shown. A good agreement is visible in the overlap region.

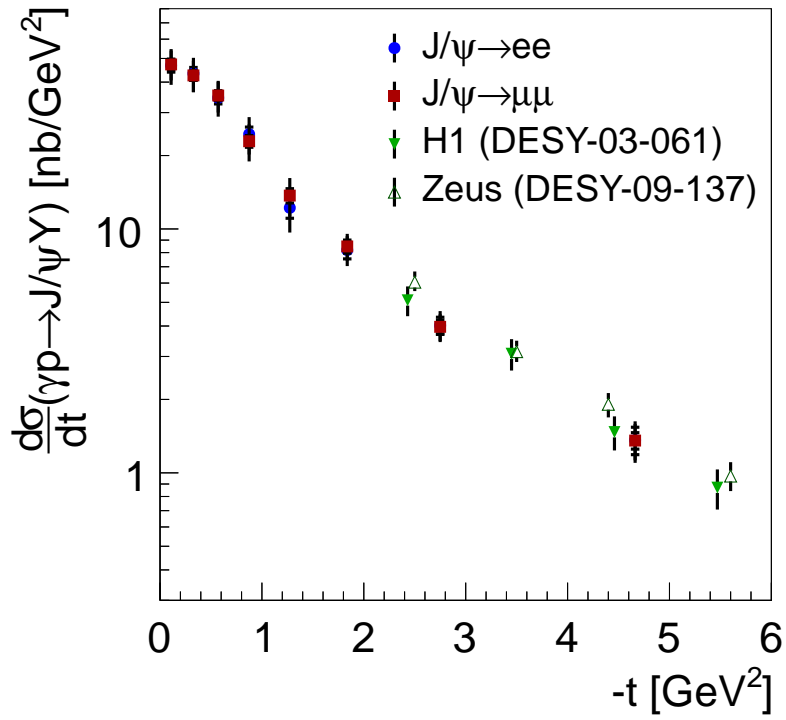
## 10.2 Differential cross sections as function of $-t$ for the low energy data period

Figure 10.3 shows the results of the differential cross sections as function of  $-t$  for the low energy data period. The representation of the data points is the same as in the high energy data period, so are the fit functions and the fitting procedure. Due to a lower proton beam energy the phase space in  $W_{\gamma p}$  is 25 – 110 GeV, but otherwise identical to the high energy data period. Because of statistical reasons the range in  $|t|$  in the proton dissociative process is restricted to  $|t| < 5 \text{ GeV}$ .

The fit parameters are given in Table 10.1. The evaluated  $b$ -slope value in the elastic case is smaller compared to the value obtained in the high energy data period. This can be explained by expressing the measured  $b$  value as  $b = b_0 + 4\alpha_1 \log(W_{\gamma p}/W_0)$ . A positive trajectory slope  $\alpha_1$  and a lower  $W_{\gamma p}$  range compared to the high energy data period causes a smaller  $b$  value.

<sup>(1)</sup>In fact the expected  $b$ -slope at a lower  $W_{\gamma p}$  value would be smaller, since  $b = b_0 + 4\alpha_1 \log(W_{\gamma p}/W_0)$  with a positive slope  $\alpha_1$ .

<sup>(2)</sup>Since this is regarded as a cross check, no full systematic evaluation is performed. The given error therefore represents only the statistical uncertainty.



**Figure 10.2:** Differential cross section as function of  $-t$  for the proton dissociative  $\gamma p \rightarrow J/\psi Y$  process obtained at a centre of mass energy of 318 GeV. The red circles and blue square represent the measurement of this thesis, the solid and open green triangles show the measurements [30,34] performed in the high  $|t|$  region ( $|t| \geq 2$  GeV<sup>2</sup>).

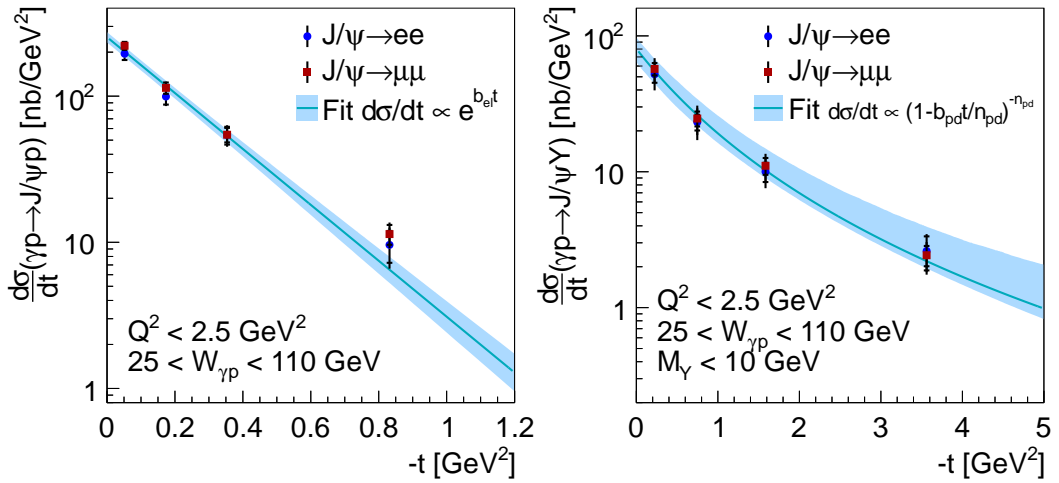


**Figure 10.3:** Differential cross section as function of  $-t$  for elastic  $\gamma p \rightarrow J/\psi p$  (left) and proton dissociative  $\gamma p \rightarrow J/\psi Y$  (right) process for the low energy data period obtained at a centre of mass energy of 225 GeV. The red circles and blue squares represent the cross sections measured in the decay channel  $J/\psi \rightarrow ee$  and  $J/\psi \rightarrow \mu\mu$ , respectively. The turquoise solid line represents the combined fits to both data sets. The inner and outer error bars reflect the square root of the diagonal elements in the covariance matrix  $\sqrt{V_{ii}}$  for only statistical and statistical plus systematic uncertainties. The normalisation uncertainties as given in Table 9.1 are not included in the systematic uncertainty representation of the data points.

### 10.3 Cross sections as function of $W_{\gamma p}$ for high and low energy data periods

In Fig. 10.4 the unfolded differential cross sections as function of  $W_{\gamma p}$  for the elastic (left) and proton dissociative (right) process are shown. The blue circles and red squares represent the cross section for the high energy data period in the reconstruction channels  $J/\psi \rightarrow ee$  and  $J/\psi \rightarrow \mu\mu$ . The pink upwards and green downwards triangles show the cross section for the low energy data period also for the two reconstruction channels  $J/\psi \rightarrow ee$  and  $J/\psi \rightarrow \mu\mu$ . The phase space in virtuality for both process is  $Q^2 \lesssim 2.5 \text{ GeV}^2$  and the  $-t$  range for elastic

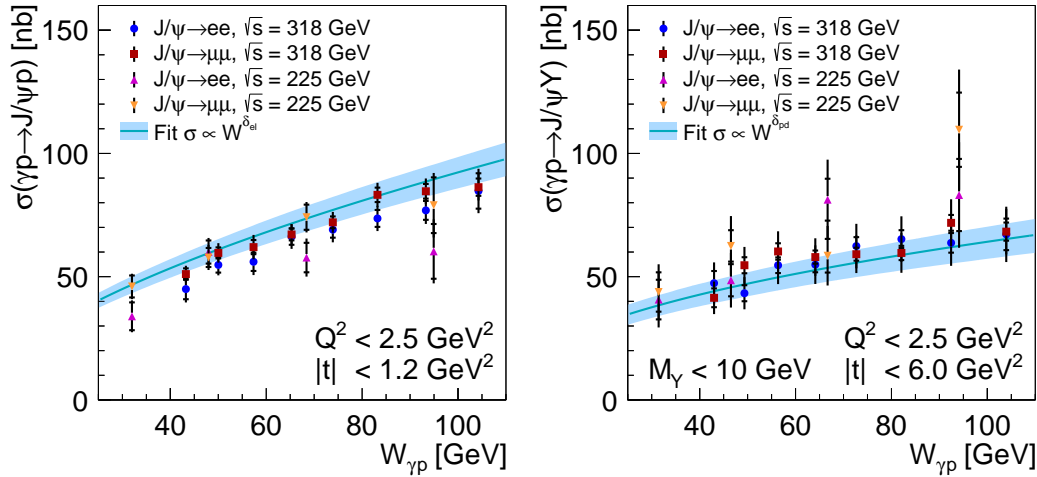


**Figure 10.4:** Cross section as function of  $W_{\gamma p}$  for elastic  $\gamma p \rightarrow J/\psi p$  (left) and proton dissociative  $\gamma p \rightarrow J/\psi Y$  (right) process for the high and low energy data period obtained at a centre of mass energy of 318 GeV and 225 GeV, respectively. The red circles and blue squares represent the cross sections measured in the decay channel  $J/\psi \rightarrow ee$  and  $J/\psi \rightarrow \mu\mu$ , respectively, for the high energy data period obtained at a centre of mass energy of 318 GeV. The pink upwards and green downwards triangles represent the cross sections measured in the decay channel  $J/\psi \rightarrow ee$  and  $J/\psi \rightarrow \mu\mu$ , respectively, for the low energy data period obtained at a centre of mass energy of 225 GeV. The turquoise solid lines represents the combined fits including all four data sets. The inner and outer error bars reflect the square root of the diagonal elements in the covariance matrix  $\sqrt{V_{ii}}$  for only statistical and statistical plus systematic uncertainties. The normalisation uncertainties as given in Table 9.1 are not included in the systematic uncertainty representation of the data points.

is  $|t| < 1.2 \text{ GeV}^2$ . For proton dissociative the measurement is done for low proton remnant mass of  $M_Y < 10 \text{ GeV}$  and  $|t| < 6 \text{ GeV}^2$ .

Because the actual measurement for proton dissociative process for the low energy data period is only performed in  $|t|$  up to  $5 \text{ GeV}^2$ , a phase space correction,  $c$ , is added to the

shown data points. It is calculated by

$$c = \frac{\int_0^{6 \text{ GeV}^2} dT \left( \frac{d\sigma}{dT} \right)_{\text{pdis,LER}}}{\int_0^{5 \text{ GeV}^2} dT \left( \frac{d\sigma}{dT} \right)_{\text{pdis,LER}}} = 1.012 \quad (10.3)$$

with  $T \equiv |t|$  and using the parameters evaluated in the proton dissociative fit of Fig. 10.3.

As in all presented cross sections, the elastic and the proton dissociative cross section data points are correlated. In case of the cross section as function of  $W_{\gamma p}$  this is nicely visible, since an up fluctuation of a data point in one process has usually a corresponding down fluctuation in the other process.

The combined cross section fit of elastic and proton dissociative process is using for both processes a power law function

$$\sigma_{\text{el}}(W) = N_{\text{el}} \left( \frac{W}{90 \text{ GeV}} \right)^{\delta_{\text{el}}} \quad (10.4)$$

$$\sigma_{\text{pd}}(W) = N_{\text{pd}} \left( \frac{W}{90 \text{ GeV}} \right)^{\delta_{\text{pd}}} . \quad (10.5)$$

The applied fit procedure and the performed bin centre correction are equal to the description as given in Sec. 10.1.

It appears that the fit tends to lay above the data points in the elastic cross section, but below in the proton dissociative case. This is caused by the combined fitting procedure applied. The behaviour that a fit function after minimisation is not crossing the data points if a  $\chi^2$  definition is used which incorporates systematic shifts is a general feature (see for instance [298]). For example in [299] a similar  $\chi^2$  definition is used, resulting in similar effects. In ratio plots (fit function over data) in [299] the data points are shifted for better visibility by the size of the normalisation nuisance parameter. This procedure however is not applied here.

### 10.3.1 Comparison with published results

The  $\delta$  fit parameters for the elastic and proton dissociative process are determined to be  $\delta_{\text{el}} = 0.597 \pm 0.032 \pm 0.011$  and  $\delta_{\text{pd}} = 0.44 \pm 0.05_{-0.03}^{+0.02}$ . The elastic  $\delta$  slope was measured to be smaller than in [29] giving a value of  $0.75 \pm 0.03 \pm 0.03$  and [37] states also a smaller value of  $0.69 \pm 0.02 \pm 0.03$ . However both publication also include data points at very large  $W_{\gamma p}$  values. Part of the difference in the parameter value can be explained by this effect. Restricting the cross section range to  $W_{\gamma p} = 40 \text{ GeV} - 110 \text{ GeV}$  and refitting the data sets results in a smaller  $\delta$  value.

Figure 10.5 shows the elastic cross section as function of  $W_{\gamma p}$  in the range  $W_{\gamma p} = 40 \text{ GeV} - 110 \text{ GeV}$ . The measurement [29] is given as solid green triangles and the measurement [37] as open green triangles. A small normalisation difference is visible between the muon channel of this measurement and the published results.

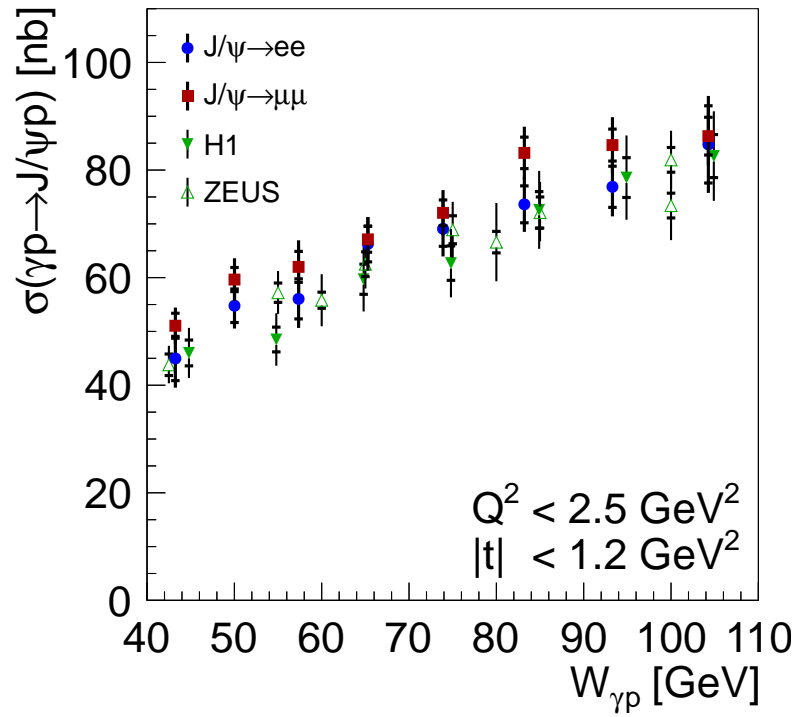


**Figure 10.5:** Cross section as function of  $W_{\gamma p}$  for elastic  $\gamma p \rightarrow J/\psi p$  process obtained at a centre of mass energy of 318 GeV. The red circles and blue squares represent the cross section created with reconstruction channel  $J/\psi \rightarrow ee$  and  $J/\psi \rightarrow \mu\mu$ , respectively. The solid green triangles represent the measurement [29] and data points taken from [37] are represented by the open green triangles.

Data period	Process	Parameter	Fit value
HER	$\gamma p \rightarrow J/\psi p$	$N_{\text{el}}$	$336 \pm 5^{+21}_{-18} \text{ nb/GeV}^2$
		$b_{\text{el}}$	$5.15 \pm 0.07 \pm 0.05 \text{ GeV}^{-2}$
	$\gamma p \rightarrow J/\psi Y$	$N_{\text{pd}}$	$66.9 \pm 1.7^{+6.7}_{-5.8} \text{ nb/GeV}^2$
		$b_{\text{pd}}$	$1.25 \pm 0.06 \pm 0.02 \text{ GeV}^{-2}$
		$n_{\text{pd}}$	$6.1^{+1.0+0.9}_{-0.7-0.7}$
LER	$\gamma p \rightarrow J/\psi p$	$N_{\text{el}}$	$253 \pm 13^{+21}_{-18} \text{ nb/GeV}^2$
		$b_{\text{el}}$	$4.40^{+0.21+0.14}_{-0.20-0.17} \text{ GeV}^{-2}$
	$\gamma p \rightarrow J/\psi Y$	$N_{\text{pd}}$	$80^{+12+17}_{-10-12} \text{ nb/GeV}^2$
		$b_{\text{pd}}$	$1.78^{+0.50+0.37}_{-0.36-0.15} \text{ GeV}^{-2}$
		$n_{\text{pd}}$	$3.5^{+2.0+2.3}_{-0.9-0.8}$
HER + LER	$\gamma p \rightarrow J/\psi p$	$N_{\text{el}}$	$86.7 \pm 1.0^{+6.3}_{-5.6} \text{ nb}$
		$\delta_{\text{el}}$	$0.597 \pm 0.032 \pm 0.011$
	$\gamma p \rightarrow J/\psi Y$	$N_{\text{pd}}$	$61.2 \pm 1.1^{+6.5}_{-5.5} \text{ nb}$
		$\delta_{\text{pd}}$	$0.44 \pm 0.05^{+0.02}_{-0.03}$

**Table 10.1:** Fit parameter values. HER and LER denote the high and low energy data period. The fit functions are given in the text. The first error gives the statistical error, the second the systematic uncertainty.

$\begin{pmatrix} 12.5 & & & & \\ 53.0 & 40.3 & & & \\ -9.6 & -8.1 & 30.8 & & \\ 6.8 & 16.5 & -23.8 & -79.7 & \\ N_{\text{el}} & b_{\text{el}} & N_{\text{pd}} & b_{\text{pd}} & n_{\text{pd}} \end{pmatrix}$	$\begin{pmatrix} 23.0 & & & & \\ 1.2 & 36.3 & & & \\ -13.7 & -42.6 & 14.5 & & \\ 8.5 & 51.0 & 9.7 & -89.7 & \\ N_{\text{el}} & b_{\text{el}} & N_{\text{pd}} & b_{\text{pd}} & n_{\text{pd}} \end{pmatrix}$
(a)	(b)
$\begin{pmatrix} 18.4 & & & \\ 1.7 & -4.1 & & \\ -14.3 & -29.5 & 5.0 & \\ N_{\text{el}} & \delta_{\text{el}} & N_{\text{pd}} & \delta_{\text{pd}} \end{pmatrix}$	
(c)	

**Table 10.2:** The correlation values in percent for the differential cross section fits as function of  $t$  in the high and low energy data period are given in table (a) and (b). Table (c) shows the correlation values in percent for the parameters of the cross section fit as function of  $W_{\gamma p}$ . The correlation to the systematic uncertainty (nuisance) parameters are dropped.

### 10.3.2 Rapidity gap survival probability corrections

From the elastic and proton dissociative cross section as function of  $W_{\gamma p}$  as shown in Fig. 10.4 and from the  $\delta$  slopes determined by the fitting procedure, it is clear that the shape and normalisation differ between the two  $J/\psi$  production “modes”. But in the picture of factorisation in the proton vertex (see for instance [300]) one would expect the elastic and proton dissociative cross section as function of  $W_{\gamma p}$  to agree.

As described in Sec. 2.1.10 for proton dissociative processes the rapidity gap survival probability  $S^2$  is smaller than 1 and therefore must be considered if one compares the elastic with the proton dissociative cross section in  $W_{\gamma p}$ . In [131] an explicit calculation is performed to evaluate the size of  $S^2$  for  $J/\psi$  production in  $\gamma p$  scattering.

The actual values for  $S^2$  in [131] are only given as a plot in  $W_{\gamma p}$  for certain  $Q^2$  values. The applied correction is read of the plot in [131] as  $S^2 = 0.8550$  for  $W_{\gamma p} = 40$  GeV and  $S^2 = 0.7833$  at  $W_{\gamma p} = 110$  GeV for  $Q^2 = 1$  GeV<sup>2</sup>. The correction factors for the  $W_{\gamma p}$  values in between are approximated by a linear function.

Figure 10.6 shows on the left side the the cross section as function of  $W_{\gamma p}$  for the elastic and proton dissociative process for the high energy data period for both decay channels used in this analysis. On the right side the same distributions are shown but the proton dissociative cross section is corrected by the evaluated rapidity gap survival factor  $S^2$ . The agreement of the shape and normalisation between the elastic and proton dissociative cross section after applying the correction is better. But due to the extraction of the survival probability this evaluation has more a qualitative than a quantitative character.

However, the agreement, achieved by taking into account the rapidity gap survival probability correction, suggests that the proton vertex factorisation is fulfilled.

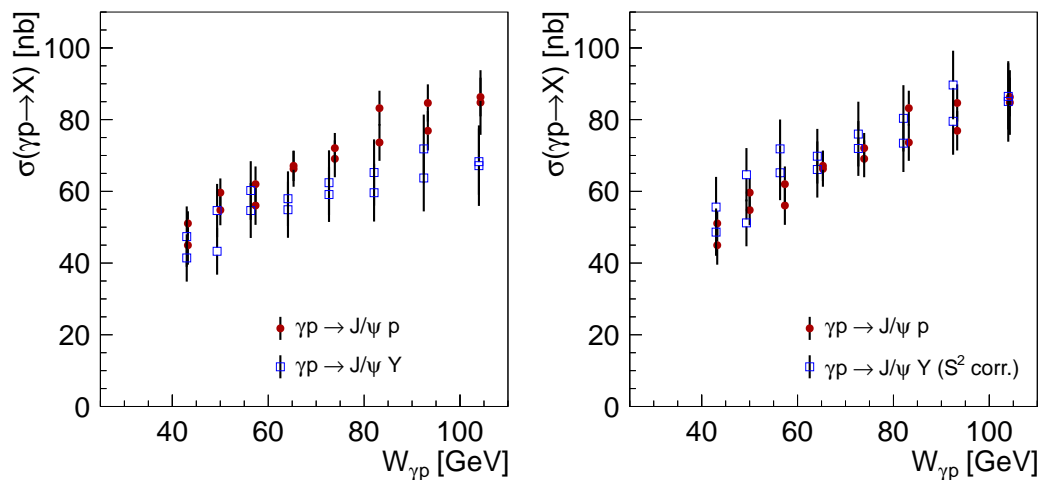


**Figure 10.6:** The left plot shows the elastic and proton dissociative cross section as function of  $W_{\gamma p}$  for the high energy data period as solid red circles and open blue squares, respectively, for both used decay channels. On the right plot the proton dissociative cross section is corrected by the rapidity gap survival probability extracted from [131].



## Summary, conclusion and outlook

In this thesis a simultaneous measurement of elastic ( $ep \rightarrow J/\psi p$ ) and proton dissociative ( $ep \rightarrow J/\psi Y$ ) photoproduction of  $J/\psi$  vector mesons in the photon virtuality phase space of  $Q^2 \lesssim 2.5 \text{ GeV}^2$  is performed. For this purpose two run periods are used, designated as high and low energy data period, recorded at two different  $ep$  centre of mass energies of 318 GeV and 225 GeV, obtained with different proton energies of 920 GeV and 460 GeV. They correspond to an integrated luminosity of  $130 \text{ pb}^{-1}$  and  $10.8 \text{ pb}^{-1}$ , respectively. The data set recorded at the reduced nominal proton energy allows to access a lower kinematic phase space in the photon proton centre of mass energy  $W_{\gamma p}$  for  $J/\psi$  events reconstructed from central tracks, than was previously possible. The combined range in  $W_{\gamma p}$  for both data periods is  $20 \text{ GeV} < W_{\gamma p} < 110 \text{ GeV}$ .

The used online selection is based on the Fast Track Trigger, reconstructing during the data recording both tracks from the leptonic decay channels  $J/\psi \rightarrow ee$  and  $J/\psi \rightarrow \mu\mu$ .

Differential cross sections for the high and low energy data period in both decay channels as function of the squared momentum transfer at the proton vertex,  $t$ , and as function of  $W_{\gamma p}$  are simultaneously determined for the elastic and proton dissociative process by means of an unfolding procedure. This unfolding technique allows not only to take into account the correlations of the elastic and proton dissociative process, but also to properly account for the correlations of bins in which the differential cross sections are determined.

The unfolded differential cross section data points are used in a combined fit of the elastic and proton dissociative process. The fit includes the measurements for both decay channels,  $J/\psi \rightarrow ee$  and  $J/\psi \rightarrow \mu\mu$ , to determine the normalisation and shape parameters of the used fit functions. The performed fits take properly into account the full covariance matrices of the cross section data points and also account for correlations of the systematic uncertainties of the different data sets by use of an adequate  $\chi^2$  definition.

The measured cross sections and parameters from the cross section fits are generally in agreement with previous measurements, where such exist, or the source of differences, where

they occur, are discussed and understood. The differential elastic cross section as function of  $t$  is fitted with an exponential distribution  $d\sigma/dt \propto e^{bt}$ , which yields a  $b$ -slope value of  $5.15 \pm 0.07(\text{stat.}) \pm 0.05(\text{syst.}) \text{ GeV}^{-2}$  for the high energy data sample. The measurement is performed as function of  $t$ , as defined at the proton vertex, instead of its approximation by the squared transverse momentum of the  $J/\psi$ , as previous measurements used to do. The differential cross section as function of  $t$  for the proton dissociative process in photoproduction at low  $t$  values ( $|t| < 2 \text{ GeV}^2$ ) was measured last in [31]. The luminosity used in this analysis overtops that measurement by about a factor of 50. The data obtained within this thesis may be used in the future to further test theories or parameters relevant in elastic and proton dissociative  $J/\psi$  photoproduction. For instance, this data set could be used to extract the triple pomeron coupling as done in [80].

The cross section dependence as function of  $W_{\gamma p}$  for elastic and proton dissociative process was fitted with a power law function,  $\sigma(W_{\gamma p}) \propto W_{\gamma p}^\delta$ , with  $\delta$  being the slope parameter, for which values of  $0.597 \pm 0.032(\text{stat.}) \pm 0.011(\text{syst.})$  and  $0.44 \pm 0.05(\text{stat.})_{-0.03}^{+0.02}(\text{syst.})$  are determined for the two processes. The simultaneous measurement of the  $W_{\gamma p}$  dependence may be an interesting test ground for theoretical predictions of  $J/\psi$  production. For example it could be shown in this thesis that taking into account the corrections due to a non unity rapidity gap survival probability the cross section as function of  $W_{\gamma p}$  between the elastic and proton dissociative process agree nicely. To allow further studies on the data obtained in this work, the full data tables, including statistical covariance matrices and systematic uncertainties for each source, are listed in the appendix.

$J/\psi$  and in general vector meson measurements will be an important topic of the physics program at the future LHeC (Large Hadron Electron Collider) collider, as can be seen in the following statement taken from [301]

GPDs<sup>(1)</sup> can also be accessed in the production of vector mesons. Measurements of the  $t$  and  $W$  dependence of light ( $\rho$ ) and heavy ( $J/\psi, \Upsilon$ ) vector meson production will be important for the determination of proton structure and saturation effects at low  $x$  at the LHeC.

From the authors personal experience obtained by performing such an analysis at HERA, it is just to hope that a future LHeC detector will be equipped in the forward direction with highly efficient detector systems covering the needed acceptance region for separating elastic and proton dissociative events, in order to make such measurements feasible with the required precision to achieve the addressed goals.

---

<sup>(1)</sup>Generalized parton distributions, author's note



## Derivations

### A.1 Derivation of inelasticity $y_{mh}$ using the modified Jacquet Blondel method

The inelasticity is defined as

$$y \equiv \frac{(p \cdot q)}{(p \cdot k)}, \quad (\text{A.1})$$

whereas  $p$ ,  $k$  and  $q$  denote the four-momenta of the beam proton and electron, and the four-momentum transfer at the electron vertex, respectively.

The denominator can be expressed as  $(p \cdot k) \simeq 2E_P E_e$  with  $E_P$  and  $E_e$  representing the beam proton and electron energies. The approximation in the formula contains the neglect of the proton and electron mass contributions which is assumed to be small with respect to the energies.

The nominator can be rewritten taking into account the four-momentum conservation of a scattering process. I.e.

$$(p \cdot q) = p \cdot (p' - p + p_\psi) \quad (\text{A.2})$$

$$= (p \cdot p') - M_p^2 + (p \cdot p_\psi), \quad (\text{A.3})$$

whereas the variables  $p'$  and  $p_\psi$  denote the four-momentum of the outgoing proton (or proton remnant) and the  $J/\psi$ , respectively. Neglecting also in this equation the proton mass  $M_p$  contribution Eq. (A.2) can be written as

$$(p \cdot q) = E_p E_p' (1 - \cos \theta_p') + E_p (E_\psi - p_{z,\psi}). \quad (\text{A.4})$$

Since the outgoing proton cannot be measured the first term in Eq. (A.4) is neglected. This is however not a large approximation since  $\theta_p'$  and therefore the whole first term is small.

Putting the approximation for the denominator and nominator together reveals the reconstructed inelasticity as it is used in the analysis to be

$$y_{mh} = \frac{(E - p_z)_\psi}{2E_e}. \quad (\text{A.5})$$

## A.2 Derivation of reconstruction of $t$

A short derivation is given for the reconstruction of  $t$  as  $-p_{t,\psi}^2$ . The variable  $t$  is defined as

$$\begin{aligned} t &\equiv (p_p - p'_p)^2 \\ &= (p_\psi - q)^2, \quad \text{since } p_p + p_e = p'_p + p'_e + p_\psi \\ &\quad \text{with } q \equiv p_e - p'_e \\ &= -Q^2 + m_\psi^2 - 2E_\gamma E_\psi + 2|\mathbf{p}_\gamma||\mathbf{p}_\psi| \cos \theta_{\gamma\psi} \end{aligned} \quad (\text{A.6})$$

Four-momenta are displayed as  $p$ , energies as  $E$ , three vectors as  $\mathbf{p}$  and masses as  $m$ . With sub scripts  $p, p', e, e', \gamma$  and  $\psi$  denote the incoming and outgoing proton and electron, the photon and the  $J/\psi$ , respectively.

In photoproduction  $Q^2 \sim 0$  the photon energy is  $E_\gamma = |\mathbf{p}_\gamma|$  and the angle between the photon and the  $J/\psi$  is  $\theta_{\gamma\psi} = \pi - \theta_\psi$ . Hence

$$t \simeq m_\psi^2 - 2E_\gamma E_\psi (1 + \cos \theta_\psi). \quad (\text{A.7})$$

The center of mass energy in the photon proton rest frame  $W_{\gamma p}$  is defined as

$$W_{\gamma p}^2 = (p_\gamma + p_p)^2 \simeq 4E_\gamma E_p, \quad (\text{A.8})$$

but can in photoproduction also be written as

$$\begin{aligned} W_{\gamma p}^2 &\simeq sy, \quad \text{with } y_{mh} = \frac{(E - p_z)_\psi}{2E_e} \\ &\quad \text{and } s \simeq 4E_p E_e \\ &\simeq 2(E - p_z)_\psi E_p. \end{aligned} \quad (\text{A.9})$$

Combining Eq. (A.8) with Eq. (A.9) gives the photon energy as

$$E_\gamma \simeq \frac{1}{2}(E - p_z)_\psi, \quad (\text{A.10})$$

Inserting Eq. (A.10) into Eq. (A.7) and using the identity  $E_\psi(1 + \cos \theta_\psi) = (E + p_z)_\psi$  gives the approximation

$$t \simeq -p_{t,\psi}^2. \quad (\text{A.11})$$

### A.3 Derivation of “or” efficiency correction as applied for muon identification

The muon identification efficiencies can be seen as probabilities for identification. Therefore here  $p$  is used to represent these probabilities. The question at hand is: what is the probability of identifying either track 1 or 2, or of both:<sup>(1)</sup>

$$p(1|2) = p(1\bar{2}) + p(\bar{1}2) + p(12) \quad (\text{A.12})$$

$$= p_1(1 - p_2) + (1 - p_1)p_2 + p_1p_2 \quad (\text{A.13})$$

$$= p_1 + p_2 - p_1p_2. \quad (\text{A.14})$$

Therefore the correction can be written as

$$w = \frac{p^{\text{D}}(1|2)}{p^{\text{MC}}(1|2)} \quad (\text{A.15})$$

$$= \frac{p_1^{\text{D}} + p_2^{\text{D}} - p_1^{\text{D}}p_2^{\text{D}}}{p_1^{\text{MC}} + p_2^{\text{MC}} - p_1^{\text{MC}}p_2^{\text{MC}}}. \quad (\text{A.16})$$

$$(\text{A.17})$$

With  $p_i^{\text{D}}$  and  $p_i^{\text{MC}}$  the probabilities for data and MC simulation, respectively.

The formula can be rewritten only as efficiencies from MC simulation and single track efficiency correction factors  $w_i = p_i^{\text{D}}/p_i^{\text{MC}}$  as

$$w = \frac{w_1p_1^{\text{MC}} + w_2p_2^{\text{MC}} - w_1p_1^{\text{MC}}w_2p_2^{\text{MC}}}{p_1^{\text{MC}} + p_2^{\text{MC}} - p_1^{\text{MC}}p_2^{\text{MC}}}. \quad (\text{A.18})$$

### A.4 Derivation of shift $\Delta x$ on true, unfolded output vector, due to alternative response matrix

The true vector  $x$  is calculated by

$$\begin{aligned} x &= By, \quad \text{with } B = EA^{\text{T}}V_y^{-1}, \\ E &= F^{-1} \text{ and} \\ F &= A^{\text{T}}V_y^{-1}A + \tau^2L^2 \end{aligned}$$

as given in Eq. 9.7. The contribution from the additional feature in TUnfold of area preservation is neglected here.

---

<sup>(1)</sup>As stated in the main text, the same idea is exploited for KALEP or iron muon identification. But for clarity the picture of two tracks is used.

Appendix A Derivations

An alternative response matrix  $A'$  causes a different true vector  $x'$  and therefore the shift in  $x$  is defined as  $\Delta x = x' - x$ . The above equation for  $x'$  reads

$$\begin{aligned}
 x' &= B'y \\
 \Leftrightarrow [(A + \Delta A)^\top V_y^{-1}(A + \Delta A) + \tau^2 L^2] (x + \Delta x) &= (A + \Delta A)^\top V_y^{-1}, \\
 \text{with } A' &= A + \Delta A \\
 \Leftrightarrow Fx + F\Delta x + \Delta A^\top V_y^{-1}Ax + A^\top V_y^{-1}\Delta Ax + \mathcal{O}(\Delta A^2) + \mathcal{O}(\Delta A\Delta x) &= (A + \Delta A)^\top V_y^{-1} \\
 \text{for } \Delta A \rightarrow 0 \text{ and } \Delta x \rightarrow 0.
 \end{aligned}$$

Therefore by neglecting the higher order terms it follows directly

$$\Delta x \simeq E\Delta A^\top V_y^{-1}(y - Ax) - B\Delta Ax.$$

APPENDIX



**Number of  $J/\psi$  events**

## B.1 Di-muon mass distribution fits

### B.1.1 Di-muon mass distribution fits for the high energy data period

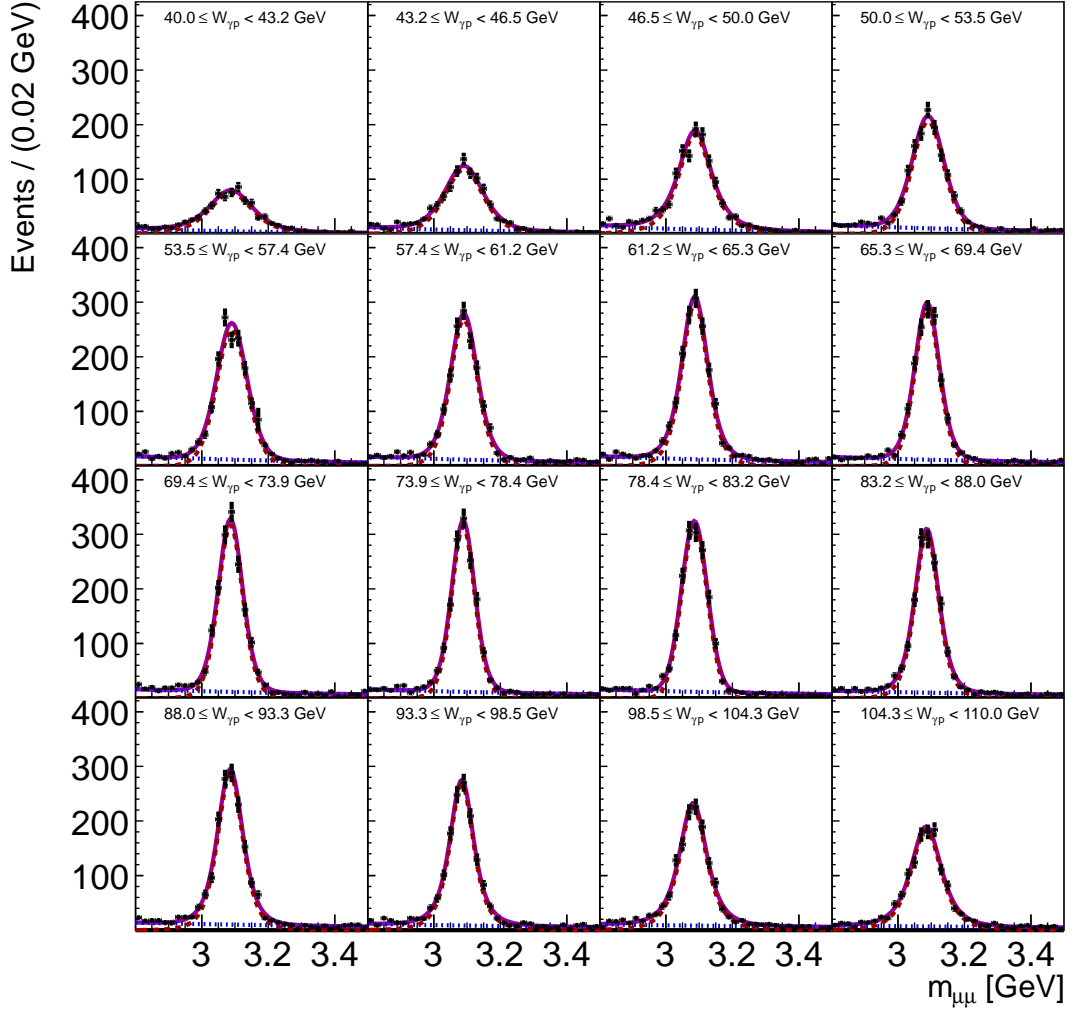


**Figure B.1:** The di-muon mass distributions shown in bins of reconstructed  $W_{\gamma p}$  for the high energy data period in the  $\overline{\text{tag}_W}$  sample are given as black circles. The solid magenta coloured line represents the combined signal and background fit used to evaluate the number of  $J/\psi$  events. The  $J/\psi$  signal function of the fit is given as dashed red line, the background distribution as dashed blue line. The di-muon mass distributions are shown in the range 2.8 - 3.5 GeV for better visibility, although the fits are performed in the range 2.3 - 5 GeV.

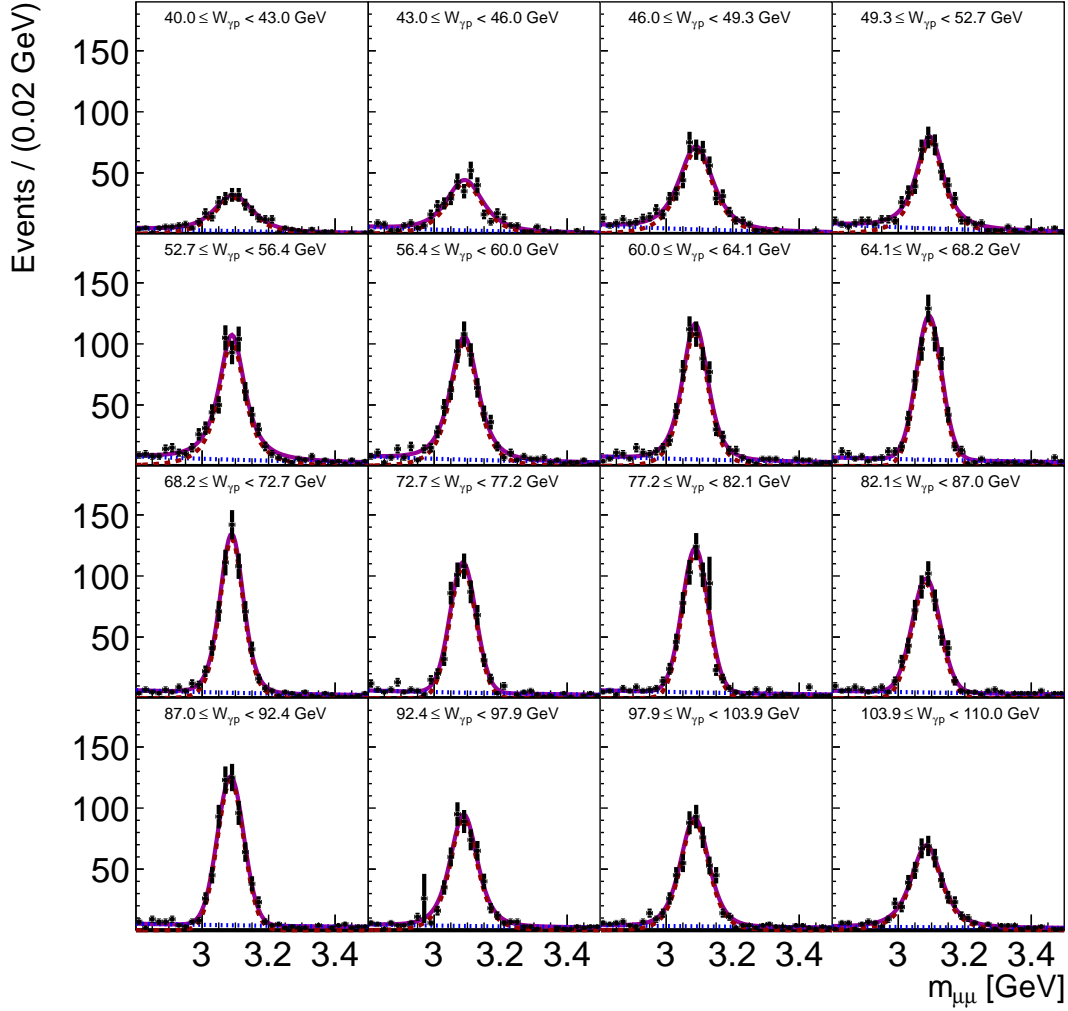


**Figure B.2:** The di-muon mass distributions shown in bins of reconstructed  $W_{\gamma p}$  for the high energy data period in the  $\text{tag}_W$  sample are given as black circles. The solid magenta coloured line represents the combined signal and background fit used to evaluate the number of  $J/\psi$  events. The  $J/\psi$  signal function of the fit is given as dashed red line, the background distribution as dashed blue line. The di-muon mass distributions are shown in the range 2.8 - 3.5 GeV for better visibility, although the fits are performed in the range 2.3 - 5 GeV.

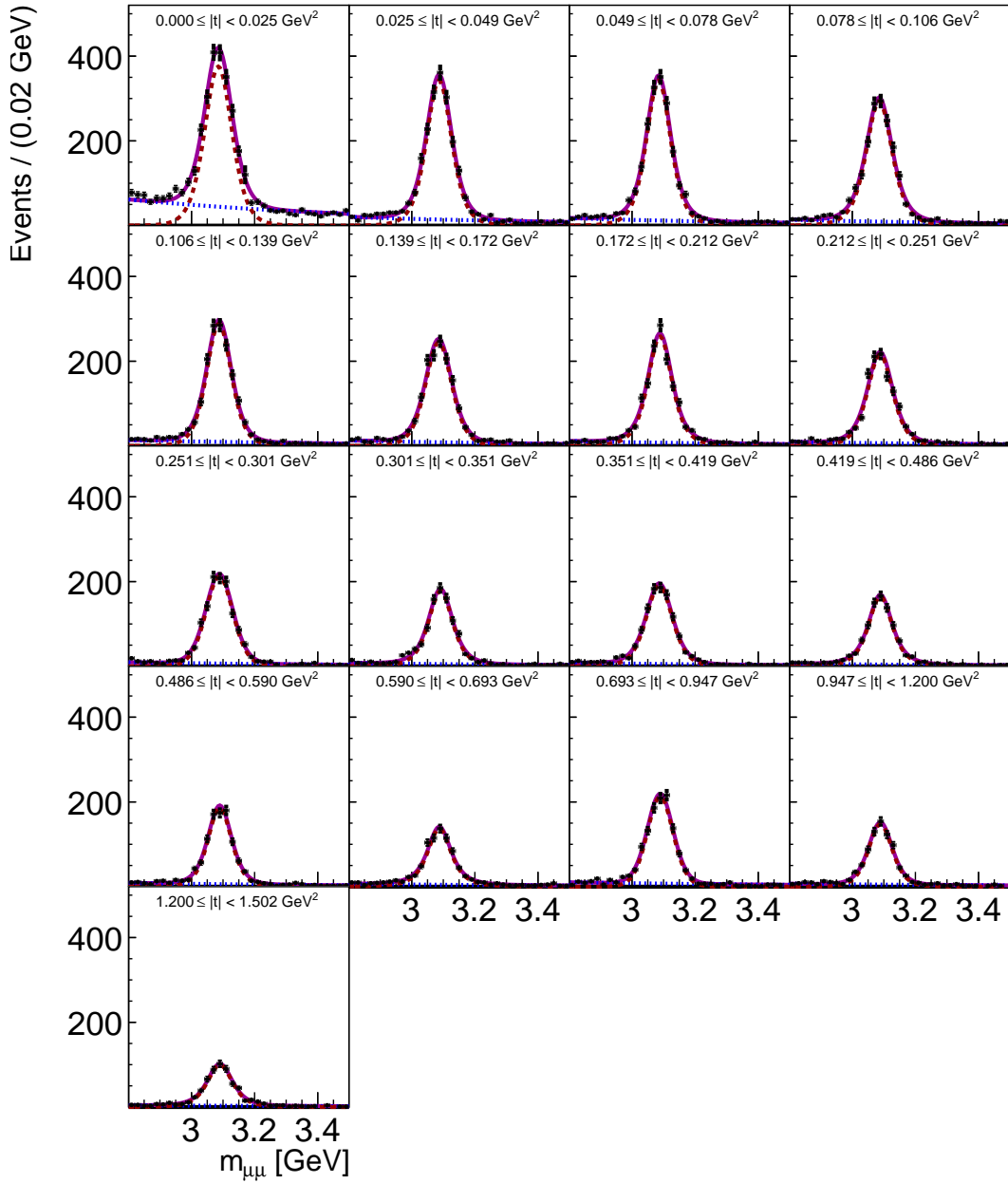


**Figure B.3:** The di-muon mass distributions shown in bins of reconstructed  $|t|$  for the high energy data period in the non-tagged sample are given as black circles. The solid magenta coloured line represents the combined signal and background fit used to evaluate the number of  $J/\psi$  events. The  $J/\psi$  signal function of the fit is given as dashed red line, the background distribution as dashed blue line. The di-muon mass distributions are shown in the range 2.8 - 3.5 GeV for better visibility, although the fits are performed in the range 2.3 - 5 GeV.

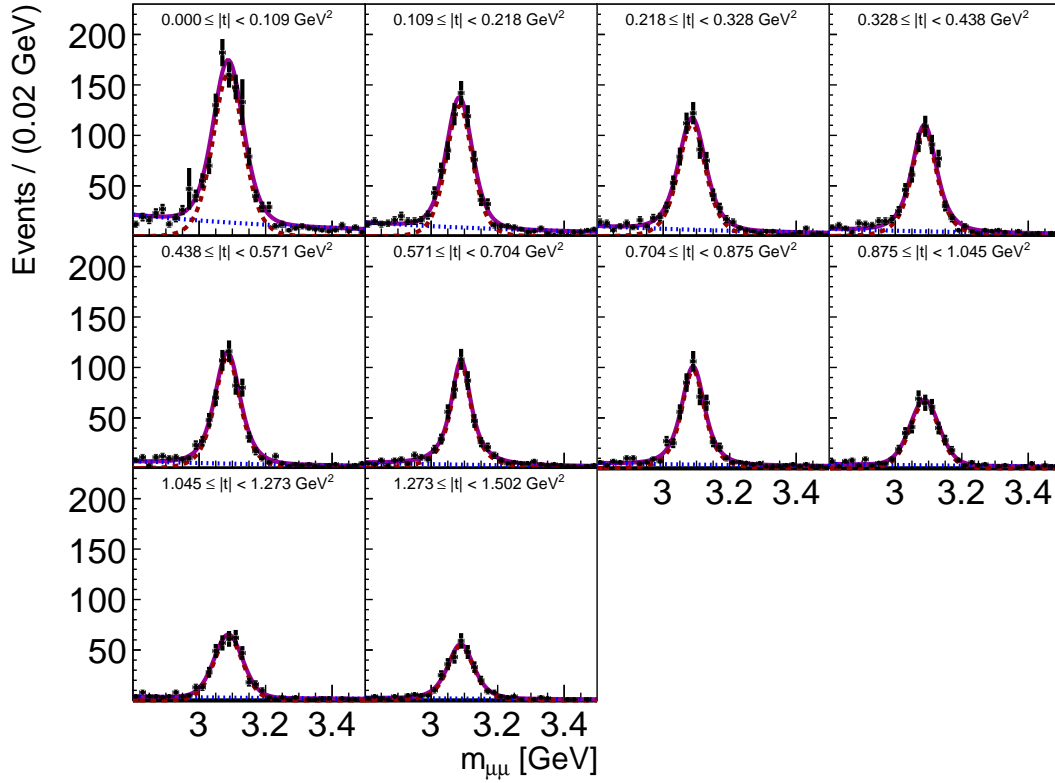


**Figure B.4:** The di-muon mass distributions shown in bins of reconstructed  $|t|$  for the high energy data period in the tagged sample are given as black circles. The solid magenta coloured line represents the combined signal and background fit used to evaluate the number of  $J/\psi$  events. The  $J/\psi$  signal function of the fit is given as dashed red line, the background distribution as dashed blue line. The di-muon mass distributions are shown in the range 2.8 - 3.5 GeV for better visibility, although the fits are performed in the range 2.3 - 5 GeV.

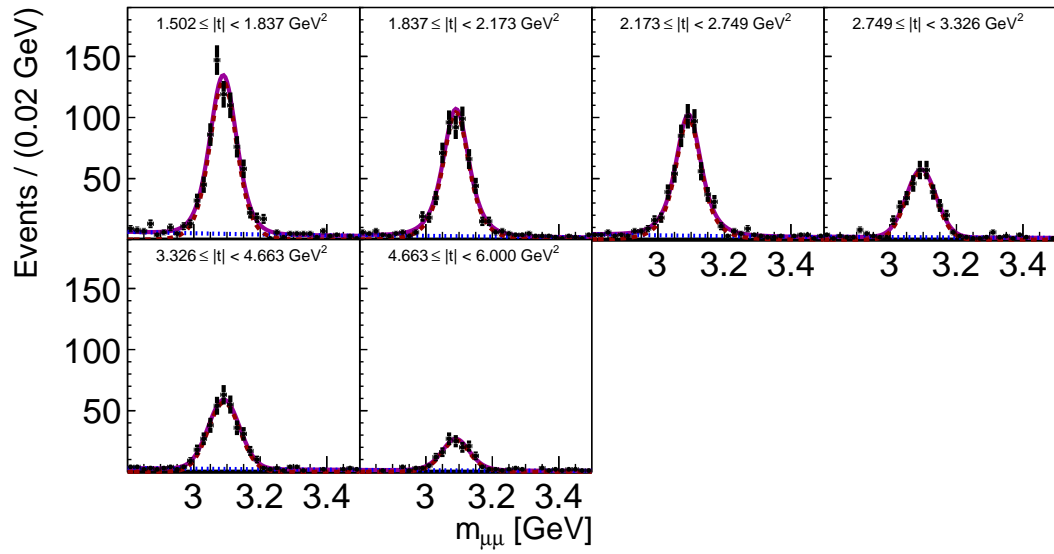


**Figure B.5:** The di-muon mass distributions shown in bins of reconstructed  $|t|$  for the high energy data period in the high  $|t|$  sample are given as black circles. The solid magenta coloured line represents the combined signal and background fit used to evaluate the number of  $J/\psi$  events. The  $J/\psi$  signal function of the fit is given as dashed red line, the background distribution as dashed blue line. The di-muon mass distributions are shown in the range 2.8 - 3.5 GeV for better visibility, although the fits are performed in the range 2.3 - 5 GeV.

## B.1.2 Di-muon mass distribution fits for the low energy data period

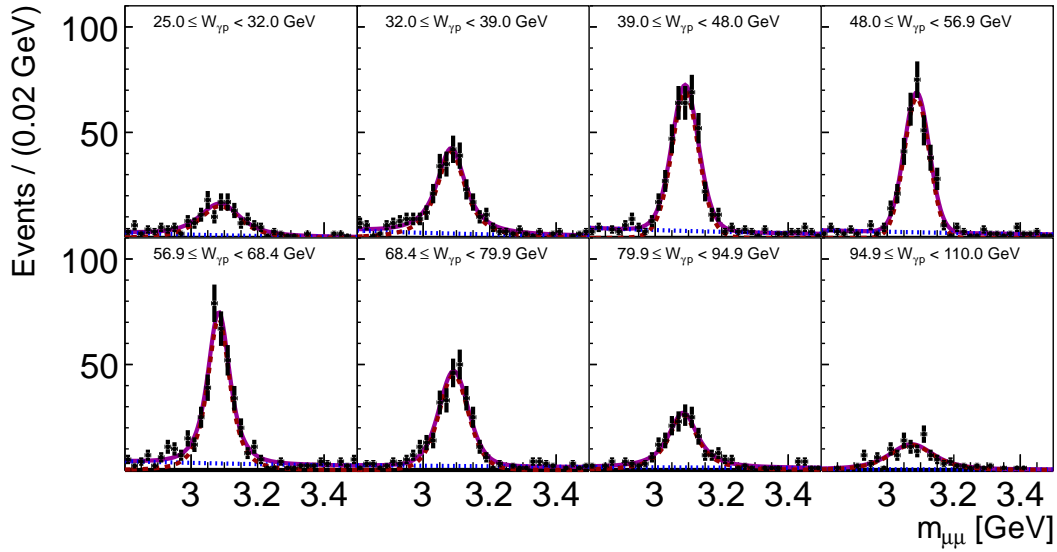


**Figure B.6:** The di-muon mass distributions shown in bins of reconstructed  $W_{\gamma p}$  for the low energy data period in the  $\overline{\text{tag}}_W$  sample are given as black circles. The solid magenta coloured line represents the combined signal and background fit used to evaluate the number of  $J/\psi$  events. The  $J/\psi$  signal function of the fit is given as dashed red line, the background distribution as dashed blue line. The di-muon mass distributions are shown in the range 2.8 - 3.5 GeV for better visibility, although the fits are performed in the range 2.3 - 5 GeV.

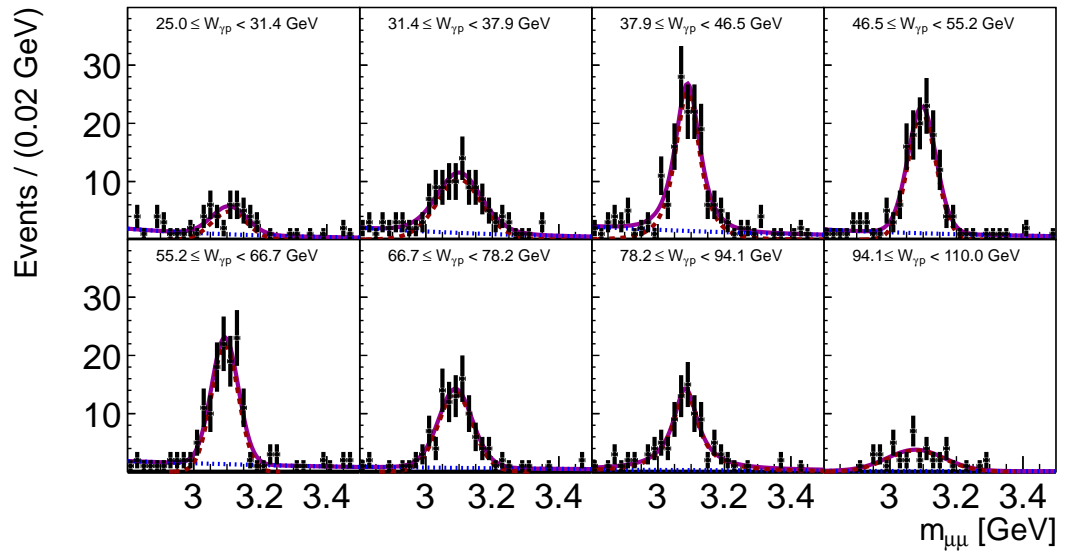


**Figure B.7:** The di-muon mass distributions shown in bins of reconstructed  $W_{\gamma p}$  for the low energy data period in the  $\text{tag}_W$  sample are given as black circles. The solid magenta coloured line represents the combined signal and background fit used to evaluate the number of  $J/\psi$  events. The  $J/\psi$  signal function of the fit is given as dashed red line, the background distribution as dashed blue line. The di-muon mass distributions are shown in the range 2.8 - 3.5 GeV for better visibility, although the fits are performed in the range 2.3 - 5 GeV.

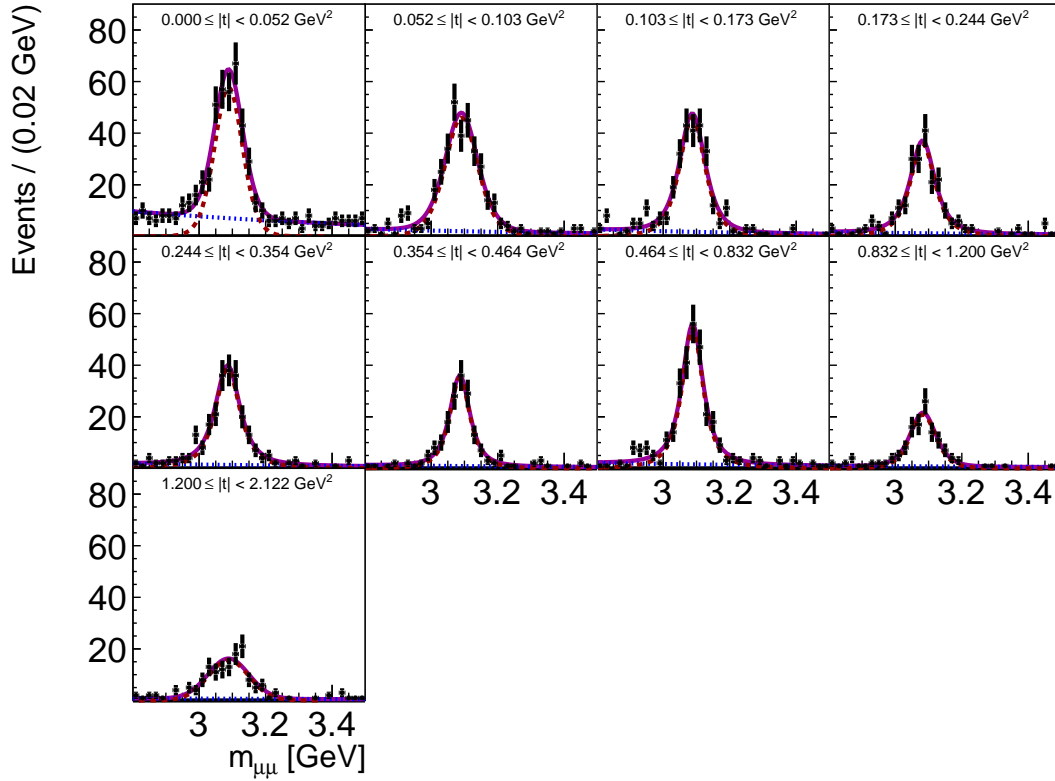


**Figure B.8:** The di-muon mass distributions shown in bins of reconstructed  $|t|$  for the low energy data period in the non-tagged sample are given as black circles. The solid magenta coloured line represents the combined signal and background fit used to evaluate the number of  $J/\psi$  events. The  $J/\psi$  signal function of the fit is given as dashed red line, the background distribution as dashed blue line. The di-muon mass distributions are shown in the range 2.8 - 3.5 GeV for better visibility, although the fits are performed in the range 2.3 - 5 GeV.

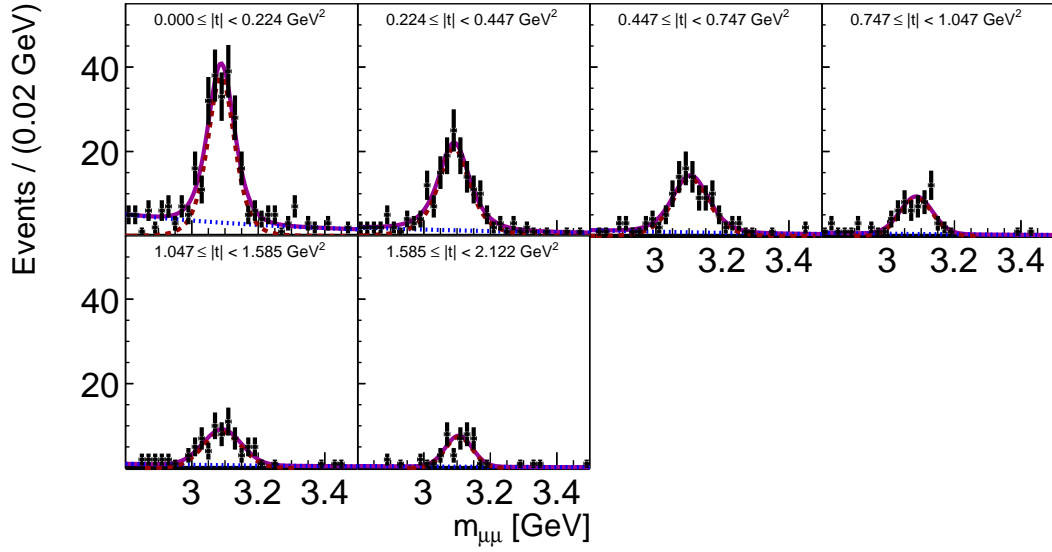


**Figure B.9:** The di-muon mass distributions shown in bins of reconstructed  $|t|$  for the low energy data period in the tagged sample are given as black circles. The solid magenta coloured line represents the combined signal and background fit used to evaluate the number of  $J/\psi$  events. The  $J/\psi$  signal function of the fit is given as dashed red line, the background distribution as dashed blue line. The di-muon mass distributions are shown in the range 2.8 - 3.5 GeV for better visibility, although the fits are performed in the range 2.3 - 5 GeV.

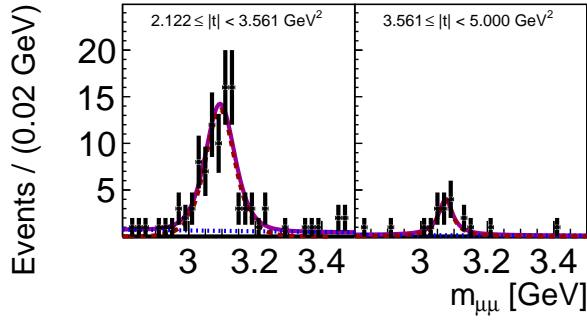


**Figure B.10:** The di-muon mass distributions shown in bins of reconstructed  $|t|$  for the low energy data period in the high  $|t|$  sample are given as black circles. The solid magenta coloured line represents the combined signal and background fit used to evaluate the number of  $J/\psi$  events. The  $J/\psi$  signal function of the fit is given as dashed red line, the background distribution as dashed blue line. The di-muon mass distributions are shown in the range 2.8 - 3.5 GeV for better visibility, although the fits are performed in the range 2.3 - 5 GeV.

## B.2 Number of $J/\psi$ events from di-muon mass fits

Number of  $J/\psi$  events for the high energy data period

$W_{\gamma p}$ range	$N_{J/\psi}$	$\Delta N_{J/\psi}$	$\chi^2$	ndf	$\chi^2/\text{ndf}$
40.0 – 43.2	660	30	105.3	135	0.78
43.2 – 46.5	910	30	130.9	135	0.97
46.5 – 50.0	1250	40	137.3	135	1.02
50.0 – 53.5	1290	40	134.1	135	0.99
53.5 – 57.4	1480	40	151.4	135	1.12
57.4 – 61.2	1430	40	137.6	135	1.02
61.2 – 65.3	1570	40	132.8	135	0.98
65.3 – 69.4	1400	40	173.0	135	1.28
69.4 – 73.9	1520	40	180.7	135	1.34
73.9 – 78.4	1420	40	140.4	135	1.04
78.4 – 83.2	1530	40	208.3	135	1.54
83.2 – 88.0	1450	40	145.9	135	1.08
88.0 – 93.3	1470	40	144.6	135	1.07
93.3 – 98.5	1360	40	190.7	135	1.41
98.5 – 104.3	1300	40	159.5	135	1.18
104.3 – 110.0	1160	40	157.5	135	1.17

(a)  $\overline{\text{tag}_W}$  sample in high energy data period

$W_{\gamma p}$ range	$N_{J/\psi}$	$\Delta N_{J/\psi}$	$\chi^2$	ndf	$\chi^2/\text{ndf}$
40.0 – 43.0	230	20	100.1	135	0.74
43.0 – 46.0	310	20	128.0	135	0.95
46.0 – 49.3	490	30	98.7	135	0.73
49.3 – 52.7	460	30	124.7	135	0.92
52.7 – 56.4	590	30	117.7	135	0.87
56.4 – 60.0	590	30	135.6	135	1.00
60.0 – 64.1	580	30	130.0	135	0.96
64.1 – 68.2	570	30	136.8	135	1.01
68.2 – 72.7	600	30	144.0	135	1.07
72.7 – 77.2	520	20	145.3	135	1.08
77.2 – 82.1	580	30	152.9	135	1.13
82.1 – 87.0	500	20	120.2	135	0.89
87.0 – 92.4	610	30	127.4	135	0.94
92.4 – 97.9	510	20	185.0	135	1.37
97.9 – 103.9	510	30	150.9	135	1.12
103.9 – 110.0	430	20	106.6	135	0.79

(b)  $\text{tag}_W$  sample in high energy data period

$ t $ range	$N_{J/\psi}$	$\Delta N_{J/\psi}$	$\chi^2$	ndf	$\chi^2/\text{ndf}$
0.000 – 0.025	2170	60	130.9	135	0.97
0.025 – 0.049	1840	50	136.2	135	1.01
0.049 – 0.078	1800	50	128.0	135	0.95
0.078 – 0.106	1660	40	158.6	135	1.17
0.106 – 0.139	1510	40	114.8	135	0.85
0.139 – 0.172	1350	40	187.9	135	1.39
0.172 – 0.212	1380	40	175.1	135	1.30
0.212 – 0.251	1180	40	119.2	135	0.88
0.251 – 0.301	1180	40	137.8	135	1.02
0.301 – 0.351	940	30	143.5	135	1.06
0.351 – 0.419	1060	30	121.0	135	0.90
0.419 – 0.486	880	30	123.9	135	0.92
0.486 – 0.590	940	30	161.1	135	1.19
0.590 – 0.693	740	30	182.8	135	1.35
0.693 – 0.947	1120	40	169.7	135	1.26
0.947 – 1.200	740	30	156.0	135	1.16
1.200 – 1.502	550	30	151.4	135	1.12

(c) non-tagged sample high energy data period

$ t $ range	$N_{J/\psi}$	$\Delta N_{J/\psi}$	$\chi^2$	ndf	$\chi^2/\text{ndf}$
0.000 – 0.109	970	40	179.5	135	1.33
0.109 – 0.218	680	30	120.9	135	0.90
0.218 – 0.328	620	30	137.5	135	1.02
0.328 – 0.438	560	30	142.1	135	1.05
0.438 – 0.571	590	30	149.5	135	1.11
0.571 – 0.704	490	30	118.0	135	0.87
0.704 – 0.875	480	20	148.6	135	1.10
0.875 – 1.045	370	20	133.3	135	0.99
1.045 – 1.273	350	20	103.3	135	0.77
1.273 – 1.502	290	20	125.7	135	0.93

(d) tagged sample in high energy data period

$ t $ range	$N_{J/\psi}$	$\Delta N_{J/\psi}$	$\chi^2$	ndf	$\chi^2/\text{ndf}$
1.502 – 1.837	700	30	161.9	135	1.20
1.837 – 2.173	560	30	121.9	135	0.90
2.173 – 2.749	540	30	149.7	135	1.11
2.749 – 3.326	310	20	137.6	135	1.02
3.326 – 4.663	340	20	110.1	135	0.82
4.663 – 6.000	141	13	117.7	135	0.87

(e) high  $|t|$  sample in high energy data period

**Table B.1:** Overview of number of  $J/\psi$  events determined from the di-muon mass distribution fits in the high energy data period for the  $\overline{\text{tag}_W}$  (a) and  $\text{tag}_W$  (b) sample in bins of  $W_{\gamma p}$  and for the non-tagged (c), tagged (d) and high  $|t|$  (e) sample in bins of  $|t|$ . The first column in each table shows the bin range in  $W_{\gamma p}$  or  $|t|$ . The second ( $N_{J/\psi}$ ) and third ( $\Delta N_{J/\psi}$ ) column give the evaluated number of  $J/\psi$  events and the error extracted by use of an extended log likelihood fit. The last three columns show the values from the  $\chi^2$  goodness-of-fit test, the number of degree of freedom (ndf) and  $\chi^2$  value divided by ndf.

Appendix B Number of  $J/\psi$  events

Number of  $J/\psi$  events for the low energy data period

$W_{\gamma p}$ range	$N_{J/\psi}$	$\Delta N_{J/\psi}$	$\chi^2$	ndf	$\chi^2/\text{ndf}$
25.0 – 32.0	128	14	111.0	135	0.82
32.0 – 39.0	270	20	101.3	135	0.75
39.0 – 48.0	360	20	129.2	135	0.96
48.0 – 56.9	310	20	111.8	135	0.83
56.9 – 68.4	350	20	146.0	135	1.08
68.4 – 79.9	260	20	124.9	135	0.93
79.9 – 94.9	170	20	135.8	135	1.01
94.9 – 110.0	108	11	127.9	135	0.95

(a)  $\overline{\text{tag}}_{\text{W}}$  sample in low energy data period

$W_{\gamma p}$ range	$N_{J/\psi}$	$\Delta N_{J/\psi}$	$\chi^2$	ndf	$\chi^2/\text{ndf}$
25.0 – 31.4	32	7	94.8	135	0.70
31.4 – 37.9	90	11	101.7	135	0.75
37.9 – 46.5	134	14	125.9	135	0.93
46.5 – 55.2	117	12	141.2	135	1.05
55.2 – 66.7	111	11	146.4	135	1.08
66.7 – 78.2	89	10	129.6	135	0.96
78.2 – 94.1	88	10	118.1	135	0.87
94.1 – 110.0	40	6	126.5	135	0.94

(b)  $\text{tag}_{\text{W}}$  sample in low energy data period

$ t $ range	$N_{J/\psi}$	$\Delta N_{J/\psi}$	$\chi^2$	ndf	$\chi^2/\text{ndf}$
0.000 – 0.052	310	20	95.3	135	0.71
0.052 – 0.103	300	20	132.2	135	0.98
0.103 – 0.173	250	20	158.5	135	1.17
0.173 – 0.244	190	20	136.8	135	1.01
0.244 – 0.354	210	20	132.0	135	0.98
0.354 – 0.464	157	14	136.0	135	1.01
0.464 – 0.832	260	20	153.8	135	1.14
0.832 – 1.200	110	12	115.9	135	0.86
1.200 – 2.122	121	12	126.2	135	0.94

(c) non-tagged sample low energy data period

$ t $ range	$N_{J/\psi}$	$\Delta N_{J/\psi}$	$\chi^2$	ndf	$\chi^2/\text{ndf}$
0.000 – 0.224	200	20	161.6	135	1.20
0.224 – 0.447	138	14	123.9	135	0.92
0.447 – 0.747	98	11	126.4	135	0.94
0.747 – 1.047	54	8	108.9	135	0.81
1.047 – 1.585	62	9	136.7	135	1.01
1.585 – 2.122	38	6	107.8	135	0.80

(d) tagged sample in low energy data period

$ t $ range	$N_{J/\psi}$	$\Delta N_{J/\psi}$	$\chi^2$	ndf	$\chi^2/\text{ndf}$
2.122 – 3.561	82	10	136.5	135	1.01
3.561 – 5.000	15	3	117.1	135	0.87

(e) high  $|t|$  sample in low energy data period

**Table B.2:** Overview of number of  $J/\psi$  events determined from the di-muon mass distribution fits in the low energy data period for the  $\overline{\text{tag}}_{\text{W}}$  (a) and  $\text{tag}_{\text{W}}$  (b) sample in bins of  $W_{\gamma p}$  and for the non-tagged (c), tagged (d) and high  $|t|$  (e) sample in bins of  $|t|$ . The first column in each table shows the bin range in  $W_{\gamma p}$  or  $|t|$ . The second ( $N_{J/\psi}$ ) and third ( $\Delta N_{J/\psi}$ ) column give the evaluated number of  $J/\psi$  events and the error extracted by use of an extended log likelihood fit. The last three columns show the values from the  $\chi^2$  goodness-of-fit test, the number of degree of freedom (ndf) and  $\chi^2$  value divided by ndf.

### B.3 Di-electron mass distribution after background subtraction

#### B.3.1 Di-electron muon mass distribution after background subtraction for the high energy data period

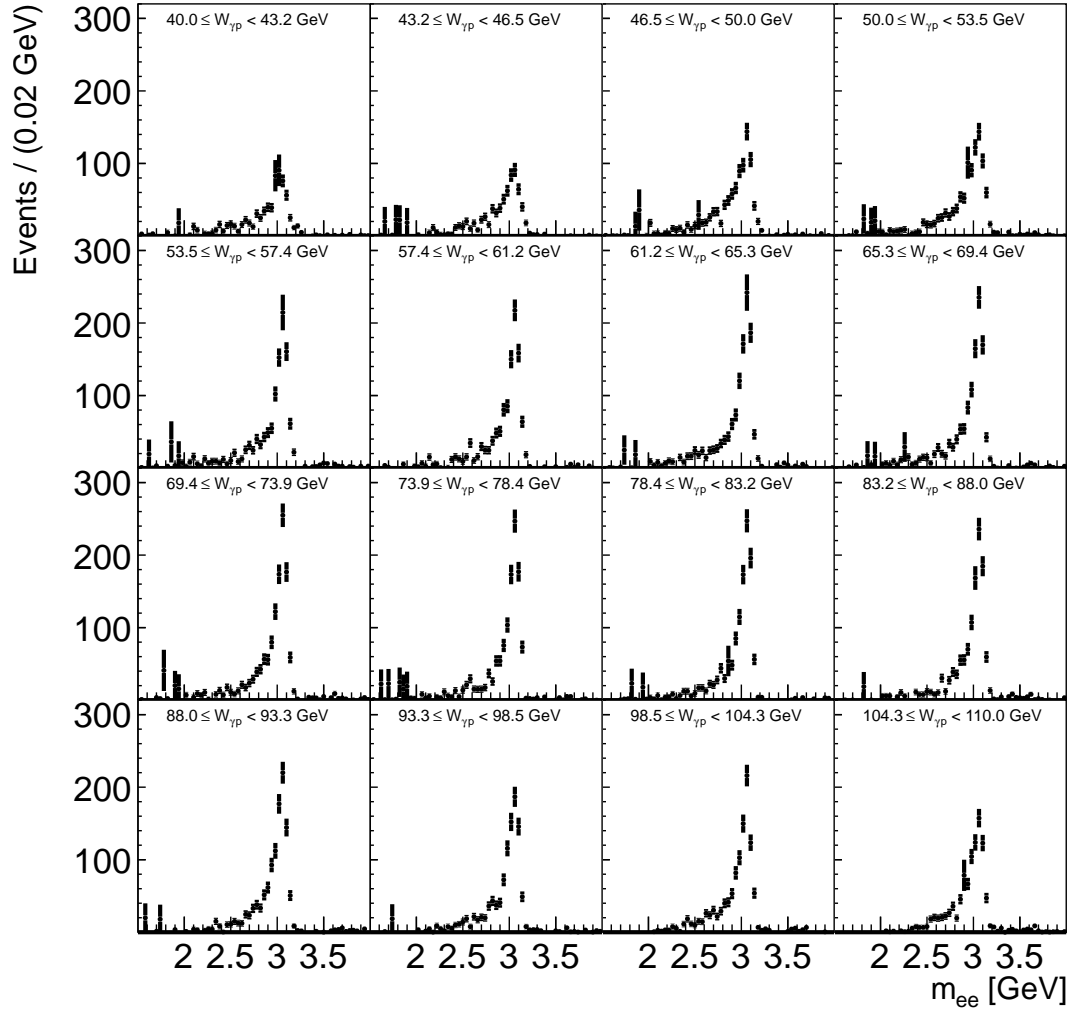


**Figure B.11:** The di-electron mass distributions after background subtraction shown in bins of reconstructed  $W_{\gamma p}$  for the high energy data period in the  $\text{tag}_{\overline{W}}$  sample are given as black circles.

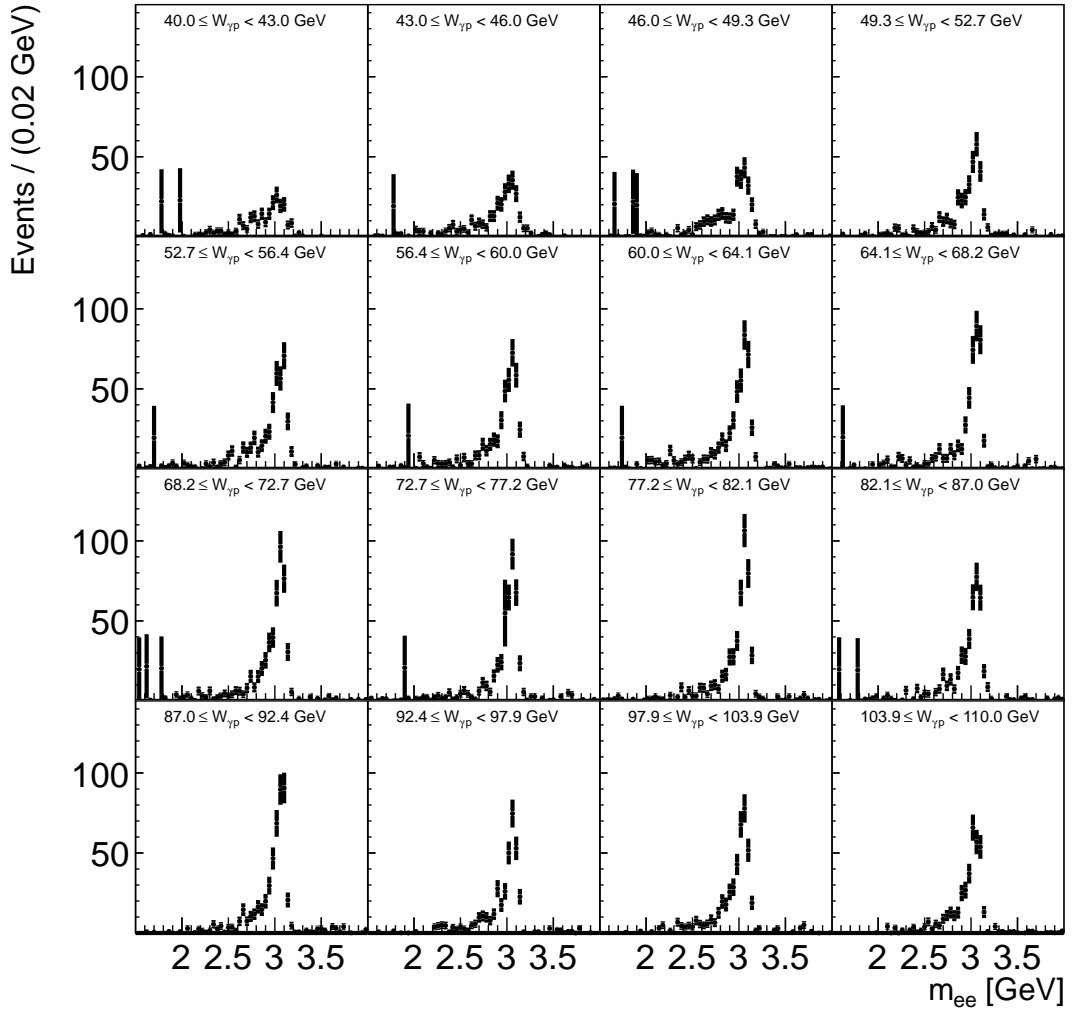


**Figure B.12:** The di-electron mass distributions after background subtraction shown in bins of reconstructed  $W_{\gamma p}$  for the high energy data period in the tag $_W$  sample are given as black circles.

B.3 Di-electron mass distribution after background subtraction

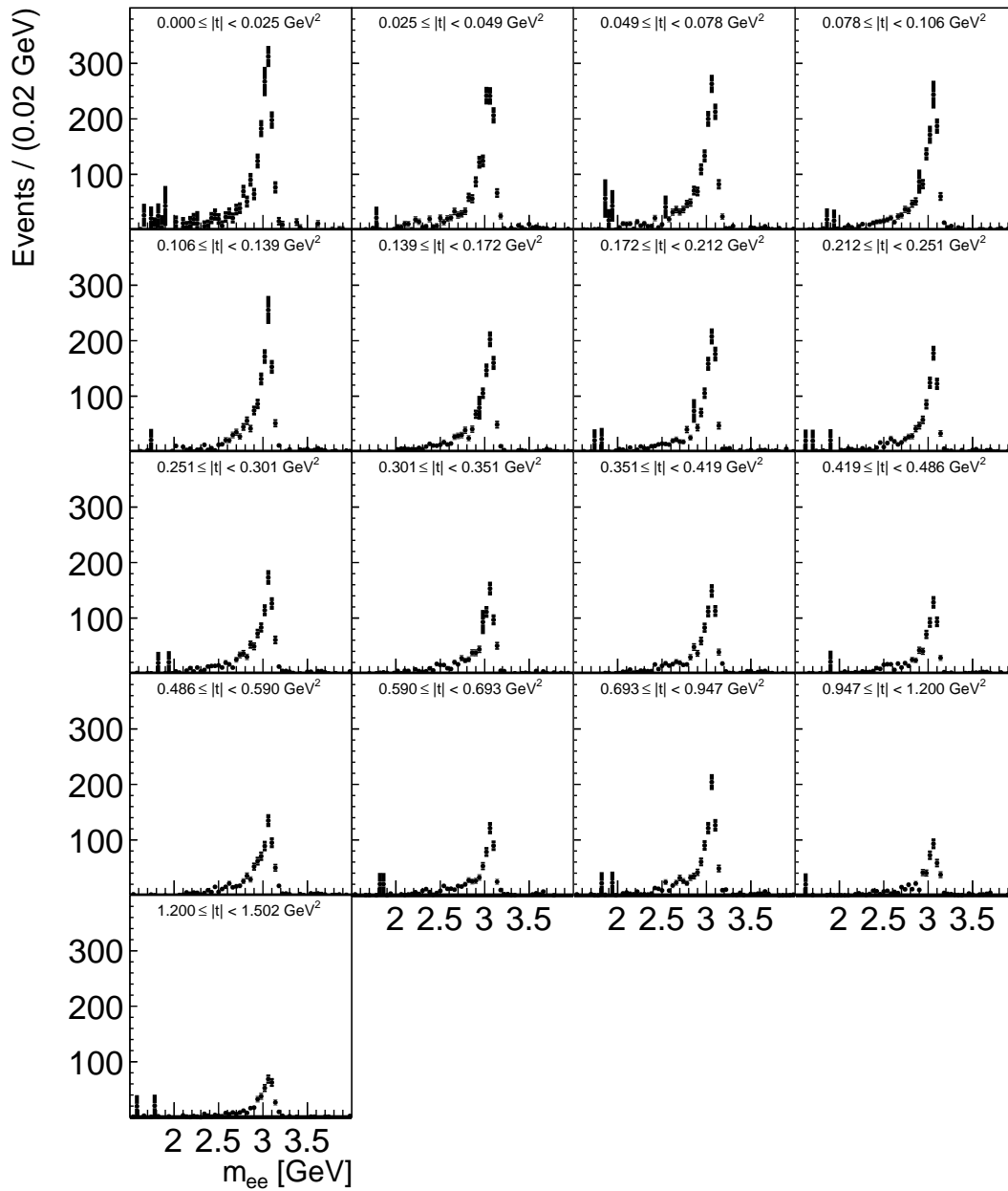


**Figure B.13:** The di-electron mass distributions after background subtraction shown in bins of reconstructed  $|t|$  for the high energy data period in the non-tagged sample are given as black circles.

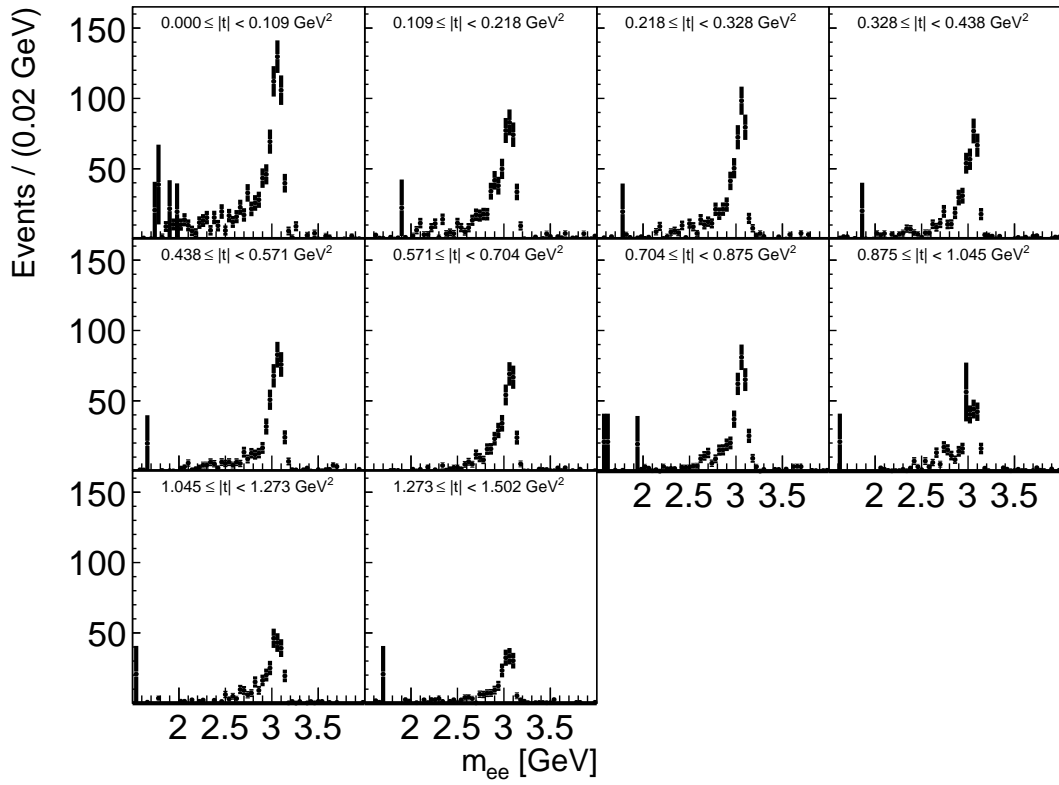


**Figure B.14:** The di-electron mass distributions after background subtraction shown in bins of reconstructed  $|t|$  for the high energy data period in the tagged sample are given as black circles.

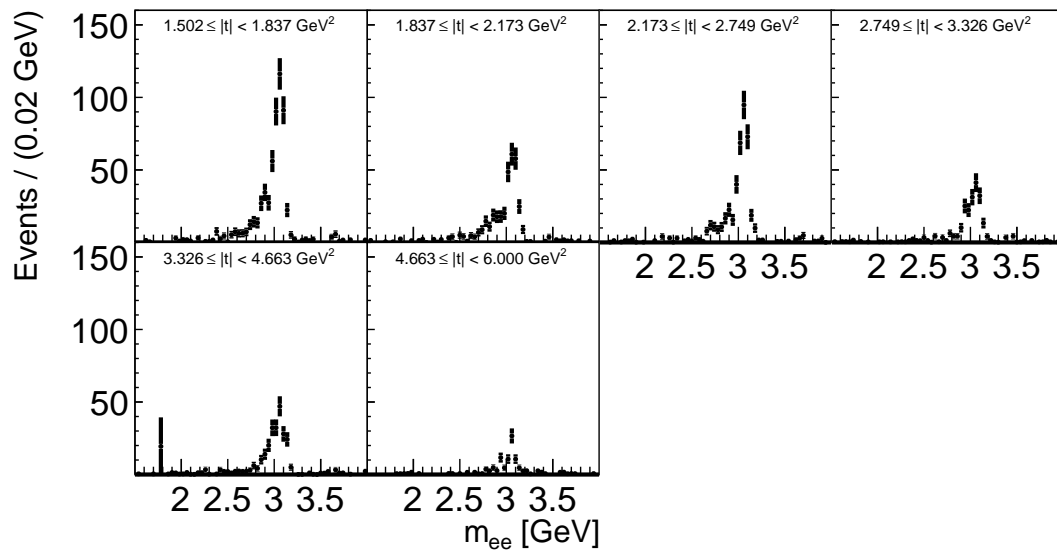


**Figure B.15:** The di-electron mass distributions after background subtraction shown in bins of reconstructed  $|t|$  for the high energy data period in the high  $|t|$  sample are given as black circles.

### B.3.2 Di-electron muon mass distribution after background subtraction for the low energy data period

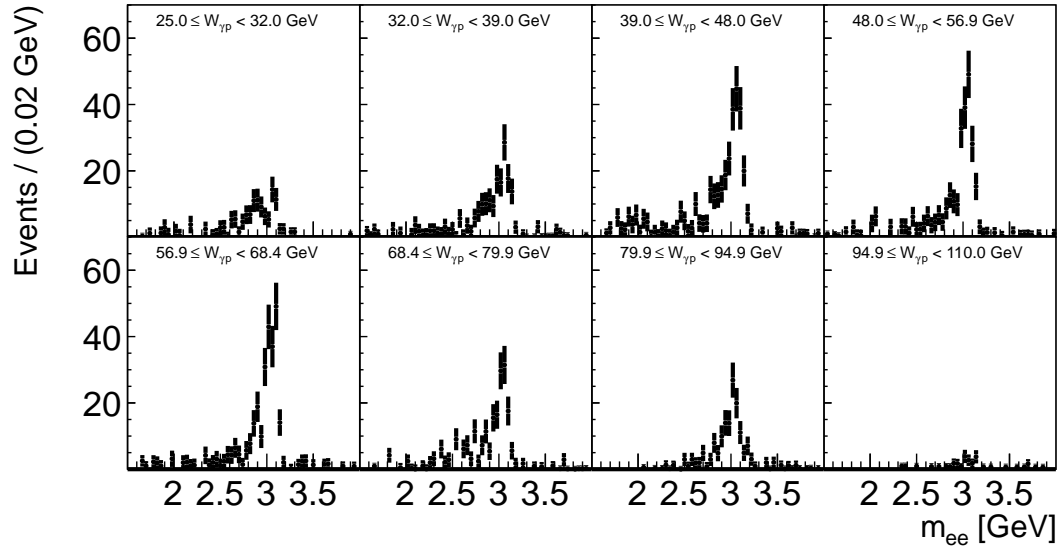


**Figure B.16:** The di-electron mass distributions after background subtraction shown in bins of reconstructed  $W_{\gamma p}$  for the low energy data period in the  $\overline{\text{tag}}_W$  sample are given as black circles.

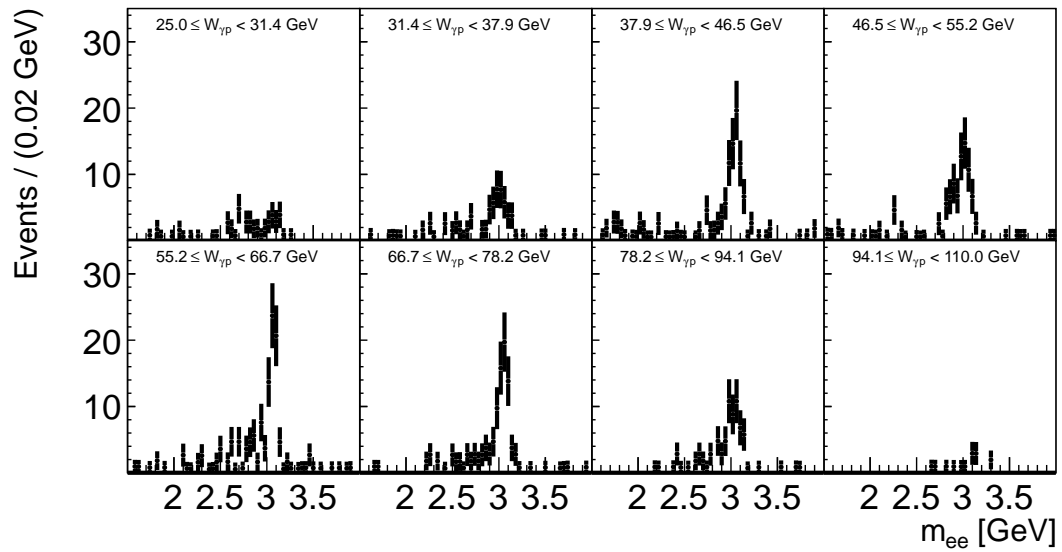


**Figure B.17:** The di-electron mass distributions after background subtraction shown in bins of reconstructed  $W_{\gamma p}$  for the low energy data period in the  $\text{tag}_W$  sample are given as black circles.

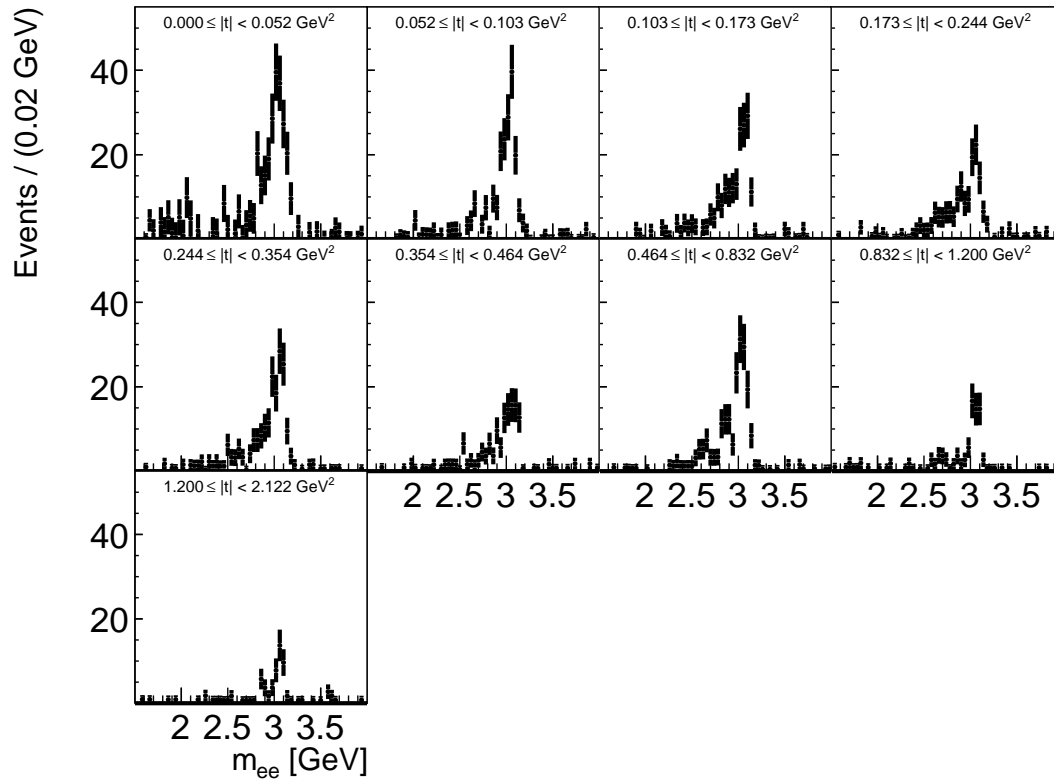


**Figure B.18:** The di-electron mass distributions after background subtraction shown in bins of reconstructed  $|t|$  for the low energy data period in the non-tagged sample are given as black circles.

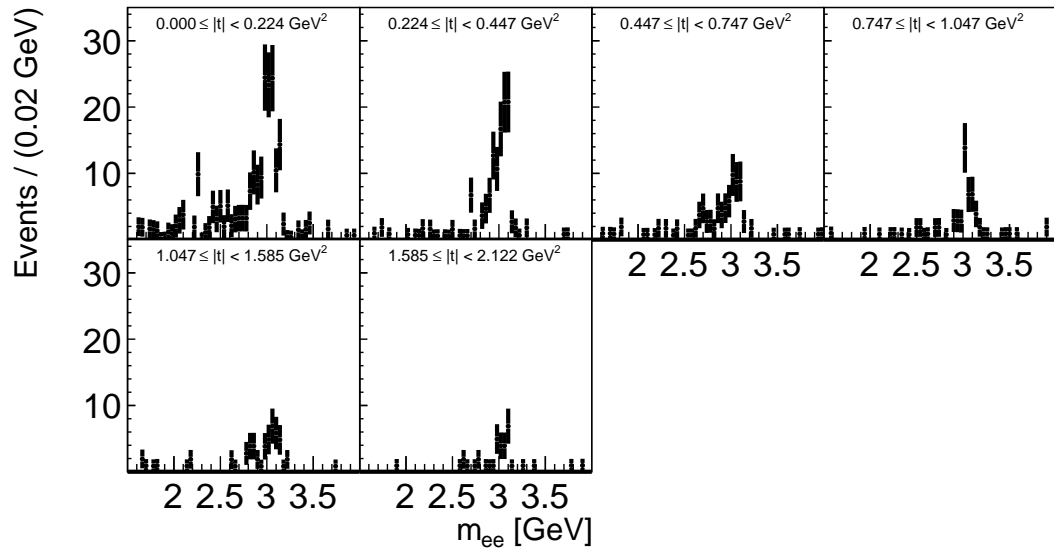


**Figure B.19:** The di-electron mass distributions after background subtraction shown in bins of reconstructed  $|t|$  for the low energy data period in the tagged sample are given as black circles.

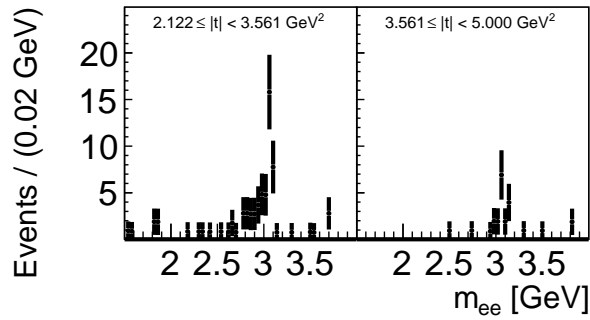


**Figure B.20:** The di-electron mass distributions after background subtraction shown in bins of reconstructed  $|t|$  for the low energy data period in the high  $|t|$  sample are given as black circles.

## B.4 Number of $J/\psi$ signal events from di-electron mass distributions

Number of  $J/\psi$  events for the high energy data period

$W_{\gamma p}$ range	$N_{J/\psi}$	$\Delta N_{J/\psi}$
40.0 – 43.2	680	40
43.2 – 46.5	690	30
46.5 – 50.0	960	40
50.0 – 53.5	1010	40
53.5 – 57.4	1110	40
57.4 – 61.2	1110	40
61.2 – 65.3	1240	40
65.3 – 69.4	1190	40
69.4 – 73.9	1240	40
73.9 – 78.4	1200	40
78.4 – 83.2	1220	40
83.2 – 88.0	1170	40
88.0 – 93.3	1160	40
93.3 – 98.5	1050	40
98.5 – 104.3	1100	40
104.3 – 110.0	990	40

(a)  $\overline{\text{tag}}_W$  sample in high energy data period

$W_{\gamma p}$ range	$N_{J/\psi}$	$\Delta N_{J/\psi}$
40.0 – 43.0	220	20
43.0 – 46.0	290	20
46.0 – 49.3	310	20
49.3 – 52.7	350	20
52.7 – 56.4	440	20
56.4 – 60.0	430	20
60.0 – 64.1	460	20
64.1 – 68.2	440	20
68.2 – 72.7	490	20
72.7 – 77.2	440	30
77.2 – 82.1	490	20
82.1 – 87.0	430	20
87.0 – 92.4	480	20
92.4 – 97.9	360	20
97.9 – 103.9	430	20
103.9 – 110.0	370	20

(b)  $\text{tag}_W$  sample in high energy data period

$ t $ range	$N_{J/\psi}$	$\Delta N_{J/\psi}$
0.000 – 0.025	1690	60
0.025 – 0.049	1470	40
0.049 – 0.078	1530	50
0.078 – 0.106	1330	50
0.106 – 0.139	1260	40
0.139 – 0.172	1120	40
0.172 – 0.212	1130	40
0.212 – 0.251	900	30
0.251 – 0.301	1000	30
0.301 – 0.351	830	40
0.351 – 0.419	870	30
0.419 – 0.486	690	30
0.486 – 0.590	810	30
0.590 – 0.693	630	30
0.693 – 0.947	970	30
0.947 – 1.200	490	20
1.200 – 1.502	400	20

(c) non-tagged sample high energy data period

$ t $ range	$N_{J/\psi}$	$\Delta N_{J/\psi}$
0.000 – 0.109	820	30
0.109 – 0.218	580	30
0.218 – 0.328	550	20
0.328 – 0.438	470	20
0.438 – 0.571	470	20
0.571 – 0.704	400	20
0.704 – 0.875	420	20
0.875 – 1.045	330	30
1.045 – 1.273	290	20
1.273 – 1.502	200	15

(d) tagged sample in high energy data period

$ t $ range	$N_{J/\psi}$	$\Delta N_{J/\psi}$
1.502 – 1.837	560	20
1.837 – 2.173	340	20
2.173 – 2.749	430	20
2.749 – 3.326	220	20
3.326 – 4.663	240	20
4.663 – 6.000	93	10

(e) high  $|t|$  sample in high energy data period

**Table B.3:** Overview of number of  $J/\psi$  events determined from the di-electron mass distributions after background subtraction in the high energy data period for the  $\overline{\text{tag}}_W$  (a) and  $\text{tag}_W$  (b) sample in bins of  $W_{\gamma p}$  and for the non-tagged (c), tagged (d) and high  $|t|$  (e) sample in bins of  $|t|$ . The first column in each table shows the bin range in  $W_{\gamma p}$  or  $|t|$ . The second ( $N_{J/\psi}$ ) and third ( $\Delta N_{J/\psi}$ ) column give the evaluated number of  $J/\psi$  events and the error.

Number of  $J/\psi$  events for the low energy data period

$W_{\gamma p}$ range	$N_{J/\psi}$	$\Delta N_{J/\psi}$
25.0 – 32.0	113	12
32.0 – 39.0	170	20
39.0 – 48.0	290	20
48.0 – 56.9	260	20
56.9 – 68.4	260	20
68.4 – 79.9	190	20
79.9 – 94.9	147	13
94.9 – 110.0	23	5

 (a)  $\overline{\text{tag}_W}$  sample in low energy data period

$W_{\gamma p}$ range	$N_{J/\psi}$	$\Delta N_{J/\psi}$
25.0 – 31.4	37	6
31.4 – 37.9	58	8
37.9 – 46.5	93	10
46.5 – 55.2	80	9
55.2 – 66.7	113	11
66.7 – 78.2	97	10
78.2 – 94.1	70	9
94.1 – 110.0	12	4

 (b)  $\text{tag}_W$  sample in low energy data period

$ t $ range	$N_{J/\psi}$	$\Delta N_{J/\psi}$
0.000 – 0.052	270	20
0.052 – 0.103	200	20
0.103 – 0.173	197	15
0.173 – 0.244	155	13
0.244 – 0.354	188	14
0.354 – 0.464	128	12
0.464 – 0.832	196	15
0.832 – 1.200	86	10
1.200 – 2.122	57	8

(c) non-tagged sample low energy data period

$ t $ range	$N_{J/\psi}$	$\Delta N_{J/\psi}$
0.000 – 0.224	173	14
0.224 – 0.447	115	11
0.447 – 0.747	72	9
0.747 – 1.047	54	8
1.047 – 1.585	43	7
1.585 – 2.122	30	6

(d) tagged sample in low energy data period

$ t $ range	$N_{J/\psi}$	$\Delta N_{J/\psi}$
2.122 – 3.561	54	8
3.561 – 5.000	20	5

 (e) high  $|t|$  sample in low energy data period

**Table B.4:** Overview of number of  $J/\psi$  events determined from the di-electron mass distributions after background subtraction in the low energy data period for the  $\overline{\text{tag}_W}$  (a) and  $\text{tag}_W$  (b) sample in bins of  $W_{\gamma p}$  and for the non-tagged (c), tagged (d) and high  $|t|$  (e) sample in bins of  $|t|$ . The first column in each table shows the bin range in  $W_{\gamma p}$  or  $|t|$ . The second ( $N_{J/\psi}$ ) and third ( $\Delta N_{J/\psi}$ ) column give the evaluated number of  $J/\psi$  events and the error.



## Least square parameter estimation with normalisation uncertainty

A standard approach for parameter estimation of overdetermined problems is based on least square methods. The problem of parameter estimation or fitting of a theoretical function  $f(x; \boldsymbol{\theta})$  is to determine the optimal values for a set of parameters  $\boldsymbol{\theta}$  given a set of measurement of  $(x_i, y_i)$  pairs. For simplicity here the theory function is  $\mathbb{R} \rightarrow \mathbb{R}$  but the least square method can easily be extended to higher orders. The  $\chi^2(\boldsymbol{\theta})$  is defined as the sum over all measured pairs of the weighted, squared difference between the theory prediction and the measured value  $y_i$  for a given  $x_i$ . The method then defines the best estimation of the parameter values to be where the  $\chi^2$  becomes minimal. The simplest case takes the form

$$\chi^2(\boldsymbol{\theta}) = \sum_{i=1}^N \frac{[y - f(x_i; \boldsymbol{\theta})]^2}{\sigma_i^2} \quad (\text{C.1})$$

with the applied weights  $\sigma_i^2$ , the variance of the measurement of point  $i$ . Even so this may look trivial, issues arise when a concrete problem must be solved, see for instance [282] for a discussion of binned least square parameter estimation concerning biases by choosing  $\sigma_i$ .

The given expression neglects the case when it is known that the data points are correlated with each other. In this situation the diagonal variances  $\sigma_i^2$  are replaced by a full covariance matrix  $V_{ij}$  and the  $\chi^2$  expression takes in matrix notation the form

$$\chi^2(\boldsymbol{\theta}) = [\mathbf{y} - \mathbf{f}]^T \underline{V}^{-1} [\mathbf{y} - \mathbf{f}], \quad (\text{C.2})$$

with  $\mathbf{f} = (f_1, f_2, \dots)$  and  $f_i = f(x_i; \boldsymbol{\theta})$ .

This case is exactly what is needed for fitting the cross sections. Because if this measurement would rely on a bin-by-bin method correction for cross section construction, the given cross

section points, would only get the diagonal part of the covariance matrix. Due to the unfolding the full covariance matrix, including all correlations, is known.

## C.1 A different representation

The explanation given above can basically be found in every statistic introduction book. But what is usually not shown is that Eq. (C.2) can be rewritten, if the covariance matrix fulfills some conditions.

Lets assume the covariance matrix  $\underline{V}$  has two components, in order not to drift too far away from the actual situation this analysis is located in, they will be called  $\underline{V}^{\text{stat}}$  and  $\underline{V}^{\text{sys}}$  and can be seen as the covariance matrix given due to statistical and systematic sources. Further  $\underline{V}^{\text{sys}}$  is defined to be of rank 1, i.e. composed from a vector  $\mathbf{w}$  as

$$\underline{V}^{\text{sys}} = \mathbf{w}\mathbf{w}^{\text{T}}. \quad (\text{C.3})$$

Then Eq. (C.2) is equal to

$$\chi^2(\boldsymbol{\theta}) = [(\mathbf{f} - \beta\mathbf{w}) - \mathbf{y}]^{\text{T}} (\underline{V}^{\text{stat}})^{-1} [(\mathbf{f} - \beta\mathbf{w}) - \mathbf{y}] + \beta^2, \quad (\text{C.4})$$

with additional parameter  $\beta$ . The proof is straight forward by using the Sherman-Morison formula [302]. More information are provided in [303, 304] and an elaborate discussion can be found in Appendix B of [305].

The assumption of Eq. (C.3) may look too rigid for a general purpose use. But it should not be regarded as a try to explain a variety of systematic effects, it should be seen as accounting for just one systematic source. As given in Sec. 9.4.2 the total systematic covariance matrix is the sum of rank-1 produced covariance matrices each caused by one systematic source. Taking into account  $M$  systematic sources the above formula can be rewritten by the replacements  $\beta\mathbf{w} \rightarrow \sum_{j=1}^M \beta^{(j)}\mathbf{w}^{(j)}$  and  $\beta^2 \rightarrow \sum_{j=1}^M (\beta^{(j)})^2$ , giving it the form

$$\chi^2(\boldsymbol{\theta}) = \sum_{i,j} [y_i - \alpha_i f_i] (V_{ij}^{\text{stat}})^{-1} [y_j - \alpha_j f_j] + \sum_{j=1}^M \beta_j^2, \quad (\text{C.5})$$

with

$$\alpha_i = 1 - \sum_{j=1}^M \beta^{(j)} \gamma_i^{(j)}. \quad (\text{C.6})$$

The  $\gamma^{(j)}$  vectors are the relative shifts

$$\gamma_i^{(j)} = \frac{w_i^{(j)}}{f_i} \quad (\text{C.7})$$

for each systematic source or in case of a normalisation uncertainty

$$\gamma_i = \varepsilon \quad (\text{C.8})$$

with  $\varepsilon$  the size of the uncertainty.

A P P E N D I X



## Cross section tables

Appendix D Cross section tables

$ t $ range [GeV]	$\langle  t ^{bc} \rangle$ [GeV]	$\sigma (\langle  t ^{bc} \rangle)$ [nb]	$\Delta_{\text{stat}}$ [nb]	$\delta_{\text{sys}}^{\text{corr}}$ [%]	$\delta_{\text{sys}}^{eT}$ [%]	$\delta_{\text{sys}}^{\mu T}$ [%]	$\delta_{\text{sys}}^{\mathcal{L}_H}$ [%]	$\delta_{\text{sys}}^{\text{LAr10}}$ [%]	$\delta_{\text{sys}}^{\text{PLUG}}$ [%]	$\delta_{\text{sys}}^{\text{FTS}}$ [%]	$\delta_{\text{sys}}^{\alpha_{1,\text{pd}}}$ [%]	$\delta_{\text{sys}}^{\varepsilon_M}$ [%]	$\delta_{\text{sys}}^{\alpha_{1,\text{el}}}$ [%]	$\delta_{\text{sys}}^{e\text{ID}}$ [%]	$\delta_{\text{sys}}^{\mu\text{ID}}$ [%]	$\delta_{\text{sys}}^{Q^2}$ [%]	$\delta_{\text{sys}}^{\text{RLT}}$ [%]	$\delta_{\text{sys}}^{\text{EC}}$ [%]	$\delta_{\text{sys}}^{e\text{Sig}}$ [%]	$\delta_{\text{sys}}^{\mu\text{Sig}}$ [%]
High energy data period in $J/\psi \rightarrow ee$ decay channel for elastic $J/\psi$ production																				
0.00 - 0.05	0.02	310.00	20.00	4.40	4.00	-	2.70	-1.43	0.19	-0.06	0.14	0.20	0.01	0.51	-	-0.92	0.00	0.53	2.71	-
0.05 - 0.11	0.08	243.00	9.00	4.40	4.00	-	2.70	-1.59	0.22	-0.07	-0.04	0.22	0.02	0.50	-	-0.85	0.00	0.57	0.87	-
0.11 - 0.17	0.14	159.00	8.00	4.40	4.00	-	2.70	-2.14	0.29	-0.10	-0.31	0.30	0.05	0.53	-	-0.82	0.00	0.74	1.13	-
0.17 - 0.25	0.21	100.00	6.00	4.40	4.00	-	2.70	-3.00	0.42	-0.14	-0.28	0.47	0.08	0.51	-	-0.73	0.00	1.11	1.25	-
0.25 - 0.35	0.30	69.00	5.00	4.40	4.00	-	2.70	-3.76	0.54	-0.19	-0.31	0.61	0.10	0.57	-	-0.50	0.00	1.51	1.84	-
0.35 - 0.49	0.41	36.00	3.00	4.40	4.00	-	2.70	-6.34	0.93	-0.33	-0.91	1.02	0.15	0.61	-	-0.15	0.00	2.55	1.13	-
0.49 - 0.69	0.58	18.00	2.00	4.40	4.00	-	2.70	-11.00	1.69	-0.61	-2.43	1.87	0.27	0.47	-	0.97	0.00	4.73	2.55	-
0.69 - 1.20	0.89	5.00	1.00	4.40	4.00	-	2.70	-29.17	4.74	-1.63	-10.24	5.20	0.07	0.90	-	9.01	0.00	13.07	5.51	-
High energy data period in $J/\psi \rightarrow ee$ decay channel for proton dissociative $J/\psi$ production																				
0.00 - 0.22	0.11	47.00	3.00	4.40	4.00	-	2.70	14.49	-1.96	0.65	0.78	-1.07	0.00	0.52	-	-0.58	0.00	-4.70	1.95	-
0.22 - 0.44	0.32	43.00	3.00	4.40	4.00	-	2.70	13.60	-1.95	0.68	0.55	-0.69	-0.01	0.60	-	-0.52	0.00	-4.81	2.56	-
0.44 - 0.70	0.57	34.00	2.00	4.40	4.00	-	2.70	14.02	-2.16	0.79	1.05	-0.68	0.00	0.59	-	-0.74	0.00	-5.43	0.87	-
0.70 - 1.05	0.87	24.00	2.00	4.40	4.00	-	2.70	14.49	-2.32	0.81	1.77	-0.84	0.07	0.59	-	-1.51	0.00	-5.65	1.70	-
1.05 - 1.50	1.26	12.00	1.00	4.40	4.00	-	2.70	16.48	-2.87	0.75	2.44	-0.71	-0.05	0.87	-	-1.90	0.00	-7.24	1.32	-
1.50 - 2.17	1.82	8.20	0.70	4.40	4.00	-	2.70	9.90	-1.78	0.39	-1.34	0.30	0.02	0.91	-	2.43	0.00	-4.45	1.74	-
2.17 - 3.33	2.70	4.00	0.30	4.40	4.00	-	2.70	7.44	-1.36	0.24	-6.48	1.10	0.03	0.91	-	5.66	0.00	-2.94	1.92	-
3.33 - 6.00	4.44	1.40	0.20	4.40	4.00	-	2.70	9.21	-1.77	0.26	-8.53	1.22	0.02	1.02	-	4.11	0.00	-4.40	3.00	-
High energy data period in $J/\psi \rightarrow \mu\mu$ decay channel for elastic $J/\psi$ production																				
0.00 - 0.05	0.02	334.00	8.00	4.40	-	2.00	2.70	-1.07	0.15	-0.05	0.12	0.19	0.01	-	-2.43	0.00	0.00	0.46	-	0.71
0.05 - 0.11	0.08	237.00	6.00	4.40	-	2.00	2.70	-1.37	0.19	-0.06	-0.03	0.24	0.02	-	-2.42	0.00	0.00	0.59	-	0.46
0.11 - 0.17	0.14	159.00	5.00	4.40	-	2.00	2.70	-1.84	0.25	-0.08	-0.33	0.32	0.04	-	-2.51	0.00	0.00	0.77	-	0.17
0.17 - 0.25	0.21	114.00	4.00	4.40	-	2.00	2.70	-2.35	0.34	-0.10	-0.25	0.41	0.05	-	-2.39	0.00	0.00	1.03	-	0.42
0.25 - 0.35	0.30	69.00	3.00	4.40	-	2.00	2.70	-3.57	0.53	-0.15	-0.33	0.63	0.09	-	-2.54	0.01	0.00	1.57	-	1.43
0.35 - 0.49	0.41	43.00	2.00	4.40	-	2.00	2.70	-5.00	0.76	-0.22	-0.87	0.90	0.11	-	-2.43	0.01	0.00	2.16	-	0.63
0.49 - 0.69	0.58	18.00	2.00	4.40	-	2.00	2.70	-10.71	1.67	-0.47	-2.63	1.94	0.21	-	-2.78	-0.02	0.00	4.68	-	0.80
0.69 - 1.20	0.89	5.00	0.70	4.40	-	2.00	2.70	-24.99	4.12	-1.11	-7.62	4.27	0.47	-	-2.37	0.24	0.00	10.91	-	1.51
High energy data period in $J/\psi \rightarrow \mu\mu$ decay channel for proton dissociative $J/\psi$ production																				
0.00 - 0.22	0.11	47.00	2.00	4.40	-	2.00	2.70	11.85	-1.62	0.51	0.61	-1.13	0.00	-	-2.52	-0.63	0.00	-4.48	-	0.46
0.22 - 0.44	0.32	43.00	2.00	4.40	-	2.00	2.70	12.66	-1.87	0.54	0.60	-0.74	0.01	-	-2.80	-0.54	0.00	-4.82	-	0.46
0.44 - 0.70	0.57	35.00	2.00	4.40	-	2.00	2.70	12.74	-1.98	0.56	1.03	-0.66	-0.01	-	-2.66	-0.40	0.00	-4.75	-	0.81
0.70 - 1.05	0.87	23.00	1.00	4.40	-	2.00	2.70	14.80	-2.43	0.67	1.52	-0.80	-0.03	-	-2.93	-0.26	0.00	-5.77	-	0.76
1.05 - 1.50	1.26	13.70	0.90	4.40	-	2.00	2.70	14.79	-2.53	0.62	1.75	-0.66	-0.09	-	-3.07	0.14	0.00	-5.96	-	2.24
1.50 - 2.17	1.82	8.50	0.50	4.40	-	2.00	2.70	9.38	-1.67	0.36	-1.05	0.36	-0.05	-	-3.00	0.75	0.00	-3.87	-	1.93
2.17 - 3.33	2.70	4.00	0.30	4.40	-	2.00	2.70	7.01	-1.34	0.25	-6.21	1.14	0.01	-	-3.22	1.96	0.00	-2.92	-	1.66
3.33 - 6.00	4.44	1.36	0.11	4.40	-	2.00	2.70	9.67	-1.77	0.24	-9.31	1.18	0.01	-	-3.51	2.82	0.00	-4.72	-	1.40

**Table D.1:** Elastic and proton dissociative cross sections as function of  $|t|$  in the decay channel  $J/\psi \rightarrow ee$  and  $J/\psi \rightarrow \mu\mu$  for the high energy data period obtained by use of unfolding technique. The first and second column show the bin range and the determined bin centre [297]. The cross section value is represented by  $\sigma (\langle |t|^{bc} \rangle)$  and the square root of the diagonal elements of the statistical covariance matrix is given by  $\Delta_{\text{stat}}$ . The remaining columns give the relative systematic uncertainties for the different sources: total correlated uncertainty  $\delta_{\text{sys}}^{\text{corr}}$ , the electron and muon track reconstruction uncertainty ( $\delta_{\text{sys}}^{eT}$ ,  $\delta_{\text{sys}}^{\mu T}$ ), the luminosity uncertainties for the high energy data period  $\delta_{\text{sys}}^{\mathcal{L}_H}$ , the tagging uncertainties for LAr10, PLUG and FTS ( $\delta_{\text{sys}}^{\text{LAr10}}$ ,  $\delta_{\text{sys}}^{\text{PLUG}}$ ,  $\delta_{\text{sys}}^{\text{FTS}}$ ), the uncertainties due to variation of  $\alpha_{1,\text{pd}}$ ,  $\varepsilon_M$  and  $\alpha_{1,\text{el}}$  ( $\delta_{\text{sys}}^{\alpha_{1,\text{pd}}}$ ,  $\delta_{\text{sys}}^{\varepsilon_M}$ ,  $\delta_{\text{sys}}^{\alpha_{1,\text{el}}}$ ), lepton identification for electron and muon decay channel ( $\delta_{\text{sys}}^{e\text{ID}}$ ,  $\delta_{\text{sys}}^{\mu\text{ID}}$ ), the  $Q^2$  dependence  $\delta_{\text{sys}}^{Q^2}$ , the  $R_{\text{LT}}$  variation  $\delta_{\text{sys}}^{\text{RLT}}$ , the uncertainty for the empty calorimeter cut  $\delta_{\text{sys}}^{\text{EC}}$  and the uncertainty caused by the signal extraction for the electron and muon decay channel ( $\delta_{\text{sys}}^{e\text{Sig}}$ ,  $\delta_{\text{sys}}^{\mu\text{Sig}}$ ).

$ t $ range [GeV]	$\langle  t ^{bc} \rangle$ [GeV]	$\sigma(\langle  t ^{bc} \rangle)$ [nb]	$\Delta_{\text{stat}}$ [nb]	$\delta_{\text{sys}}^{\text{corr}}$ [%]	$\delta_{\text{sys}}^{eT}$ [%]	$\delta_{\text{sys}}^{\mu T}$ [%]	$\delta_{\text{sys}}^{\mathcal{L}L}$ [%]	$\delta_{\text{sys}}^{\text{LAr10}}$ [%]	$\delta_{\text{sys}}^{\text{PLUG}}$ [%]	$\delta_{\text{sys}}^{\text{FTS}}$ [%]	$\delta_{\text{sys}}^{\alpha_{1,pd}}$ [%]	$\delta_{\text{sys}}^{\varepsilon_M}$ [%]	$\delta_{\text{sys}}^{\alpha_{1,el}}$ [%]	$\delta_{\text{sys}}^{eID}$ [%]	$\delta_{\text{sys}}^{\mu ID}$ [%]	$\delta_{\text{sys}}^{Q^2}$ [%]	$\delta_{\text{sys}}^{\text{RLT}}$ [%]	$\delta_{\text{sys}}^{\text{EC}}$ [%]	$\delta_{\text{sys}}^{e\text{Sig}}$ [%]	$\delta_{\text{sys}}^{\mu\text{Sig}}$ [%]
Low energy data period in $J/\psi \rightarrow ee$ decay channel for elastic $J/\psi$ production																				
0.0 - 0.1	0.05	200.00	20.00	4.40	4.00	-	5.00	-2.29	0.33	-0.09	0.51	0.27	0.02	0.59	-	-0.91	0.00	0.92	4.33	-
0.1 - 0.2	0.17	99.00	12.00	4.40	4.00	-	5.00	-4.15	0.59	-0.17	-0.14	0.50	-0.03	0.69	-	-0.91	0.00	1.67	5.54	-
0.2 - 0.5	0.34	54.00	8.00	4.40	4.00	-	5.00	-5.47	0.77	-0.18	-1.48	0.68	-0.05	0.58	-	-0.46	0.00	2.31	7.03	-
0.5 - 1.2	0.75	10.00	2.00	4.40	4.00	-	5.00	-13.74	2.06	-0.35	-2.25	1.58	0.38	0.55	-	1.26	0.00	6.13	11.50	-
Low energy data period in $J/\psi \rightarrow ee$ decay channel for proton dissociative $J/\psi$ production																				
0.0 - 0.4	0.20	52.00	7.00	4.40	4.00	-	5.00	16.43	-2.32	0.60	0.96	-0.56	0.01	0.56	-	-0.68	0.00	-6.12	8.71	-
0.4 - 1.0	0.72	23.00	3.00	4.40	4.00	-	5.00	20.51	-3.06	0.60	1.48	-0.29	-0.18	0.81	-	-0.64	0.00	-8.73	2.58	-
1.0 - 2.1	1.52	10.00	2.00	4.40	4.00	-	5.00	16.00	-2.63	0.24	-1.31	0.41	-0.05	0.79	-	0.56	0.00	-7.26	4.50	-
2.1 - 5.0	3.28	2.60	0.70	4.40	4.00	-	5.00	10.23	-1.83	0.07	-9.90	2.01	0.19	0.99	-	7.09	0.00	-5.12	4.31	-
Low energy data period in $J/\psi \rightarrow \mu\mu$ decay channel for elastic $J/\psi$ production																				
0.0 - 0.1	0.05	221.00	14.00	4.40	-	2.00	5.00	-2.16	0.31	-0.04	0.49	0.28	0.05	-	-2.75	0.00	0.00	0.96	-	0.49
0.1 - 0.2	0.17	114.00	10.00	4.40	-	2.00	5.00	-3.59	0.51	-0.07	-0.01	0.47	-0.07	-	-2.86	0.00	0.00	1.58	-	1.00
0.2 - 0.5	0.34	54.00	6.00	4.40	-	2.00	5.00	-5.97	0.84	-0.12	-1.70	0.78	-0.08	-	-2.84	0.04	0.00	2.66	-	1.97
0.5 - 1.2	0.75	11.00	2.00	4.40	-	2.00	5.00	-10.89	1.72	-0.20	-1.17	1.28	0.04	-	-2.46	0.07	0.00	5.15	-	1.16
Low energy data period in $J/\psi \rightarrow \mu\mu$ decay channel for proton dissociative $J/\psi$ production																				
0.0 - 0.4	0.20	57.00	6.00	4.40	-	2.00	5.00	15.41	-2.17	0.31	1.15	-0.61	-0.04	-	-2.89	-0.73	0.00	-6.24	-	0.53
0.4 - 1.0	0.72	25.00	3.00	4.40	-	2.00	5.00	18.72	-2.95	0.34	0.47	-0.13	-0.14	-	-3.66	-0.24	0.00	-8.18	-	0.65
1.0 - 2.1	1.52	11.00	2.00	4.40	-	2.00	5.00	15.22	-2.55	0.21	-0.43	0.50	-0.10	-	-3.26	0.78	0.00	-7.37	-	1.86
2.1 - 5.0	3.28	2.40	0.40	4.40	-	2.00	5.00	9.04	-1.61	0.11	-14.44	1.38	0.02	-	-2.90	3.38	0.00	-4.19	-	1.38

**Table D.2:** Elastic and proton dissociative cross sections as function of  $|t|$  in the decay channel  $J/\psi \rightarrow ee$  and  $J/\psi \rightarrow \mu\mu$  for the low energy data period obtained by use of unfolding technique. The first and second column show the bin range and the determined bin centre [297]. The cross section value is represented by  $\sigma(\langle |t|^{bc} \rangle)$  and the square root of the diagonal elements of the statistical covariance matrix is given by  $\Delta_{\text{stat}}$ . The remaining columns give the relative systematic uncertainties for the different sources: total correlated uncertainty  $\delta_{\text{sys}}^{\text{corr}}$ , the electron and muon track reconstruction uncertainty ( $\delta_{\text{sys}}^{eT}$ ,  $\delta_{\text{sys}}^{\mu T}$ ), the luminosity uncertainties for the low energy data period  $\delta_{\text{sys}}^{\mathcal{L}L}$ , the tagging uncertainties for LAr10, PLUG and FTS ( $\delta_{\text{sys}}^{\text{LAr10}}$ ,  $\delta_{\text{sys}}^{\text{PLUG}}$ ,  $\delta_{\text{sys}}^{\text{FTS}}$ ), the uncertainties due to variation of  $\alpha_{1,pd}$ ,  $\varepsilon_M$  and  $\alpha_{1,el}$  ( $\delta_{\text{sys}}^{\alpha_{1,pd}}$ ,  $\delta_{\text{sys}}^{\varepsilon_M}$ ,  $\delta_{\text{sys}}^{\alpha_{1,el}}$ ), lepton identification for electron and muon decay channel ( $\delta_{\text{sys}}^{eID}$ ,  $\delta_{\text{sys}}^{\mu ID}$ ), the  $Q^2$  dependence  $\delta_{\text{sys}}^{Q^2}$ , the  $R_{LT}$  variation  $\delta_{\text{sys}}^{\text{RLT}}$ , the uncertainty for the empty calorimeter cut  $\delta_{\text{sys}}^{\text{EC}}$  and the uncertainty caused by the signal extraction for the electron and muon decay channel ( $\delta_{\text{sys}}^{e\text{Sig}}$ ,  $\delta_{\text{sys}}^{\mu\text{Sig}}$ ).

## Appendix D Cross section tables

$W_{\gamma p}$ range [GeV]	$\langle W_{\gamma p}^{\text{bc}} \rangle$ [GeV]	$\sigma(\langle W_{\gamma p}^{\text{bc}} \rangle)$ [nb]	$\Delta_{\text{stat}}$ [nb]	$\delta_{\text{sys}}^{\text{corr}}$ [%]	$\delta_{\text{sys}}^{\text{eT}}$ [%]	$\delta_{\text{sys}}^{\mu\text{T}}$ [%]	$\delta_{\text{sys}}^{\mathcal{L}_M}$ [%]	$\delta_{\text{sys}}^{\mathcal{L}_L}$ [%]	$\delta_{\text{sys}}^{\text{LAr10}}$ [%]	$\delta_{\text{sys}}^{\text{PLUG}}$ [%]	$\delta_{\text{sys}}^{\text{FTS}}$ [%]	$\delta_{\text{sys}}^{\alpha_{1,\text{pd}}}$ [%]	$\delta_{\text{sys}}^{\varepsilon_M}$ [%]	$\delta_{\text{sys}}^{\alpha_{1,\text{el}}}$ [%]	$\delta_{\text{sys}}^{\text{eID}}$ [%]	$\delta_{\text{sys}}^{\mu\text{ID}}$ [%]	$\delta_{\text{sys}}^{Q^2}$ [%]	$\delta_{\text{sys}}^{\text{RLT}}$ [%]	$\delta_{\text{sys}}^{\text{EC}}$ [%]	$\delta_{\text{sys}}^{\text{eSig}}$ [%]	$\delta_{\text{sys}}^{\mu\text{Sig}}$ [%]
High energy data period in $J/\psi \rightarrow ee$ decay channel for elastic $J/\psi$ production																					
40.0 - 46.5	43.2	45.0	4.0	4.40	4.00	-	2.70	-	-3.69	0.57	-0.17	3.83	0.63	0.35	0.70	-	-0.62	0.00	1.64	5.38	-
46.5 - 53.5	50.0	55.0	3.0	4.40	4.00	-	2.70	-	-2.85	0.46	-0.14	3.26	0.51	0.19	0.52	-	-0.58	0.00	1.19	2.47	-
53.5 - 61.2	57.3	56.0	4.0	4.40	4.00	-	2.70	-	-3.38	0.54	-0.16	3.91	0.61	0.19	0.45	-	-0.71	0.00	1.48	4.26	-
61.2 - 69.4	65.3	66.0	3.0	4.40	4.00	-	2.70	-	-3.05	0.48	-0.14	3.35	0.54	0.11	0.39	-	-0.65	0.00	1.33	2.77	-
69.4 - 78.4	73.9	69.0	3.0	4.40	4.00	-	2.70	-	-3.50	0.54	-0.16	3.60	0.62	0.05	0.40	-	-0.75	0.00	1.51	2.09	-
78.4 - 88.0	83.2	74.0	3.0	4.40	4.00	-	2.70	-	-3.41	0.52	-0.16	3.29	0.60	0.02	0.46	-	-0.74	0.00	1.37	1.01	-
88.0 - 98.5	93.3	77.0	4.0	4.40	4.00	-	2.70	-	-3.25	0.50	-0.15	3.14	0.56	0.00	0.59	-	-0.73	0.00	1.38	1.58	-
98.5 - 110.0	104.3	85.0	7.0	4.40	4.00	-	2.70	-	-3.40	0.53	-0.16	3.02	0.59	-0.08	0.70	-	-0.78	0.00	1.43	4.10	-
High energy data period in $J/\psi \rightarrow ee$ decay channel for proton dissociative $J/\psi$ production																					
40.0 - 46.0	43.0	47.0	5.0	4.40	4.00	-	2.70	-	11.64	-1.83	0.52	-1.33	-0.06	-0.34	0.86	-	0.63	0.00	-5.14	6.26	-
46.0 - 52.7	49.3	43.0	3.0	4.40	4.00	-	2.70	-	11.50	-1.82	0.56	-2.72	-0.12	-0.32	0.67	-	0.80	0.00	-4.41	2.66	-
52.7 - 60.0	56.3	55.0	3.0	4.40	4.00	-	2.70	-	11.18	-1.81	0.53	-3.31	-0.19	-0.18	0.61	-	0.84	0.00	-4.19	1.98	-
60.0 - 68.2	64.1	55.0	3.0	4.40	4.00	-	2.70	-	11.57	-1.81	0.54	-3.52	-0.23	-0.16	0.67	-	0.95	0.00	-4.39	1.15	-
68.2 - 77.2	72.7	62.0	4.0	4.40	4.00	-	2.70	-	11.77	-1.80	0.55	-3.46	-0.27	-0.09	0.74	-	0.93	0.00	-4.40	0.90	-
77.2 - 87.0	82.0	65.0	4.0	4.40	4.00	-	2.70	-	11.71	-1.80	0.55	-3.27	-0.27	-0.04	0.69	-	1.00	0.00	-4.06	0.80	-
87.0 - 97.9	92.4	64.0	4.0	4.40	4.00	-	2.70	-	11.71	-1.81	0.55	-3.56	-0.28	0.01	0.59	-	1.04	0.00	-4.33	1.08	-
97.9 - 110.0	103.9	67.0	6.0	4.40	4.00	-	2.70	-	12.11	-1.87	0.55	-3.73	-0.32	0.05	0.94	-	1.17	0.00	-4.51	1.28	-
High energy data period in $J/\psi \rightarrow \mu\mu$ decay channel for elastic $J/\psi$ production																					
40.0 - 46.5	43.2	51.0	2.0	4.40	-	2.00	2.70	-	-2.59	0.42	-0.11	3.34	0.50	0.26	-	-1.31	-0.13	0.00	1.17	-	1.28
46.5 - 53.5	50.0	60.0	2.0	4.40	-	2.00	2.70	-	-2.92	0.48	-0.12	4.00	0.56	0.19	-	-1.11	-0.14	0.00	1.30	-	1.35
53.5 - 61.2	57.3	62.0	3.0	4.40	-	2.00	2.70	-	-3.22	0.51	-0.13	4.16	0.62	0.14	-	-1.01	-0.16	0.00	1.44	-	3.25
61.2 - 69.4	65.3	67.0	2.0	4.40	-	2.00	2.70	-	-2.88	0.46	-0.12	3.62	0.54	0.12	-	-0.97	-0.16	0.00	1.28	-	1.66
69.4 - 78.4	73.9	72.0	2.0	4.40	-	2.00	2.70	-	-2.79	0.45	-0.12	3.33	0.53	0.06	-	-0.97	-0.16	0.00	1.27	-	1.22
78.4 - 88.0	83.2	83.0	3.0	4.40	-	2.00	2.70	-	-2.59	0.41	-0.11	2.98	0.49	0.02	-	-0.98	-0.16	0.00	1.22	-	1.84
88.0 - 98.5	93.3	85.0	3.0	4.40	-	2.00	2.70	-	-3.06	0.48	-0.13	3.37	0.58	0.00	-	-1.01	-0.17	0.00	1.41	-	0.97
98.5 - 110.0	104.3	86.0	4.0	4.40	-	2.00	2.70	-	-2.91	0.46	-0.12	3.11	0.54	-0.07	-	-1.12	-0.18	0.00	1.29	-	0.89
High energy data period in $J/\psi \rightarrow \mu\mu$ decay channel for proton dissociative $J/\psi$ production																					
40.0 - 46.0	43.0	41.0	4.0	4.40	-	2.00	2.70	-	10.42	-1.66	0.44	-1.74	-0.08	-0.37	-	-1.43	0.14	0.00	-4.51	-	5.68
46.0 - 52.7	49.3	55.0	3.0	4.40	-	2.00	2.70	-	10.40	-1.70	0.44	-3.52	-0.13	-0.27	-	-1.29	0.15	0.00	-4.08	-	2.81
52.7 - 60.0	56.3	60.0	3.0	4.40	-	2.00	2.70	-	10.56	-1.67	0.44	-3.54	-0.22	-0.18	-	-1.20	0.18	0.00	-4.01	-	3.08
60.0 - 68.2	64.1	58.0	3.0	4.40	-	2.00	2.70	-	10.72	-1.72	0.44	-3.88	-0.26	-0.15	-	-1.16	0.23	0.00	-3.95	-	1.31
68.2 - 77.2	72.7	59.0	3.0	4.40	-	2.00	2.70	-	10.61	-1.70	0.45	-3.81	-0.27	-0.09	-	-1.15	0.22	0.00	-3.95	-	0.60
77.2 - 87.0	82.0	60.0	3.0	4.40	-	2.00	2.70	-	10.89	-1.73	0.45	-4.02	-0.32	-0.04	-	-1.16	0.27	0.00	-4.28	-	0.59
87.0 - 97.9	92.4	72.0	3.0	4.40	-	2.00	2.70	-	10.92	-1.71	0.45	-3.87	-0.32	0.01	-	-1.18	0.23	0.00	-4.24	-	0.66
97.9 - 110.0	103.9	68.0	4.0	4.40	-	2.00	2.70	-	10.91	-1.71	0.46	-3.59	-0.29	0.05	-	-1.24	0.26	0.00	-4.18	-	0.50
Low energy data period in $J/\psi \rightarrow ee$ decay channel for elastic $J/\psi$ production																					
25.0 - 39.0	31.9	34.0	6.0	4.40	4.00	-	-	5.00	-4.98	0.77	-0.14	2.72	0.61	0.71	0.56	-	-0.45	0.00	2.39	6.82	-
39.0 - 56.9	47.9	60.0	5.0	4.40	4.00	-	-	5.00	-3.80	0.57	-0.11	2.07	0.47	0.25	0.51	-	-0.42	0.00	1.69	2.66	-
56.9 - 79.9	68.3	58.0	6.0	4.40	4.00	-	-	5.00	-6.19	0.96	-0.16	2.90	0.80	0.10	0.61	-	-0.47	0.00	2.73	3.91	-
79.9 - 110.0	94.8	60.0	11.0	4.40	4.00	-	-	5.00	-6.91	1.01	-0.17	3.13	0.88	-0.12	0.62	-	-0.50	0.00	3.29	7.32	-
Low energy data period in $J/\psi \rightarrow ee$ decay channel for proton dissociative $J/\psi$ production																					
25.0 - 37.9	31.3	41.0	8.0	4.40	4.00	-	-	5.00	15.89	-2.49	0.44	-0.30	0.34	-0.48	0.77	-	0.50	0.00	-7.44	8.11	-
37.9 - 55.2	46.4	49.0	7.0	4.40	4.00	-	-	5.00	16.40	-2.43	0.48	-1.85	0.15	-0.46	0.63	-	0.68	0.00	-6.62	4.01	-
55.2 - 78.2	66.5	81.0	8.0	4.40	4.00	-	-	5.00	15.47	-2.41	0.40	-1.39	0.13	-0.11	0.71	-	0.48	0.00	-6.07	2.32	-
78.2 - 110.0	93.9	83.0	15.0	4.40	4.00	-	-	5.00	16.14	-2.36	0.40	-2.58	0.15	0.01	0.85	-	0.69	0.00	-7.34	5.03	-
Low energy data period in $J/\psi \rightarrow \mu\mu$ decay channel for elastic $J/\psi$ production																					
25.0 - 39.0	31.9	46.0	4.0	4.40	-	2.00	-	5.00	-3.71	0.59	-0.06	2.55	0.48	0.44	-	-1.26	-0.10	0.00	1.76	-	2.50
39.0 - 56.9	47.9	58.0	4.0	4.40	-	2.00	-	5.00	-4.30	0.66	-0.07	2.71	0.56	0.26	-	-0.98	-0.13	0.00	2.06	-	0.93
56.9 - 79.9	68.3	74.0	5.0	4.40	-	2.00	-	5.00	-3.52	0.53	-0.06	1.93	0.47	0.11	-	-1.03	-0.11	0.00	1.78	-	1.01
79.9 - 110.0	94.8	79.0	11.0	4.40	-	2.00	-	5.00	-6.44	0.99	-0.11	3.55	0.84	-0.26	-	-1.60	-0.28	0.00	3.15	-	1.21
Low energy data period in $J/\psi \rightarrow \mu\mu$ decay channel for proton dissociative $J/\psi$ production																					
25.0 - 37.9	31.3	44.0	8.0	4.40	-	2.00	-	5.00	14.64	-2.33	0.24	-1.34	0.36	-0.59	-	-1.47	0.12	0.00	-6.54	-	7.75
37.9 - 55.2	46.4	62.0	6.0	4.40	-	2.00	-	5.00	14.80	-2.28	0.26	-2.10	0.14	-0.35	-	-1.29	0.20	0.00	-6.26	-	1.24
55.2 - 78.2	66.5	59.0	7.0	4.40	-	2.00	-	5.00	15.24	-2.30	0.26	-2.03	0.07	-0.21	-	-1.30	0.16	0.00	-6.80	-	0.57
78.2 - 110.0	93.9	110.0	20.0	4.40	-	2.00	-	5.00	15.41	-2.38	0.27	-2.74	0.27	0.05	-	-1.56	0.32	0.00	-7.23	-	1.05

**Table D.3:** Elastic and proton dissociative cross sections as function of  $W_{\gamma p}$  in the decay channel  $J/\psi \rightarrow ee$  and  $J/\psi \rightarrow \mu\mu$  for the high and low energy data period obtained by use of unfolding technique. The first and second column show the bin range and the determined bin centre [297]. The cross section value is represented by  $\sigma(\langle W_{\gamma p}^{\text{bc}} \rangle)$  and the square root of the diagonal elements of the statistical covariance matrix is given by  $\Delta_{\text{stat}}$ . The remaining columns give the relative systematic uncertainties for the different sources: total correlated uncertainty  $\delta_{\text{sys}}^{\text{corr}}$ , the electron and muon track reconstruction uncertainty ( $\delta_{\text{sys}}^{\text{eT}}$ ,  $\delta_{\text{sys}}^{\mu\text{T}}$ ), the luminosity uncertainties for the high and low energy data period ( $\delta_{\text{sys}}^{\mathcal{L}_H}$ ,  $\delta_{\text{sys}}^{\mathcal{L}_L}$ ), the tagging uncertainties for LAr10, PLUG and FTS ( $\delta_{\text{sys}}^{\text{LAr10}}$ ,  $\delta_{\text{sys}}^{\text{PLUG}}$ ,  $\delta_{\text{sys}}^{\text{FTS}}$ ), the uncertainties due to variation of  $\alpha_{1,\text{pd}}$ ,  $\varepsilon_M$  and  $\alpha_{1,\text{el}}$  ( $\delta_{\text{sys}}^{\alpha_{1,\text{pd}}}$ ,  $\delta_{\text{sys}}^{\varepsilon_M}$ ,  $\delta_{\text{sys}}^{\alpha_{1,\text{el}}}$ ), lepton identification for electron and muon decay channel ( $\delta_{\text{sys}}^{\text{eID}}$ ,  $\delta_{\text{sys}}^{\mu\text{ID}}$ ), the  $Q^2$  dependence  $\delta_{\text{sys}}^{Q^2}$ , the  $R_{\text{LT}}$  variation  $\delta_{\text{sys}}^{\text{RLT}}$ , the uncertainty for the empty calorimeter cut  $\delta_{\text{sys}}^{\text{EC}}$  and the uncertainty caused by the signal extraction for the electron and muon decay channel ( $\delta_{\text{sys}}^{\text{eSig}}$ ,  $\delta_{\text{sys}}^{\mu\text{Sig}}$ ).

-21.06																	1
-27.93	18.05																2
1.49	-30.33	3.39															3
3.03	-7.35	-30.12	0.39														4
-3.02	-1.21	-3.83	-25.05	0.68													5
-2.76	-3.50	-1.52	-2.75	-19.28	-2.99												6
-2.84	-2.36	-2.71	-3.61	-5.29	-16.83	-6.38											7
-17.16	-22.54	-17.46	-8.12	2.42	8.54	12.02	3.98										8
4.32	4.81	3.38	-11.42	-25.93	-27.15	-9.35	18.35	-12.64									9
6.54	5.68	7.29	6.20	-5.17	-26.44	-36.29	-23.50	-28.04	18.58								10
4.16	1.59	2.71	5.35	11.53	10.55	-19.08	-62.11	-4.13	-28.81	24.70							11
1.88	0.54	1.18	1.34	3.39	9.93	9.71	-24.45	0.74	-10.09	-19.96	20.03						12
0.23	0.02	0.63	-0.15	-0.09	0.21	4.88	11.59	-0.17	0.21	-9.23	-14.05	16.37					13
0.97	-0.71	-0.47	-0.58	-0.22	-0.74	-1.26	1.97	0.09	-0.17	0.32	-1.12	-9.40	-10.98				14
1.50	0.21	0.52	0.12	-0.16	-0.48	-0.41	-2.04	0.57	-0.02	-0.02	1.02	0.22	-9.46	-22.95			15
1	2	3	4	5	6	7	8	9	10	11	12	13	14	15	16		16

**Table D.4:** Statistical correlation matrix  $\rho_{ij}$  for the high energy data period in the  $J/\psi \rightarrow ee$  decay channel for bins in  $|t|$ . The indices  $i = 1, \dots, 8$  and  $i = 9, \dots, 16$  represent elastic and proton dissociative bins, respectively. The correlations values are given in %.

-9.94																	1
-9.04	5.44																2
2.08	-12.60	-1.75															3
-1.56	-1.85	-14.36	-2.08														4
-3.24	-3.17	-2.27	-10.29	1.67													5
-4.29	-4.80	-4.58	-2.01	-7.37	3.88												6
-3.52	-3.40	-3.65	-4.36	-5.44	-7.87	17.83											7
-21.14	-25.20	-25.14	-12.16	1.73	6.62	11.08	5.49										8
1.39	2.75	1.08	-13.90	-31.35	-29.50	-11.47	9.47	-7.74									9
5.49	5.97	6.17	2.35	-6.95	-27.83	-46.53	-29.64	-22.18	23.87								10
2.23	2.12	2.49	3.79	6.86	2.75	-30.47	-61.64	-6.61	-15.97	32.16							11
0.57	0.50	0.70	1.50	2.72	6.73	6.07	-31.55	-1.00	-8.48	-11.52	23.44						12
-0.70	-0.48	-0.19	0.02	0.20	1.39	5.61	-2.31	-0.88	-2.50	-7.13	-5.16	25.18					13
-0.29	-0.88	-0.87	-0.91	-0.81	-0.86	-0.61	1.06	-0.65	-1.04	-1.30	-2.65	-7.00	-0.37				14
0.33	0.08	-0.01	-0.25	-0.41	-0.55	-0.96	-0.67	0.33	-0.21	-0.53	-0.98	-2.99	-10.71	-0.14			15
1	2	3	4	5	6	7	8	9	10	11	12	13	14	15	16		16

**Table D.5:** Statistical correlation matrix  $\rho_{ij}$  for the high energy data period in the  $J/\psi \rightarrow \mu\mu$  decay channel for bins in  $|t|$ . The indices  $i = 1, \dots, 8$  and  $i = 9, \dots, 16$  represent elastic and proton dissociative bins, respectively. The correlations values are given in %.

Appendix D Cross section tables

-18.67																1
4.52	-22.26															2
-0.31	4.74	-20.51														3
0.42	-0.05	3.04	-15.88													4
0.36	0.38	0.45	2.06	-14.22												5
0.24	0.24	0.41	0.13	2.44	-20.28											6
0.20	0.21	0.35	0.30	-0.28	5.73	-35.36										7
-41.09	8.22	-1.24	0.79	0.29	0.35	0.23	0.20									8
2.86	-41.64	10.85	-2.33	0.60	0.13	0.12	0.10	-13.69								9
0.96	1.91	-36.75	10.92	-1.97	0.43	0.08	0.11	2.38	-19.44							10
-0.42	2.10	-2.50	-38.34	11.29	-1.39	0.35	0.02	-0.11	2.61	-17.01						11
0.38	-0.57	2.91	-0.76	-44.65	8.58	-1.44	0.55	0.21	-0.13	2.33	-18.47					12
0.17	0.33	-0.15	1.41	1.34	-44.22	11.81	-3.12	0.19	0.10	-0.04	1.81	-13.34				13
0.17	0.15	0.39	-0.09	0.86	4.64	-46.12	16.47	0.16	0.09	0.09	-0.13	2.04	-19.82			14
0.10	0.10	0.15	0.21	-0.12	-0.41	12.39	-46.09	0.10	0.05	0.05	0.07	-0.32	4.61	-29.67		15
1	2	3	4	5	6	7	8	9	10	11	12	13	14	15	16	16

**Table D.6:** Statistical correlation matrix  $\rho_{ij}$  for the high energy data period in the  $J/\psi \rightarrow ee$  decay channel for bins in  $W_{\gamma p}$ . The indices  $i = 1, \dots, 8$  and  $i = 9, \dots, 16$  represent elastic and proton dissociative bins, respectively. The correlations values are given in %.

-3.02																1
-0.62	-2.81															2
0.05	-0.46	-2.21														3
0.02	0.04	-0.40	-4.49													4
0.03	0.01	0.15	-0.27	-4.13												5
0.01	-0.01	0.06	0.05	-0.24	-4.74											6
0.02	0.02	0.09	0.04	0.07	-0.11	-5.86										7
-52.56	3.08	0.58	-0.03	0.02	0.04	0.02	0.03									8
-2.28	-48.47	2.38	0.31	-0.02	0.04	0.02	0.04	-3.72								9
1.09	-4.83	-42.97	2.12	0.24	0.01	0.02	0.04	-0.95	-3.24							10
-0.00	0.89	-5.01	-40.85	3.59	0.09	-0.02	0.03	0.07	-0.56	-2.72						11
0.01	-0.02	1.02	-5.27	-43.08	3.30	0.07	-0.00	0.02	0.07	-0.46	-4.77					12
0.01	-0.01	0.00	1.01	-4.02	-42.90	3.72	0.16	0.01	0.01	0.05	-0.29	-4.53				13
0.01	0.01	0.05	-0.03	0.83	-2.33	-46.04	2.58	0.02	0.02	0.02	0.06	-0.22	-5.14			14
-0.00	-0.02	0.01	-0.02	-0.04	0.69	-1.72	-39.54	-0.00	-0.01	-0.01	-0.01	0.04	-0.36	-3.90		15
1	2	3	4	5	6	7	8	9	10	11	12	13	14	15	16	16

**Table D.7:** Statistical correlation matrix  $\rho_{ij}$  for the high energy data period in the  $J/\psi \rightarrow \mu\mu$  decay channel for bins in  $W_{\gamma p}$ . The indices  $i = 1, \dots, 8$  and  $i = 9, \dots, 16$  represent elastic and proton dissociative bins, respectively. The correlations values are given in %.

-16.96																1
-20.28	23.25															2
3.72	-18.60	-10.77														3
-14.31	-39.36	-38.39	-8.70													4
-0.72	-1.82	-17.36	-48.10	12.04												5
6.44	12.18	9.30	-16.97	-26.75	25.75											6
0.50	-1.46	0.58	8.38	-2.08	-20.41	-0.34										7
1	2	3	4	5	6	7	8									8

**Table D.8:** Statistical correlation matrix  $\rho_{ij}$  for the low energy data period in the  $J/\psi \rightarrow ee$  decay channel for bins in  $|t|$ . The indices  $i = 1, \dots, 4$  and  $i = 5, \dots, 8$  represent elastic and proton dissociative bins, respectively. The correlations values are given in %.





# Bibliography

- [1] CMS Collaboration Collaboration, S. Chatrchyan *et al.*, “Observation of a new boson at a mass of 125 GeV with the CMS experiment at the LHC”, *Phys.Lett.B* **716** no. 1, (2012) 30 – 61, [arXiv:1207.7235 \[hep-ex\]](#).
- [2] ATLAS Collaboration Collaboration, G. Aad *et al.*, “Observation of a new particle in the search for the Standard Model Higgs boson with the ATLAS detector at the LHC”, *Phys.Lett.B* **716** no. 1, (2012) 1 – 29, [arXiv:1207.7214 \[hep-ex\]](#).
- [3] ZEUS Collaboration Collaboration, M. Derrick *et al.*, “Observation of events with a large rapidity gap in deep inelastic scattering at HERA”, *Phys.Lett.* **B315** (1993) 481–493.
- [4] H1 Collaboration Collaboration, T. Ahmed *et al.*, “Deep inelastic scattering events with a large rapidity gap at HERA”, *Nucl.Phys.* **B429** (1994) 477–502.
- [5] A. Levy, M. Ferstl, and A. Gute, “Low- $x$  physics at HERA”, in *Lectures on QCD*, F. Lenz, H. Grißhammer, and D. Stoll, eds., vol. 496 of *Lecture Notes in Physics*, pp. 347–477. Springer Berlin / Heidelberg, 1997.
- [6] E598 Collaboration Collaboration, J. Aubert *et al.*, “Experimental Observation of a Heavy Particle J”, *Phys.Rev.Lett.* **33** (1974) 1404–1406.
- [7] SLAC-SP-017 Collaboration Collaboration, J. Augustin *et al.*, “Discovery of a Narrow Resonance in  $e^+e^-$  Annihilation”, *Phys.Rev.Lett.* **33** (1974) 1406–1408.
- [8] H1 Collaboration Collaboration, F. Aaron *et al.*, “Diffractive Electroproduction of rho and phi Mesons at HERA”, *JHEP* **1005** (2010) 032, [arXiv:0910.5831 \[hep-ex\]](#).
- [9] H1 Collaboration Collaboration, C. Adloff *et al.*, “Proton dissociative  $\rho$  and elastic  $\phi$  electroproduction at HERA”, *Z.Phys.* **C75** (1997) 607–618, [arXiv:hep-ex/9705014 \[hep-ex\]](#).
- [10] H1 Collaboration Collaboration, A. Aktas *et al.*, “Diffractive photoproduction of rho mesons with large momentum transfer at HERA”, *Phys.Lett.* **B638** (2006) 422–431, [arXiv:hep-ex/0603038 \[hep-ex\]](#).
- [11] H1 Collaboration Collaboration, C. Adloff *et al.*, “Elastic electroproduction of rho mesons at HERA”, *Eur.Phys.J.* **C13** (2000) 371–396, [arXiv:hep-ex/9902019 \[hep-ex\]](#).
- [12] H1 Collaboration Collaboration, S. Aid *et al.*, “Elastic photoproduction of rho0 mesons at HERA”, *Nucl.Phys.* **B463** (1996) 3–32, [arXiv:hep-ex/9601004 \[hep-ex\]](#).
- [13] H1 Collaboration Collaboration, S. Aid *et al.*, “Elastic electroproduction of  $\rho$  and  $J/\psi$  mesons at large  $Q^2$  at HERA”, *Nucl.Phys.* **B468** (1996) 3–36, [arXiv:hep-ex/9602007 \[hep-ex\]](#).
- [14] ZEUS collaboration Collaboration, H. Abramowicz *et al.*, “Exclusive electroproduction of two pions at HERA”, *Eur.Phys.J.* **C72** (2012) 1869, [arXiv:1111.4905 \[hep-ex\]](#).

## BIBLIOGRAPHY

- [15] ZEUS Collaboration Collaboration, S. Chekanov *et al.*, “Exclusive  $\rho^0$  production in deep inelastic scattering at HERA”, *PMC Phys. A* **1** (2007) 6, [arXiv:0708.1478 \[hep-ex\]](#).
- [16] ZEUS Collaborations Collaboration, J. Breitweg *et al.*, “Measurement of the spin density matrix elements in exclusive electroproduction of  $\rho^0$  mesons at HERA”, *Eur.Phys.J.* **C12** (2000) 393–410, [arXiv:hep-ex/9908026 \[hep-ex\]](#).
- [17] ZEUS Collaboration Collaboration, J. Breitweg *et al.*, “Elastic and proton dissociative  $\rho^0$  photoproduction at HERA”, *Eur.Phys.J.* **C2** (1998) 247–267, [arXiv:hep-ex/9712020 \[hep-ex\]](#).
- [18] ZEUS Collaboration Collaboration, M. Derrick *et al.*, “Measurement of elastic  $\rho^0$  photoproduction at HERA”, *Z.Phys.* **C69** (1995) 39–54, [arXiv:hep-ex/9507011 \[hep-ex\]](#).
- [19] ZEUS Collaboration Collaboration, M. Derrick *et al.*, “Exclusive  $\rho^0$  production in deep inelastic electron - proton scattering at HERA”, *Phys.Lett.* **B356** (1995) 601–616, [arXiv:hep-ex/9507001 \[hep-ex\]](#).
- [20] ZEUS Collaboration Collaboration, S. Chekanov *et al.*, “Measurement of proton dissociative diffractive photoproduction of vector mesons at large momentum transfer at HERA”, *Eur.Phys.J.* **C26** (2003) 389–409, [arXiv:hep-ex/0205081 \[hep-ex\]](#).
- [21] ZEUS Collaboration Collaboration, J. Breitweg *et al.*, “Measurement of diffractive photoproduction of vector mesons at large momentum transfer at HERA”, *Eur.Phys.J.* **C14** (2000) 213–238, [arXiv:hep-ex/9910038 \[hep-ex\]](#).
- [22] ZEUS Collaboration Collaboration, J. Breitweg *et al.*, “Exclusive electroproduction of  $\rho^0$  and  $J/\psi$  mesons at HERA”, *Eur.Phys.J.* **C6** (1999) 603–627, [arXiv:hep-ex/9808020 \[hep-ex\]](#).
- [23] H1 Collaboration Collaboration, C. Adloff *et al.*, “Measurement of elastic electroproduction of  $\phi$  mesons at HERA”, *Phys.Lett.* **B483** (2000) 360–372, [arXiv:hep-ex/0005010 \[hep-ex\]](#).
- [24] ZEUS Collaboration Collaboration, S. Chekanov *et al.*, “Exclusive electroproduction of  $\phi$  mesons at HERA”, *Nucl.Phys.* **B718** (2005) 3–31, [arXiv:hep-ex/0504010 \[hep-ex\]](#).
- [25] ZEUS Collaboration Collaboration, M. Derrick *et al.*, “Measurement of the reaction  $\gamma^*p \rightarrow \phi p$  in deep inelastic  $e^+p$  scattering at HERA”, *Phys.Lett.* **B380** (1996) 220–234, [arXiv:hep-ex/9604008 \[hep-ex\]](#).
- [26] ZEUS Collaboration Collaboration, M. Derrick *et al.*, “Measurement of elastic  $\phi$  photoproduction at HERA”, *Phys.Lett.* **B377** (1996) 259–272, [arXiv:hep-ex/9601009 \[hep-ex\]](#).
- [27] ZEUS Collaboration Collaboration, J. Breitweg *et al.*, “Measurement of exclusive omega electroproduction at HERA”, *Phys.Lett.* **B487** (2000) 273–288, [arXiv:hep-ex/0006013 \[hep-ex\]](#).
- [28] ZEUS Collaboration Collaboration, M. Derrick *et al.*, “Measurement of elastic omega photoproduction at HERA”, *Z.Phys.* **C73** (1996) 73–84, [arXiv:hep-ex/9608010 \[hep-ex\]](#).
- [29] H1 Collaboration Collaboration, A. Aktas *et al.*, “Elastic  $J/\psi$  production at HERA”, *Eur.Phys.J.* **C46** (2006) 585–603, [arXiv:hep-ex/0510016 \[hep-ex\]](#).
- [30] H1 Collaboration Collaboration, A. Aktas *et al.*, “Diffractive photoproduction of  $J/\psi$  mesons with large momentum transfer at HERA”, *Phys.Lett.* **B568** (2003) 205–218, [arXiv:hep-ex/0306013 \[hep-ex\]](#).
- [31] H1 Collaboration Collaboration, S. Aid *et al.*, “Elastic and inelastic photoproduction of  $J/\psi$  mesons at HERA”, *Nucl.Phys.* **B472** (1996) 3–31, [arXiv:hep-ex/9603005](#)

- [32] H1 Collaboration Collaboration, T. Ahmed *et al.*, “Photoproduction of J / psi mesons at HERA”, *Phys.Lett.* **B338** (1994) 507–518.
- [33] H1 Collaboration Collaboration, C. Adloff *et al.*, “Elastic photoproduction of J / psi and Upsilon mesons at HERA”, *Phys.Lett.* **B483** (2000) 23–35, [arXiv:hep-ex/0003020](#) [hep-ex].
- [34] ZEUS Collaboration Collaboration, S. Chekanov *et al.*, “Measurement of J/psi photoproduction at large momentum transfer at HERA”, *JHEP* **1005** (2010) 085, [arXiv:0910.1235](#) [hep-ex].
- [35] ZEUS Collaboration Collaboration, S. Chekanov *et al.*, “Exclusive electroproduction of J/psi mesons at HERA”, *Nucl.Phys.* **B695** (2004) 3–37, [arXiv:hep-ex/0404008](#) [hep-ex].
- [36] H1 Collaboration Collaboration, C. Adloff *et al.*, “Charmonium production in deep inelastic scattering at HERA”, *Eur.Phys.J.* **C10** (1999) 373–393, [arXiv:hep-ex/9903008](#) [hep-ex].
- [37] ZEUS Collaboration Collaboration, S. Chekanov *et al.*, “Exclusive photoproduction of J / psi mesons at HERA”, *Eur.Phys.J.* **C24** (2002) 345–360, [arXiv:hep-ex/0201043](#) [hep-ex].
- [38] ZEUS Collaboration Collaboration, J. Breitweg *et al.*, “Measurement of elastic J/psi photoproduction at HERA”, *Z.Phys.* **C75** (1997) 215–228, [arXiv:hep-ex/9704013](#) [hep-ex].
- [39] ZEUS Collaboration Collaboration, M. Derrick *et al.*, “Measurement of the cross-section for the reaction  $\gamma p \rightarrow J/\psi p$  with the ZEUS detector at HERA”, *Phys.Lett.* **B350** (1995) 120–134, [arXiv:hep-ex/9503015](#) [hep-ex].
- [40] H1 Collaboration Collaboration, C. Adloff *et al.*, “Diffractive photoproduction of psi(2S) mesons at HERA”, *Phys.Lett.* **B541** (2002) 251–264, [arXiv:hep-ex/0205107](#) [hep-ex].
- [41] H1 Collaboration Collaboration, C. Adloff *et al.*, “Photoproduction of psi (2S) mesons at HERA”, *Phys.Lett.* **B421** (1998) 385–394, [arXiv:hep-ex/9711012](#) [hep-ex].
- [42] ZEUS collaboration Collaboration, H. Abramowicz *et al.*, “Measurement of the t dependence in exclusive photoproduction of Upsilon(1S) mesons at HERA”, *Phys.Lett.* **B708** (2012) 14–20, [arXiv:1111.2133](#) [hep-ex].
- [43] ZEUS Collaboration Collaboration, S. Chekanov *et al.*, “Exclusive photoproduction of upsilon mesons at HERA”, *Phys.Lett.* **B680** (2009) 4–12, [arXiv:0903.4205](#) [hep-ex].
- [44] ZEUS Collaboration Collaboration, J. Breitweg *et al.*, “Measurement of elastic Upsilon photoproduction at HERA”, *Phys.Lett.* **B437** (1998) 432–444, [arXiv:hep-ex/9807020](#) [hep-ex].
- [45] M. Born and E. Wolf, *Principles of Optics: Electromagnetic Theory of Propagation, Interference and Diffraction of Light (7th Edition)*. Cambridge University Press, 7th ed., 1999.
- [46] E. Predazzi, “Diffraction: Retrospectives and perspectives”, *Nucl.Phys.Proc.Suppl.* **99A** (2001) 3–6.
- [47] A. Santoro, “New forward and diffractive physics at CMS”, *J.Phys.Conf.Ser.* **287** (2011) 012020.
- [48] *Leonardo Da Vinci: An Artabras Book*. Reynal and Company.
- [49] F. Grimaldi, *Physico-mathesis de lumine, coloribus et iride*. 1665.
- [50] A. Fresnel, “Memoire sur las diffraction de la lumiere”, *Annales de chimie et de physique* **5** (1818) .

## BIBLIOGRAPHY

- [51] C. Davisson and L. H. Germer, “The Scattering of Electrons by a Single Crystal of Nickel”, *Nature* **119** (Apr, 1927) 549 – 588.
- [52] C. Davisson and L. H. Germer, “Diffraction of Electrons by a Crystal of Nickel”, *Phys. Rev.* **30** (Dec, 1927) 705–740.
- [53] W. Elsasser, “Bemerkungen zur Quantenmechanik freier Elektronen”, *Naturwissenschaften* **13** (1925) 711–711.
- [54] L. de Broglie, “Recherches sur la théorie des quanta”. PhD thesis, 1924.
- [55] E. Feinberg and I. Pomerančuk, “High energy inelastic diffraction phenomena”, *Il Nuovo Cimento (1955-1965)* **3** (1956) 652–671.
- [56] E. Predazzi, “Diffraction: Past, present and future”, [arXiv:hep-ph/9809454](https://arxiv.org/abs/hep-ph/9809454) [hep-ph].
- [57] M. L. Good and W. D. Walker, “Diffraction Dissociation of Beam Particles”, *Phys. Rev.* **120** (Dec, 1960) 1857–1860.
- [58] Particle Data Group Collaboration, K. Nakamura *et al.*, “Review of particle physics”, *J. Phys.* **G37** (2010) 075021.
- [59] L. Landau and E. Lifschitz, *Quantenmechanik. Lehrbuch der Theoretischen Physik*. Akademie-Verlag, 1979.
- [60] G. Alberi and G. Goggi, “Diffraction of Subnuclear Waves”, *Phys.Rept.* **74** (1981) 1–207.
- [61] G. Blatter, “Quantenmechanik”, 2005.
- [62] G. B. Airy, “On the Diffraction of an Object-glass with Circular Aperture”, *Transactions of the Cambridge Philosophical Society* **Vol. 5** (1835) 283–291.
- [63] J. Forshaw, J. Forshaw, and D. Ross, *Quantum Chromodynamics and the Pomeron*. Cambridge Lecture Notes in Physics. Cambridge University Press, 1997.
- [64] S. Mandelstam, “Determination of the pion-nucleon scattering amplitude from dispersion relations and unitarity. general theory”, *Phys. Rev.* **112** (Nov, 1958) 1344–1360.
- [65] D. Perkins, *Introduction To High Energy Physics*. Cambridge University Press, 2000.
- [66] M. E. Peskin and D. V. Schroeder, *An Introduction to quantum field theory*. Westview Press, 1995.
- [67] A. R. White, “A Pseudoscalar Resonance That Could Resemble the Higgs”, [arXiv:1206.0192](https://arxiv.org/abs/1206.0192) [hep-ph].
- [68] G. F. Chew and S. C. Frautschi, “Principle of equivalence for all strongly interacting particles within the *s*-matrix framework”, *Phys. Rev. Lett.* **7** (Nov, 1961) 394–397.
- [69] G. F. Chew, “*s*-matrix theory of strong interactions without elementary particles”, *Rev. Mod. Phys.* **34** (Jul, 1962) 394–401.
- [70] J. A. Wheeler, “On the Mathematical Description of Light Nuclei by the Method of Resonating Group Structure”, *Phys. Rev.* **52** (Dec, 1937) 1107–1122.
- [71] A. White, “The Past and future of S matrix theory”, [arXiv:hep-ph/0002303](https://arxiv.org/abs/hep-ph/0002303) [hep-ph].
- [72] R. E. Cutkosky, “Singularities and Discontinuities of Feynman Amplitudes”, *Journal of Mathematical Physics* **1** no. 5, (1960) 429–433.
- [73] T. Regge, “Introduction to Complex Orbital Momenta”, *Il Nuovo Cimento (1955-1965)* **14** (1959) 951–976.
- [74] T. Regge, “Bound States, Shadow States and Mandelstam Representation”, *Il Nuovo Cimento (1955-1965)* **18** (1960) 947–956.
- [75] G. F. Chew and S. C. Frautschi, “Regge Trajectories and the Principle of Maximum Strength for Strong Interactions”, *Phys. Rev. Lett.* **8** (Jan, 1962) 41–44.
- [76] V. Gribov, “Partial waves with complex orbital angular momenta and the asymptotic

- behavior of the scattering amplitude”, *Sov.Phys.JETP* **14** (1962) 1395.
- [77] P. Desgrolard, M. Giffon, E. Martynov, and E. Predazzi, “Exchange degenerate Regge trajectories: A Fresh look from resonance and forward scattering regions”, *Eur.Phys.J. C* **18** (2001) 555–561, [arXiv:hep-ph/0006244 \[hep-ph\]](#).
- [78] A. Tang and J. W. Norbury, “Properties of regge trajectories”, *Phys. Rev. D* **62** (Jun, 2000) 016006.
- [79] A. Anselm and V. Gribov, “Zero pion mass limit in interaction at very high energies”, *Physics Letters B* **40** no. 4, (1972) 487 – 490.
- [80] E. Luna, V. Khoze, A. Martin, and M. Ryskin, “Diffractive dissociation re-visited for predictions at the LHC”, *Eur.Phys.J. C* **59** (2009) 1–12, [arXiv:0807.4115 \[hep-ph\]](#).
- [81] A. Carroll, I. Chiang, T. Kycia, K. Li, M. Marx, *et al.*, “Total Cross-Sections of  $\pi^\pm$ ,  $K^\pm$ ,  $p$  and  $\bar{p}$  on Protons and Deuterons Between 200 and 370 GeV/c”, *Phys.Lett. B* **80** (1979) 423.
- [82] A. Carroll, I.-H. Chiang, T. Kycia, K. Li, P. Mazur, *et al.*, “Total Cross-Sections of  $\pi^\pm$ ,  $K^\pm$ ,  $p$ , and  $\bar{p}$  on Protons and Deuterons Between 23-GeV/c and 280-GeV/c”, *Phys.Lett. B* **61** (1976) 303.
- [83] A. Carroll, I.-H. Chiang, T. Kycia, K. Li, P. Mazur, *et al.*, “Total Cross-Sections of  $\pi^{+-}$  and  $K^{+-}$  on Protons and Deuterons Between 50-GeV/c and 200-GeV/c”, *Phys.Rev.Lett.* **33** (1974) 932.
- [84] W. Galbraith, E. Jenkins, T. Kycia, B. Leontic, R. Phillips, *et al.*, “Total cross-sections of protons, anti-protons, and  $\pi$  and  $K$  mesons on hydrogen and deuterium in the momentum range 6-GeV/c to 22-GeV/c”, *Phys.Rev.* **138** (1965) B913–B920.
- [85] K. Foley, R. Jones, S. Lindenbaum, W. Love, S. Ozaki, *et al.*, “High-energy, small angle,  $p p$  and anti- $p p$  scattering and  $p p$  total cross-sections”, *Phys.Rev.Lett.* **19** (1967) 857–859.
- [86] K. J. Foley, R. S. Jones, S. J. Lindenbaum, W. A. Love, S. Ozaki, E. D. Platner, C. A. Quarles, and E. H. Willen, “High-Precision  $\pi^\pm - p$  Total Cross Sections from 8 to 29 BeV/c”, *Phys. Rev. Lett.* **19** (Aug, 1967) 330–332.
- [87] S. Denisov, S. Donskov, Y. Gorin, A. Petrukhin, Y. Prokoshkin, *et al.*, “Total cross-sections of  $\pi^+$ ,  $K^+$  and  $p$  on protons and deuterons in the momentum range 15-GeV/c to 60-GeV/c”, *Phys.Lett. B* **36** (1971) 415–421.
- [88] S. Denisov, Y. Dmitrevsky, S. Donskov, Y. Gorin, Y. Melnik, *et al.*, “Energy dependence of  $\pi^-$ ,  $K^-$  and anti- $p$  total cross-sections on protons in the momentum range up to 65-GeV/c”, *Phys.Lett. B* **36** (1971) 528–532.
- [89] Y. Gorin, S. Denisov, S. Donskov, A. Petrukhin, Y. Prokoshkin, *et al.*, “Differences in Total Cross-Section for Momenta Up to 65-GeV/c”, *Nucl.Phys. B* **65** (1973) 1–28.
- [90] V. Apokin, A. Vasiliev, A. Derevshchikov, Y. Matulenko, A. Meschanin, A. Mysnik, S. Nurushev, A. Saraykin, V. Siksik, E. Smirnov, L. Soloviev, and V. Solovianov, “Elastic scattering of  $\pi^-$  mesons on protons in the coulomb-nuclear interference region at 33–60 GeV/c”, *Nuclear Physics B* **106** no. 0, (1976) 413 – 429.
- [91] CERN-Pisa-Rome-Stony Brook Collaboration Collaboration, U. Amaldi *et al.*, “New Measurements of Proton Proton Total Cross-Section at the CERN Intersecting Storage Rings”, *Phys.Lett. B* **62** (1976) 460.
- [92] G. Carboni, G. Kantardjian, D. Lloyd-Owen, M. Ambrosio, G. Anzivino, *et al.*, “Measurement of the anti-proton - proton total cross-section and elastic scattering at the cern intersecting storage rings”, *Phys.Lett. B* **108** (1982) 145.
- [93] L. Okun, “The Life and legacy of Pomeranchuk”, [arXiv:physics/0307123 \[physics\]](#).
- [94] I. Pomeranchuk, “The Conservation of Isotopic Spin and the Scattering of

BIBLIOGRAPHY

- Antinucleons by Nucleons”, *Sov. Phys. JETP* **3** (1956) 306–307.
- [95] L. Okun and I. Pomeranchuk, “The conservation of Isotopic Spin and the Cross Section of the Interaction of High-Energy  $\pi$ -Mesons and Nucleons with Nucleons”, *Sov. Phys. JETP* **3** (1956) 307–308.
- [96] I. Pomeranchuk, “Equality of the nucleon and antinucleon total interaction cross section at high energies”, *Sov. Phys. JETP* **7** (1958) 499–501.
- [97] L. L. Foldy and R. F. Peierls, “Isotopic spin of exchanged systems”, *Phys. Rev.* **130** (May, 1963) 1585–1589.
- [98] T. Trueman and R. Peierls, “Restrictions Imposed by the Optical Theorem on Exchanged Quantum Numbers”, *Phys.Rev.* **143** (1964) B1365–B1367.
- [99] A. Bouquet, B. Diu, E. Leader, and B. Nicolescu, “Problems in the Phenomenological Analysis of Cross-Section Differences: Sigma p p-Sigma p n and Sigma anti-p p-Sigma anti-p n”, *Nuovo Cim.* **A31** (1976) 411.
- [100] D. Joynson, E. Leader, B. Nicolescu, and C. Lopez, “NonRegge and HyperRegge Effects in Pion-Nucleon Charge Exchange Scattering at High-Energies”, *Nuovo Cim.* **A30** (1975) 345.
- [101] F. Low, “A Model of the Bare Pomeron”, *Phys.Rev.* **D12** (1975) 163–173.
- [102] S. Nussinov, “Colored Quark Version of Some Hadronic Puzzles”, *Phys.Rev.Lett.* **34** (1975) 1286–1289.
- [103] S. Nussinov, “A Perturbative Recipe for Quark Gluon Theories and Some of Its Applications”, *Phys.Rev.* **D14** (1976) 246.
- [104] O. Nachtmann, “Pomeron physics and QCD”, [arXiv:hep-ph/0312279](https://arxiv.org/abs/hep-ph/0312279) [hep-ph].
- [105] E. Kuraev, L. Lipatov, and V. S. Fadin, “Multi - Reggeon Processes in the Yang-Mills Theory”, *Sov.Phys.JETP* **44** (1976) 443–450.
- [106] E. Kuraev, L. Lipatov, and V. S. Fadin, “The Pomeranchuk Singularity in Nonabelian Gauge Theories”, *Sov.Phys.JETP* **45** (1977) 199–204.
- [107] L. Lipatov, “Reggeization of the Vector Meson and the Vacuum Singularity in Nonabelian Gauge Theories”, *Sov.J.Nucl.Phys.* **23** (1976) 338–345.
- [108] I. Balitsky and L. Lipatov, “The Pomeranchuk Singularity in Quantum Chromodynamics”, *Sov.J.Nucl.Phys.* **28** (1978) 822–829.
- [109] R. C. Brower, J. Polchinski, M. J. Strassler, and C.-I. Tan, “The Pomeron and gauge/string duality”, *JHEP* **0712** (2007) 005, [arXiv:hep-th/0603115](https://arxiv.org/abs/hep-th/0603115) [hep-th].
- [110] A. Donnachie and P. Landshoff, “Total cross-sections”, *Phys.Lett.* **B296** (1992) 227–232, [arXiv:hep-ph/9209205](https://arxiv.org/abs/hep-ph/9209205) [hep-ph].
- [111] G. Antchev, P. Aspell, I. Atanassov, V. Avati, J. Baechler, *et al.*, “First measurement of the total proton-proton cross section at the LHC energy of  $\sqrt{s} = 7$  TeV”, *Europhys.Lett.* **96** (2011) 21002, [arXiv:1110.1395](https://arxiv.org/abs/1110.1395) [hep-ex].
- [112] M. Froissart, “Asymptotic behavior and subtractions in the Mandelstam representation”, *Phys.Rev.* **123** (1961) 1053–1057.
- [113] A. Martin, “Unitarity and high-energy behavior of scattering amplitudes”, *Phys.Rev.* **129** (1963) 1432–1436.
- [114] H. Abramowicz, E. Levin, A. Levy, and U. Maor, “A Parametrization of  $\sigma_T(\gamma^*p)$  above the resonance region  $Q^2 \geq 0$ ”, *Phys.Lett.* **B269** (1991) 465–476.
- [115] H1 Collaboration Collaboration, T. Ahmed *et al.*, “Total photoproduction cross-section measurement at HERA energies”, *Phys.Lett.* **B299** (1993) 374–384.
- [116] Y. Akimov, R. Cool, L. Golovanov, K. Goulianos, D. Gross, A. Melissinos, E. Malamud, S. Mukhin, D. Nitz, S. Olsen, H. Sticker, G. Takhtamyshev, V. Tsarev, R. Yamada, and P. Zimmerman, “Diffraction dissociation of high-energy protons in  $p - d$  interactions”, *Phys. Rev. Lett.* **35** (Sep, 1975) 766–770.

- [117] M. M. Block, “Hadronic forward scattering: Predictions for the Large Hadron Collider and cosmic rays”, *Phys.Rept.* **436** (2006) 71–215, [arXiv:hep-ph/0606215 \[hep-ph\]](#).
- [118] E. Feinberg and I. Pomeranchuk *Dokl. Akad. Nauk SSR* **93** (1953) 439.
- [119] V. A. Khoze, A. D. Martin, and M. Ryskin, “Soft diffraction and the elastic slope at Tevatron and LHC energies: A MultiPomeron approach”, *Eur.Phys.J.* **C18** (2000) 167–179, [arXiv:hep-ph/0007359 \[hep-ph\]](#).
- [120] N. P. Zotov and V. A. Tsarev, “Diffraction dissociation: 35 years on”, *Soviet Physics Uspekhi* **31** no. 2, (1988) 119.
- [121] K. A. Goulianos and J. Montanha, “Factorization and scaling in hadronic diffraction”, *Phys.Rev.* **D59** (1999) 114017, [arXiv:hep-ph/9805496 \[hep-ph\]](#).
- [122] M. Ryskin, A. Martin, and V. Khoze, “High-energy strong interactions: from ‘hard’ to ‘soft’”, *Eur.Phys.J.* **C71** (2011) 1617, [arXiv:1102.2844 \[hep-ph\]](#).
- [123] E. Luna, V. A. Khoze, A. Martin, and M. Ryskin, “Weak coupling of pomerons and the triple-Regge analysis”,.
- [124] E. Luna, V. Khoze, A. Martin, and M. Ryskin, “The possibility that the triple-Pomeron coupling vanishes at  $q_t = 0$ ”, *Eur.Phys.J.* **C69** (2010) 95–101, [arXiv:1005.4864 \[hep-ph\]](#).
- [125] V. Gribov and A. A. Migdal, “Properties of the pomeranchuk pole and the branch cuts related to it at low momentum transfer”, *Sov.J.Nucl.Phys.* **8** (1969) 583–590.
- [126] V. Khoze, A. Martin, and M. Ryskin, “The Extraction of the bare triple-Pomeron vertex: A Crucial ingredient for diffraction”, *Phys.Lett.* **B643** (2006) 93–97, [arXiv:hep-ph/0609312 \[hep-ph\]](#).
- [127] V. Gribov and A. A. Migdal, “Strong coupling in the pomeranchuk pole problem”, *Sov.Phys.JETP* **28** (1969) 784–795.
- [128] R. Cool, K. A. Goulianos, S. Segler, H. Sticker, and S. N. White, “DIFFRACTION DISSOCIATION OF  $\pi^{+-}$ ,  $K^{+-}$ , AND  $\rho^{+-}$  AT 100-GEV/C AND 200-GEV/C”, *Phys.Rev.Lett.* **47** (1981) 701–704.
- [129] CDF Collaboration, F. Abe *et al.*, “Measurement of  $\bar{p}p$  single diffraction dissociation at  $\sqrt{s} = 546$  GeV and 1800 GeV”, *Phys.Rev.* **D50** (1994) 5535–5549.
- [130] E. Gotsman, E. Levin, and U. Maor, “N=4 SYM and QCD motivated approach to soft interactions at high energies”, *Eur.Phys.J.* **C71** (2011) 1553, [arXiv:1010.5323 \[hep-ph\]](#).
- [131] E. Gotsman, A. Kormilitzin, E. Levin, and U. Maor, “Survival probability for high mass diffraction”, *Eur.Phys.J.* **C52** (2007) 295–304, [arXiv:hep-ph/0702053 \[hep-ph\]](#).
- [132] V. Gribov and L. Lipatov, “Deep inelastic e p scattering in perturbation theory”, *Sov.J.Nucl.Phys.* **15** (1972) 438–450.
- [133] V. Gribov and L. Lipatov, “e+ e- pair annihilation and deep inelastic e p scattering in perturbation theory”, *Sov.J.Nucl.Phys.* **15** (1972) 675–684.
- [134] G. Altarelli and G. Parisi, “Asymptotic Freedom in Parton Language”, *Nucl.Phys.* **B126** (1977) 298.
- [135] Y. L. Dokshitzer, “Calculation of the Structure Functions for Deep Inelastic Scattering and e+ e- Annihilation by Perturbation Theory in Quantum Chromodynamics.”, *Sov.Phys.JETP* **46** (1977) 641–653.
- [136] C. F. v. Weizsäcker, “Ausstrahlung bei Stößen sehr schneller Elektronen”, *Zeitschrift für Physik A Hadrons and Nuclei* **88** (1934) 612–625.
- [137] E. Williams, “Nature of the high-energy particles of penetrating radiation and status of ionization and radiation formulae”, *Phys.Rev.* **45** (1934) 729–730.
- [138] V. Budnev, I. Ginzburg, G. Meledin, and V. Serbo, “The Two photon particle

## BIBLIOGRAPHY

- production mechanism. Physical problems. Applications. Equivalent photon approximation”, *Phys.Rept.* **15** (1975) 181–281.
- [139] E. Fermi, “On the theory of collisions between atoms and electrically charged particles”, *Nuovo Cim.* (1925) 2,143, [arXiv:hep-th/0205086 \[hep-th\]](#). Translated from Italian by Michele Gallinaro and Sebastian White, New York, 2001.
- [140] E. Fermi, “Über die Theorie des Stoßes zwischen Atomen und elektrisch geladenen Teilchen”, *Zeitschrift für Physik A Hadrons and Nuclei* **29** (1924) 315–327.
- [141] F. Huber, “Elastic  $J/\psi$  production at low  $Q^2$  at HERA”, Diploma thesis, ETH, Zurich, 2009. [DESY: thesis10-018](#).
- [142] N. E. Berger, “Measurement of diffractive Phi meson photoproduction at HERA with the H1 fast track trigger”. PhD thesis, ETH, Zurich, 2006. <http://e-collection.library.ethz.ch/eserv/eth:29706/eth-29706-02.pdf>.
- [143] R. M. Weber, “Diffractive  $\rho^0$  photoproduction at HERA”. PhD thesis, ETH, Zurich, 2006. <http://inspirehep.net/record/738834/files/eth-29050-02.pdf>.
- [144] A. Rostovtsev and V. Soloshenko, “Corrections to the Weizsaecker- Williams Approximation of Photon Flux in ep Collisions”, H1-IN-309(08/1993), 1993.
- [145] T. Teubner, “Theory of elastic vector meson production”, [arXiv:hep-ph/9910329 \[hep-ph\]](#).
- [146] L. Stodolsky, “Hadron-like behavior of gamma, neutrino nuclear cross-sections”, *Phys.Rev.Lett.* **18** (1967) 135–137.
- [147] P. Freund, “The Decays  $\rho^0 \rightarrow \mu^- \mu^+$ ,  $\pi^- \rightarrow \mu^- \bar{\nu}_\mu$  and the Photoproduction of Vector Mesons”, *Il Nuovo Cimento A (1965-1970)* **44** (1966) 411–417.
- [148] H. Joos, “Schladming Lectures 1967”, *Acta Physica Austriaca, Supp.* **4** (1967) .
- [149] J. Sakurai, “Talk at the Summer Institute for Theoretical Physics, University of Colorado, Boulder, Colorado”, *Lectures in Theoretical Physics (Gordon and Breach)* **XI** (1968) .
- [150] D. Schildknecht *DESY Report 69/10* (1969) .
- [151] J. Sakurai, “Vector meson dominance and high-energy electron proton inelastic scattering”, *Phys.Rev.Lett.* **22** (1969) 981–984.
- [152] H. Fraas and D. Schildknecht, “Vector-meson dominance and diffractive electroproduction of vector mesons”, *Nucl.Phys.* **B14** (1969) 543–565.
- [153] J. Sakurai and D. Schildknecht, “Generalized vector dominance and inelastic electron - proton scattering”, *Phys.Lett.* **B40** (1972) 121–126.
- [154] J. J. Aubert *et al.*, “Experimental Observation of a Heavy Particle  $J$ ”, *Phys. Rev. Lett.* **33** (Dec, 1974) 1404–1406.
- [155] J. E. Augustin *et al.*, “Discovery of a Narrow Resonance in  $e^+e^-$  Annihilation”, *Phys. Rev. Lett.* **33** (Dec, 1974) 1406–1408.
- [156] J. Sakurai and D. Schildknecht, “Generalized vector dominance and inelastic electron-nucleon scattering. the neutron-to-proton ratios”, *Phys.Lett.* **B41** (1972) 489–494.
- [157] J. Sakurai and D. Schildknecht, “Generalized vector dominance and inelastic electron nucleon scattering – the small  $\omega'$  region”, *Phys.Lett.* **B42** (1972) 216.
- [158] B. Foster, “Low x physics”, *Phil.Trans.Roy.Soc.Lond.* **A359** (2001) 325–378, [arXiv:hep-ex/0008069 \[hep-ex\]](#).
- [159] E. Iancu, K. Itakura, and S. Munier, “Saturation and BFKL dynamics in the HERA data at small x”, *Phys.Lett.* **B590** (2004) 199–208, [arXiv:hep-ph/0310338 \[hep-ph\]](#).
- [160] H. Kowalski, L. Motyka, and G. Watt, “Exclusive diffractive processes at HERA within the dipole picture”, *Phys.Rev.* **D74** (2006) 074016, [arXiv:hep-ph/0606272](#)

- [161] G. Watt and H. Kowalski, “Impact parameter dependent colour glass condensate dipole model”, *Phys.Rev.* **D78** (2008) 014016, [arXiv:0712.2670 \[hep-ph\]](#).
- [162] J. Berger and A. M. Stasto, “Exclusive vector meson production and small-x evolution”, [arXiv:1205.2037 \[hep-ph\]](#).
- [163] K. J. Golec-Biernat and M. Wusthoff, “Saturation effects in deep inelastic scattering at low  $Q^{*2}$  and its implications on diffraction”, *Phys.Rev.* **D59** (1998) 014017, [arXiv:hep-ph/9807513 \[hep-ph\]](#).
- [164] K. J. Golec-Biernat and M. Wusthoff, “Saturation in diffractive deep inelastic scattering”, *Phys.Rev.* **D60** (1999) 114023, [arXiv:hep-ph/9903358 \[hep-ph\]](#).
- [165] I. Balitsky, “Operator expansion for high-energy scattering”, *Nucl.Phys.* **B463** (1996) 99–160, [arXiv:hep-ph/9509348 \[hep-ph\]](#).
- [166] Y. V. Kovchegov, “Small  $x$   $F(2)$  structure function of a nucleus including multiple pomeron exchanges”, *Phys.Rev.* **D60** (1999) 034008, [arXiv:hep-ph/9901281 \[hep-ph\]](#).
- [167] Y. V. Kovchegov, “Unitarization of the BFKL pomeron on a nucleus”, *Phys.Rev.* **D61** (2000) 074018, [arXiv:hep-ph/9905214 \[hep-ph\]](#).
- [168] N. Kivel, “Elastic electron-proton scattering: current status and perspectives”, in *Proceedings of the International Baikal Summer School on Physics of Elementary Particles and Astrophysics*, pp. 131–145. 2009.
- [169] R. Hofstadter and R. W. McAllister, “Electron scattering from the proton”, *Phys. Rev.* **98** (Apr, 1955) 217–218.
- [170] R. Hofstadter, “Electron scattering and nuclear structure”, *Rev. Mod. Phys.* **28** (Jul, 1956) 214–254.
- [171] “HERA - A Proposal for a Large Electron Proton Colliding Beam Facility at DESY”,.
- [172] G. Voss and B. Wiik, “The Electron proton collider HERA”, *Ann.Rev.Nucl.Part.Sci.* **44** no. 1, (1994) 413–452.
- [173] “H1 web page”. <http://h1.desy.de>.
- [174] J. Christenson, J. Cronin, V. Fitch, and R. Turlay, “Evidence for the  $2\pi$  Decay of the  $k(2)0$  Meson”, *Phys.Rev.Lett.* **13** (1964) 138–140.
- [175] H1 Collaboration Collaboration, I. Abt *et al.*, “The H1 detector at HERA”, *Nucl.Instrum.Meth.* **A386** (1997) 310–347.
- [176] H1 Collaboration Collaboration, I. Abt *et al.*, “The Tracking, calorimeter and muon detectors of the H1 experiment at HERA”, *Nucl.Instrum.Meth.* **A386** (1997) 348–396.
- [177] M. Minty, “Summary of recent high luminosity experiments after the HERA-II luminosity upgrade and future prospects”,.
- [178] D. Pitzl, O. Behnke, M. Biddulph, K. Bosiger, R. Eichler, *et al.*, “The H1 silicon vertex detector”, *Nucl.Instrum.Meth.* **A454** (2000) 334–349, [arXiv:hep-ex/0002044 \[hep-ex\]](#).
- [179] B. List, “The H1 central silicon tracker”, *Nucl.Instrum.Meth.* **A501** (2001) 49–53.
- [180] B. List, “The H1 silicon tracker”, *Nucl.Instrum.Meth.* **A549** (2005) 33–36.
- [181] H1 Collaboration Collaboration, B. List, “The silicon tracker of the H1 detector”, *Nucl.Instrum.Meth.* **A566** (2006) 110–113.
- [182] A. W. Jung, “Measurement of the  $D^{*+}$  meson cross section and extraction of the charm contribution,  $F_c(2)(x, Q^{*2})$  to the proton structure in deep inelastic ep scattering with the H1 detector at HERA”. PhD thesis, Heidelberg U., 2009. [DESY: thesis09-001](#).
- [183] M. Nozicka, “The forward and backward silicon trackers of H1”, *Nucl.Instrum.Meth.* **A501** (2003) 54–59.

## BIBLIOGRAPHY

- [184] H. Henschel and R. Lahmann, “The backward silicon tracker of the H1 experiment at HERA”, *Nucl.Instrum.Meth.* **A453** (2000) 93–97.
- [185] V. Blobel *et al.*, *Central Tracker software documentation*, 1992. H1 Software Note, Number 30.
- [186] D. Pitzl, “Tracking group report: DST7”. H1 plenary talk, 10/06/2009.
- [187] V. Blobel, “A new fast track-fit algorithm based on broken lines”, in *The Proceedings of PHYSTAT 2005: Statistical Problems in Particle Physics, Astrophysics and Cosmology*, pp. 68–71. 2005.
- [188] V. Blobel, “A new fast track-fit algorithm based on broken lines”, *Nucl.Instrum.Meth.* **A566** (2006) 14–17.
- [189] H1 Calorimeter Group Collaboration, B. Andrieu *et al.*, “The H1 liquid argon calorimeter system”, *Nucl.Instrum.Meth.* **A336** (1993) 460–498.
- [190] Luranyl: BASF, Ludwigshafen, Germany.
- [191] B. Krames, “Untersuchungen zum Streamer-Mechanismus und zur Optimierung der Betriebseigenschaften der H1 Muonkammern”, Diploma thesis, Aachen U., 1992. <http://www-h1.desy.de/psfiles/theses/h1th-562.pdf>.
- [192] K. Kruger, “Photoproduction of  $J/\psi$  mesons at medium and low elasticities at HERA”. PhD thesis, Hamburg U., 2001. [DESY: thesis-01-025](#).
- [193] R. Joint Institute for Nuclear Research, Dubna, “upgrade of the h1 hadron plug calorimeter”.
- [194] W. Bartel, E. Gianfelice, J. Maidment, B. Parker, N. Holtkamp, *et al.*, “HERA luminosity upgrade”.
- [195] Joint Institute for Nuclear Research, Dubna, Russia, “Upgrade of the h1 hadron plug calorimeter”. Jun, 1998.
- [196] e. Doyle, A.T., e. Grindhammer, Guenter, e. Ingelman, G., and e. Jung, H., “Monte Carlo generators for HERA physics. Proceedings, Workshop, Hamburg, Germany, 1998-1999”.
- [197] R. Brun, F. Carminati, and S. Giani, *GEANT Detector Description and Simulation Tool*, 1994.
- [198] B. List, “Diffraktive  $J/\psi$ -Produktion in Elektron-Proton-Stößen am Speicherring HERA”, Diploma thesis, Techn. Univ. Berlin, 1993.
- [199] B. List and A. Mastroberardino, “DIFFVM: A Monte Carlo Generator for Diffractive Processes in  $ep$  Scattering”, *Conf.Proc.* **C980427** (1998) 396–404.
- [200] P. J. Mohr, B. N. Taylor, and D. B. Newell, “CODATA Recommended Values of the Fundamental Physical Constants: 2010”, [arXiv:1203.5425 \[physics.atom-ph\]](#).
- [201] A. Donnachie and P. Landshoff, “Elastic Scattering and Diffraction Dissociation”, *Nucl.Phys.* **B244** (1984) 322.
- [202] T. Sjostrand, “PYTHIA 5.7 and JETSET 7.4: Physics and manual”, [arXiv:hep-ph/9508391 \[hep-ph\]](#).
- [203] T. Sjostrand, “High-energy physics event generation with PYTHIA 5.7 and JETSET 7.4”, *Comput.Phys.Commun.* **82** (1994) 74–90.
- [204] E. Barberio and Z. Was, “PHOTOS: A Universal Monte Carlo for QED radiative corrections. Version 2.0”, *Comput.Phys.Commun.* **79** (1994) 291–308.
- [205] E. Barberio, B. van Eijk, and Z. Was, “PHOTOS: A Universal Monte Carlo for QED radiative corrections in decays”, *Comput.Phys.Commun.* **66** (1991) 115–128.
- [206] Z. Was, P. Golonka, and G. Nanava, “PHOTOS Monte Carlo for precision simulation of QED in decays: History and properties of the project”, *PoS ACAT* (2007) 071, [arXiv:0707.3044 \[hep-ph\]](#).
- [207] Fermilab E760 Collaboration Collaboration, T. Armstrong *et al.*, “Observation of the

- radiative decay  $J/\psi \rightarrow e^+e^-\gamma$ , *Phys.Rev.* **D54** (1996) 7067–7070.
- [208] CLEO Collaboration Collaboration, Z. Li *et al.*, “Measurement of the branching fractions for  $J/\psi \rightarrow l^+l^-$ ”, *Phys.Rev.* **D71** (2005) 111103, [arXiv:hep-ex/0503027 \[hep-ex\]](#).
- [209] B. Heltsley via K. Krüger, 2011. Private communication.
- [210] P. Fleischmann, “Elastic  $J/\psi$  production at HERA”. PhD thesis, Hamburg U., 2004. [DESY: thesis04-013](#). Ph.D. Thesis (Advisor: B. Naroska).
- [211] T. Abe, “GRAPE dilepton (Version1.1): A Generator for dilepton production in e p collisions”, *Comput.Phys.Commun.* **136** (2001) 126–147, [arXiv:hep-ph/0012029 \[hep-ph\]](#).
- [212] T. Abe *et al.*, “GRAPE-Dilepton (Version 1.0), A Generator for Dilepton Production in ep collisions”, in *Workshop on “Monte Carlo Generators for HERA Physics”*. 1999. [http://research.kek.jp/people/tabe/SR/Phys/Workshop/HERAMC99/proceedings\\_final\\_submit1999.06.02.pdf](http://research.kek.jp/people/tabe/SR/Phys/Workshop/HERAMC99/proceedings_final_submit1999.06.02.pdf).
- [213] T. Abe, “GRAPE-Dilepton (Version 1.1): Comments on the updates”, 2002. [http://research.kek.jp/people/tabe/grape/comments\\_updates.txt](http://research.kek.jp/people/tabe/grape/comments_updates.txt).
- [214] *GRACE manual, Automatic Generation of Tree Amplitudes in Standard Models, Version 1.0*, 1993. <http://www-sc.kek.jp/grace/green.pdf>. KEK Report 92-19.
- [215] F. Yuasa, J. Fujimoto, T. Ishikawa, M. Jimbo, T. Kaneko, K. Kato, S. Kawabata, T. Kon, Y. Kurihara, M. Kuroda, N. Nakazawa, Y. Shimizu, and H. Tanaka, “Automatic computation of cross sections in hep”, *Progress of Theoretical Physics Supplement* **138** (2000) 18–23, [arXiv:hep-ph/0007053v1 \[hep-ph\]](#).
- [216] MINAMI-TATEYA Collaboration, *GRACE User’s manual, version 2.0*, 1994. <http://www-sc.kek.jp/grace/gracedoc.pdf>.
- [217] F. Brasse, W. Flauger, J. Gayler, S. Goel, R. Haidan, *et al.*, “Parametrization of the  $q^2$  Dependence of  $\gamma_{VP}$  Total Cross-Sections in the Resonance Region”, *Nucl.Phys.* **B110** (1976) 413.
- [218] H. Abramowicz and A. Levy, “The ALLM parameterization of  $\sigma_{tot}(\gamma^*p)$ : An Update”, [arXiv:hep-ph/9712415 \[hep-ph\]](#).
- [219] B. Leissner, “Muon pair production in electron proton collisions”. PhD thesis, 2002. [DESY: thesis02-049](#).
- [220] H. Jung *et al.*, “The CCFM Monte Carlo generator CASCADE 2.2.0”, *Eur. Phys. J.* **C70** (2010) 1237–1249, [arXiv:1008.0152 \[hep-ph\]](#).
- [221] H1 Collaboration, F. Aaron *et al.*, “Measurement of Beauty Photoproduction near Threshold using Di-electron Events with the H1 Detector at HERA”, [arXiv:1206.4346 \[hep-ex\]](#).
- [222] M. Urban, U. Straumann, S. Schmitt, and J. Becker, “The cip2k first level trigger system at the h1 experiment at herA”, in *Nuclear Science Symposium Conference Record, 2002 IEEE*, vol. 1, pp. 146 – 150 vol.1. Nov., 2002.
- [223] J. Dorenbosch, “Trigger in UA2 and in UA1”, *eConf* **C851111** (1985) 134–151.
- [224] P. Le Dû, “Trigger/Data Acquisition Issues”,. [http://www-zeuthen.desy.de/ILC/lcws07/pdf/DAQ/ledu\\_patrick.pdf](http://www-zeuthen.desy.de/ILC/lcws07/pdf/DAQ/ledu_patrick.pdf).
- [225] F. Sefkow, E. Elsen, H. Krehbiel, U. Straumann, and J. Coughlan, “Experience with the first level trigger of H1”, *IEEE Trans.Nucl.Sci.* **42** (1995) 900–904.
- [226] H. Schultz-Coulon, E. Elsen, T. Nicholls, J. Coughlan, and H. Rick, “A general scheme for optimization of trigger rates in an experiment with limited bandwidth”, *IEEE Trans.Nucl.Sci.* **46** (1999) 915–919.
- [227] T. Nicholls, M. Charlet, E. Elsen, D. Hoffmann, H. Krehbiel, *et al.*, “Concept, design and performance of the second level trigger of the H1 detector”, *IEEE Trans.Nucl.Sci.*

## BIBLIOGRAPHY

- 45 (1998) 810–816.
- [228] A. Gruber *et al.*, “A Neural Network Architecture for the Second Level Trigger in the H1-Experiment at the Electron Proton Collider HERA”, in *Proceedings IEEE conference, TAI 94, New Orleans*. 1994.
  - [229] J. Mock, J. Fent, W. Frochtenicht, F. Gaede, A. Gruber, *et al.*, “Artificial neural networks as a second-level trigger at the H1 experiment: Performance analysis and results”,.
  - [230] J. Kohne, J. Fent, W. Frochtenicht, F. Gaede, A. Gruber, *et al.*, “Realization of a second level neural network trigger for the H1 experiment at HERA”, *Nucl.Instrum.Meth.* **A389** (1997) 128–133.
  - [231] J. Bizot, G. Nowak, and J. Turnau, “Hardware Study for a topological level 2 trigger”, H1-IN-240(09/1992), 1992.
  - [232] L. Goerlich *et al.*, “Strategy Studies for the H1 Topological L2-Trigger (L2TT)”, H1-IN-508(01/1997), 1997.
  - [233] J. Naumann, “Entwicklung und Test der dritten H1-Triggerstufe”. PhD thesis, Dortmund U., 2002. <https://www-h1.desy.de/psfiles/theses/h1th-305.pdf>.
  - [234] M. D. Sauter, “Measurement of beauty photoproduction at threshold using di-electron events with the H1 detector at HERA”. PhD thesis, ETH, Zurich, 2009. [DESY: thesis09-047](#).
  - [235] A. J. Campbell, “A RISC multiprocessor event trigger for the data acquisition system of the H1 experiment at HERA”, *IEEE Trans.Nucl.Sci.* **39** (1992) 255–258.
  - [236] M. Minty, “HERA Performance Upgrade: Achievements and Plans for the Future”,.
  - [237] D. Mueller and F. Sefkow, “Improving the z-Vertex Trigger”, H1-IN-539(04/1998), 1998.
  - [238] M. Cuje *et al.*, “H1 High Luminosity Upgrade 2000 CIP and Level 1 vertex Trigger”, H1-IN-535(01/1998), 1998.
  - [239] M. Urban, J. Becker, S. Schmitt, and U. Straumann, “The CIP2k first-level trigger system at the H1 experiment at HERA”, *IEEE Trans.Nucl.Sci.* **50** (2003) 903–908.
  - [240] M. C. Urban, “The new CIP2k z-vertex trigger for the H1 experiment at HERA”. PhD thesis, Zurich U., 2004. [DESY: thesis-04-044](#).
  - [241] B. Olivier, A. Dubak-Behrendt, C. Kiesling, B. Reisert, A. Aktas, *et al.*, “A novel calorimeter trigger concept: The jet trigger of the H1 experiment at HERA”, *Nucl.Instrum.Meth.* **A641** (2011) 58–71.
  - [242] C. Kiesling, A. Dubak, and B. Olivier, “The liquid argon jet trigger of the H1 experiment at HERA”, *Nucl.Instrum.Meth.* **A623** (2010) 513–515.
  - [243] B. Olivier, “The Liquid Argon Jet Trigger of the H1 Experiment at HERA”, *eConf C080625* (2008) 0042, [arXiv:0811.0087 \[physics.ins-det\]](#).
  - [244] A. Dubak, “Jet trigger in the H1 experiment at HERA”, *AIP Conf.Proc.* **899** (2007) 573.
  - [245] A. Baird, E. Elsen, Y. Fleming, M. Kolander, S. Kolya, *et al.*, “A Fast high resolution track trigger for the H1 experiment”, *IEEE Trans.Nucl.Sci.* **48** (2001) 1276–1285, [arXiv:hep-ex/0104010 \[hep-ex\]](#).
  - [246] D. Meer, D. Muller, J. Muller, A. Schoning, and C. Wissing, “A Multifunctional processing board for the fast track trigger of the H1 experiment”, *IEEE Trans.Nucl.Sci.* **49** (2002) 357–361, [arXiv:hep-ex/0107010 \[hep-ex\]](#).
  - [247] H1 Collaboration Collaboration, A. Schoning, “A fast track trigger for the H1 collaboration”, *Nucl.Instrum.Meth.* **A518** (2004) 542–543.
  - [248] H1 Collaboration Collaboration, A. Baird *et al.*, “A fast track trigger for the H1 Collaboration”, *Nucl.Instrum.Meth.* **A461** (2001) 461–464.

- [249] Y. H. Fleming, “The H1 first level fast track trigger”. PhD thesis, Birmingham U., 2003. [DESY: thesis-03-045](#).
- [250] C. Wissing, “Development of a simulation program and implementation of fast track fit algorithms for the new H1 drift chamber trigger”. PhD thesis, Dortmund U., 2003. [DESY: thesis-03-003](#).
- [251] H1 Collaboration Collaboration, A. Schoning, “The Fast Track Trigger at the H1 experiment design concepts and algorithms”, *Nucl.Instrum.Meth.* **A566** (2006) 130–132.
- [252] F. Aaron *et al.*, “Measurement of the Inclusive  $e\pm p$  Scattering Cross Section at High Inelasticity  $y$  and of the Structure Function  $F_L$ ”, *Eur.Phys.J.* **C71** (2011) 1579, [arXiv:1012.4355 \[hep-ex\]](#).
- [253] B. Foster, “Lectures on HERA physics”, [arXiv:hep-ex/0206011 \[hep-ex\]](#).
- [254] H. Collaboration, “Measurement of the Diffractive Longitudinal Structure Function  $F_L^D$  at HERA”, [arXiv:1107.3420 \[hep-ex\]](#).
- [255] U. Bassler and G. Bernardi, “On the kinematic reconstruction of deep inelastic scattering at HERA: The Sigma method”, *Nucl.Instrum.Meth.* **A361** (1995) 197–208, [arXiv:hep-ex/9412004 \[hep-ex\]](#).
- [256] J. Katzy, “H1OO - an analysis framework for H1”, in *Computing in High Energy Physics and Nuclear Physics 2004*, pp. 265–267, CERN. CERN, 2005. [CERN Document Server:865583](#).
- [257] Y. Kot and F. Willeke, “On increasing the HERA luminosity”, *Conf.Proc.* **C060626** (2006) 667–669.
- [258] H. Abramowicz, A. Levy, G. Barbagli, and M. Kasprzak, “Proton diffractive dissociation at HERA: Studying the proton dissociation using forward taggers or calorimeters”, *Future physics at HERA* **Vol 2** (1995) 734–742.
- [259] E. Hennekemper, “Simulation and calibration of the specific energy loss of the central jet chambers of the H1 detector and measurement of the inclusive  $D^{*\pm}$  meson cross section in photoproduction at HERA”. PhD thesis, Heidelberg U., 2011. <http://inspirehep.net/record/946709/files/desy-thesis-11-042.pdf>.
- [260] C. Kleinwort, “Energy loss measurement with the H1 Central Jet Chamber”, H1-IN-630(08/2008), 2008.
- [261] M. Steder, “Private communication”, 2011.
- [262] H1 Collaboration, F. Aaron *et al.*, “Inelastic Production of J/psi Mesons in Photoproduction and Deep Inelastic Scattering at HERA”, *Eur.Phys.J.* **C68** (2010) 401–420, [arXiv:1002.0234 \[hep-ex\]](#).
- [263] G. Schmid, “Nachweis von Myonen im H1-Kalorimeter”. PhD thesis, Hamburg U., 1994.
- [264] B. Naroska, S. Schiek, and G. Schmidt, “Lepton Identification in the H1 Detector at Low Momenta”, H1-IN-518(05/1997), 1997.
- [265] M. Goettlich, “Study of charm and beauty production at HERA / H1 using dilepton events”. PhD thesis, Hamburg U., 2007. [DESY: thesis07-012](#).
- [266] M. Steder, “Measurement of inelastic charmonium production at HERA”. PhD thesis, Hamburg U., 2008. [DESY: thesis08-023](#).
- [267] K. Urban, “Measurement of inclusive and DiJet  $D^*$  meson photoproduction at the H1-experiment at HERA”. PhD thesis, Heidelberg U., 2009. [DESY: thesis09-010](#).
- [268] M. Kramer, “Measurement of charm and beauty cross sections in photoproduction using events with muons and dijets at HERA”. PhD thesis, Hamburg, U., 2009. [DESY: thesis09-030](#).
- [269] D. Sunar, “Measurement of  $K^{*+}-(892)$  production in deep inelastic ep scattering with

## BIBLIOGRAPHY

- the H1 detector at HERA”. PhD thesis, Antwerp U., 2009. [DESY: thesis09-023](#).
- [270] Z. Staykova, “Measurement of D\* meson with two jets in photoproduction with the H1 detector at HERA”,.
- [271] L. D. Brown, T. T. Cai, and A. Dasgupta, “Interval estimation for a binomial proportion”, *Statistical Science* **16** (2001) 101–133.
- [272] R. Brun and F. Rademakers, “ROOT: An object oriented data analysis framework”, *Nucl.Instrum.Meth.* **A389** (1997) 81–86. See also <http://root.cern.ch>.
- [273] G. Cowan, “A survey of unfolding methods for particle physics”, *Conf.Proc.* **C0203181** (2002) 248–257.
- [274] F. James and M. Roos, “Minuit: A System for Function Minimization and Analysis of the Parameter Errors and Correlations”, *Comput.Phys.Commun.* **10** (1975) 343–367.
- [275] A. Donnachie and P. Landshoff, “Exclusive vector meson production at HERA”, *Phys.Lett.* **B348** (1995) 213–218, [arXiv:hep-ph/9411368 \[hep-ph\]](#).
- [276] D. Schmidt, “Diffraaktive Photoproduktion von Charmonium im H1-Detektor bei HERA”. PhD thesis, Hamburg U., 2001.
- [277] D. L. Phillips, “A technique for the numerical solution of certain integral equations of the first kind”, *J. ACM* **9** no. 1, (Jan., 1962) 84–97.
- [278] J. N. Franklin, “On Tikhonov’s method for ill-posed problems”, *Math. Comp.* **28** (1974) 889–907.
- [279] S. Schmitt, “Correction of detector effects: bin-by-bin and unfolding”, H1-IN-633(03/2011), 2011.
- [280] V. Blobel, “An Unfolding method for high-energy physics experiments”, in *Advanced Statistical Techniques in Particle Physics*. Durham, 2002.
- [281] V. Blobel, “Unfolding, Linear Inverse Problems”, in *Terascale workshop at DESY*. Hamburg, 2010.
- [282] G. Cowan, *Statistical Data Analysis*. Oxford University Press Inc., 2004.
- [283] V. Blobel, “Data Unfolding”, in *Terascale Statistics Tools School – Spring 2010*. Hamburg, 2010.
- [284] V. Blobel, “Advanced unfolding techniques”, in *Terascale Statistics Tools School*. Hamburg, 2008.
- [285] V. Blobel, “Unfolding for HEP experiments”, in *DESY Computing Seminar*. Hamburg, 2008.
- [286] R. Barlow, *A Guide to the Use of Statistical Methods in the Physical Sciences*. John Wiley & Sons Ltd., 1991.
- [287] F. James, *Statistical Methods in Experimental Physics*. World Scientific Publishing Co. Pte. Ltd., 2008.
- [288] V. Blobel and E. Lohrmann, *Statistische und numerische Methoden der Datenanalyse*. Teubner Verlag, 1 ed., 1998.
- [289] R. Barlow, “Lecture 9: Unfolding”, in *SLUO Lectures on Statistics and Numerical Methods in HEP*. 2000.
- [290] M. Schmelling, “The Method of reduced cross entropy: A General approach to unfold probability distributions”, *Nucl.Instrum.Meth.* **A340** (1994) 400–412.
- [291] S. Schmitt, “TUnfold: an algorithm for correcting migration effects in high energy physics”, [arXiv:1205.6201 \[physics.data-an\]](#).
- [292] P. C. Hansen, “The l-curve and its use in the numerical treatment of inverse problems”, in *in Computational Inverse Problems in Electrocardiology, ed. P. Johnston, Advances in Computational Bioengineering*, pp. 119–142. WIT Press, 2000.
- [293] W. Verkerke and D. P. Kirkby, “The RooFit toolkit for data modeling”, *eConf* **C0303241** (2003) MOLT007, [arXiv:physics/0306116 \[physics\]](#).

- [294] H1 and ZEUS Collaboration Collaboration, F. Aaron *et al.*, “Multi-Leptons with High Transverse Momentum at HERA”, *JHEP* **0910** (2009) 013, [arXiv:0907.3627 \[hep-ex\]](#).
- [295] H1 Collaboration Collaboration, A. Aktas *et al.*, “Muon pair production in ep collisions at HERA”, *Phys.Lett.* **B583** (2004) 28–40, [arXiv:hep-ex/0311015 \[hep-ex\]](#). Report-no: DESY-03-159.
- [296] H1 Collaboration Collaboration, F. Aaron *et al.*, “Determination of the Integrated Luminosity at HERA using Elastic QED Compton Events”, [arXiv:1205.2448 \[hep-ex\]](#).
- [297] G. Lafferty and T. Wyatt, “Where to stick your data points: The treatment of measurements within wide bins”, *Nucl.Instrum.Meth.* **A355** (1995) 541–547.
- [298] S. Chiba and D. L. Smith, “Impacts of Data Transformations on Least-Squares Solutions and Their Significance in Data Analysis and Evaluation”, *Journal of Nuclear Science and Technology* **31** no. 8, (1994) 770–781.
- [299] H1 Collaboration Collaboration, F. Aaron *et al.*, “Inclusive Deep Inelastic Scattering at High  $Q^2$  with Longitudinally Polarised Lepton Beams at HERA”, [arXiv:1206.7007 \[hep-ex\]](#).
- [300] CTEQ Collaboration Collaboration, R. Brock *et al.*, “Handbook of perturbative QCD; Version 1.1: September 1994”, *Rev. Mod. Phys.* (1994) .
- [301] J. Dainton, M. Klein, P. Newman, E. Perez, and F. Willeke, “Deep inelastic electron-nucleon scattering at the LHC”, *JINST* **1** (2006) P10001, [arXiv:hep-ex/0603016 \[hep-ex\]](#).
- [302] J. Sherman and W. J. Morrison, “Adjustment of an inverse matrix corresponding to a change in one element of a given matrix.”, *Ann. Math. Stat.* **21** (1950) 124–127.
- [303] V. Blobel, “Comments on  $\chi^2$  minimisation”, 2003.
- [304] V. Blobel, “Dealing with systematics for chi-square and for log likelihood goodness of fit statistics”, in *Statistical Inference Problems in High Energy Physics*. Banff International Research Station, 2006.
- [305] D. Stump, J. Pumplin, R. Brock, D. Casey, J. Huston, *et al.*, “Uncertainties of predictions from parton distribution functions. 1. The Lagrange multiplier method”, *Phys.Rev.* **D65** (2001) 014012, [arXiv:hep-ph/0101051 \[hep-ph\]](#).



## Acknowledgement

The last three years journey is ending but before the last sentence will be written, I would like to say “thank you” to all the great people who contributed to this work. I will always look backwards on a period of great inspiration, a wonderful time filled with characters, different as only a poet could describe, but always ready to help, discuss and share different perspectives on physics problems or other topics. I learned a lot from you! Names may fade with time but impressions are carried within a person for a lifetime.